NORTHWESTERN UNIVERSITY

Biochemical, spectroscopic, and computational studies of metalloenzyme structure and mechanism

A DISSERTATION

SUBMITTED TO THE GRADUATE SCHOOL
IN PARTIAL FULFULLMENT OF THE REQUIREMENTS

for the degree

DOCTOR OF PHILOSOPHY

Chemistry

By

Richard Jacob Jodts

EVANSTON, ILLINOIS

September 2023

ABSTRACT

Metalloenzymes catalyze remarkable reactions in Nature using transition metal ions. Common earth-abundant metals like copper, iron, zinc, and magnesium catalyze reactions that are the basis of life. These metal sites lend their chemistries to facilitate these reactions, making studying the structure and properties important in understanding the enzymes' abilities and the greater role in the life processes. This thesis combines techniques of biochemistry, inorganic spectroscopy, and computational chemistry to understand three different metalloenzyme active sites and mechanism.

The first part of this thesis investigates Nature's predominate enzyme for methane oxidation, particulate methane monooxygenase(pMMO). Specifically, it investigates on an atomic level the copper centers that perform this oxidation. These chapters highlight the importance of parallel structural and spectroscopy experiments to understanding metal sites within biology. These two techniques complement each other and allowed for more in-depth assignments and characterization of the copper centers. Importantly, within this thesis is the first evidence of a copper center in pMMO interacting with a hydrocarbon-based molecule, a product analogue. This finding identifies one of the copper sites as the site of methane oxidation, representing major progress in understanding the chemical mechanism of pMMO and methane oxidation in Nature.

This thesis also studies a diiron enzyme cofactor within an enzyme involved in a natural product biosynthesis, MbnBC. These chapters highlight again the need for parallel methods and approaches to better understand enzyme mechanism. Using parallel spectroscopy and biochemical activity assays, the active state of the catalytic cofactor was elucidated. Structural and additional spectroscopic studies were then used to determine the coordination environments of the catalytic iron ions as well as how substrate binds.

Lastly, a combination of biochemistry, spectroscopy, and computational methods was employed to understand the universal intermediates of one of the largest and most important superfamilies of metalloenzymes, the radical SAM enzymes. This section presents some of the first applications of computational methods, as well as new theory, to accurately characterizing these intermediates.

Together these three sections present progress in understanding the structure and mechanism of important metalloenzymes.

ACKNOWLEDGMENTS

There are so many individuals during the progress of my Ph.D. to whom I owe a debt of gratitude, aiding me in ways professional and personal throughout the year.

First, I must thank both of my thesis advisors, Amy and Brian, for their constant support and mentorship. I could have not imagined better mentors for my Ph.D. and being a joint student within your groups was a blessing. I thank you both also for your enduring patience with me during this process. Both of you taught me an incredible amount in scholarship, writing, and leadership. I continue to be inspired by both of your work ethics, intelligences, and abilities to communicate ideas clearly. I also will greatly miss near daily conversations about science and off-topic subjects, alike.

I am also ever grateful for having excellent lab members during my Ph.D. in the Rosenzweig and Hoffman labs. There are several individuals to thank specifically. Thank you to Dr. Grace Kenney for teaching me the world of methanobactin, as well as beginning my training in the Rosenzweig lab. I wish to thank Dr. Yun Ji Park for a very fruitful collaboration, working together to figure out MbnBC was an excellent experience and great science. I must thank Dr. Matthew Ross for a true introduction to working with pMMO and the Hoffman lab, especially for his patience in teaching me all the equipment. Dr. Anastasia Manesis, thank you for being an excellent coworker, teaching me many skills within the world of metalloenzymes and inorganic chemistry, as well as your constant motivation and support. Thanks to Dr. Hao Yang and Dr. Ajay Sharma for helping me out with all things ENDOR.

I want to also thank Dr. Peter Doan for being a dependable mentor in instrumentation, spin physics, and inorganic chemistry. When I had a problem I was stuck on I knew I could always turn to you for excellent advice in getting me back on track. A big thanks to Dr. Joshua Telser for educating me on so many matters. I will miss the both of you, and our many long conversations in the lab about science, Chicago, history, pop culture, and any other random topic of the day.

To Madi Ho and Frank Tucci thanks for not only being excellent coworkers, but also being great friends. Madi, it was fun to tackle the challenges of the instruments and hang out in the office with you every day. I look forward to seeing all your successes as you complete your studies. Frank, working on pMMO with you was my favorite research experience at NU, and I am very proud of the work we accomplished.

Thank you for being an excellent scientist and teaching me the world of CryoEM. I will really miss our RCC Thursdays.

There have been so many great collaborators during my Ph.D. I would specifically like to thank Professor Joan Broderick and her team at Montana State. Being a part of the radical SAM project team was a privilege. I would like to thank Roman Davydov for teaching me and working together on projects using gamma-irradiation and cryo-annealing EPR. Also, to Martín Mosquera - thank you for teaching me so much about computational chemistry. I really enjoyed our teamwork in solving some complex problems. There were mentors who introduced me to science and research at Wisconsin - Lynn Haynes, Professor Eric Streiter, Professor Judith Burstyn and Professor Thomas Brunold – all of who I still hold in such high regard. The opportunities you granted and lessons you taught me during undergraduate set me up for success during my Ph.D.

I also would like to thank individuals outside of the research setting who mean a lot to me. There were several friends I have made at Northwestern, and I enjoyed the time spent with you all. Many friends from high school, college, both in and out of Chicago, have had to endure my complaints or rants about science, yet were always willing to listen. I also would like to thank my family, especially my parents and my siblings, for their support during my Ph.D., but more importantly the support in following my interests to embark on it initially.

Lastly, thank you to Emily Ma. In my mind, there is no other person that helped me more during this time and thank you for all the amazing memories we share from this experience. From stresses to celebrations, I am so grateful each moment was with you. And I am very excited for our next chapter together.

TABLE OF CONTENTS

ABSTRACT 2
ACKNOWLEDGMENTS 3
TABLE OF FIGURES 8
CHAPTER 1: Introduction 9
Metalloenzymes 10
EPR and ENDOR spectroscopy 10
Particulate methane monooxygenase 11
Methanobactin Biosynthesis 13
Radical SAM Enzymes and Intermediates 15
CHAPTER 2: EPR and ENDOR analysis of detergent solubilized particulate methane monooxygenase 17
INTRODUCTION 18
RESULTS 21
X-band EPR analysis of Type II pMMO 21
^{15}N pulsed ENDOR to study Cu_B nitrogen coordination. 23
Stochastic CW ^{1}H ENDOR on the Cu_B Site 24
^{15}N Pulsed ENDOR of Cu_C nitrogen coordination 26
^{1}H ENDOR Analysis of the Cu_C site 29
METHODS 32
Growth of *Mc.* sp str. Rockwell. 32
Preparation of whole cell EPR and ENDOR Samples. 32
Mc. sp. str. Rockwell pMMO Purification. 32
pMMO Nanodisc Reconstitution. 33
Preparation of Purified *Mc.* sp. str. Rockwell pMMO EPR and ENDOR Samples. 34
EPR and ENDOR Measurements. 34
Hyperfine Sign Determination. 35
CHAPTER 3: Product analogue binding identifies the copper active site in particulate methane monooxygenase 36
INTRODUCTION 37
RESULTS 39
Cu_D occupancy is associated with the pMMO EPR signal and with methane oxidation activity: 39
Spectroscopic detection of an interaction between Cu_D and the product analog TFE 42
Conclusions: 47
METHODS 48
Culturing of methanotrophic bacteria 48
Isolation of pMMO-containing membranes 48
Solubilization and isolation of pMMO 48
Native lipid extraction 49
Membrane scaffold protein expression and purification 49
Nanodisc reconstitution and purification 50
Product analog loading 51

Methane oxidation activity assay ... 51
Inductively coupled plasma mass spectrometry (ICP-MS) ... 51
Metal depletion and reloading ... 52
EPR and ENDOR spectroscopy ... 52
Cryoelectron microscopy sample preparation ... 53
CryoEM data collection ... 54
CryoEM data processing ... 54

CHAPTER 4: The universal step in methanobactin biosynthesis is performed by a mixed-valent Fe(II)Fe(III) center ... **55**

INTRODUCTION ... **56**

RESULTS ... **58**
Determining reduced MbnBC is correlated with activity ... 58
X-band EPR of MbnA binding to the Fe(II)Fe(III) center ... 61
Site directed mutants establish a diiron cofactor over a triiron cofactor ... 63
Summary ... 64

METHODS ... **65**
Sample preparation ... 65
EPR Measurements ... 66
Activity assays ... 66

CHAPTER 5: MbnBC active site and substrate binding mechanism elucidated by ENDOR spectroscopy ... **68**

INTRODUCTION ... **69**

RESULTS ... **71**
EPR Spectra of ascorbate-reduced MbnBC ... 71
^{15}N Pulsed ENDOR of mixed-valent MbnBC ... 71
^{1}H CW ENDOR of mixed-valent MbnBC ... 73
ENDOR studies of the MbnABC complex ... 76

CONCLUSIONS ... **78**

METHODS ... **79**
Protein expression and purification: ... 80
ENDOR and EPR Spectroscopy ... 80
Fe(II)Fe(III) hyperfine coupling analysis ... 80

CHAPTER 6: Computational chemistry applied to radical SAM enzyme intermediates ... **82**

RESULTS ... **84**
Analysis and DFT modeling of the 5'-dAdo radical: ... 84
Computational modeling and EPR analysis of SPL stable protein radicals: ... 86
Computational modeling to understand the Jahn-Teller effect in SAM Enzymes: ... 89
Computational Aspects ... 94
DFT of the 5'dAdo radical ... 94
DFT of the SPL residue radicals ... 95
Jahn-teller computations ... 95

CHAPTER 7: Computational description of alkylated multi-iron clusters ... **96**

INTRODUCTION ... **97**

THEORY ... **99**

RESULTS **104**
Validation of 2C-DFT through comparison to CASSCF computations on the models and to experiment 104
2C-DFT of experimentally observed alkylated-4Fe4S clusters. 107
CONCLUSIONS **109**
METHODS **110**
CHAPTER 8: Conclusions and Outlook **111**
PROSPECTUS **112**
Advances in understanding particulate methane monooxygenase 112
Implications from determining the mechanism of MbnBC 113
Establishing computational modeling of radical SAM enzyme intermediates 114
FUTURE WORK **115**
Determining metal loading in the pmoC subunit 115
EPR and ENDOR of Ammonia monooxygenase 118
REFERENCES **121**
APPENDIX 1: Supplemental Figures **132**
APPENDIX 2: Supplemental Tables **171**

TABLE OF FIGURES

Figure 1.1 pMMO structure and reaction. 12
Figure 1.2 Structure of Methanobactin. 14
Figure 1.3 Structure of the 4Fe-4S cofactor of radical SAM enzymes and the intermediate W 15
Figure 2.1. X-ray crystal structure of pMMO.. 19
Figure 2.2. CW X-band EPR spectra of *Mc.* sp. str. Rockwell pMMO 22
Figure 2.3. 2K Q-band ^{15}N pulsed ENDOR on the *Mc.* sp. str. Rockwell in vivo pMMO Cu_B site.. 23
Figure 2.4. ^{1}H CW Stochastic ENDOR of the Cu_B site. 25
Figure 2.5. 2K Q-band EPR of purified and in vivo pMMO. 27
Figure 2.6. Pulsed ^{15}N ENDOR of the Cu_C site..... 28
Figure 2.5. ^{1}H CW Swept ENDOR of pMMO Cu_C sites.. 30
Figure 3.1 CryoEM structure of M. capsulatus (Bath) pMMO in native lipid nanodiscs.. 38
Figure 3.2..... 41
Figure 3.3. ENDOR spectroscopic analysis of TFE interacting with the pMMO copper sites in native lipid nanodiscs..... 44
Figure 3.4. ENDOR detection of a specific interaction of the pMMO Cu_D site with TFE in native lipid nanodiscs..... 45
Figure 4.1. Reaction catalyzed by MbnBC and a model for the MbnB Fe binding site..... 56
Figure 4.3. EPR spectra of ^{56}Fe MbnBC treated with ascorbate.. 59
Figure 4.4. Reaction of MbnBC with MbnA..... 60
Figure 4.5. Effect of MbnA on the EPR spectrum of redMbnBC_asc. 61
Figure 4.6. EPR spectra of D208S and H210S variants.. 64
Figure 5.1. ..... ./70
Figure 5.2. Q-band Davies ENDOR of ^{15}N labeled mixed-valent MbnBC. 72
Figure 5.3. Q-band CW ENDOR spectra of mixed-valent MbnBC 74
Figure 5.4. The mixed-valent MbnBC active site architecture 76
Figure 5.5 ^{1}H CW ENDOR of MbnA binding to MbnBC mixed-valent diiron center. 77
Figure 5.6 Schematic of the MbnBC mechanism of MbnA and O_2 binding..... 79
Figure 6.1 Radical SAM mechanism schematic.. 83
Figure 6.2. DFT model of 5'dAdo T..... 85
Figure 6.3. The X-band EPR simulations of Val172• with the hyperfine coupling parameters from DFT.. 87
Figure 6.4. Computational Models of V172 and I172 radicals. 88
Figure 6.5. X-band EPR simulation of Ile172•. 89
Figure 6.6. Comparisons of SAM configurations that yield photoinduced cleavage to form 5′-dAdo· or ·CH3,..... 91
Figure 6.7: DFT computed energy levels and MO diagrams for $S(CH_3)_3^+$ 92
Figure 6.8: Splitting of 2E orbital degeneracy with JT distortion..... 93
Figure 7.1. Representative structures of three [4Fe-4S] clusters with an alkylated unique iron..... 97
Figure 7.2. Structures of computational models examined in this chapter.. 99
Figure 7.3. 2C-DFTmodel for the analysis of the HFCC of an alkyl bound to a [4Fe-4S] cluster 100
Figure 8.1 ^{15}N Davies ENDOR of Nanodisc pMMO and detergent pMMO..... 116
Figure 8.2 ^{15}N Mims ENDOR of Nanodisc pMMO. 117
Figure 8.3 X-band EPR of nanodisc AMO. 119
Figure 8.4 Q-band Davies ^{1}H and ^{14}N ENDOR of Nanodisc AMO..... 120

CHAPTER 1: Introduction

Metalloenzymes

Nature's catalysts, enzymes, have long been studied by chemists due to their ability to perform impressive chemical transformations under ambient conditions. About 40% of all identified enzymes have been found to be metalloenzymes, or enzymes that coordinate a metal ion with amino acid residues within the protein matrix.[1, 2] These metal ions in enzyme can perform diverse functions such as electron transfer, redox chemistry, or substrate activation. During catalysis, they can obtain high valent states and form highly reactive intermediates to accomplish their tasked chemistry.[3]

The number of metalloenzymes is ever expanding, as well as the knowledge of the relationship between transition metal properties, function, and enzyme structure - all of which is of interest to the field of bioinorganic chemistry.[1, 4, 5] These metal sites can also play structural roles, and discerning the composition, role and active form of metal cofactors within a protein is important to understanding biology.

Several metalloenzymes are already utilized in industrial settings or are targets for pharmaceuticals. Understanding their mechanisms and properties can improve these applications. Also driving the study of metalloenzymes is the progress in the ability to take lessons from these systems to apply in a widespread of areas. This thesis advances the understanding of three different metalloenzyme systems described below.

EPR and ENDOR spectroscopy

Metalloenzyme metal cofactors can often access ground states in which they have unpaired electrons (paramagnets). Because of this, electron paramagnetic resonance (EPR) spectroscopy has long been employed to study biological systems.[6] The EPR experiment consists of a magnetic field applied and swept while a microwave field at a fixed energy, which for this thesis is either 9 GHz for X-band or 35 GHz for Q-band, is also applied.[7] This causes resonant transitions to occur at field positions characteristic of the electronic structure, which are described in terms of a g-tensor, and usually take the tensor form of g_x, g_y, and g_z. These three g-values are reflective of the environment of the paramagnet, and their field position and intensity offers a wealth of information including the identity of the ion, the spin and oxidation state, and even the coordination environment for certain centers. EPR is incredibly useful in studying metalloenzymes due to the ability to directly probe the metal site and its vicinity without interference of the many other atoms that are within the protein matrix.

Electron nuclear double resonance spectroscopy (ENDOR) expands on EPR and is a powerful technique used to study the electronic structure of paramagnetic molecules.[6, 8, 9] ENDOR has been described as “EPR detected NMR” due to its ability to provide information about the interactions between unpaired electrons and nuclear spins in the molecule.[6, 10] ENDOR works by first using microwaves to excite the molecule’s unpaired electron to be in resonance within the high and low energy states. Then, a radiofrequency (RF) is applied at frequencies to selectively excite the nuclear spin of a nucleus in the molecule. The resulting changes in the EPR signal are detected, and one then can determine the hyperfine interaction of the nucleus with the paramagnetic center. The hyperfine coupling (denoted A, and which makes up an A-tensor) is observed as a doublet centered at the Larmor frequency (ν_N) and separated by $|A|$ or as two peaks separated by $2\nu_N$ and centered at $|A/2|$.[11] The observed A across the magnetic field where EPR signals are present provides detailed information about the identity, position, and orientation of nuclei in respect to the metal site. While very large hyperfine splittings can be observed in the EPR spectrum, multiple atoms of interest that couple to the center are lost in the EPR linewidth, whereas with ENDOR they are resolved. In this thesis, both continuous wave (CW) and pulsed Q-band ENDOR are utilized. These methods allows for determination of the coordination environment, the electronic structure of the ligand field, or the geometry of substrate binding to the metal center. Another advantage is the ability to measure hyperfine only on signals present at the field where the experiment is performed, which is helpful when discerning different paramagnets or states of a paramagnetic center.

Particulate methane monooxygenase

Methane (CH_4) is a potent greenhouse gas and is the second most abundant a greenhouse gas in the atmosphere after carbon dioxide (CO_2). Methane is as a potential fuel source, and could also be converted to desirable chemicals, which could be an economic driver while also mitigating the effects on the climate. However, this is challenging due to the 105 kcal/mol C-H bonds that require functionalization for this to occur. Current industrial methods rely on Fischer-Tropsch chemistries, which are expensive in process as well as infrastructure.

Methanotrophs, a subset of bacteria that aerobically oxidize methane, perform conversion of methane under ambient conditions. These bacteria utilize methane as their sole source of carbon and primarily utilize the membrane-bound particulate methane monooxygenase (pMMO) to catalyze the

oxidation of methane to methanol (**Figure 1.1**). The study of methanotrophs and their metabolic pathways is an active area of research, with potential applications of producing biofuels and bioplastics from methane. However, successful deployment in biotechnology requires understanding the pMMO active site and mechanism.

pMMO is a trimer with each protomer consisting of three subunits, denoted PmoA, PmoB, and PmoC. It has been established that pMMO requires copper for activity, and several copper binding sites have been observed in X-ray crystallographic structures, but the composition required for activity as well as the identity of the active site remain open questions due to the challenges associated with studying pMMO.[12, 13]

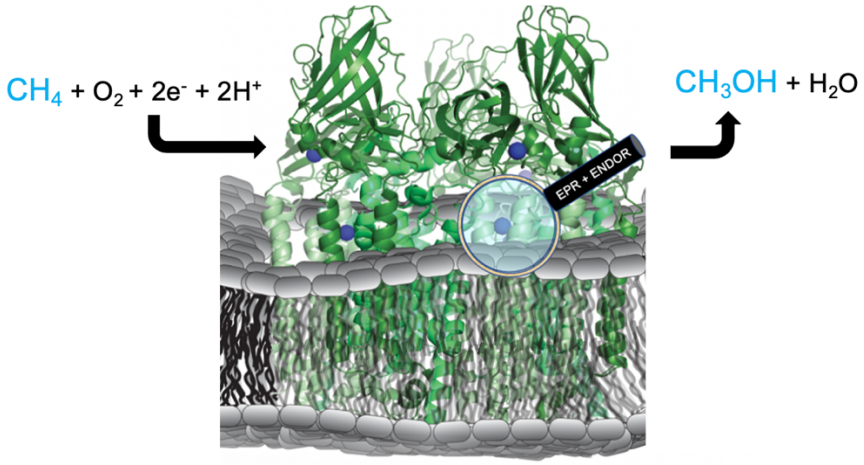

Figure 1.1 pMMO structure and reaction. This figure depicts pMMO embedded in the natural membrane bilayer as well as the balanced methane oxidation reaction it catalyzes. It also represents how EPR and ENDOR spectroscopy can easily analyze the copper centers within.

At the beginning of my Ph.D., the PmoB metal binding site (denoted Cu_B) was unambiguously assigned as a monocopper center, resolving debate in the field. This was done by an extensive EPR and ENDOR study.[14] As stated above, these methods are powerful tools in studying metalloenzymes, and provide a wealth of information about the copper centers within the 300 kDa enzyme complex. This report resolved the EPR spectra of isolated pMMO as a sum of two signals from two distinct type 2 copper centers through biochemical and double electron-electron resonance (DEER) spectroscopy analysis. This study provided the foundation for paramagnetic spectroscopic studies of pMMO.

Chapter 2 expands upon that foundational study, continuing characterization of the Cu_B site. More importantly, this work characterized the other Cu(II) center observed in the EPR, both in electronic and atomic structure, and suggested tat it is the site of methane oxidation due to the presence of an open coordination site.

During my Ph.D., significant progress in the use of membrane mimetic technologies for studying pMMO occurred.[15] pMMO embedded into a nanodisc, a system consisting of a membrane scaffold protein and lipids extracted and purified from the native organism, yielded the highest in vitro methane oxidation activity. This system also granted the ability to solve the structure of pMMO by cryogenic electron microscopy (cryoEM).[16] These cryoEM structures revealed a new metal binding site in the PmoC subunit, denoted the Cu_D site, and it was suggested this was the active site of pMMO.

Chapter 3 addresses questions raised by the cryoEM structures through a combination of biochemistry, cryoEM, and EPR/ENDOR spectroscopy. This work first rationalizes that in the nanodisc, the new observed metal binding site by cryoEM is indeed a copper center, Cu_D. More importantly, a parallel study of cryoEM structural determination and ENDOR of pMMO incubated with an inhibitor/product analog highly suggests that Cu_D is the site of catalysis. These results not only identify the active site, but provide geometric and structural information that can inform future mechanistic work. This progress in characterizing the pMMO copper centers is an important step towards utilizing the enzyme as a biotechnology or bioinspired technology.

Methanobactin Biosynthesis

Natural product biosynthesis is an emerging field in biochemistry, especially since the advances of genome sequencing technologies. The biosynthetic pathways typically involve the modification of a precursor molecule through a series of enzymatic reactions to produce the final product.[17] This area has drawn interest not only due to the products formed, which include complex organic compounds with a range of desired bioactivities, but also because the enzymes perform impressive reactions that current laboratory synthetic methods cannot achieve, neither in terms yield or a single step.[18]

As mentioned above, there is a correlation of pMMO copper centers occupancy and its ability to catalyze methane oxidation to methanol. pMMO is overexpressed in methanotrophs, which require copper levels four-fold higher than iron for optimal growth,[19, 20] which is unlike other organisms that

typically require higher iron levels.[20] To obtain this copper, some methanotrophs biosynthesize and secrete of a high affinity copper chelator known as methanobactin (Mbn) (**Figure 1.2**). Past work involved the identification, purification, and structural determination of these molecules from various species of methanotrophic bacteria.[20-24]

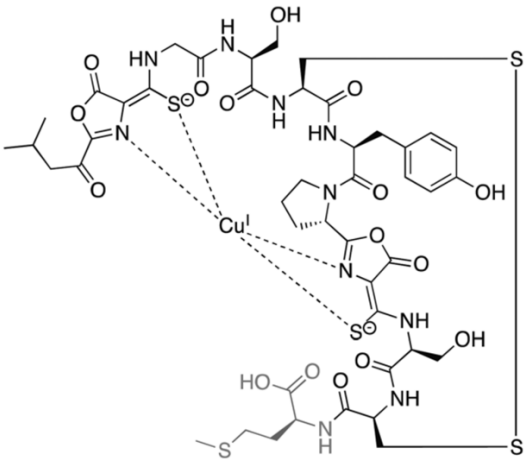

Figure 2.2 Structure of Methanobactin. Depicted is the *Ms. trichosporium* OB3b Mbn which was characterized via X-ray crystallography and nuclear magnetic resonance. All Mbns chelate Cu with two nitrogen and two sulfur atoms derived from nitrogen-containing heterocycles and neighboring thioamide groups

Recent studies have focused on understanding the Mbn biosynthesis, starting from several bioinformatic studies.[25, 26] These studies lead to the identification of operons encoding the Mbn precursor peptide (MbnA) as well as many putative biosynthetic enzymes and transport proteins. These operons are found in snon-methanotrophic bacteria as well, suggesting a broader role for Mbns in copper homeostasis or metal acquisition. Two proteins of unknown function ae also conserved in all the Mbn operons. These proteins in a complex, denoted MbnB and MbnC, were found to catalyze the transformation of two cysteine residues in MbnA to oxazolone rings and thioamide groups, present in all Mbns characterized thus far, and required for the copper binding by Mbns.[27] This complex requires iron and dioxygen to perform MbnA modification[27], but the identity of the active site cofactor and the mechanism of the catalysis remained an open question.

Chapter 4 tackles the identity of the active cofactor in MbnBC. Here parallel biochemistry and spectroscopy experiments were performed to identify the iron cofactor responsible for the universal step in Mbn biosynthesis. This study is expanded in **Chapter 5,** describing ENDOR experiments on this active cofactor to determine its coordination environment and electronic structure. The initial mechanistic steps of

substrate binding and oxygen activation by the iron center were also elucidated through advanced paramagnetic spectroscopies. These chapters not only advance understanding of Mbn biosynthesis, but also expand the knowledge of iron cofactor structure and mechanism.

Radical SAM Enzymes and Intermediates

Radical *S*-adenosyl-L-methionine (SAM) enzymes are a superfamily of enzymes that play critical roles in a wide range of biological processes.[28] These enzymes contain a four-iron-four-sulfur [4Fe-4S] cluster where three of the irons are chelated by conserved cysteine residues and the remaining iron chelates a molecule of SAM through the methanine amino group.[29] In radical SAM enzymes, substrate binding induces electron transfer from the reduced $[4Fe\text{-}4S]^{+}$ cluster, which then cleaves the 5'C-S bond in SAM to release a 5'-dAdo· radical. This highly reactive radical abstracts a hydrogen atom from substrate (usually a C-H bond activation) as part of many metabolic pathways and biosynthesis of cofactors and natural products.[30, 31] Prior to substrate H-atom extraction, the liberated 5'-dAdo· first forms a universal paramagnetic organometallic intermediate, denoted Ω where the unique Fe of the cluster, in a $[4Fe\text{-}4S]^{3+}$ state forms a Fe-C5' bond (**Figure 1.3**).[32, 33]

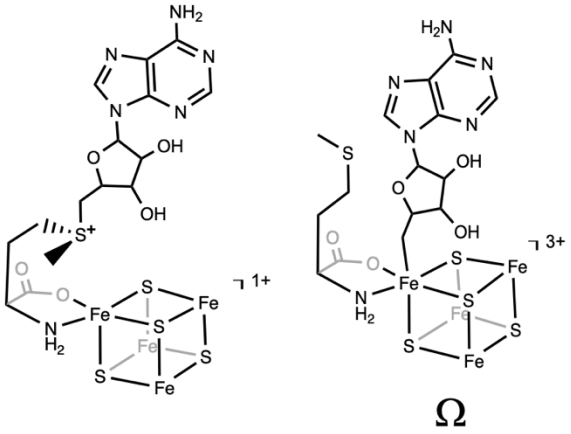

Figure 3.3 Structure of the 4Fe-4S cofactor of radical SAM enzymes and the intermediate Ω

The 5'-dAdo·, Ω, and H-abstracted substrates are all intermediates that lend themselves to study and characterization by paramagnetic spectroscopies. Studies of radical SAM enzymes have utilized EPR and ENDOR to characterize the cofactor successfully, but as **Chapter 6** and **Chapter 7** show, recently they

have been expanded using computational chemistry. Density function theory (DFT) methods have been utilized in the past few decades to calculate and describe the electronic structure of multiatom systems.[34] In **Chapter 6,** we use DFT to characterize intermediates observed in radical SAM enzymes, enhancing the EPR description of radical intermediates and states. **Chapter 7** begins work to accurately describe the electronic structure of the Ω intermediate through a combination of Broken-Symmetry DFT and theory. These two chapters show how biochemistry, spectroscopy, and computational chemistry methods together successfully elucidate important steps in the mechanism of this enzyme superfamily.

CHAPTER 2: EPR and ENDOR analysis of detergent solubilized particulate methane monooxygenase

Results from this chapter have been published previously in the following article:

R.J. Jodts, M. O. Ross, C. W. Koo, P. E. Doan, A. C. Rosenzweig, B. M. Hoffman, J. Am. Chem. Soc, **2021**, 143, 15358−15368

INTRODUCTION

Copper-dependent monooxygenase enzymes exploit the Cu(I)/Cu(II) redox couple to activate O_2 and insert one oxygen atom into organic substrates with strong C-H bonds, including the alpha carbon of glycine (C-H bond enthalpy, 87 kcal/mol),[35] polysaccharides (~100 kcal/mol),[36] and methane, with the strongest C-H bond (105 kcal/mol).[37] The enzymes that oxidize these three substrates, respectively peptidylglycine α-hydroxylating monooxygenase (PHM),[38] lytic polysaccharide monooxygenases (LPMOs), and particulate methane monooxygenase (pMMO), have been studied intensively with the goal of elucidating their chemical mechanisms. Members of the PHM family contain two well-characterized monocopper centers[39] (denoted as Cu_M and Cu_H),[38] while LPMO enzymes feature a single histidine brace-coordinated mononuclear copper active site.[40, 41] By contrast, mechanistic characterization of pMMO has been hindered by the absence of a molecular understanding of its active site location, nuclearity, and coordination environment.[37, 42] Such details are not only a prerequisite for mechanistic characterization, but are also crucial if pMMO is to be utilized in biotechnological applications.[43]

pMMO is an integral-membrane enzyme comprising three subunits, PmoA, PmoB, and PmoC, arranged in a 300 kDa $\alpha_3\beta_3\gamma_3$ complex. On the basis of multiple pMMO crystal structures, two copper centers have emerged as potential active sites, one located in PmoB (Cu_B) and one located in PmoC (Cu_C) (**Figure 2.1**). The Cu_B site includes three histidine ligands, His29, His133, and His 135, using type II *Methylocystis* (*Mc.*) species (sp.) strain (str.) Rockwell pMMO numbering, and in crystal structures has been modeled as being both mononuclear and dinuclear.[13, 44-46] However, several recent studies have firmly established its identity as mononuclear, including quantum refinement of the original *Methylococcus (M.) capsulatus* (Bath) pMMO crystal structure[47] and native top-down mass spectrometry (nTDMS), which revealed the presence of a single copper ion localized to the amino terminus of PmoB.[15] Most importantly, comprehensive electron

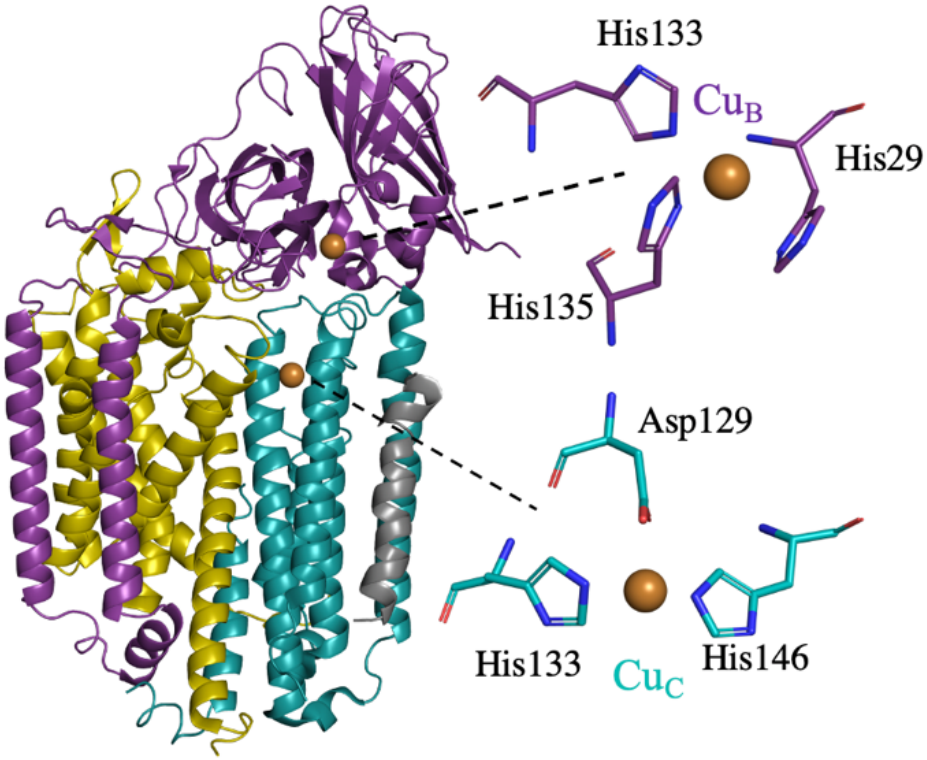

Figure 2.1. X-ray crystal structure of pMMO. A single protomer from the crystal structure of *Mc.* sp. str. Rockwell pMMO (PDB accession code 4PHZ). PmoA is light gold, PmoB is purple, PmoC is teal, and an unidentified helix is gray. The two copper ions are shown as spheres and to the right are expanded to show the modeled coordinating residues.

paramagnetic resonance (EPR) and electron nuclear double resonance (ENDOR) spectroscopic analysis of *M. capsulatus* (Bath) whole cells cultivated on ^{15}N isotopically enriched media indicated that the Cu_B site of this type I pMMO is mononuclear, revealed its coordination environment (three histidine ligands and an axially bound water), and showed that it is primarily present in the cell as $Cu_B(II)$.[14] The assignment of Cu_B as mononuclear is also supported by a recent reinvestigation of pMMO by X-ray absorption spectroscopy.[48] Given the saturated equatorial coordination found for Cu_B and its presence as Cu(II) even in vivo, it is not likely to be the site of dioxygen and methane binding. In support of this conclusion, the three Cu_B histidine ligands are not conserved in a subset of pMMOs from type III methanotrophic verrucomicrobia.[49]

Comprehensive EPR and ENDOR analysis of the Cu_B site was possible because it is conveniently monitored without overlap from the signal from Cu_C, which is readily reduced to Cu(I). However, the Cu_C EPR signal overlaps with that of Cu_B, and cannot be observed unhindered by selective reduction of Cu_B.

Moreover, our previous detailed EPR and ENDOR studies[14, 50] focused on pMMO from *M. capsulatus* (Bath), a type I methanotroph, while the crystal structures guiding the interpretations include pMMOs from type II methanotrophs as well. These two methanotroph subclasses differ in cell morphologies, metabolic aspects, and lipid content,[51] and their pMMOs exhibit structural differences, including an unidentified helix in the type II methanotroph pMMO structures.[49] In addition, some type I methanotroph pMMOs contain a third "bis-His" copper site in the PmoB subunit[13] that has not been observed in the type II methanotroph pMMOs.[45, 52, 53]

In this report we show that the *Mc.* sp. str. Rockwell type II pMMO likewise contains two monocopper sites and that the electronic and coordination environment of the Cu_B site is conserved across pMMOs from both types I and II methanotrophs. In doing so, we have collected EPR spectra of *Mc.* sp. str. Rockwell whole cells and of its purified/reduced type II pMMO, and have used ^{1}H and ^{15}N ENDOR to probe its Cu_B site, while carrying out additional measurements on the type I *M. capsulatus* (Bath) pMMO that reveal further details of the Cu_B site.

Of primary importance, ^{15}N ENDOR studies of Cu_C were carried out on purified ^{15}N, ^{63}Cu isotopically enriched pMMOs from both type I and type II methanotrophs by performing the measurements at fields where the Cu_C EPR signal does not overlap that of Cu_B. The results are the same for the two pMMO types, and for the first time identify the presence of two histidyl ligands that coordinate the spectroscopically observed Cu_C, thereby showing that the spectroscopic Cu_C is appropriately assigned to the conserved and crystallographically observed metal-binding site in the PmoC subunit. ^{1}H ENDOR spectra in combination with the crystallographic data further suggest that Cu_C exhibits only three equatorial ligands, and reveal that it is without axial ligation. The redox activity of the strictly conserved Cu_C site under conditions in which the Cu_B site remains oxidized, in conjunction with the nitrite interaction at the open coordination site of Cu_C,[14] and the nTDMS data correlating the extent of copper binding to PmoC with activity,[15] together strongly suggest that Cu_C is the active site of biological methane oxidation by pMMO, a conclusion that lays the foundation for future mechanistic proposals and studies.

RESULTS

X-band EPR analysis of Type II pMMO

CW X-band EPR spectra of ^{15}N, ^{63}Cu enriched *Mc.* sp. str. Rockwell cells (**Figure 2.2A**) exhibit a strong signal from a single type 2 Cu(II) site (**g** = [2.24, 2.07, 2.035], ^{63}Cu hyperfine splitting, $A_{||}$ = 580 MHz) and a hyperfine pattern associated with the $g_{\perp}$ region of the spectrum that arises from coordinated ^{15}N. In addition, an isotropic g ~ 2 radical signal overlaps with $g_{\perp}$ region. This spectrum is consistent with previous EPR investigations of whole cell methanotrophs grown under copper-replete conditions,[54, 55] and is identical to that assigned to the *M. capsulatus* (Bath) Cu_B site.[14] When the membranes are isolated, the radical signal mostly disappears, the Cu_B signal persists, and a minority Cu(II) signal appears (**g** = [2.31, 2.07, 2.05], ^{63}Cu $A_{||}$ = 440 MHz coupling) (**Figure 2.2B**). The latter is shown by simulation to represent ~15% of the total Cu(II) signal and is assigned as the previously observed Cu_C signal.[14] This spectrum is the first reported observation of the Cu_C signal in a membrane-bound type II pMMO. Once the enzyme is solubilized and purified, the Cu_C center becomes further oxidized and simulations of the composite Cu_B and Cu_C spectrum show that within error this EPR signal comprises equal contributions from Cu_B and Cu_C (**Figure 2.2C**), the observed proportions varying somewhat with sample preparation.

An overlay of the spectra of solubilized/purified *M. capsulatus* (Bath) (type I) and *Mc.* sp. str. Rockwell (type II) pMMO **(Figure S2.1**) shows that each site is identical between the two enzymes. This is the first report of preparations of a type II pMMO that, like the type I pMMO, exhibit both Cu_B and Cu_C signals in near equal occupancy and without additional adventitious Cu(II) signals (**Figures S2.2, S2.3**). Importantly, the presence of the Cu_C signal in the type II *Mc.* sp. str. Rockwell pMMO completely eliminates the possibility that this signal in the type I *M. capsulatus* (Bath) pMMO[14] derives from the bis-His site in its PmoB subunit. The type II pMMOs, including *Mc.* sp. str. Rockwell pMMO, lack one of the two histidine residues that comprise this site.

Notably, there is an outlier crystal structure of *Mc.* sp. str. Rockwell pMMO in which the Cu_C site is occupied by Zn(II), which binds a fourth ligand, modeled as PmoC residue Glu201.[10] In a recent computational study, this residue was assumed to be a ligand when Cu(II) is bound in the Cu_C site.[56] However, this cannot be so. If such a 4-coordinate 'square planar' Cu(II) site with two nitrogen and two oxygen ligands were present, the ^{63}Cu $A_{||}$ value would differ significantly (closer to ~500 MHz)[57] from that

observed for Cu_C (440 MHz). Correspondingly, the Cu_C site has a ratio, $g_{||}/A_{||}$ = 156 cm ($A_{||}$ = 1.46 x 10^{-2} when expressed in wavenumbers (cm^{-1})), whereas such square-planar complexes have ratios, $g_{||}/A_{||}$ ~ 105-135 cm.[58] Thus, it is clear that Glu201 is only a ligand when Zn(II) occupies the site, and computational models based on its coordination to Cu[56] cannot reflect the biological mechanism.

Addition of eight equivalents of ascorbate to purified *Mc.* sp. str. Rockwell pMMO eliminates the Cu_C signal, leaving the Cu_B signal with unchanged amplitude (**Figure 2.2D**) and indicating that the reduction potential of Cu_B is substantially more negative than that of Cu_C. An ability of the Cu_C site to cycle between the Cu(I) and Cu(II) states is consistent with proposals that it is the site of oxygen activation and methane conversion. Interestingly, we followed the previously published methods for isolation of *Mc.* sp. str. Rockwell pMMO and included as a necessary step the addition of $CuSO_4$ during cell lysis in order to achieve enzyme activity upon addition of detergent. An examination of purified samples by EPR

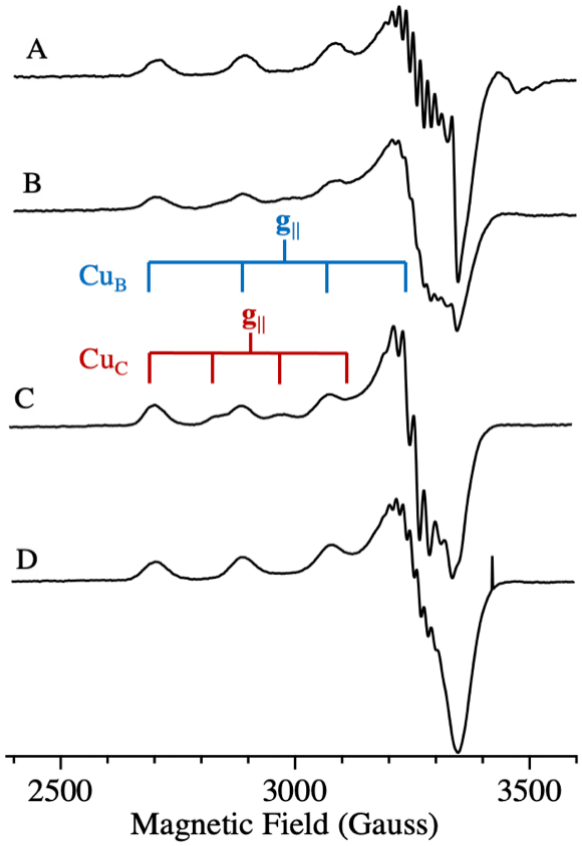

Figure 2.2. CW X-band EPR spectra of *Mc.* sp. str. Rockwell pMMO. (A) In vivo pMMO. (B) Membrane-bound pMMO. (C) Purified pMMO. The brackets indicate the ^{63}Cu $A_{||}$ hyperfine splitting of the two signals present in the spectra. (D) Purified/reduced pMMO. *Conditions*: 9.36 GHz microwave frequency, 200 μW MW power, temperature 20K, 320 ms time constant, 12.5 G modulation, 5 scans each, 10 G/s scan rate

(**Figure S2.4**) that did not include this step shows only the Cu_B spectrum, similar to purified reduced enzyme (**Figure 2.2D**), without the Cu_C(II) signal seen when this step is included (**Figure 2.2C**). This observation provides further evidence that the presence of a copper ion in the Cu_C site is required for methane oxidation.

^{15}N pulsed ENDOR to study Cu_B nitrogen coordination

To further probe the molecular and electronic structure of the *Mc.* sp. str. Rockwell pMMO Cu_B site, we examined whole cell and purified/partially reduced samples by ENDOR. Our previous EPR and ENDOR studies of pMMO from the type I methanotroph *M. capsulatus* (Bath) clearly showed that the crystallographic Cu_B site is mononuclear.[14] The use of quantitative ^{15}N ENDOR to count nitrogen ligands to Cu_B established that it is coordinated by four nitrogenous ligands, three from histidyl imidazoles and one from the terminal NH_2 of His33 (*M.* capsulatus (Bath) pMMO numbering). Using ^{15}N, ^{63}Cu-enriched type II *Mc.* sp. str. Rockwell whole cells, Davies ENDOR at g = 2.25 reveals two ^{15}N signals of A = ~ -48 and A = ~ -55 MHz (**Figure 2.3**, **left**). The PESTRE method shows that the ^{15}N couplings (which correspond to the sign of A/gN) are negative, indicating a positive spin density on the coordinated ^{15}N **(Figure S2.5**). This is expected for in plane Cu(II)-coordinated nitrogen. As reported previously for the type I *M.* capsulatus (Bath)

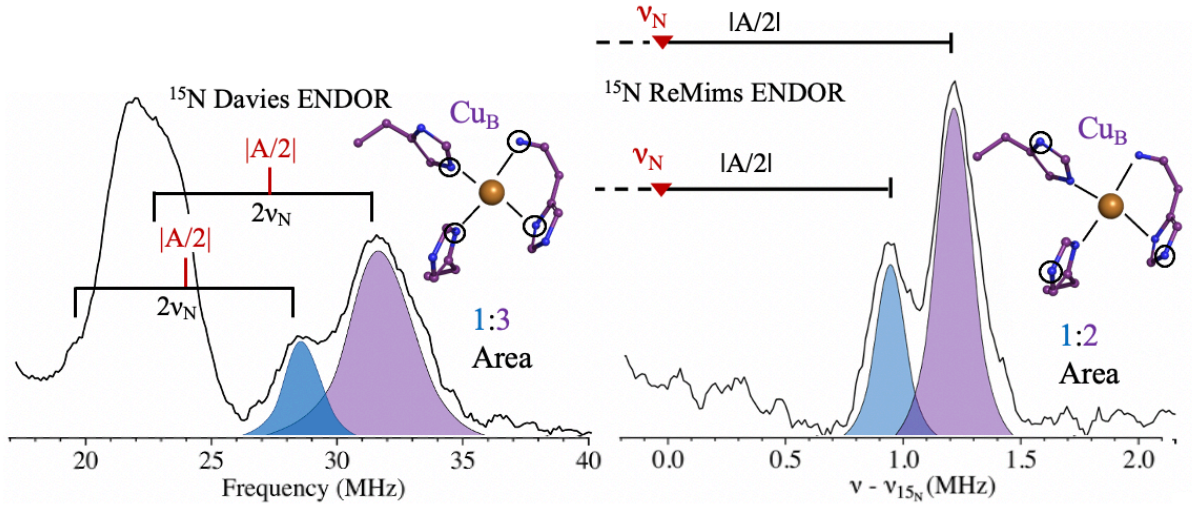

Figure 2.3. 2K Q-band ^{15}N pulsed ENDOR on the *Mc.* sp. str. Rockwell in vivo pMMO Cu_B site. (Left) Pulsed Davies ENDOR spectra at g = 2.25 of directly coordinated ^{15}N. The brackets represent twice the ^{15}N Larmor frequency, and are centered at the value of |A/2| (red)|. (Right) Doan/ReMims spectra at g = 2.24 for distally coupled ^{15}N ("backside nitrogen"), ^{15}N Larmor subtracted for centering. The solid right bracket represents |A/2|, where (▼) represents the ^{15}N Larmor frequency. To show the analysis better, the ν- peaks are omitted, but see below. *Davies ENDOR conditions*: 34.684 GHz, 100 ms repetition time, π = 80 ns, τ = 600 ns, T_{RF} = 35 μs, RF tail = 5μs, ~100 scans. *ReMims conditions:* 34.712 GHz, 20 ms repetition time, π = 60 ns, τ1 = 200 ns, τ2 = 400 ns, TRF = 60 μs, and RF tail = 10 μs.

pMMO, Gaussian fitting of the peaks yields areas with a 1:3 ratio, demonstrating that four nitrogens are coordinated to Cu_B, and the signs of the couplings are equivalent as well.[14]

To identify the four Cu_B nitrogenous ligands, we probed for weakly-coupled ^{15}N signals from the remote ("backside") nitrogens of histidyl imidazole ligands using ReMims protocol.[59] Spectra collected at g = 2.24 show ^{15}N signals exhibiting hyperfine couplings of ~1.7 MHz and ~2.4 MHz (**Figure 2.3, right**) characteristic of such remote nitrogens. These signals have relative areas of 1:2, indicating that three of the four nitrogenous ligands to Cu_B in type II as in type I pMMOs, are histidyl imidazoles, with the fourth then assignable to the terminal amine. Finally, the values of the hyperfine couplings to both the coordinated and the remote ^{15}N of the histidines bound to the Cu_B sites are essentially the same for *M. capsulatus* (Bath) pMMO and *Mc.* sp. str. Rockwell pMMO, as is the coupling to the amine, demonstrating a complete equivalence of the Cu_B coordination in the two pMMO types. This identification of the coordination sphere of Cu_B in both types of pMMO, combined with other work identifying Cu_B as a monocopper site,[15, 47, 48] is incompatible with a recent cryoelectron microscopy structure of *M. capsulatus* (Bath) pMMO.[60]

Stochastic CW ^1H ENDOR on the Cu_B Site

To refine our picture of the electronic and molecular structure of the Cu_B site, we employed 35 GHz field modulated stochastic CW ^1H ENDOR on whole cell *Mc.* sp. str. Rockwell. The stochastic technique resolves line shapes better by eliminating relaxation distortion of the ENDOR response, although with some sacrifice in signal intensity, and with "inversion" of the distant-ENDOR responses with small couplings as a consequence of relaxation effects.

The single-crystal-like ^1H spectrum collected at the $g_{||}$ edge of the EPR spectrum for the Cu_B site (at a field corresponding to a g value of g = 2.31) shows a pair of broad responses that appear to be the superposition of two doublets with ^1H couplings of A ~13 MHz and ~10 MHz (**Figure 2.4, top**). PESTRE measurements of the hyperfine coupling signs indicate that the intensity associated with the larger coupling exhibits a negative coupling, A ~ -13 MHz, while that for the smaller exhibits a positive one, A ~ +10 MHz (**Figure S2.6**). These signals are lost upon exchange into a D_2O buffer (**Figure 2.4**, **top,** gray spectrum),

indicating that they arise from two distinct classes of exchangeable protons. Similar observations were made for the type I *M. capsulatus* (Bath) enzyme,[14] except that the previous study used only Davies pulsed ENDOR, and did not resolve the presence of two distinct classes of exchangeable protons. In addition, there is a well-resolved doublet from non-exchangeable proton(s), with a coupling of A ~ +5 MHz (sign determined by PESTRE protocol), as well as (inverted) distant-ENDOR signals near ν_H.

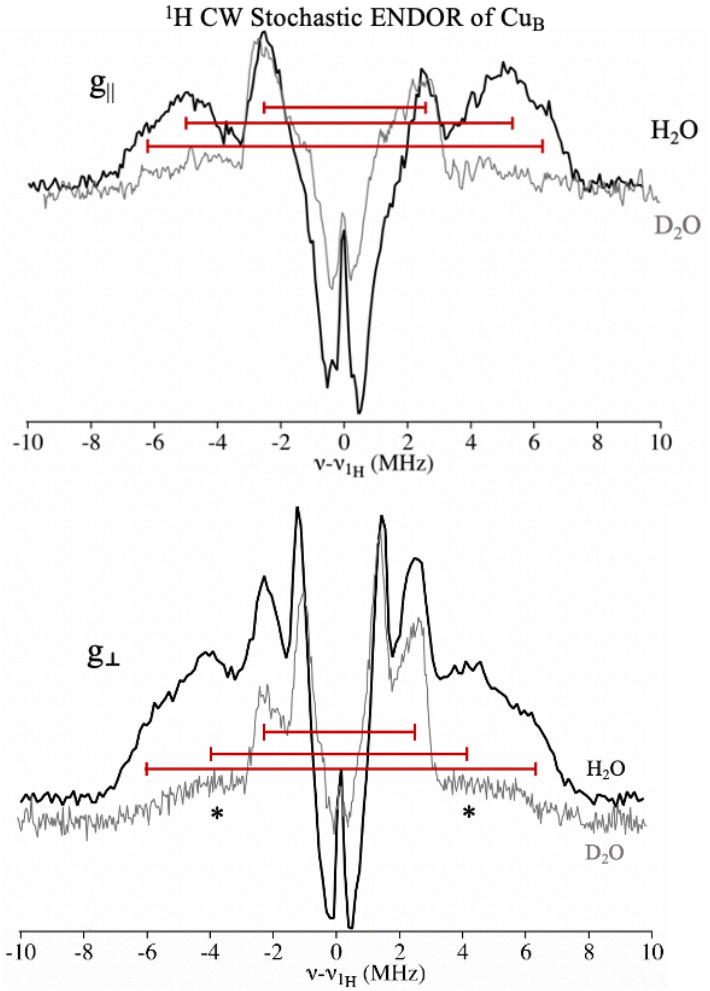

Figure 2.4. ^{1}H CW Stochastic ENDOR of the Cu$_B$ site. *Mc.* sp. str. Rockwell in vivo pMMO Cu$_B$ site Q-band 2K stochastic ^{1}H ENDOR at fields corresponding to g = 2.31(top) and g = 2.02 (bottom). Gray trace is D_2O exchanged samples at the same fields. Asterisks denote ^{63}Cu ENDOR response that underlies the ^{1}H pattern. The stochastic sequence enhances resolution, and resolved couplings are shown by the brackets, whose length represents the value of A (see text). *Conditions*: 34.78 GHz, 4G modulation, 1μW MW power, 2s rf on, 2s rf off, 0.5s wait time, ~2000 scans each.

The field modulated detected stochastic ^{1}H ENDOR spectrum at $g_\perp$ (**Figure 2.4, bottom**) again reveals two resolved large couplings from exchangeable protons, but in this case with the same (negative)

sign, A ~ -12 MHz and ~ -8 MHz (**Figure S2.6**), as well as a nonexchangeable doublet with A ~ +5 MHz (**Figure 2.4,** bottom, gray spectrum). Again, the two large couplings resolved here in the stochastic experiment (most evident for the v_+ peak) were observed in the previous study as a single broad peak with A ~11 MHz.[14] The ~+5 MHz coupling was assigned as a His Cε-H, consistent with the signs determined in this study.

The enhanced resolution of the exchangeable ^{1}H signals in the stochastic CW ^{1}H spectra allows for a reconsideration and further assignment of the large proton couplings. Previous ^{17}O ENDOR measurements showed the presence of an axial water on Cu_B,[14] and the present ^{1}H ENDOR measurements confirm this assignment. The appearance of a hyperfine-split doublet with A ~ +10 MHz at $g_{||}$ is characteristic of the protons of a water molecule bound axially to a square-planar Cu(II) site.[58, 61, 62] At $g_\perp$, the exchangeable protons of this water molecule would give a coupling of A ~ -5 MHz; they are likely obscured by the signals from the non-exchangeable imidazole ring protons of the three histidine residues.

The exchangeable ^{1}H signals with A ~ -13 MHz at $g_{||}$ and A~ -12 MHz at $g_\perp$ are somewhat surprisingly assignable to the protons of the in-plane terminal amino group. Previous studies of protons of an amino group bound in-plane to Cu(II) reported couplings of these magnitudes, but without determination of signs.[58, 63, 64] To better understand the hyperfine couplings to in-plane amine protons, we carried out a preliminary study of $[Cu(II)(NH_3)_4]^{2+}$ using ^{1}H ENDOR. The preliminary results of field modulated detected stochastic ENDOR and PESTRE show couplings of A ~ -12 MHz at $g_{||}$ and -12 MHz at $g_\perp$ (**Figure S2.7**), and DFT calculations of the ^{1}H hyperfine tensors gave corresponding results. In retrospect, the previous lower-resolution ^{1}H ENDOR study of *M. capsulatus* (Bath) pMMO[14] is consistent with the present, more complete study, leading to the conclusion that the Cu_B site is completely conserved across the types I and II pMMOs.

^{15}N Pulsed ENDOR of Cu_C nitrogen coordination

Although purified pMMO exhibits strongly overlapping EPR signals from Cu_B and Cu_C, the enhanced "g-spread" at Q-band versus X-band causes the difference in g_1 between the Cu_B and Cu_C sites to shift the four-line ^{63}Cu g_1 hyperfine pattern of Cu_C by ~250 G to lower field than that of Cu_B, as observed when overlaying the spectra of purified pMMO and in vivo pMMO (**Figure 2.5**). Within this low-field range,

for the first time it is possible to exclusively probe the ^{15}N ENDOR of the Cu_C site without interference from signals that arise from Cu_B. The penalty paid for attempting such studies is the low Cu_C EPR signal intensity at these fields, which makes it necessary to use highly concentrated samples (> 2 mM 100 kDa protomer) to obtain signals of reasonable signal/noise. Using such samples enabled us to obtain ^{15}N ENDOR spectra for the Cu_C site within the field range indicated in **Figure 2.5 (inset, gray bracket region)**. A bonus of measurements taken within this field range is that these spectra are "single-crystal-like",[65] meaning that they are selectively associated with the small subset of Cu_C sites oriented in the frozen sample so that the external field lies along the normal to the Cu_C ligand plane, a situation that yields the highest resolution and most easily analyzed signals.

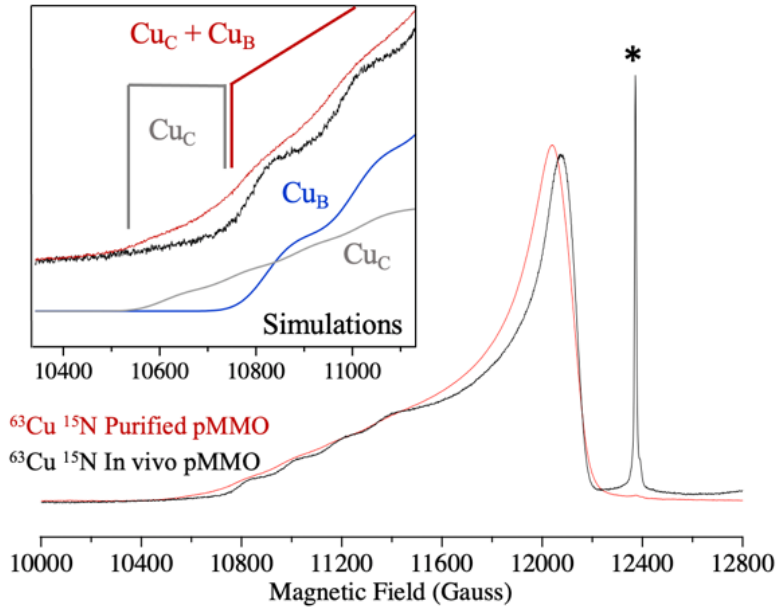

Figure 2.5. 2K Q-band EPR of purified and in vivo pMMO. Absorption EPR with the spectra of in vivo (black) and purified (red) Mc. sp. str. Rockwell pMMO overlayed. At this frequency, the +3/2 63Cu hyperfine of the CuC site is separated from the CuB site, as also shown by individual simulations of the two sites (inset). The asterisk marks a radical that is present in whole cell samples. Conditions: ~34.8 MHz, 1G modulation, 1μW MW power, 128 ms time constant, 20 G/s sweep rate.

Using an isotopically enriched, purified *Mc.* sp. str. Rockwell type II pMMO sample, ^{15}N Davies pulsed ENDOR was used to analyze the coordination environment and electronic structure of the Cu_C site. When the magnetic field is set within the "clean" low-field window (**Figure 2.5**), at a value corresponding to g = 2.32, the ^{15}N ENDOR spectrum of Cu_C exhibits resolved features that correspond to ^{15}N hyperfine couplings from two coordinating nitrogenous ligands, with couplings of A = ~ -46 MHz and A= ~ -50 MHz

(**Figure 2.6**, black); the negative signs were determined by the PESTRE technique as discussed for Cu_B above (**Figure S2.8**). Spectra from an ^{15}N enriched, concentrated purified type I pMMO sample from *M. capsulatus* (Bath) at this field reveal identical ^{15}N couplings (**Figure S2.9**), signifying that the Cu_C nitrogen coordination is conserved between pMMOs from types I and II methanotrophs, as shown above for the Cu_B nitrogen coordination.

As a control to ensure we were not observing signals from the Cu_B site, ENDOR spectra were collected at the same g-value from an ^{15}N, ^{63}Cu *Mc.* sp. str. Rockwell whole-cell sample, which exhibits only a Cu_B EPR signal. There is no ^{15}N ENDOR signal at this field (**Figure 2.6**, red spectrum), whereas the Cu_B signals are strong at higher fields, within the Cu_B envelope, thus confirming that the observed signals (**Figure 2.6**, red spectrum) derive exclusively from the Cu_C site.

Interestingly, the resolution of the ENDOR signal of both of the two Cu_C ^{15}N ligands changes at still lower field (corresponding to a g-value, g = 2.34; **Figure S2.10**). This variation is attributable to differences in the orientations of their hyperfine tensors relative to the g-tensor, an indication of the low symmetry of the

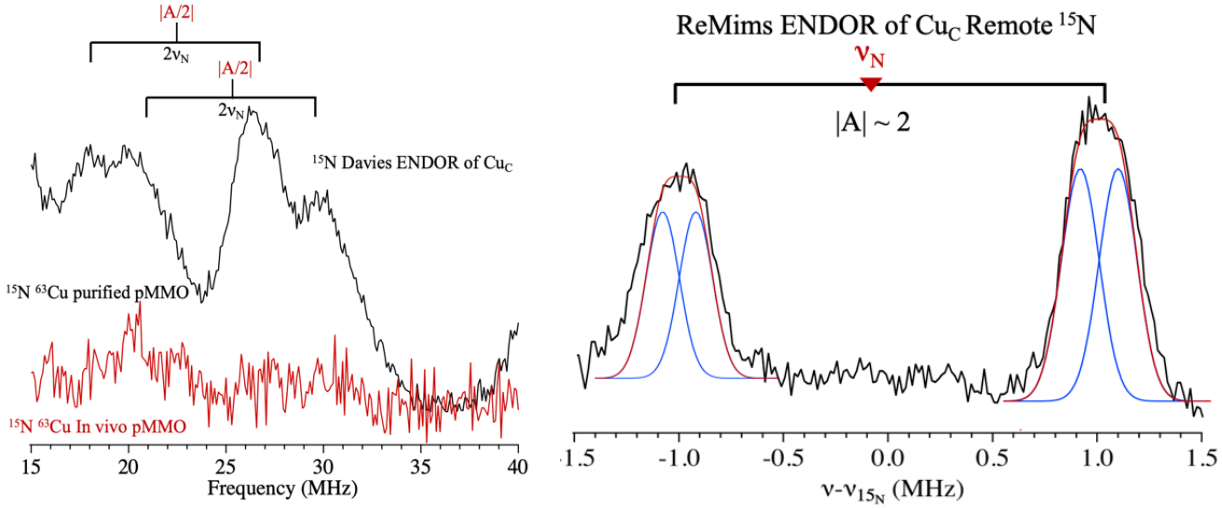

Figure 2.6. Pulsed 15 ENDOR of the Cu_C site. Left: Q-band Davies pulsed ^{15}N ENDOR at a field corresponding to a g-value, g = 2.32 for purified (black) and in vivo (red) *Mc.* sp. str. Rockwell pMMO. The brackets represent twice the ^{15}N Larmor frequency and are centered at the value of |A/2|. *Conditions:* 2K, 34.684/34.774 GHz, 100 ms repetition time, π = 80 ns, τ = 600 ns, T_{RF} = 35 μs, RF tail = 5μs, ~100 scans. **Right:** Q-Band Doan/ReMims ^{15}N pulsed ENDOR at 10700G (g = 2.32) for purified ^{63}Cu ^{15}N *Mc.* sp. str. Rockwell pMMO (black). The bracket represents |A| for the remote ^{15}N couplings and the spectrum is centered on the ^{15}N Larmor frequency. The breadth of the individual peaks is much larger than the widths of the individual responses for Cu_B, which suggests multiple ^{15}N couplings are overlapped. The spectrum was fit to the overlap of two ^{15}N doublets whose individual peaks were taken to have the same widths of the individual remote ^{15}N of Cu_B. Conditions are identical to the ones described in **Fig. 2.3.**

Cu_C coordination sphere (**Figure S2.11)**. The X-band EPR spectrum of the Cu_C site gives a ratio $g_{||}/A_{||}$ = 156 cm (see above), which would suggest a distorted tetrahedral geometry.[58]

To identify the two nitrogenous ligands to Cu_C revealed by the Q-band Davies pulsed ^{15}N-ENDOR, we performed a ReMims ENDOR experiment to determine the presence and number of signals from the remote ^{15}N of histidyl ligands, as done for the Cu_B site (**Figure 2.3, right**). The Cu_C ReMims ^{15}N ENDOR spectra reveal one doublet associated with weakly coupled ^{15}N, |A| ~ 2 MHz (**Figure 2.7**), typical for a remote nitrogen of a histidine residue. However, these peaks are broad compared to the remote ^{15}N peaks for Cu_B, which is evident upon overlay with the peaks in **Figure 2.3** (see **Figure S2.12**). As shown in **Figure 7**, the spectrum is best interpreted as arising from unresolved doublets from two slightly inequivalent remote ^{15}N remote histidyl ^{15}N (|A| = 1.8, 2.1 MHz), as expected for Cu_C bound to the two conserved histidine residues in the PmoC crystallographic site (**Figure 2.1**).

^{1}H ENDOR Analysis of the Cu_C site

We further investigated the Cu_C site by ^{1}H CW ENDOR. Spectra of concentrated, purified *Mc.* sp. str. Rockwell pMMO in H_2O and D_2O were again collected in the low-field window, at 10600G (**g** = 2.34) (**Figure 2.8, upper)**. The results for this type II pMMO Cu_C site are indistinguishable from those obtained for the type I pMMO from *M. capsulatus* (Bath).[14] The H_2O spectrum shows broad peaks from several doublets: a clearly resolved doublet with A ~ +5 MHz, where the sign has been determined by the PESTRE protocol (**Figure S2.13**), and a pair of doublets with A ~ 2 and |A| ~1 MHz (**Figure 2.8, upper**, solid black). The sign of the first of these two was again determined by PESTRE; sign determination was not possible for the second.

Examination of a sample exchanged into D_2O buffer and incubated for 24 h at room temperature reveals loss of the doublet with A ~ +5 MHz, leaving a broad ill-resolved feature extending to nearly |A| ~ 5 MHz. Although some of this signal may arise from residual H_2O after exchange, PESTRE shows a negative sign for A ~ -2 to -5 MHz, (**Figure 2.8, upper,** dashed gray, **Figure S14**), definitively showing that the signal arises from non-exchangeable protons. The exchangeable ~1 MHz doublet may well be associated with

the remote N-H of the histidine residues[66] (**Figure 2.7**). The nonexchangeable doublets most likely arise from Cε or Cδ protons of the histidine residues.[67]

In the 2.6 Å resolution crystal structure of *Mc.* sp. str. Rockwell pMMO (PDB 4PHZ),[45] electron density 3.3 Å from Cu_C is modeled as solvent molecule axial to the Cu 2N1O plane, but is not coordinated to the copper ion. The exchangeable proton signal with A ~ +5 MHz likely is associated with this solvent molecule, aligning the X-ray and ENDOR measurements. This assignment revises the suggestion based on the interpretation of an ^{17}O ENDOR measurement on purified *M. capsulatus* (Bath) pMMO in buffer prepared with $H_2{}^{17}O$.[14] The assignment is supported by additional examination of the ^{17}O ENDOR response (**Figure S2.14**) and by the absence of signals attributable to coordinated ^{17}O at fields where the

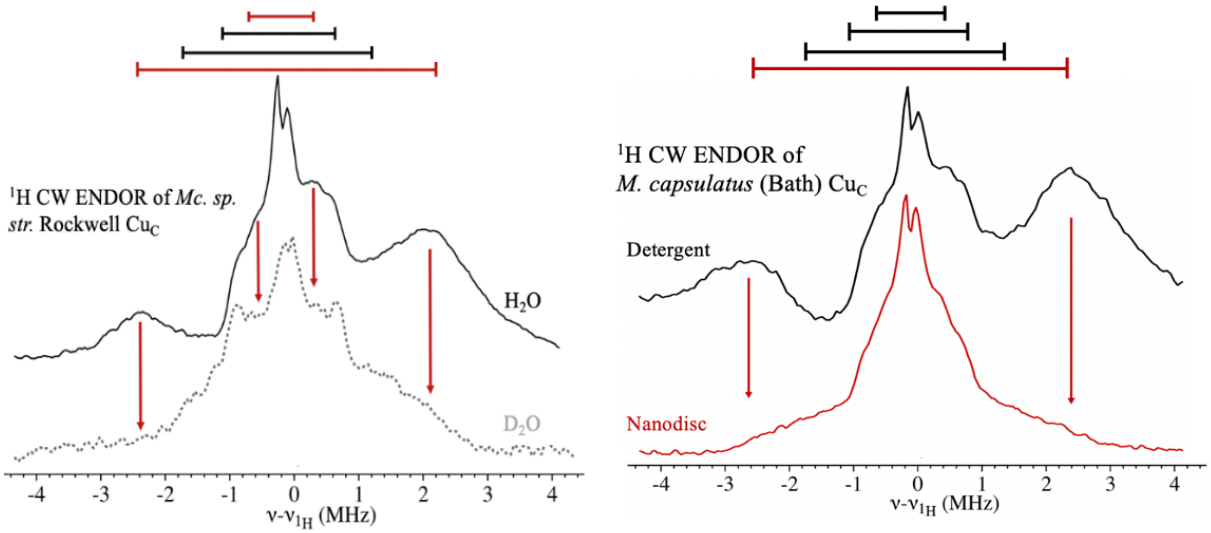

Figure 2.5. ^{1}H CW Swept ENDOR of pMMO Cu_C sites. Left: Q-band CW ^{1}H ENDOR spectra of *Mc.* sp. str. Rockwell pMMO Cu_C site (10650 G). Black trace, purified pMMO in H_2O; dotted gray trace, purified pMMO in D_2O. Red arrows indicate the loss of the ~5 MHz and ~1 MHz couplings upon D_2O exchange. *Conditions:* 34.8 GHz microwave frequency, 4G Modulation, 32ms TCs, 1μW MW power, Forward sweep, ~75 scans, 0.25 MHz/s. **Right:** Q-Band CW ^{1}H ENDOR of Cu_C site of purified *M. capsulatus* (Bath) pMMO in detergent (*black*) and in a nanodisc (*red*). Red arrows indicate the absence in the nanodisc of the A ~ +5 MHz coupling assigned as a distal water, seen also in measurements on detergent-purified *Mc.* sp. str. Rockwell pMMO. *Conditions* are identical, except the nanodisc sample, with a lower enzyme concentration, required ~400 scans.

Cu_C EPR signal is not overlapped with that from Cu_B (**Figure S2.15)**

The absence of any ^{1}H signals with |A| > 5 MHz at g|| (**Figure S2.16**) is additional evidence against a coordinated water; if such a ligand were present, it would exhibit a ^{1}H doublet with |A| ~10 MHz,[61, 62] contrary to experiment. We therefore conclude that Cu_C does not have a coordinated water. The signal might be imagined to derive from protons on a nearby arginine residue (Arg 138, ~5 Å from Cu_C), but these

are too remote to give rise to the observed coupling. We therefore attribute the exchangeable signal to the crystallographically observed ordered water within the secondary coordination sphere. The equivalence of the ^{1}H ENDOR measurements for the types I and II pMMOs indicates that the solvent molecule near Cu_C is present in both, expanding the extent to which the site is highly conserved.

. Because the Cu_C site adopts the Cu(I) state in vivo and cannot be examined by EPR, we sought to recreate a membrane environment in lipid nanodiscs, as recently used for nTDMS characterization of pMMO.[15] The reconstitution of pMMO in nanodiscs in the presence of additional copper has led to higher enzymatic activity and higher copper loading of the PmoC subunit compared to detergent-solubilized pMMO. The X-band EPR spectrum of purified *M. capsulatus* (Bath) pMMO reconstituted into nanodiscs is nearly identical to those of the purified enzyme[14] in detergent (**Figure S2.17, Figure 2.2C**). However, as a result of the higher Cu_C copper loading in the nanodisc, the Cu_C EPR signal has greater intensity than that of the detergent purified sample. Thus, the Cu_C(II) coordination does not change despite the fact that it is within the transmembrane region adjacent to a part of PmoC that is disordered in the crystal structures, and might be expected to have a different environment in the nanodisc.

However, the overall environment of the Cu_C site is altered by nanodisc incorporation. The Cu_C ^{1}H ENDOR spectrum collected at the low magnetic field edge of the EPR spectrum of the nanodisc sample is dramatically different from that of pMMO in detergent (**Figure 2.8, lower**). The broad A ~ +5 MHz doublet seen for detergent-solubilized pMMO and assigned to protons from the non-coordinated distal water molecule is lost upon incorporation into the nanodisc. The remaining intensity in this frequency range corresponds to the signals in the D_2O sample of purified enzyme, which are assigned to the histidine ligands (**Figure 2.8, upper, gray**). Thus, although the ligation to Cu_C is unchanged in the nanodisc, the solvent molecule near this site is lost.

We correspondingly tested for possible effects of nanodisc incorporation on the Cu_B site in the solvent-exposed PmoB subunit, using enzyme in which Cu_C has been reduced to the Cu(I) state through the addition of 10 equivalents ascorbic acid per pMMO protomer. Both the X-band EPR spectrum (**Figure S2.18**) and the ^{1}H ENDOR spectra (**Figure S2.19**) are unchanged, indicating that the Cu_B ligation, including the presence of an axial water, is unchanged. Whereas the Cu_B site is essentially identical in vivo, in detergent-solubilized pMMO, and in pMMO reconstituted into nanodiscs, the Cu_C surroundings are altered

in the membrane-like environment of a nanodisc. Thus, changes in pMMO activity in the different environments may be associated with changes in the Cu_C site.

METHODS

Growth of *Mc.* sp str. Rockwell

To produce $^{63}CuSO_4$ for enrichment growths, 50 mg aliquots of ^{63}CuO (Cambridge Isotope Laboratories) were dissolved in 1.5 mL of 3M trace metal grade H_2SO_4 while heating at 60-80°C and shaking at 300 rpm. The reaction was judged to be complete when no black ^{63}CuO particles were visible in the blue $^{63}CuSO_4$ solution after several days. *Mc.* sp. str. Rockwell was grown in a 12 L fermentor as previously described[45] with minor adjustments. The medium consisted of 3.9 mM phosphate buffer, pH 6.8, 40 μM NaFe(III)EDTA, 1X trace element solution, 50 μM $CuSO_4$ ($^{63}CuSO4$ prepared as described above was used for enrichment growths), and 1X nitrate mineral salts (NMS) (potassium ^{15}N-nitrate, 99.98% enrichment, Cambridge Isotopes Laboratories, was used for isotope enriched samples) with a constant gas flow of ~1 liter/min with a 1:4 methane:air gas mixture. The pH was maintained between 6.7 and 7.2 by addition of NaOH and H_2SO_4 as the growth proceeded. Cells were harvested by centrifugation (8,000 g for 35 min at 4 ºC) at an OD_{600} of 10.6 and were either used immediately or frozen in liquid nitrogen and stored at -80ºC. *M. capsulatus* (Bath) was grown and purified as described previously.[46]

Preparation of whole cell EPR and ENDOR Samples

Freshly harvested cell paste (0.75 g) was resuspended in 50 mL of 12.2 mM dibasic sodium phosphate, 7.8 mM monobasic sodium phosphate, 5 mM magnesium chloride, pH 7.2. The resuspended cells were then centrifuged for 15 min at 10,000 g. The supernatant was removed, and this wash procedure was repeated twice more. After the third spin, the cells were resuspended in 150 μL of the phosphate buffer and aliquoted into a Wilmad quartz X-band EPR tube (Sigma Aldrich) and a custom quartz Q-band EPR tube. EPR samples were frozen in liquid nitrogen and stored in a liquid nitrogen dewar until analysis.

Mc. sp. str. Rockwell pMMO Purification

Frozen cells were resuspended in room temperature 25 mM PIPES, 250 mM NaCl, pH 7.2 and lysed by sonication (1 s on, 1 s off, 10 min, 90% power setting). The cell debris was removed, and the membranes were isolated and washed as described previously.[45] The washed membranes were then

resuspended in the PIPES buffer to 300 μM total protein, as determined by the Bio-Rad DC Lowry assay (with BSA as a standard), aliquoted in X-band and Q-band EPR tubes, and frozen in liquid nitrogen until analysis. Membranes were aliquoted, flash frozen in liquid nitrogen, and stored at -80ºC until further purification. *Mc.* sp. str. Rockwell pMMO was further purified and solubilized as described previously, but with PIPES instead of Tris buffer to avoid copper chelation by the buffer.[45] In brief, membranes were solubilized with *n*-dodecyl β-d-maltopyranoside (DDM), diluted with 25 mM PIPES, 0 M NaCl buffer, pH 7.2, centrifuged at 100,000 x g for 1 h, and the soluble fraction was loaded onto a Source 15Q column (GE Healthcare). Fractions were assessed for purity by SDS PAGE, and those deemed pure were collected, concentrated, and flash frozen for later use. The protein concentration was determined by measuring the absorbance at 280 nm and using the extinction coefficient, 7.66 x 10^3 M^{-1} cm^{-1}.[45]

pMMO Nanodisc Reconstitution

DDM-solubilized *M. capsulatus* (Bath) pMMO was incorporated into lipid nanodiscs with membrane scaffold protein (MSP1E3D1) and 1-palmitoyl-2-oleoyl-glycero-3-phosphocholine (POPC) using established methods.[68] pMSP1E3D1 (Addgene) was transformed into *E. coli* BL21(DE3) cells and grown in TB media for 4 h at 37 °C until an OD_{600} of 2.1 was reached. Expression was induced by adding 1 mM IPTG, and cells were grown for another 4 h at 37 °C before pelleting and flash freezing. Cells were resuspended in lysis buffer containing 40 mM Tris, pH 7.3, 250 mM NaCl, and 10 mM imidazole along with DNAse, EDTA-free protease inhibitor cocktail (Roche) and 1% Triton X-100. Cells were lysed by sonication (10 min, 1 s on, 2 s off), and debris was removed by centrifugation at 10,000 x g for 30 min. The soluble fraction was applied to a Ni-NTA column and washed with 5 column volumes of lysis buffer containing 50 mM sodium cholate followed by 10 column volumes of lysis buffer. MSP1E3D1 was eluted with lysis buffer containing 250 mM imidazole. TEV protease was added at a ratio of 1:20, and the sample was dialyzed overnight at 4 °C against lysis buffer containing 1 mM EDTA. Cleaved MSP1E3D1 was collected from the NiNTA column flow-through and dialyzed overnight against the PIPES buffer before concentrating and flash freezing. POPC solubilized in chloroform (Avanti) was dried to a thin layer in a glass vial against a stream of argon and then overnight in a vacuum desiccator. POPC was suspended at 50 mM in buffer containing 25 mM PIPES, pH 7.3, 250 mM NaCl, and 100 mM cholate by alternating heating at 60 °C, sonicating in an ultrasonic bath, and vortexing. Nanodisc components were mixed for 30 min at 4 °C at a ratio of 1:4:240

pMMO:MSP1E3D1:POPC. Bio-beads SM-2 (Bio-Rad) washed with the PIPES buffer were added at 0.8 mg/mL and mixed end-over-end for 2 h before removal. Nanodiscs containing pMMO were purified using a Superose 6 10/300 column (Cytiva). EPR and ENDOR sample preparation is described below.

Preparation of Purified *Mc.* sp. str. Rockwell pMMO EPR and ENDOR Samples

Samples of purified pMMO were loaded into X- and Q-band tubes and flash frozen. For partially reduced pMMO samples, an aliquot of pMMO was brought into a Coy anaerobic chamber and left for 24 h at 4 ºC shaking at 400 rpm to remove dioxygen from the sample. 12 equivalents of sodium ascorbic acid per 100 kDa protomer of pMMO was then added to the sample and allowed to incubate for 2 h at room temperature prior to freezing in an EPR tube anaerobically with liquid nitrogen and storing under liquid nitrogen. D_2O samples were produced by adding purified pMMO to D_2O buffer in a 1:10,000 dilution. This sample was kept for ~24 h at room temperature to exchange the protons within the enzyme and then concentrated with a 100 kD MWCO Amicon concentrator. The concentration of purified *Mc.* sp. str. Rockwell pMMO was determined by using the absorbance at 280 nm and the calculated extinction coefficient of 7.66 x 10^3 M^{-1} cm^{-1}. The concentrated sample was then either frozen in an EPR tube or brought into the anaerobic chamber and reduced as described above.

EPR and ENDOR Measurements.

All CW (continuous wave) X-band EPR measurements were performed on a Bruker ESP-300 spectrometer with a liquid helium flow Oxford Instruments ESR-900 cryostat. EPR simulations were carried out in EasySpin.[69] Pulsed ENDOR measurements were collected at ~2 K on a spectrometer described previously, with SpinCore PulseBlaster ESR_PRO 400 MHz digital word generator and Agilent Technologies Acquiris DP235 500 MS/sec digitizer using SpecMan4EPR software.[70, 71] For weakly-coupled remote ^{15}N ENDOR measurements, a Refocused Mims ENDOR (ReMims) pulse sequence [$\pi/2–\tau_1–\pi/2–$TRF$–\pi/2–\tau_2–\pi–(\tau_1+\tau_2)–$echo] was utilized in which TRF denotes the interval during which the RF was applied.[59] Strongly coupled ^{15}N ENDOR measurements employed a Davies pulse sequence [$\pi–$TRF$–\pi/2–\tau–\pi–\tau–$echo].[11] 35 GHz CW ENDOR spectra were recorded on a modified Varian E-110 spectrometer equipped with a helium immersion dewar.[72] Cu_B site ^1H CW ENDOR spectra were collected using the field modulation detected stochastic ENDOR sequence[73] in order to resolve the strongly coupled protons. The

Cu_B ^{15}N signals show peaks from two ligand types; to obtain the relative intensities of the two contributions, the signals were fit to a sum of gaussians to determine their area ratio

Hyperfine Sign Determination

To obtain the signs of the measured hyperfine couplings (more precisely to determine the sign of $A/\mathbf{g}_n$), the Pulsed-Endor-SaTuration and REcovery (PESTRE) method was used at 35 GHz as described in detail previously.[74]

CHAPTER 3: Product analogue binding identifies the copper active site in particulate methane monooxygenase

Results from this chapter are part of a submitted publication:

F. J. Tucci*, R. J. Jodts*, B.M. Hoffman, and A.C. Rosenzweig, **2023**

INTRODUCTION

Conversion of methane, the primary component of natural gas, to methanol, an in-demand liquid fuel and chemical feedstock, is one of the "holy grails" of catalysis.[75] This reaction is intrinsically difficult due to methane's strong C-H bonds (105 kcal/mol)[76] and the reactivity of methanol, which is easily oxidized to formaldehyde or formic acid. As a result, industrial methanol production involves conversion of methane first to syngas (carbon monoxide and hydrogen) and entails significant capital and operating expenses.[77, 78] Development of high-yield homogeneous or heterogeneous catalysts for direct methane conversion presents a major challenge, as such catalysts typically involve the use of precious metals like platinum or palladium.[79, 80]

An alternative approach is biological catalysis employing microorganisms or their isolated enzymes, which oxidize methane to methanol under ambient conditions using earth-abundant metals[43]. Aerobic methane oxidation is performed by methanotrophs,[81] bacteria that convert methane to methanol in the first step of their metabolic pathway using methane monooxygenase (MMO) enzymes. MMOs react with methane and dioxygen to produce methanol and water, consuming two protons and two electrons during the conversion. Two distinct MMOs can catalyze this reaction: a soluble enzyme (sMMO) that uses a dinuclear iron catalytic site, and a membrane-bound or particulate enzyme (pMMO) whose activity is dependent on copper.[12, 37, 82] pMMO is expressed by almost all known methanotrophs,[37] while sMMO is expressed by a subset of methanotroph strains under conditions of copper starvation.[83] The active-site chemistry and catalytic mechanism of sMMO are well established.[82] By contrast, even the location and molecular details of the pMMO copper active site remain under debate, hindering progress toward elucidating its catalytic mechanism.

Several different mononuclear copper binding sites have been identified in structures of pMMO (**Figure 3.1a**). The bis-His site (**Figure 3.1b**), coordinating a copper by two histidine residues conserved in

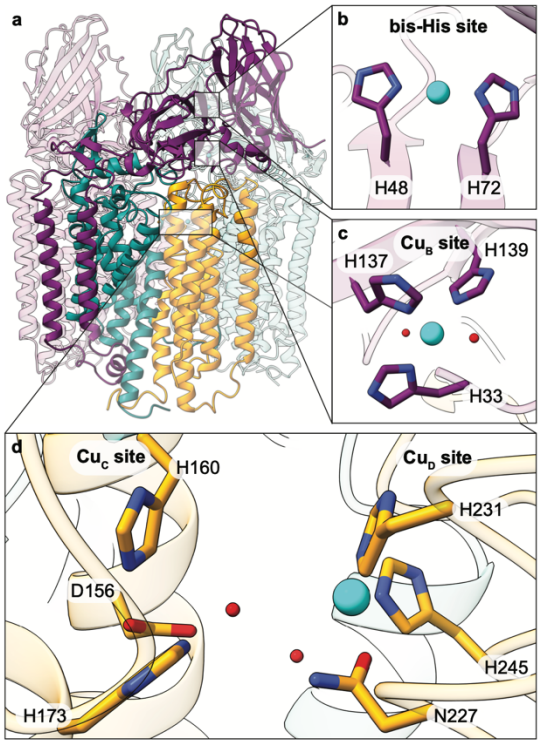

Figure 3.1 CryoEM structure of M. capsulatus (Bath) pMMO in native lipid nanodiscs. a, The $\alpha_3\beta_3\gamma_3$ C3 symmetrical trimer with one protomer highlighted (PDB accession code 7S4H). The PmoB, PmoA, and PmoC subunits are shown in purple, teal, and gold, respectively, with the copper ions as cyan spheres. b, The bis-His site. c,The Cu_B site. d, The neighboring Cu_C and Cu_D sites. The Cu_C site is unoccupied, and the Cu_D site is modeled as copper.

gammaproteobacterial PmoB sequences, is only occupied in crystal and cryoelectron microscopy (cryoEM) structures of *Methylococcus capsulatus* (Bath) pMMO, where it binds Cu(I).[14] The Cu_B site, located at the PmoB N-terminus and present in all structurally-characterized pMMOs, coordinates copper by residues His33, His137, and His139 (*M. capsulatus* (Bath) numbering), along with the amino group of His33 (Fig. 1c).[37] Cu_B is unlikely to be the site of methane and oxygen binding because it contains coordinatively saturated, Cu(II) in vivo,[14, 84] and is not conserved in pMMOs from the Verrucomicrobia phylum.[85, 86] A third metal binding site in the PmoC subunit, Cu_C, can bind either copper[87, 88] or zinc,[13, 45, 53] with strictly conserved ligands Asp156, His160, and His173 (**Figure 3.1d**). Cu_C neighbors a conserved region of PmoC that is disordered in all the crystal structures, but was recently resolved in cryoEM structures of *M. capsulatus* (Bath) pMMO in lipid nanodiscs. The cryoEM structures further revealed a previously undetected metal-binding site located ~5.7 Å from Cu_C, containing a metal ion coordinated by Asn227, His231, and His245 (**Figure 3.1d**). The metal ion in this site was assigned as copper by comparing cryoEM maps of

metal-depleted and copper-reloaded pMMO samples. This site, denoted Cu_D, is adjacent to a hydrophobic cavity lined by several conserved phenylalanine residues and next to a conserved arginine.[16]

The cryoEM structures completed the picture of the pMMO structure, but raised several key questions. *First*, while metal ions can be identified in crystal structures using anomalous diffraction data,[89] there is no parallel method for cryoEM data. Thus, the evidence for copper in this site remains indirect. *Second*, electron paramagnetic resonance (EPR) analysis of pMMO in whole cells, isolated membranes, detergent, bicelles, and synthetic lipid nanodiscs revealed the presence of two Cu(II) sites, assigned on the basis of electron nuclear double resonance (ENDOR) data to the crystallographic Cu_B and Cu_C sites.[14, 46, 84] However, Cu_C and Cu_D, assuming Cu_D is occupied by copper, are both coordinated by one oxygen and two nitrogen ligands, confounding assignment of that EPR signal. *Third*, the cryoEM structure was determined using pMMO embedded in nanodiscs prepared with lipids isolated from *M. capsulatus* (Bath). Unlike the pMMO crystal structures, which were determined using detergent-solubilized samples with no enzymatic activity, these nanodiscs exhibit methane oxidation activity approaching that of membrane-bound pMMO[16]. Thus, the occupancy of the Cu_D site with density attributable to a metal ion in most of the cryoEM structures raises the possibility that this site, rather than Cu_C or in combination with Cu_C, is the active site.

To address these questions, we have performed parallel spectroscopic and structural studies of the catalytically active *M. capsulatus* (Bath) pMMO in native lipid nanodiscs. Crucially, all our biochemical data, EPR and ENDOR spectra, and cryoEM structures were obtained from the same samples to interrogate the enzyme from orthogonal perspectives while minimizing sample-dependent variations. The use of EPR and ENDOR spectroscopies in parallel with cryoEM addresses a significant limitation in cryoEM, the difficulty of interpreting metal ion and small molecule densities in cryoEM maps. The combined data indicate that the Cu_D site is indeed occupied by copper and is associated with enzymatic activity. Moreover, this orthogonal approach allowed us to model the interaction of a product analog, 2,2,2,-trifluoroethanol (TFE), with the Cu_D site, revealing functionally relevant interaction with a pMMO copper site, and implicating Cu_D and the surrounding hydrophobic pocket as the active site.

RESULTS

Cu_D occupancy is associated with the pMMO EPR signal and with methane oxidation activity

Although EPR and ENDOR data are available for pMMO in 1-palmitoyl-2-oleoyl-glycero-3-phosphocholine (POPC) nanodiscs[84], pMMO in native lipid nanodiscs exhibits significantly higher methane

oxidation activity[16], and is therefore the focus of our study. pMMO was thus reconstituted into nanodiscs prepared with lipids isolated directly from *M. capsulatus* (Bath) (native lipids) for EPR spectroscopic characterization. The 30 K X-band EPR spectra of samples of pMMO in native lipid nanodiscs (**Figure 3.2a**) reveal signals from two Cu(II) species, both unchanged from those consistently observed in prior pMMO samples[14, 84]. The most intense signal (~58% of total Cu(II) by simulation) arises from a type 2 Cu(II) center with **g** = [2.24, 2.07, 2.04] and $^{63/65}$Cu $A_{||}$ = 584 MHz, corresponding to the extensively characterized Cu_B site. The second type 2 Cu(II) species, with **g** = [2.31, 2.07, 2.05] and $^{63/65}$Cu $A_{||}$ = 440 MHz, was previously assigned as the Cu_C site.[14, 84] However, only the Cu_D site is occupied in the cryoEM structure of pMMO in native lipid nanodiscs[16] and the 2N-1O distorted tetrahedral coordination of both Cu_C and Cu_D is consistent with the observed EPR parameters[57, 58] (**Figure 3.2a**, see bracket). Thus, we have reinvestigated the origin of the EPR signal previously assigned to Cu_C, but which may instead arise from the Cu_D site in pMMO in native nanodiscs. To correlate this EPR signal with the structurally-characterized copper centers and with methane oxidation activity, parallel samples of pMMO depleted of metal ions and reloaded with copper were prepared. Isolated *M. capsulatus* (Bath) membranes, of which pMMO comprises more than 80% of the total protein[90], were first depleted of metals using potassium cyanide[45]. These metal-depleted membranes were split into two fractions, of which one was kept metal free and the other was reloaded with copper. pMMO was solubilized and purified from both fractions and then reconstituted into native lipid nanodiscs. Metal depletion abolished methane oxidation activity while copper reloading recovered ~50% of the activity observed for untreated pMMO in native lipid nanodiscs (**Figure 3.2b**, **Figure S3.1**). The X-band EPR spectrum of the metal-depleted sample exhibited a weak signal from the Cu_B site and a low-intensity response from other unresolvable and thus unassignable type 2 Cu(II) signals[14, 84] (**Figure 3.2a**, **Figure S3.2**). Reloading with Cu(II) regenerates an EPR spectrum with the two distinct Cu(II) signals corresponding to the Cu_B site and either the Cu_C or Cu_D site, as observed in the native nanodisc (**Figure 3.2a**) and other[14, 84] samples of pMMO.

To establish which copper sites are associated with the EPR signals regenerated through copper reloading, the same samples were used for cryoEM data collection. The cryoEM structures of metal-depleted and copper-reloaded *M. capsulatus* (Bath) pMMO in native nanodiscs were determined previously to 3.65 and 3.39 Å resolutions, respectively, providing indirect evidence for the presence of copper in the

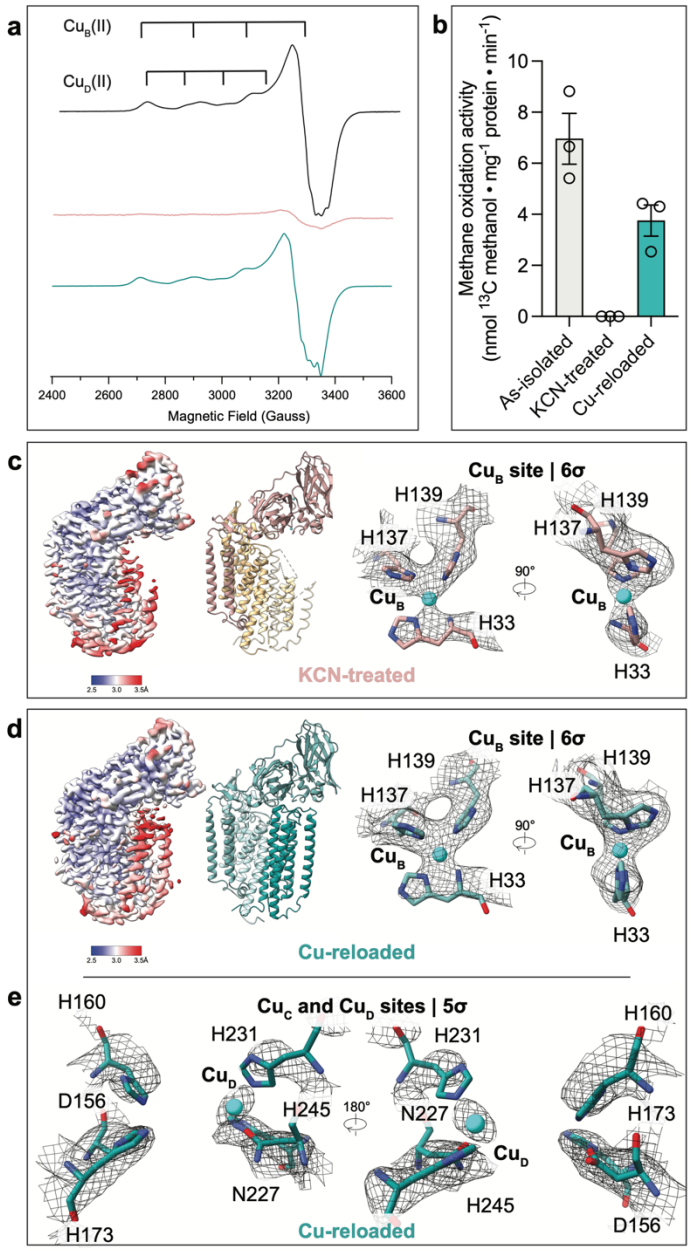

Figure 3.2 X-band CW EPR spectra of pMMO (black), metal-depleted pMMO (pink), and copper-reloaded pMMO (teal). The top bracket represents the signal attributed to the Cu_B site, and the bottom bracket represents the secondary species, shown in this report to arise from Cu_D. X-band EPR conditions: 9.371 GHz, 30 K, 12.5 G modulation, 250 μW microwave power, 320 ms time constant, 10 G/s scan rate, 3 scans. b, Methane oxidation activity for as-isolated pMMO, metal-depleted pMMO, and copper-reloaded pMMO in native lipid nanodiscs. c, CryoEM map and model for one protomer of metal-depleted pMMO (3.22 Å resolution) and its Cu_B site showing attenuated density for the copper ion. The PmoC subunit is disrupted in this structure, and the ligands for the Cu_C and Cu_D sites cannot be modeled in the density. d, CryoEM map and model for one protomer of copper-reloaded pMMO (3.12 Å resolution) and its Cu_B site showing recovered density for the copper ion. Maps are shown with local resolution coloring (blue 2.5 Å, white 3.0 Å, red 3.5 Å). e, CryoEM density at the Cu_C and Cu_D sites in copper-reloaded pMMO.

Cu_D site[16], but parallel EPR analysis was not performed. The results from the current higher resolution structures are consistent with the prior study and can be directly correlated with the EPR analysis. The 3.22 Å global resolution map of the inactive, metal-depleted pMMO shows severe disruption of the PmoC subunit, with no density for a metal ion in the Cu_C and Cu_D sites and poor local resolution (**Figure 3.2c** and **Figure S3.3a**). Weak metal-ion density is present for the Cu_B (**Figure 3.2d, Figure S3.3a**) and bis-His (**Figure S3.3a**) sites, consistent with the presence of a weak EPR signal attributable to Cu_B (**Figure 3.2a** and **Figure S3.2**).

By contrast, the cryoEM map of active, copper-reloaded pMMO at a global resolution of 3.12 Å shows interpretable metal-ion density for the PmoC subunit, albeit at lower local resolution than the bulk of the structure (**Figure 3.2c** and **Figure S3.3b**). This reordering of PmoC is accompanied by the appearance of strong side chain density for the bis-His, Cu_B, Cu_C, and Cu_D ligands, but with metal ions occupying only the bis-His (**Figure S3.3b**), Cu_B (**Figure 3.2d** and **Figure S3.3b**), and Cu_D (**Figure 3.2e** and **Figure S3.3b**) sites, and not the Cu_C site (**Figure 3.3e** and **Figure S3.3b**). As the bis-His site contains Cu(I)[13], these observations correlate with the increase in intensity of the Cu_B EPR signal. But most importantly, the reappearance of the second EPR signal correlates with both occupancy of the Cu_D site and recovery of methane oxidation activity. Thus, the Cu_D site contains Cu(II), is the site that gives rise to the second EPR signal in the samples of active pMMO in native lipid nanodiscs and is plausibly associated with the activity as well.

Spectroscopic detection of an interaction between Cu_D and the product analog TFE

Definitive assignment of an EPR signal to Cu_D provided a means of addressing its potential identity as the active site. In the case of sMMO, binding of the product methanol[91] along with the product analogs ethanol and TFE[92] to the mixed-valent diiron active site was observed by ^1H and ^{19}F ENDOR. TFE is ideal for these experiments because fluorine is not present in protein samples, so any ^{19}F ENDOR detected must come from TFE interacting with a paramagnetic center. Another benefit of using ^{19}F as a nuclear-spin probe is that the ^{19}F signals are easily resolved by ENDOR methods, and fluorine atoms are observable at substantial distances from the EPR-active metal center. Because pMMO also oxidizes ethane to ethanol[93] and ethanol inhibits methanotroph growth,[94, 95] we hypothesized that ethanol and its analog TFE might bind

at the pMMO copper active site. We first investigated the activity of native nanodisc samples in the presence of ethanol and TFE. Both inhibit methane oxidation activity in vitro, although TFE requires as little as 10 molar equivalents to inhibit activity while ethanol requires as much as 1000 molar equivalents per protomer. These data are consistent with the notion that TFE occupies the pMMO active site.

To directly probe for TFE binding, native nanodisc samples of pMMO were incubated with 20 molar equivalents of TFE per protomer and then examined by ENDOR. We hypothesized that TFE likely would coordinate to a copper site through its oxygen atom, by analogy to what was observed in sMMO.[92] In this case, ^{19}F couplings from TFE interacting with Cu(II) would be attenuated by the relatively large Cu(II)-F distance, and thus would best be observed by pulsed Mims ENDOR. The Mims ENDOR spectrum measured at $g_{||}$ (g = 2.14) for pMMO in the absence of added TFE (**Figure 3.3a, gold**) exhibits ^{1}H signals centered at the ^{1}H Larmor with maximum resolved hyperfine splittings of ~5 MHz; the appearance of multiple frequencies with nulled intensity in this range is associated with Mims-ENDOR suppression effects.[96-98] The addition of TFE introduces a weakly-split doublet (~1 MHz) centered at the ^{19}F Larmor (ν_{19F}), which lies below the ^{1}H Larmor frequency by the shift, $\nu - \nu_{1H} \approx -3$ MHz (**Figure 3.3a, blue**). A series of Mims spectra collected at various τ values (Supplementary Fig. 5) to test for Mims "suppression effects" confirmed that the observed peaks are not new proton ENDOR signals from the addition of TFE, but indeed arise from ^{19}F couplings.[98] Therefore, the ENDOR spectra at $g_{||}$ reveal a hyperfine coupling to the ^{19}F of TFE with $A_{||}$ = ~1 MHz.

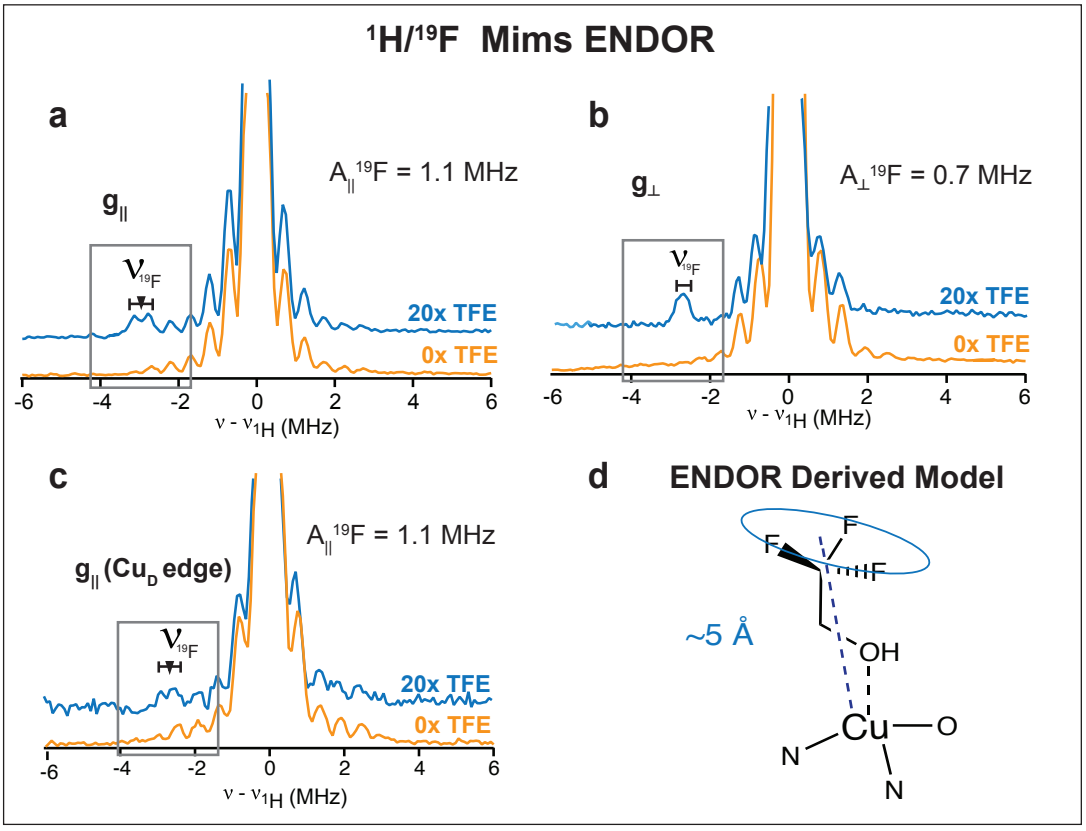

Figure 3.3. ENDOR spectroscopic analysis of TFE interacting with the pMMO copper sites in native lipid nanodiscs. a-c, Q-band $^{1}H/^{19}F$ Mims pulsed ENDOR of pMMO with (blue) and without (gold) the addition of 20x TFE at different magnetic field positions. Mims conditions: microwave (MW) frequency = 34.72 GHz (with) and 34.59 GHz (without), 2 K, π/2 = 50 ns, τ = 900 ns, T_{RF} = 60 μs, RF tail = 5 μs, repetition time of 100 ms, ~20-50 scans each. **d,** Model derived from the ENDOR data.

The ^{19}F doublet is observed at fields across the EPR envelope, with a splitting that varies with field, as illustrated by a spectrum at $g_{\perp}$ = 2.05 (**Figure 3.3b, blue**), with a ^{19}F coupling of ~0.6 MHz (**Figure 3.3b**). Again, these signals are not observed in the absence of TFE (**Figure 3.3b, gold**). Most important, as can be seen in Fig 3**a**, at these g-values, the signals from Cu_D and Cu_B overlap, and so the spectra do not determine the TFE binding site. Thus, a ^{19}F spectrum was collected at at g = 2.32, the extreme low-field edge of the EPR pattern, where it has been shown that only the Cu_D EPR signal is present.[84] This spectrum (Fig. 3c, blue) again exhibits the ^{19}F doublet with ~1 MHz splitting, which demonstrates that the TFE is interacting with the Cu_D site.

Analysis of the field dependency of the ^{19}F hyperfine couplings (**Figure 3.3a-c**) yields an essentially axial ^{19}F tensor of $A_{19F} \approx$ [1.1, -0.6, -0.6] MHz, with the unique axis roughly along $g_{||}$ (**Figure 3.3a**). As that axis lies normal to the Cu_D ligand plane, this implies that the TFE molecule binds axial to this plane. The tensor has the form of a through-space dipolar coupling, in which case the values of the tensor components imply that the fluorine-atom centroid is ~5 Å above the plane of the Cu_D(II). A model for TFE-bound Cu_D generated with a Cu(II)-O distance slightly greater than 2 Å, similar to Cu(II)-O interactions observed for other biological copper centers,[99, 100] exhibits such a Cu-F distance (**Figure 3.3d**). Likewise, TFE interacting with the diiron center of MMO cofactor was also found to be describable by such a model.[92] Finally, to test for the possibility that TFE could be altering or disrupting the pMMO structure, a sample of pMMO in nanodiscs was prepared with 0.05% glutaraldehyde crosslinker and incubated with 20x TFE. The X-band EPR spectrum (**Figure S3.6**) and the Mims ENDOR (**Figure S3.7**) of this sample are identical to those of pMMO in native lipid nanodiscs in the presence of 20x TFE.

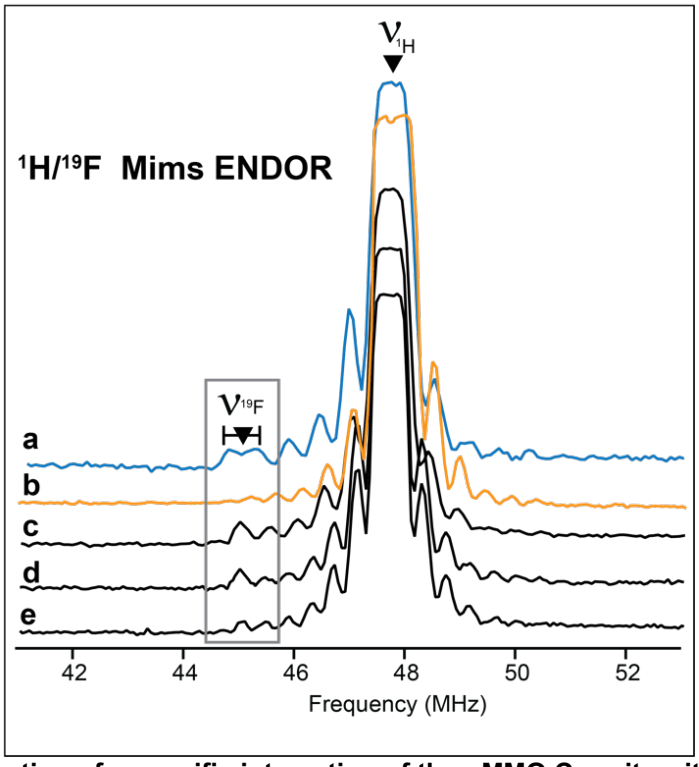

Figure 3.4. ENDOR detection of a specific interaction of the pMMO Cu_D site with TFE in native lipid nanodiscs. Q-band $^1H/^{19}F$ Mims pulsed ENDOR of pMMO **a**, + 20x TFE; **b**, without fluorocarbon addition; **c**, reduced with ascorbate + 20x TFE; **d**, solubilized in DDM + 20x TFE; e, + 20x 4-fluorophenol. All spectra were acquired at $g_{||}$ (g = 2.16). Mims conditions: MW frequency = 34.59 – 34.74, 2 K, π/2 = 50 ns, τ = 900 ns, TRF = 60 µs, RF tail = 15 µs, repetition time of 100 ms, ~20 scans each.

The conclusion that TFE specifically interacts with Cu_D, and not with Cu_B, was confirmed by comparing the Q-band $^1H/^{19}F$ Mims pulsed ENDOR spectra of pMMO with 20x TFE (**Figure 3.4a**) with ENDOR spectra collected from samples without added TFE (**Figure 3.4b**), and with ENDOR spectra of samples to which 20x TFE was added following elimination of the Cu_D signal, but not that of Cu_B,[14, 84] by treatment with 15 molar equivalents of ascorbate per protomer, (**Figure 3.4c**). In spectra obtained across the Cu_B EPR envelope of the latter two samples, the ^{19}F doublet from Cu-bound TFE is absent; only a weak distant ENDOR peak centered at the ^{19}F Larmor frequency,[101] derived from free TFE in the volume surroundings of Cu_B can be detected (**Figure 3.4b,c**). This result establishes that TFE does not interact with the Cu_B site, and that it specifically interacts with the Cu_D site.

To assess whether the interaction with Cu_D is specific to TFE, native lipid nanodisc pMMO samples were also incubated with 20x 4-fluorophenol. Unlike sMMO, pMMO cannot oxidize cyclic and aromatic hydrocarbons[93, 102] so 4-fluorophenol would not be expected to bind in the active site. The addition of the 4-fluorophenol does not denature the protein or alter the two copper centers as shown by X-band EPR measurements (**Figure S3.6c**). The $^1H/^{19}F$ Mims ENDOR of pMMO + 20x 4-fluorophenol exhibits an extremely weak ^{19}F distant ENDOR peak, at ν_{19F} but not the resolvable ^{19}F couplings (**Figure 3.4d**) **t**hat we would predict from a model for 4-fluorophenol in the active site and bound to Cu_D (~0.5 MHz).

Interestingly, when a sample of pMMO solubilized in the detergent n-dodecyl-b-D-maltoside (DDM) was treated with 20x TFE and examined by $^1H/^{19}F$ Mims ENDOR, the Mims ENDOR spectrum spectrum shows no ^{19}F doublet from TFE interacting with Cu_D, only a very weak distant ENDOR ^{19}F ENDOR response at ν_{19F} from non-specifically located TFE (**Figure 3.4e**). The lack of interaction with pMMO in DDM likely results from destabilization of the helices providing the Cu_D ligands. These helices are not observed in the crystal structures of detergent-solubilized pMMO, and only become ordered in the cryoEM structures of pMMO in native lipid nanodiscs (**Figure 3.1**).[16] This observation suggests that an appropriately ordered active-site environment is important for TFE binding.

CryoEM structures of TFE added to nanodisc pMMO showed a new density stemming from the CuD site, density that was absent in the previous cryoEM structures. This evidence supports and expands the ENDOR experiments, as the density is able to modeled as TFE axial to the Cu-ligand plane, and where the OH group of the TFE is ~2.2 Å, identical to what was determined by ENDOR.

Since pMMO can also oxidize butane[93], we further investigated product analog binding using 4,4,4-trifluorobutanol (TFB), which should be distinguishable from TFE in a cryoEM map. Samples of pMMO in native nanodiscs, prepared with and without 0.05% glutaraldehyde crosslinker, were treated with 20 molar equivalents of TFB and analyzed by EPR, ENDOR, and cryoEM. CyroEM sturctures showed new density compared to those without TFB added, yet the density was not well resolved. The crosslinked sample showed the canonical pMMO EPR signals along with a resolved Mims ENDOR ^{19}F doublet (**Figure S3.8**), while the sample without crosslinker showed a perturbed EPR signal and no meaningful ^{19}F response by ENDOR (**Figure S3.8**). The couplings for the crosslinked sample are smaller than those observed with TFE, and $A(g_{\perp}) > A(g_{||})$, indicating that the orientation of the fluorine atoms relative to the Cu_D(II) plane is different.

Conclusions:

Our combined data identify Cu_D as Cu(II), associate Cu_D with methane oxidation activity, and show that Cu_D interacts with TFE, a pMMO product analog. The binding of TFE in the pocket adjacent to Cu_D implicates this region as a part of the pMMO active site and the location of substrate binding. This pocket is lined with conserved residues, both hydrophobic and charged, which likely mediate substrate binding and regulate the local redox environment. These conclusions derive from a multipronged investigation of pMMO in native lipid nanodiscs, which mimic the physicochemical properties of its membrane environment, stabilizing transmembrane helices, the Cu_D site, and the active site pocket. ENDOR spectroscopy specifically detects TFE ^{19}F hyperfine couplings to Cu_D that support a model for TFE binding consistent with cryoEM structures showing that the TFE probe is bound in the Cu_D active site. The combination of cryoEM and ENDOR spectroscopy addresses a significant limitation of cryoEM, the inability to clearly identify metal ions and small molecules from cryoEM maps alone. This approach may be generalizable to the investigation of other metalloenzymes by cryoEM. Most important, identification of the location of the pMMO active site and the site of product formation has profound implications for the understanding of pMMO catalysis. Discerning the molecular details of Nature's primary methane oxidation catalyst will inform the rational design of catalysts for the conversion of methane to methanol.

METHODS

Culturing of methanotrophic bacteria

Methylococcus capsulatus (Bath) was cultured in a 12 L fermentor (BioFlo 4500, New Brunswick Scientific) as described previously[13, 16]. Liquid media were comprised of 1X nitrate mineral salts (NMS), 3.9 mM phosphate buffer (pH 6.8), 40 μM NaFe(III)EDTA, trace element solution, and 50 μM $CuSO_4$. *M. capsulatus* (Bath) was cultured at 45°C, with agitation of 200 rpm and a constant gas flow of 1 L/min at a 1:3 ratio of methane:air. Upon reaching an optical density at 600 nm (OD_{600}) of 8-10, cells were harvested by centrifugation at 5,000 xg for 25 min, frozen in liquid nitrogen, and stored at -80°C.

Isolation of pMMO-containing membranes

M. capsulatus (Bath) cells were resuspended in 25 mM PIPES (pH 7.3), 250 mM NaCl in the presence of DNase (Sigma-Aldrich) and EDTA-free cOmplete protease inhibitor cocktail (Sigma-Aldrich). Resuspended cells were lysed by sonication at 80% power (45 amplitude, 1 s on/ 1 s off) for 10 min (QSonica Q700). The lysate was clarified by centrifugation at 10,000 xg for 45 min and then another round of centrifugation at 10,000 xg for 25 mins. To isolate membranes, the supernatant was ultracentrifuged at 150,000 xg for 60 min. The pelleted membranes were washed in a 40 mL Dounce homogenizer using fresh PIPES buffer, and then pelleted once more by ultracentrifugation at 150,000 xg for 30 min. This process was repeated for a total of two washes in the 40 mL Dounce homogenizer before resuspending the washed membrane pellet in a 7 mL Dounce homogenizer. Membrane protein concentration was determined using the DC Lowry Assay (Bio-Rad), and the membranes were frozen in liquid nitrogen at 10 mg/mL for storage at -80°C.

Solubilization and isolation of pMMO

Membranes were solubilized using n-dodecyl-β-D-maltopyranoside (DDM, Anatrace) at a ratio of 1.2 mg DDM:1 mg protein with gentle agitation at 15 rpm for 2 h at 4°C. The solubilized membrane fraction was clarified by ultracentrifugation at 150,000 xg for 60 min. The supernatant was then concentrated and washed with 30 mL of buffer (25 mM PIPES (pH 7.3), 250 mM NaCl, 0.02% DDM) in a 100 kDa molecular

weight cutoff (MWCO) Amicon centrifugal concentrator. The protein concentration was measured by the DC Lowry Assay, and solubilized pMMO was frozen at 10 mg/mL in liquid nitrogen.

Native lipid extraction

As reported previously[16], native lipids were extracted using a modified literature protocol[103, 104]. To extract native lipid fractions from *M. capsulatus* (Bath), cells were resuspended in 20 mL methanol per 1 g of cells. Cells were sheared in a Dounce homogenizer with an additional 10 mL dichloromethane and 5 mL 40 mM phosphate buffer (pH 7.4). The organic and aqueous layers were allowed to separate. Upon layer separation, the organic layer was removed by aspiration and dried under a constant stream of gaseous nitrogen to form a solid layer. The solidified lipid extract was dried further in a vacuum desiccator overnight, weighed, and resolubilized in 25 mM PIPES (pH 7.3), 250 mM NaCl, 100 mM sodium cholate. Lipids were resolubilized to an estimated concentration of 50 mM assuming an average molecular weight of 700 g/mol for the extracted lipids.

Membrane scaffold protein expression and purification

Membrane scaffold proteins were expressed from plasmid pMSP1E3D1 (Addgene) transformed into *E. coli* BL21 Star (DE3) cells. Cultures were grown in Terrific Broth (TB) media (Millipore) at 37°C with shaking at 200 rpm to an OD_{600} of 2.0 and then induced for 4 h using 1 mM isopropyl β-D-1-thiogalactopyranoside (IPTG). Cells were harvested by centrifugation for 10 min at 8,000 xg and frozen in liquid nitrogen.

Cells were resuspended in 40 mM Tris (pH 7.2), 250 mM NaCl, 20 mM imidazole in the presence of EDTA-free cOmplete protease inhibitor, DNase, and 1% Triton-X 100 (Sigma-Aldrich). Resuspended cells were lysed by sonication at 80% power (amplitude 45, 1 s on/1 s off) for 10 min, and the lysate was clarified by centrifugation at 10,000 xg for 30 min. Clarified lysate was applied to a gravity-flow purification column containing 10 mL Ni-NTA resin (Invitrogen). The column was washed with 5 column volumes (CV) 40 mM Tris (pH 7.2), 250 mM NaCl, 20 mM imidazole, 50 mM sodium cholate followed by 15 CV 40 mM Tris (pH 7.2), 250 mM NaCl, 20 mM imidazole. Protein was eluted with 5 CV 40 mM Tris (pH 7.2), 250 mM NaCl, 250 mM imidazole, incubated with TEV protease at a ratio of 1:20 protease:protein, and dialyzed

against 1 L 40 mM Tris (pH 7.2), 250 mM NaCl, 1 mM EDTA at 4°C using a 10 kDA MWCO dialysis membrane.

To remove the TEV protease, dialyzed protein was reapplied to the gravity-flow column containing Ni-NTA resin and the flowthrough was collected. The column was washed with 4 CV 40 mM Tris (pH 7.2), 250 mM NaCl, 20 mM imidazole and the flowthrough was collected. The flowthrough containing purified MSPs was concentrated in a 10 kDa MWCO Amicon centrifugal filter, quantified by absorbance at 280 nm, and frozen in liquid nitrogen at a concentration of 2-4 mg/mL.

Nanodisc reconstitution and purification

Native lipid nanodiscs containing pMMO were prepared using previously reported protocols[15, 16, 105]. A mixture containing 25 mM PIPES (pH 7.3), 250 mM NaCl, 20 mM sodium cholate, $CuSO_4$, MSPs, and DDM-solubilized pMMO was prepared. Three equivalents of $CuSO_4$ were added per protomer of pMMO. pMMO, MSPs, and lipids were added at a ratio 1:4:240, respectively. The reconstitution mixture, totaling 5 mL in volume, was mixed by rotation at a 45° angle at 15 rpm for 30 min. SM-2 Bio-Beads (Bio-Rad) were then added to 0.8 g/mL and mixed by rotation at a 45° angle at 15 rpm for 2 h. Bio-Beads were removed from the reconstitution mixture by syringe filtration, and the protein mixture was concentrated to 500 µL in a 100 kDa MWCO Amicon centrifugal filter before purification in 25 mM PIPES (pH 7.3), 250 mM NaCl by size exclusion chromatography using a Superose 6 Increase 10/300 GL column (Cytiva). pMMO in nanodiscs eluted at ~15 mL, as monitored by the absorbance at 280 nm. The pMMO nanodisc-containing fractions were collected and concentrated in a 100 kDa MWCO Amicon centrifugal filter.

To measure the pMMO concentration without signal interference by MSPs, pMMO was quantified by SDS-PAGE. pMMO-containing nanodiscs were analyzed by SDS-PAGE using nanodiscs diluted to 0.5-2 mg/mL as measured by the DC Assay. A standard curve was created by analyzing DC Lowry Assay-quantified, DDM-solubilized pMMO at 2, 1, and 0.5 mg/mL. ImageJ was used to quantify the band representing PmoB for each lane, band intensities for purified pMMO in DDM were used to generate a standard curve, and band intensities for nanodisc pMMO samples were used to calculate the concentration for nanodisc-embedded pMMO.

Product analog loading

To probe the active site of pMMO, trifluoroethanol (Thermo Fischer Scientific), trifluorobutanol (Sigma-Aldrich) or 4-fluorophenol (Sigma-Aldrich) were added to nanodisc-pMMO samples and allowed to incubate overnight at 4°C or for 2 h at room temperature before experimental analysis.

Methane oxidation activity assay

Methane oxidation activity was measured using previously reported methods[15, 16, 46]. 100 µL pMMO samples were diluted to 0.5-2 mg/mL and mixed with excess duroquinol in 2 mL screw top vials (Agilent). Then 1 mL headspace gas was removed from the vials and replaced by 1.5 mL ^{13}C methane (Sigma-Aldrich). The reaction mixture was shaken at 200 rpm in a water bath at 45°C for 5 min and then frozen at -20°C. Control vials containing no methane and no duroquinol were also prepared. For GC/MS analysis, 500 µL chloroform containing 1 mM dicholoromethane was added to each sample. The vials were shaken at 200 rpm for 10 min followed by centrifugation at 2,000 xg for 10 min.

For analysis, 2.5 µL of sample were applied to a PoraBOND Q column (25 m x 250 µm x 3 µm) on an Agilent 7890B/5977A MSD GC/MS instrument with a split ratio of 10:1. The gas chromatograph was maintained under a constant flow of helium of 1.2 mL/min. The oven temperature was initiated at 80°C for 3.5 min, increased by 50°C/min to 150°C, and held for 1.5 min. A second ramp rate of 15°C/min was maintained to reach a final temperature of 300°C, which was held for 1 min. The mass spectrometer was maintained at a temperature of 230°C, quad temperature of 150°C, 70 eV, and a detector voltage of 2,999 V. Masses 31, 33, and 49 were monitored for the detection of ^{12}C methanol, ^{13}C methanol, and dichloromethane. The ^{13}C methanol peak was integrated, quantified against a standard curve, and normalized to the concentration of dichloromethane.

Inductively coupled plasma mass spectrometry (ICP-MS)

Either 25 or 50 µL of sample were incubated in concentrated nitric acid to a volume of 250 µL, then diluted to 5 mL for a final concentration of 5% nitric acid, and analyzed using an iCAP Q ICP-MS (Thermo) against a suite of standards. From these measurements, the molar equivalents of metal per protomer of pMMO were calculated, using the pMMO protomer concentration determined by SDS-PAGE band quantification as described above.

Metal depletion and reloading

Potassium cyanide metal depletion and reloading were achieved according to previously reported methods[16, 45]. Isolated membranes were resuspended in a Dounce homogenizer and stirred for 30 min at 4°C in 50 mM MOPS (pH 8.0), 250 mM NaCl with 10 molar equivalents of KCN and ascorbate. The membrane suspension was pelleted via ultracentrifugation at 150,000 xg for 1 h. The supernatant was discarded, the pellet was resuspended in 40 mL 25 mM PIPES (pH 7.3), 250 mM NaCl, and the membrane suspension was ultracentrifuged at 150,000 xg for 30 min. This homogenization and ultracentrifugation process was repeated once more before a final homogenization step in 7 mL 25mM PIPES (pH 7.3), 250mM NaCl. The protein content of the metal-depleted membranes was quantified by the DC Lowry Assay.

The metal-depleted membranes were then divided into parallel batches of which one was reloaded with $CuSO_4$ and the other was left to incubate in a metal-free conical tube. For reloading, 10 molar equivalents of $CuSO_4$ per protomer were added to one batch of metal-depleted membranes in a metal-free conical tube, while both batches were mixed by rotation end-over-end for 30 min at 4°C.

The metal-depleted and copper-reloaded membranes were then solubilized in DDM as described above, and the protein concentration and metal content were measured as described above. Nanodiscs were prepared as reported above with the modification that the mixing steps were performed in metal-free conical tubes. The metal-depleted pMMO nanodiscs were prepared with 0 equivalents of additional $CuSO_4$ while the copper-reloaded pMMO nanodiscs were prepared with 3 equivalents of additional $CuSO_4$, as described above.

EPR and ENDOR spectroscopy

All X-band EPR samples were loaded into Wilmad quartz X-band EPR tubes (Sigma Aldrich). Q-band ENDOR, samples were loaded into custom-made 2.5 mm OD thin-wall quartz Q-band EPR tubes and flash frozen in liquid nitrogen. Samples were stored in liquid nitrogen.

CW (continuous wave) X-band EPR experiments were performed on a modified Bruker ESP-300 equipped with a variable-temperature liquid helium flow Oxford Instruments ESR-900 cryostat. Exact EPR conditions are included in the figure captions or text. Pulsed ENDOR experiments were performed on a custom built 35 GHz spectrometer described previously[70, 106]. The pulse spectrometer is equipped with a SpinCore PulseBlaster ESR_PRO 400 MHz digital word generator and an Agilent Technologies Acquiris

DP235 500 MS/s digitizer using SpecMan4EPR software. All experiments were performed at 2 K. The methodology in this study consents of ^{1}H Davies ENDOR, which employed a [π−T_{RF}−π/2−τ−π−τ−echo] pulse sequence[11], and ^{19}F/^{1}H Mims ENDOR, which utilized a [π/2−τ−π/2−T_{RF}−π/2] pulse sequence. In both the Davies and Mims sequences, T_{RF} denotes the interval in which RF is applied and τ denotes the microwave pulse duration.

ENDOR derived Cu(II)-nuclear distances:

A nucleus in the vicinity of a type 2 Cu(II) center experiences a distance-dependent point-dipolar hyperfine coupling that takes the form of a simple axial tensor:

(1) $\mathbf{T}(r_n) = T(r_n)\,[-1,-1,2]$

where the distance-dependent scaling factor is given by **eq 2**,

(2) $$T(r_n) = \frac{C_n}{r_n^3}$$

(3) $C_{1H} = 80.0 \cdot \text{MHz Å}^3$ $C_{19F} = 75.3\ \text{MHz}\cdot\text{Å}^3$

and **eq 3** give the nucleus-specific constant, C_n, for nuclei of interest here. The interaction tensor $\mathbf{T}(r_n)$ for the ^{19}F nucleui of TFE is determined from a 2D field-frequency set of ^{19}F ENDOR spectra collected at fields across the Cu(II) EPR spectrum[107], thus yielding the Cu(II)–F distance to the nuclei giving rise to the ^{19}F signal.

Cryoelectron microscopy sample preparation

pMMO nanodisc samples were diluted to ~4-5 mg/mL as measured by absorbance at 280 nm and then applied to C-Flat™ holey carbon copper grids with 1.2 μm holes, 1.3 μm spacing, and 400 mesh (Electron Microscopy Sciences) using an FEI Vitrobot. Grids were plasma cleaned using a Solarus plasma cleaner (Gatan) for 10 s at a voltage of 10 W. 3 μL of sample were applied to grids in the Vitrobot chamber

at 100% humidity and 4°C. Samples were blotted with a wait time of 30 s, a blot time of 4 s, and a blot force of 5 before vitrification in liquid ethane and storage in liquid nitrogen.

CryoEM data collection

CryoEM data for structure determination were collected at the National Center for CryoEM Access and Training (NCCAT) using a Titan Krios (Thermo-Fisher) at 300kV.

CryoEM data processing

CryoEM data were processed using cryoSPARC v3.3[108]. Movie frames were aligned using patch motion correction[109]. CTF parameters were estimated using patch CTF estimation[110, 111]. Particles were picked using the Blob Picker with a particle diameter range of 120-150 Å and extracted using a box size of 256 pixels. Extracted particles were subjected to 2D classification, and pMMO classes were selected and used as templates for template picker. Particles picked using the template picker were then refined using heterogenous refinement with C1 where a previously published pMMO volume (PDB 7T4P)[16] was used as a reference against the same volume lowpass filtered to 100 Å resolution as a decoy reference. Heterogenous refinement at a box size of 128 pixels was repeated until the estimated resolution achieved the Nyquist limit. Refined particles were then subjected to unmasked homogenous refinement at C1 symmetry, masked homogenous refinement at C1 symmetry, masked non-uniform refinement at C1 symmetry, and masked non-uniform refinement at C3 symmetry.[112] This refined volume was then subjected to several rounds of global CTF refinements alternated with masked non-uniform refinements at C3 symmetry to correct the relevant CTF parameters and achieve optimal resolution and map quality. The CTF-corrected volume was then subjected to local CTF correction and non-uniform refinement. This volume was then corrected using local motion correction at a box size of 512 pixels, which was used as the final volume if the resolution improved[113]. DeepEMhancer post processing was tested for deep learning sharpening of all reported reconstructions, but in these cases did not improve the clarity of copper centers, ligands, or disordered protein regions[114]. Local resolution estimation and local filtering were used to sharpen the final volume. All resolution are reported as Gold-Standard Fourier Shell Correlation (GCFSC) values at a cutoff of 0.143. [115]

CHAPTER 4: The universal step in methanobactin biosynthesis is performed by a mixed-valent Fe(II)Fe(III) center

Results from this chapter have been published previously in the following article:

Y. J. Park, R. J. Jodts, J. W. Slater, R. M. Reyes, V. J. Winton, R. A. Montaser, P. M. Thomas, W. B. Dowdle, A. Ruiz, N. L. Kelleher, J. M. Bollinger, Jr., C. Krebs, B. M. Hoffman, and A. C. Rosenzweig, P.N.A.S., **2022**, *119* (13), e2123566119

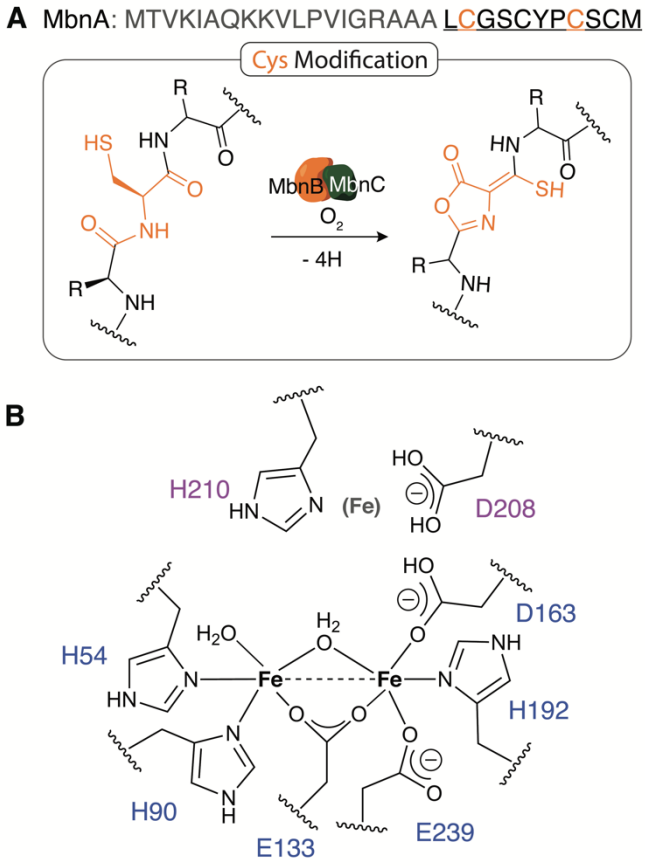

Figure 4.1. Reaction catalyzed by MbnBC and a model for the MbnB Fe binding site. (*A*) A representative MbnA sequence from *Methylosinus trichosporium* OB3b contains a leader sequence (gray) and a core sequence (underlined). The cysteine residues that are modified are colored in orange. MbnBC performs a four-electron oxidation to generate an oxazolone ring and a thioamide group from each cysteine residue and neighboring carbonyl group. (*B*) The proposed metal binding site in MbnB showing potential diiron and triiron clusters. Disruption of the amino acid ligands labeled in blue significantly diminished activity. Two other residues, D208 and H210 (labeled in purple), are proposed to bind a third Fe ion.

The MbnBC enzyme complex is central to the biosynthesis of methanobactins (Mbns), copper-binding metallophores isolated from methane-oxidizing (methanotrophic) bacteria and currently under investigation as therapeutics for Wilson disease.[27, 116] Mbns are ribosomally synthesized, post-translationally modified peptide (RiPP) natural products generated from a precursor peptide, MbnA.[117] Operons encoding MbnA along with the Mbn biosynthetic and transport machinery are found in a range of bacteria besides methanotrophs and are predicted to yield a diverse array of natural products.[25] Mbns chelate copper with high affinity by using two nitrogen and two sulfur atoms derived from nitrogen-containing

heterocycles and neighboring thioamide groups.[22, 24, 118-121] These paired oxazolone ring and thioamide groups, present in all Mbns characterized thus far, are generated from two conserved cysteine residues and the carbonyl groups of their preceding residues (**Figure 4.1A**) by two proteins, MbnB and MbnC, which form a heterodimeric complex denoted MbnBC.[27]

MbnB is the only biochemically characterized member of the DUF692 protein family, which includes >13,000 sequences (UniProt), while MbnC belongs to a completely uncharacterized protein family.[27] Initial studies showed that MbnBC requires both Fe and O_2 to convert cysteine into an oxazolone/thioamide pair (Fig. 1*A*). According to top-down native mass spectrometry (nTDMS) measurements, MbnB ejected from the MbnBC complex contains three Fe ions. Mössbauer spectroscopic analysis further indicated that MbnBC contains a mixture of triferric $[Fe(III)]_3$ and diferric $[Fe(III)]_2$ clusters, and model of MbnBC based on the unpublished crystal structure of a diiron center-containing homolog from *Haemophilus somnus* 129pt (PDB accession code 3BWW) suggested possible ligand sets for three Fe ions (**Figure 4.1**).[27] Variants in which predicted ligands His54, His90, Glu133, Asp163, His192, and Glu239 were individually replaced with alanine or serine (**Figure 4.1**) exhibited diminished Fe content and significantly less cysteine modification activity, supporting a functional role for Fe coordinated by these residues.[27]

Despite these advances, heterogeneity in the MbnBC Fe site, as evidenced by the observation of both dinuclear $[Fe(III)]_2$ and trinuclear $[Fe(III)]_3$ clusters by Mössbauer spectroscopy, has complicated identification of the catalytically active species. Here we provide evidence through electron paramagnetic resonance (EPR) combined with enzymatic activity assays that the active species of MbnBC is a mixed-valent Fe(II)Fe(III) cluster coordinated by conserved residues in MbnB. These findings set the stage for detailed mechanistic studies and expand the diversity of reactions attributable to nonheme diiron enzymes in natural product biosynthesis.

RESULTS

Determining reduced MbnBC is correlated with activity

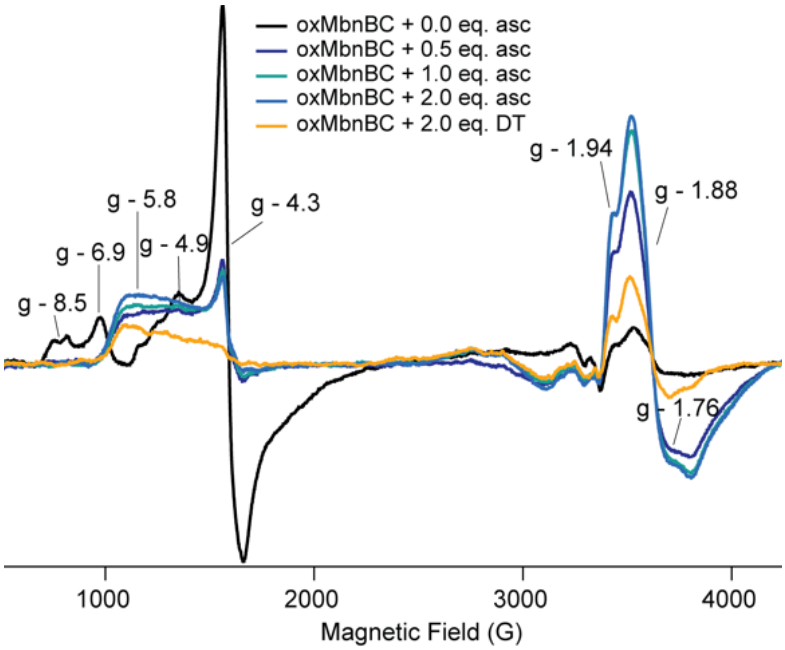

Figure 4.2. **EPR of MbnBC.** EPR spectra of ^{57}Fe MbnBC treated with different amounts of ascorbate (asc) and dithionite (DT).

To identify the Fe species of the enzyme that reacts with MbnA and O_2, EPR and activity data were acquired for MbnBC samples in various oxidation states. *Methylosinus* (*Ms.*) *trichosporium* OB3b MbnBC was heterologously expressed in *E. coli* in the presence of 250 μM supplemental ^{57}Fe and purified using established protocols.[27] The resultant protein was first treated with ferricyanide to generate a fully oxidized (all ferric) sample (oxMbnBC). The EPR spectrum of this sample (**Figure 4.2**, oxMbnBC + 0.0 eq. asc) exhibits a strong signal at g_{eff} = 4.3 and several weaker signals with g_{eff}-values of ~ 8.5, 6.9, 4.9, characteristic of "rhombic" S = 5/2 Fe(III). In addition, there is a weak signal at g < 2 attributable to the S = 1/2 ground state of an antiferromagnetically coupled Fe(II)Fe(III) cluster (**Figure 4.2**); double integration of this signal reveals the presence of 9 μM Fe(II)Fe(III) clusters (~1% of the total Fe in the sample). This spectrum of oxMbnBC is nearly the same as that obtained for aerobically purified MbnBC, but lacks features previously observed above 4000 Gauss.[27]

Treatment of oxMbnBC with ascorbate (redMbnBC_asc) results in marked changes to the EPR spectrum. First, a rhombic EPR signal with $\boldsymbol{g}$ = [1.94, 1.88, 1.76, g_{ave} = ~1.9] is observed and is well resolved

at ~10-30 K (**Figure 4.2**). This signature is attributed to an antiferromagnetically coupled Fe(II)Fe(III) cluster with an *S* = 1/2 ground state, a unit that has been characterized extensively in both diiron enzymes and synthetic model complexes thereof [122-124]. The intensity of the *S* = 1/2 EPR signal reached maximum upon the addition of 1-2 equiv of ascorbate (**Figure 4.2**), spin, and persisted upon addition of 5 equivalents of ascorbate, indicating that ascorbate cannot lead to efficient reduction of the cluster (**Figure 4.3**).

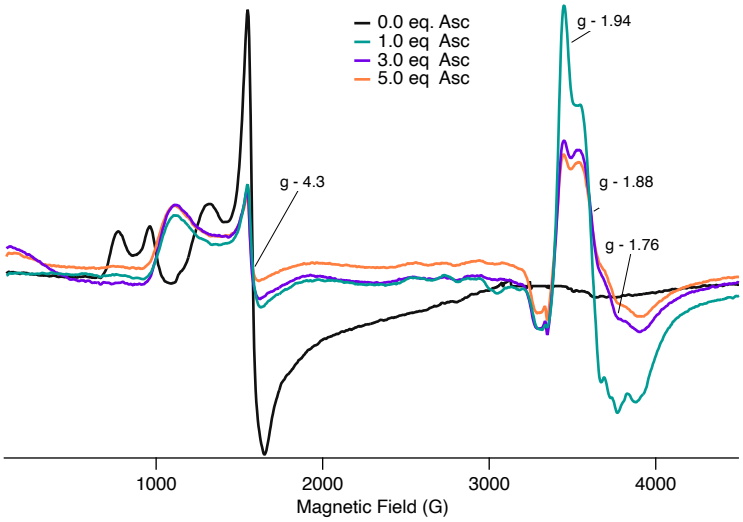

Figure 4.3. EPR spectra of ^{56}Fe MbnBC treated with 0, 1, 3, and 5 equiv of ascorbate. This experiment shows that excess ascorbate cannot reduce the Fe(II)Fe(III) site to $[Fe(II)]_2$.

Addition of 2 equivalents of dithionite (redMbnBC_dt), however, results in a decrease of the intensity of the *S* = 1/2 signal, suggesting further reduction to an $[Fe(II)]_2$ cluster (**Figure 4.2**). In addition, the pronounced signal at g_{eff} = 4.3 is reduced ~5-fold in intensity and the low-field signals disappear completely, suggesting that the majority of the *S* = 5/2 rhombic Fe(III) is reduced. A new, broad signal extending from *g* = 4.5 to *g* = 6.7 appears as well, and could derive from an alteration in the zero-field splitting of residual high-spin Fe(III) or from a $2e^-$ reduced $[Fe(II)]_2$/Fe(III) cluster.

MbnBC samples in each of the three oxidation states, oxMbnBC, redMbnBC_asc prepared with 2 equiv of ascorbate, and redMbnBC_dt, were then tested for MbnA modification activity (**Figure 4.4**). For each assay, MbnBC prepared in the anaerobic chamber was mixed with an equal volume of MbnA in O_2-saturated buffer using a stopped-flow apparatus, and MbnA modification was monitored by the appearance

of an optical feature at 335 nm, arising from the oxazolone ring and the thioamide group [27]. Although the oxidized protein has an overlapping optical feature at 340 nm, this feature forms slowly and is much weaker, suggesting that the absorbance is primarily attributable to product formation [27]. A comparison of the kinetictraces indicates that redMbnBC_asc produces the modified MbnA product with the greatest initial velocity and yield at completion.

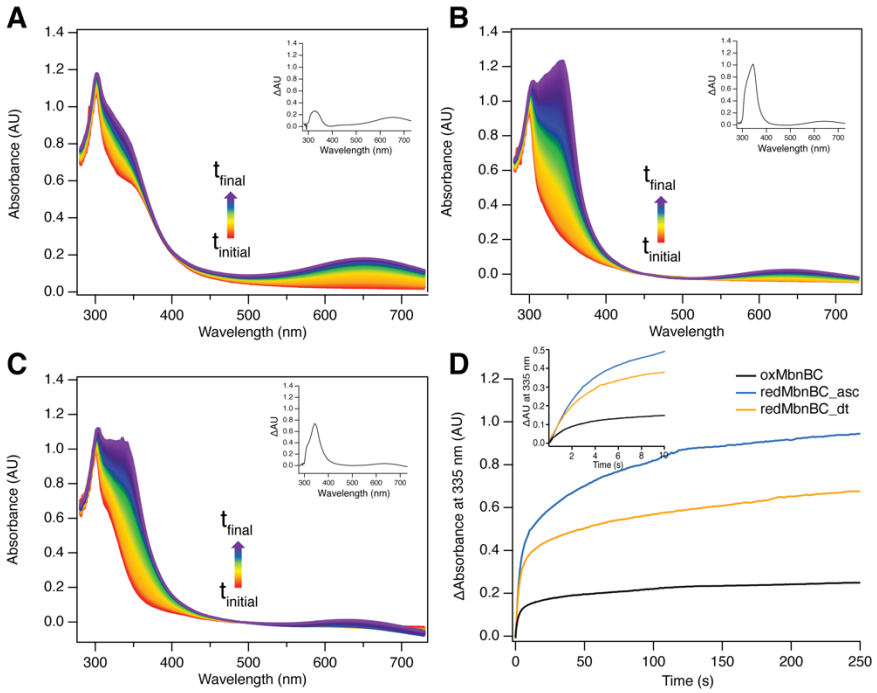

Figure 4.4. Reaction of MbnBC with MbnA: 150 μM (*A*) oxMbnBC, (*B*) redMbnBC_asc, and (*C*) redMbnBC_dt with 300 μM MbnA in oxygenated buffer using stopped-flow spectroscopy over period of 250 s. Arrows indicate the increase at 335 nm as a function of time with the starting spectrum colored red and the ending spectrum colored purple. Each inset shows the difference spectrum between the initial and final timepoints. The feature at 650 nm is proposed to derive from a charge transfer transition associated with the MbnA/oxidized MbnBC complex (*D*) Difference absorbance traces at 335 nm attributed to the formation of an oxazolone ring and a thioamide group, obtained by subtracting the absorbance at each point from the initial time point. Inset shows the traces plotted between 0.01 and 10 s.

X-band EPR of MbnA binding to the Fe(II)Fe(III) center

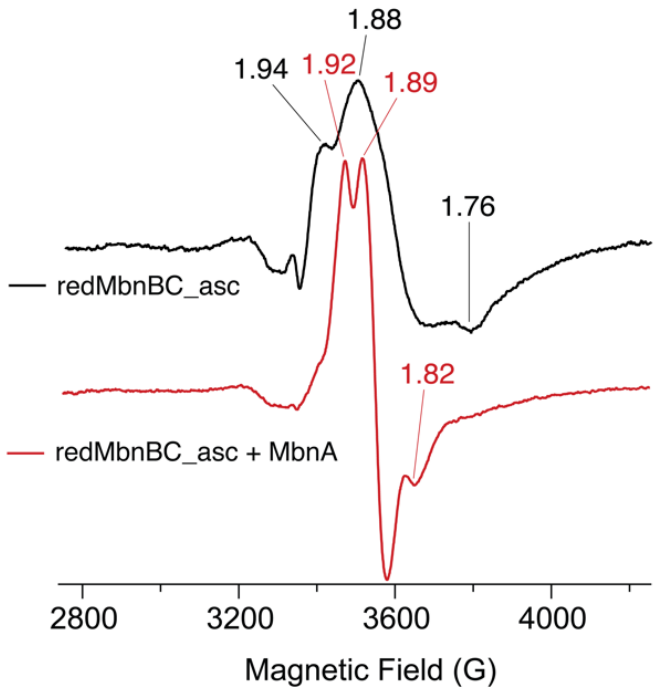

Figure 4.5. Effect of MbnA on the EPR spectrum of redMbnBC_asc. Samples were prepared with 1.2 mM redMbnBC_asc and 2 equiv of MbnA per MbnBC complex

Given that redMbnBC_asc gave the highest rate and extent of MbnA modification, 2 equiv MbnA were added to redMbnBC_asc under anaerobic conditions to generate the reactant complex, and the effects of substrate binding on different Fe species was examined by EPR and Mössbauer spectroscopies. In the EPR spectrum, the S = 1/2 g_{ave} ~ 1.9 feature attributed to the antiferromagnetically coupled Fe(II)Fe(III) center is converted to a new, sharper feature with g-values of 1.92, 1.89, 1.82 (**Figure 4.5**). The perturbation suggests that MbnA binding modifies the coordination sphere of the Fe(II)Fe(III) cluster. Indeed, similar perturbations upon addition of substrate have been observed for all three HD-domain mixed-valent diiron oxygenases and oxidases (MVDOs) that have been studied to date.[125-127] The residual g = ~5.8 signal also is perturbed upon substrate addition (**Figure S4.1**).

To further correlate activity with the prevalence of the Fe(II)Fe(III) cluster, catalytically-impaired variants in which the proposed Fe ligands were replaced with alanine or serine (H54A, H90S, E133A, D163S, H192A, and E239A) (**Figure 4.1**) [27], were isolated, treated with 2 equiv ascorbate, and examined

by EPR spectroscopy (**Figure S4.2**). With the exception of D163S, these substitutions abolished the signals from the Fe(II)Fe(III) cluster, consistent with a first coordination sphere including H54, H90, E133, H192, and E239. The D163S substitution changed, but did not abolish, the Fe(II)Fe(III) EPR signal, consistent with this residue as a weakly interacting ligand.

The correlation between activity and the presence of a Fe(II)Fe(III) cluster combined with the observation of both [Fe(III)]2 and [Fe(III)]3 clusters by Mössbauer spectroscopy and nTDMS [27] suggested that our MbnBC sample preparation could be improved to maximize the amount of active Fe(II)Fe(III) species. We therefore tried to prepare an MbnBC sample with a homogeneous [Fe(III)]2 cluster. Initial attempts to remove Fe from MbnBC using ferrozine, which significantly diminishes activity [27], and to reload with either Fe(II) or Fe(III) were unsuccessful. As an alternative approach, MbnBC was heterologously expressed in E. coli with less Fe in the growth medium (160 μM compared to 250 μM used above and >250 μM used in prior work [27]). Inductively coupled plasma mass spectrometry (ICP-MS) measurements indicated that the MbnBC isolated from these cultures (MbnBClowFe) contained 0.82 ± 0.02 equiv of Fe, whereas MbnBC isolated from cultures with 250 μM Fe ($MbnBC_{highFe}$, used for above experiments) contained 1.05 ± 0.2 equiv Fe.

The enzymatic activities of $MbnBC_{lowFe}$ and $MbnBC_{highFe}$ were then compared. The samples were first treated with 2 equiv of ascorbate to maximize the presence of the Fe(II)Fe(III) species ($redMbnBC_{lowFe}$_asc, $redMbnBC_{highFe}$_asc). Activity assays were then initiated by adding 1.3 equiv of the substrate MbnA to ascorbate treated MbnBC under ambient aerobic conditions to provide excess O_2 to the reaction as a cosubstrate. Strikingly, the reaction with $redMbnBC_{lowFe}$_asc yielded significantly more product (~1.8x) than the reaction with $MbnBC_{highFe}$_asc.

To discern the differences between the $MbnBC_{highFe}$ and $MbnBC_{lowFe}$ samples, $MbnBC_{lowFe}$ was examined by EPR spectroscopy. The EPR spectra of $redMbnBC_{lowFe}$_asc are similar to those of $MbnBC_{highFe}$_asc, exhibiting identical features at g_{ave} ~ 1.9 and g_{eff} = 4.3, of which the latter signal likely derives from underloaded diiron cluster (**Figure S4.3**). The signal at S = 1/2 with g_{ave} ~1.9 integrates to ~35 μM spin, which corresponds to ~19% of total Fe and ~60% reduction yield of $[Fe(III)]_2$, which is consistent with the yield observed for $MbnBC_{highFe}$. The activity profiles of $MbnBC_{lowFe}$ in the three oxidation states (**Figure S4.3**) recapitulate those of $MbnBC_{highFe}$ (**Figure 4.3**). The lesser quantity of $[Fe(III)]_3$ cluster in the

highest activity redMbnBC$_{lowFe}$_asc sample further supports the identification of the MbnBC active species as a mixed-valent Fe(II)Fe(III) cluster.

The combined data indicate that the active cofactor is a mixed-valent Fe(II)Fe(III) species, leaving the role of the third Fe binding site detected by Mössbauer spectroscopy, nTDMS of MbnBC$_{highFe}$ [27], and crystallography unclear. To probe the functional significance of this site, two of its ligands, D208 and H210 (**Figure 4.1**), were individually replaced with serine and the resultant D208S and H210S variants expressed in the presence of 250 μM Fe. According to ICP-MS measurements, the D208S and H210S variants contained 0.92 ± 0.084 and 1.17 ± 0.04 equiv Fe, respectively, slightly less than or comparable to Fe content of MbnBC$_{highFe}$ (also expressed with 250 μM Fe).

Site directed mutants establish a diiron cofactor rather than a triiron cofactor

Activity assays were then performed as described for redMbnBC_asc. Both variants were able to modify MbnA. While D208S yielded about half as much product as wildtype MbnBC$_{lowFe}$, the H210S variant was significantly less active. Nevertheless, these results indicate that a third Fe ion is not essential for activity. To assess the presence of the active Fe(II)Fe(III) species, both variants were reduced with 2 equiv ascorbate and examined by EPR spectroscopy. Each variant exhibits the g_{ave} = ~1.9 feature attributed to the S = 1/2 Fe(II)Fe(III) species (**Figure 4.6**). While the D208S spectrum is identical to that of wildtype MbnBC in terms of g-values, the spectrum of H210S at 10 K exhibits unresolved g-values, possibly reflecting the presence of multiple cofactor conformers. It is possible that this substitution disrupts the active site geometry, as evidenced by the EPR spectrum, leading to reduced MbnA modification activity. This perturbation is even more evident in the EPR spectrum of the H210S MbnBC-MbnA complex, which is very different from that of wildtype MbnBC in the presence of MbnA. This substitution likely impairs the ability to

properly bind the substrate. These combined findings further support the assignment of a diiron Fe(II)Fe(III) active species.

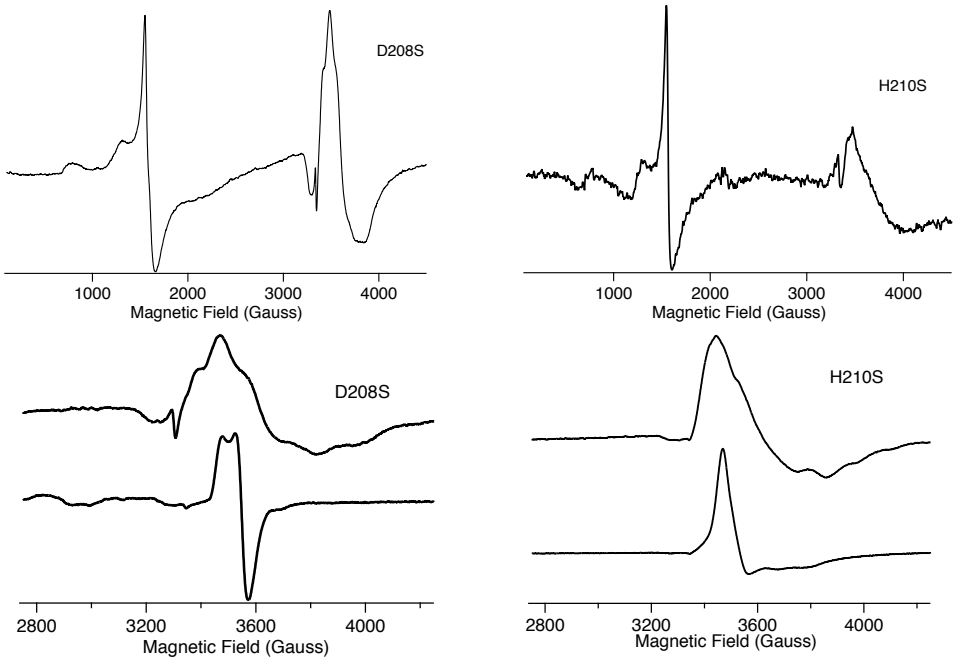

Figure 4.6. EPR spectra of D208S and H210S variants. Top: EPR spectra of the at 4 K full magnetic range. Bottom: 10 K spectra of Fe(II)Fe(III) features with and without MbnA substrate. The Fe(II)Fe(III) signal of the D208S variant is very similar to that of wildtype MbnBC whereas the H210S variant shows multiple perturbed signals as well as a very different substrate-bound signal compared to wildtype.

Summary

The identification of the MbnBC active species as a diiron, rather than triiron, cluster adds to an ever-expanding group of enzymes that use nonheme diiron cofactors to activate dioxygen and oxidize substrates [128, 129]. There are three major families of nonheme diiron enzymes: (i) the ferritin-like oxidases and oxygenases (FDOs), which include soluble methane monooxygenase [82], ribonucleotide reductase [130], aldehyde deformylating oxygenase [131], and stearoyl-acyl carrier protein desaturase [132], (ii) the recently discovered family of heme-oxygenase-like diiron enzymes (HDOs), and (iii) the mixed-valent diiron oxygenases and oxidases (MVDOs). All FDOs and HDOs studied to date activate O_2 with the $[Fe(II)]_2$ forms of their cofactors; a two-electron oxidative addition forms a peroxo-$[Fe(III)]_2$ intermediate, which can either directly transform the substrate or convert to high-valent, substrate-oxidizing intermediates upon O-O cleavage. FDOs and HDOs typically carry out $2e^-$ oxidations of their substrates and require two additional

electrons, which are usually provided by a reduced nicotinamide, to convert the $[Fe(III)]_2$ "product" of substrate oxidation back to the O_2-reactive $[Fe(II)]_2$ form.

By contrast, the MVDOs, which include the enzymes *myo*-inositol dioxygenase (MIOX), PhnZ, and TmpB [125-127] activate O_2 via a one-electron oxidative addition at the Fe(II) of their Fe(II)Fe(III) cofactors, while the Fe(III) site coordinates the substrate. The resultant superoxo-$[Fe(III)]_2$ intermediate can initiate substrate oxidation by abstraction of hydrogen from a partially activated aliphatic carbon. Importantly, this strategy allows MVDOs to carry out four-electron oxidations of their substrates and not to require a co-substrate. The four-electron oxidation of a cysteine to an oxazolone ring and thioamide amide group by MbnBC is yet another new reaction for this family. Given evidence that the Fe(II)Fe(III) cofactor of MbnBC can interact with its substrate MbnA in the absence of dioxygen, it may be that the reaction is initiated similarly to the MIOX and PhnZ reactions[129]. While the Fe(III) ion binds to the cysteine thiol, O_2 binds to the Fe(II), forming an iron-superoxo intermediate. Then an oxidative cyclization analogous to that in the isopenicillin *N* synthase (IPNS) mechanism [133] could occur by cleaving the Cβ–H bond in the cysteine residue to form a β-lactam ring. After C–S desaturation, presumably by a ferryl intermediate, the β-lactam ring would be opened by an enzyme nucleophile followed by formation of a five-membered oxazolone ring.[129] However, we cannot exclude the possibility that O_2 addition occurs before substrate binding. While these mechanistic steps are speculative, the identification of an Fe(II)Fe(III) cluster as the starting point for the catalytic cycle sets the stage for future spectroscopic and kinetic investigations. Moreover, MbnBC is unique in that it performs the reaction twice on the same substrate, modifying two specific cysteine residues. How MbnBC distinguishes the modifiable cysteines from other cysteines in MbnA and why disruption of Cys_{21} precludes modification of Cys_{27} [27] remain open questions.

METHODS

Sample preparation

A construct of *Ms. trichosporium* OB3b MbnBC that includes the *mbnC* gene with an N-terminal His_6 tag and a tobacco etch virus (TEV) cleavage site and the *mbnB* gene with a C-terminal Strep-II tag was used [27]. The D208S and H210S MbnBC variants were generated by site-directed mutagenesis using a QuikChange Lightning kit. All three proteins were expressed and purified as reported previously except that the concentration of Fe in the autoinduction growth medium was varied. $MbnBC_{lowFe}$ was expressed

with 160 μM ferrous ammonium sulfate while all other proteins including $MbnBC_{highFe}$, D208S, and H210S were expressed with 250 μM ferrous ammonium sulfate (MilliporeSigma). ^{57}Fe-labeled MbnBC was also prepared as described previously[27] except that the concentration of ^{57}Fe (Isoflex) added to the growth medium was 160 μM for $MbnBC_{lowFe}$. A buffer containing 25 mM MOPS, pH 7.2, 250 mM NaCl, and 10% glycerol was used for all experiments unless noted.

EPR Measurements

X-band EPR measurements were performed on a Bruker ESP-300 spectrometer with a liquid helium flow Oxford Instruments ESR-900 cryostat. All samples were measured using 200 μW of microwave power, 6 G modulation, 10 G/s scan rate, and 320 ms time constant. Spectra were acquired at 3.9 K to optimize the signals from rhombic high spin Fe(III) and at 10-12 K to optimize the signals from Fe(II)Fe(III) antiferromagnetically coupled species and subsequently scaled to relative intensities to facilitate comparison. Spectra were also subtracted against a spectrum of buffer in order to correct the baseline and to remove the signal of a copper contaminant associated with buffer reagents.

Activity assays

Stopped-flow absorption spectroscopy was performed using an Applied Photophysics Ltd. (Leatherhead, UK) SX20 stopped-flow spectrophotometer at 5 °C in an anoxic chamber (Labmaster, MBraun, Stratham, USA). The instrument was set for single-mixing with an optical path length of 1 cm and a photodiode-array (PDA) detector. An anaerobic solution of MbnBC (300 μM) in purification buffer (25 mM MOPS, pH 7.2, 250 mM NaCl, 10% glycerol) was rapidly mixed with an equal volume of O_2-saturated buffer containing MbnA (600 μM), and 1000 points of absorption spectra were acquired in a logarithmic time scale.

All other activity assays were performed using an Agilent Cary 3500 Compact Peltier UV-vis spectrophotometer. For the comparison between $MbnBC_{lowFe}$ and $MbnBC_{highFe}$ samples, 100 μM MbnBC (150 μL) was reduced with 2 equiv sodium ascorbate (Acros Organics) in a Coy anaerobic chamber and transferred into a quartz cuvette. The reaction was initiated by adding 1 μL of 20 mM MbnA (Bio-Synthesis Inc.) and exposure to air. Spectra were collected every 15 s for 15 min. Activity assays with ^{57}Fe-labeled $MbnBC_{lowFe}$ to compare different oxidation states and with the D208S and H210S variants were initiated by mixing 80 μM MbnBC in 120 μL of deoxygenated buffer with 400 μM MbnA in 120 μL aerobic buffer (aerobic

buffer was used to provide O_2 for the reaction). The reaction was then monitored for 1 h, collecting spectra with an interval of 15 s.

CHAPTER 5: MbnBC active site and substrate binding mechanism elucidated by ENDOR spectroscopy

Results from this chapter are from an article in preparation:
R. J. Jodts, R. M. Reyes, Y. J. Park, A. C. Rosenzweig, B. M. Hoffman, **2023**

INTRODUCTION

Non-heme diiron enzymes have fascinated chemists due to their abilities to activate dioxygen and catalyze a diverse and impressive set of reactions.[5, 128] These centers are ubiquitous amongst all domains of life and serve a function in several required life processes.[129]. Within this, is their role in the synthesis of natural products, with a rapid growth of new diiron enzymes implicated in these biosynthetic pathways due to advances in genomic sequencing technologies and bioinformatic methods.

Methanobactins (Mbns) are ribosomally synthesized, post-translationally modified peptide (RiPP) based natural products that chelate copper with some of the highest affinities reported.[20, 25, 117] Mbns are synthesized from a precursor peptide, denoted MbnA. A heterodimeric enzyme MbnBC catalyzes a conserved step in the biosynthetic pathway, the transformation of cysteine residues in MbnA to an oxazolone rings with an adjacent thioamide group through a four-electron oxidation reaction (**Figure 4.1**)[27, 134] Initial work revealed that the enzyme requires iron and O_2 for the reaction to occur, while mass spectrometry revealed that all iron is only within MbnB subunit of MbnBC, however the active oxidation, coordination, and occupation of these irons remained unknown. Subsequently, we found that the active form of the iron cofactor in MbnBC catalysis is an antiferromagnetically coupled mixed-valent Fe(II)Fe(III) diiron site.[134] This was determined through parallel electron paramagnetic resonance (EPR) spectroscopy, Mössbauer spectroscopy, and UV-vis activity assays, as well as supported with both iron loading and site directed mutagenesis experiments. This study also revealed that the S = ½ EPR signals of the spin-coupled Fe(II)Fe(III) center are perturbed upon the anaerobic addition of MbnA, suggesting substrate binds to this form of the center and further implicating it as an active species. In parallel, crystal structures of MbnBC were solved, revealing the active site architecture (Figure 5.1).[134, 135]

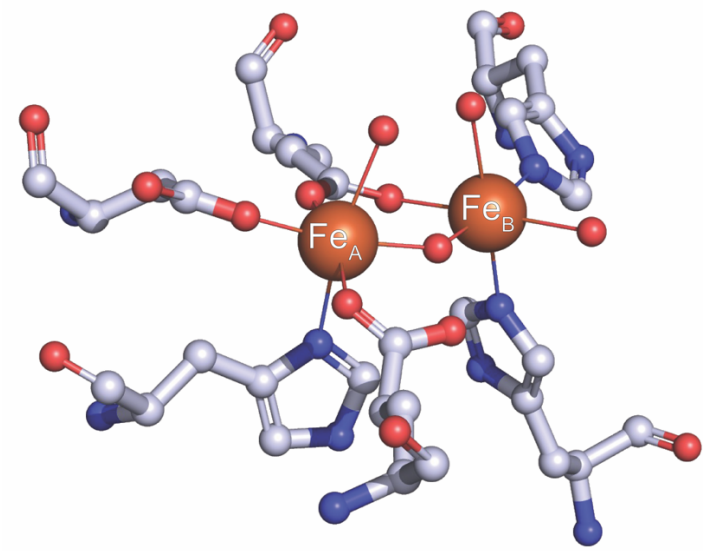

Figure 5.1. Previous work determined these two irons required for MbnA catalysis are in a mixed-valent oxidation state. The crystal structure also revealed other non-residue ligands to both iron centers. Model is from PDB 7TCX.

With this finding, MbnBC joins the family of mixed-valent diiron oxidases and oxygenases (MVDOs). Only a few MVDOs electronic structure, reactivity and mechanism have been studied, including myo-inositol dioxygenase (MIOX), which catalyzes myo-inositol conversion to glucaric acid[136], as well as PhnZ[126] and TmpB[137], enzymes that catalyzescarbon-phosphorous bond cleavage. However, the MVDOs' structure and mechanisms remain less examined than the diiron enzymes where a diferrous cofactor is utilized.[124, 128, 138]

Previous diiron enzyme studies have utilized electron nuclear double resonance (ENDOR) to elucidate key atomic and electronic structure details of the active site, as well as to understand how substrate, products, and analogues bind to the center.[92, 139] However, these extensive studies were on inactive forms of the cofactor like in soluble methane monooxygenase (sMMO) or intermediate states thereof.[122] MIOX is the only MVDO studied with ENDOR, but only substrate binding was investigated and not advanced electronic structure elements of the cofactor.[140]

In this study, we apply ENDOR spectroscopy towards the understanding of MbnBC mixed-valent diiron active site. This work not only informs the mechanism in MbnBC, but also expands the knowledge of MVDO active sites. Analysis of ^{1}H and ^{15}N ENDOR of the mixed-valent form of the enzyme allows for a true picture of its molecular and electronic structure. Furthermore, the mechanism of MbnA binding is

established with ENDOR studies upon the S = ½ MbnABC complex, showing how the substrate binds. These data combined with the ENDOR on the MbnBC active form also allows for better mechanism proposal.

RESULTS

EPR Spectra of ascorbate-reduced MbnBC

As previously reported, and shown in detail in **Chapter 4**, ascorbate reduced MbnBC exhibits a rhombic EPR signature with $\boldsymbol{g}$ = [1.94, 1.88, 1.76]; g_{eff} = 1.9, characteristic of an antiferromagnetically coupled Fe(II)Fe(III) cluster with a ground state of S = ½.[134, 141] The signal is well resolved at 10 K and below, but cannot be observed above temperatures of ~ 40 K. When MbnA is added anaerobically, the S = ½ EPR signal converts to a new rhombic S = ½ EPR signal with $\boldsymbol{g}$ = [1.92, 1.89, 1.82] with equivalent relaxation characteristics. These signals are well-resolved in absorption-display Q-band EPR spectra (**Figure S5.1**), and the S= ½ Fe(II)Fe(III) center is readily studied using 2K Q-band ENDOR, both with and without bound MbnA.

^{15}N Pulsed ENDOR of mixed-valent MbnBC

Unlike diiron enzymes previously studied by ENDOR[122, 139, 140, 142, 143], X-ray crystallography showed that one Fe ion has two coordinating histidine residues, the other with a single coordinating histidine.[134, 135] This has enabled us to use ^{15}N ENDOR to identify which of the crystallographically identified Fe ions is in the Fe(III) state and which the Fe(II) state. The intrinsic ^{15}N couplings are largely independent of the Fe-ion valency, and thus as **eq 5.1** shows, a histidyl ^{15}N bound to Fe(III) will have couplings that are ~2x larger, and of opposite sign, than those bound to the Fe(II). An illustration of this is given by soluble methane monooxygenase (sMMO), a mixed-valent Fe(II)Fe(III) enzyme center with one histidine bound to each Fe, examined previously. Continuous wave (CW) ^{15}N ENDOR at g_1 of sMMO revealed two ^{15}N signals, one with a greater intensity and corresponding to A_{15N} = ~ 25 MHz from the Fe(III)-bound His, the other with A_{15N} = ~ 7 MHz, from Fe(II) -bound His (signs were not determined).[122]

Similarly, pulsed Davies ^{15}N ENDOR plus PESTRE measurements of hyperfine-coupling signs for mixed-valent (ascorbate-reduced) ^{15}N-enriched MbnBC reveals two resolvable $\nu_+(^{15}N)$ signals at g = 1.93 ~ g_1 (**Figure 5.2**): the slightly-structured higher-frequency peak corresponds to A_{15N} = +22 MHz, with sign

determined by PESTRE, and can be assigned to Fe(III)-bound His; the lower-intensity $\nu_+(^{15}N)$ peak, which is narrower and unstructured, and corresponds to A_{15N} = -8 MHz, then corresponds to Fe(II)-bound His.

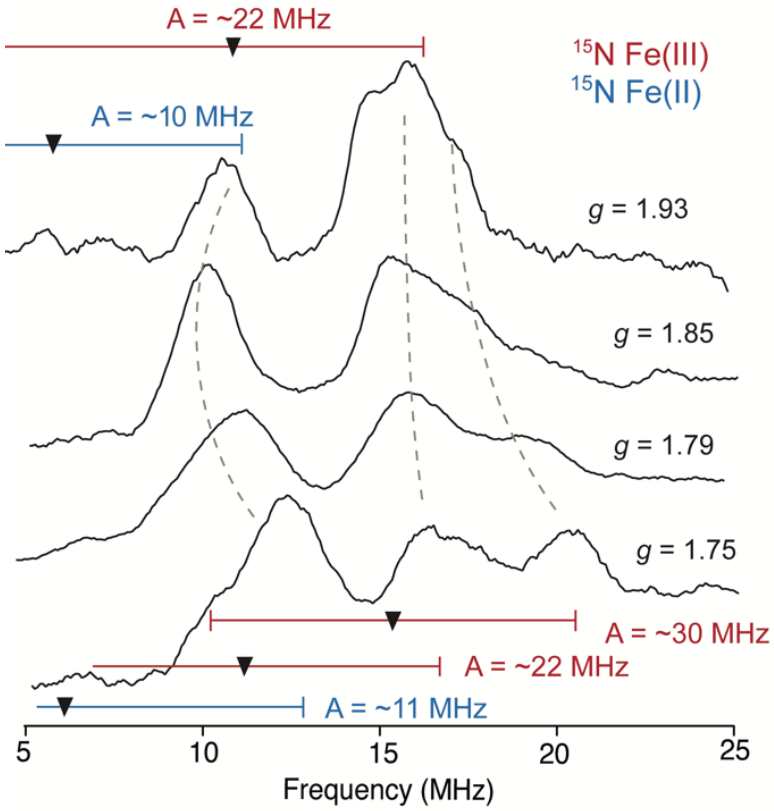

Figure 5.2. Q-band Davies ENDOR of ^{15}N labeled mixed-valent MbnBC. The brackets represent twice the Larmor frequency ($2n_{15N}$), but some n- extend into frequencies unmeasurable. The ▼ represents |A/2|. (A) ^{15}N Davies ENDOR at g_1 (g = 1.93). (B) ^{15}N Davies ENDOR with increasing magnetic field around g_2 (g = ~1.85) As field increases the presence of an addition Fe(III) ^{15}N coupling is resolved. (C) ^{15}N Davies ENDOR at high field end of the EPR envelope within g_3 (g =1.76). *Davies ENDOR conditions*: 2 K, 34.63

In ^{15}N ENDOR spectra collected as the magnetic field is increased across the EPR envelope to g_3, the $\nu_+(^{15}N)$ signal from Fe(II)-coordinated His remains a single peak though shifts somewhat in response to a slight anisotropy in the hyperfine-coupling tensor, **Figure 5.2**. The $\nu_+(^{15}N)$ signal from Fe(III)-coordinated His instead becomes two distinct signals. At g_3, one of the peaks exhibits a hyperfine coupling of A_{15N} = ~+22 MHz, the other with A_{15N} = ~+30 MHz. This observation reveals that there are two distinct ^{15}N ligands coordinated to the Fe(III) center, and is confirmed by ^{15}N ReMims ENDOR spectra collected at g_3, an experiment that monitors the remote nitrogen atoms of an Fe-coordinated His.[84, 142] The ReMims ENDOR

spectra likewise exhibit two signals. However, comparison with previous work that characterized the couplings to both coordinated and remote histidyl nitrogens[142] shows that these signals are associated with the two Fe(III)-coordinated His ^{15}N (**Figure S5.2**). The same comparisons support the conclusion that the hyperfine coupling of the single remote ^{15}N of the Fe(II)-bound histidine is small, and its signal is 'lost' in the 'Mims hole' at the ^{15}N Larmor frequency.

The ^{15}N ENDOR results allow us to assign the specific oxidations in the mixed-valence Fe(III)Fe(II) enzyme state of the two Fe ions observed crystallographically in the diferric state (**Figure 5.1**):[134, 135] Fe_B, has two His ligands, and thus it must remain Fe(III) upon the reduction; it is Fe_A, with a single His ligand that is reduced to Fe(II). We note that the finding that Fe(III) having the second N-coordination is perhaps surprising, as simple considerations of charge interactions would suggest the Fe(III) ion would likely favor coordination by more negatively charged carboxyl ligands. It is thus likely elements of the protein scaffolding support this coordination-valency combination.

^{1}H CW ENDOR of mixed-valent MbnBC

Crystal structures of MbnBC from three different species all were solved with crystals of protein purified under aerobic conditions,[134, 135] and therefore likely represent the structure of the inactive, diferric form of the enzyme cofactor.[27] All those structures show evidence of exogenous protonated ligands to the diiron center. ^{1}H CW ENDOR here is applied to the catalytically active MbnBC mixed-valent state and to look for similarities and differences to the diferric crystal structures, as done previously for other diiron centers.[139, 142, 144]

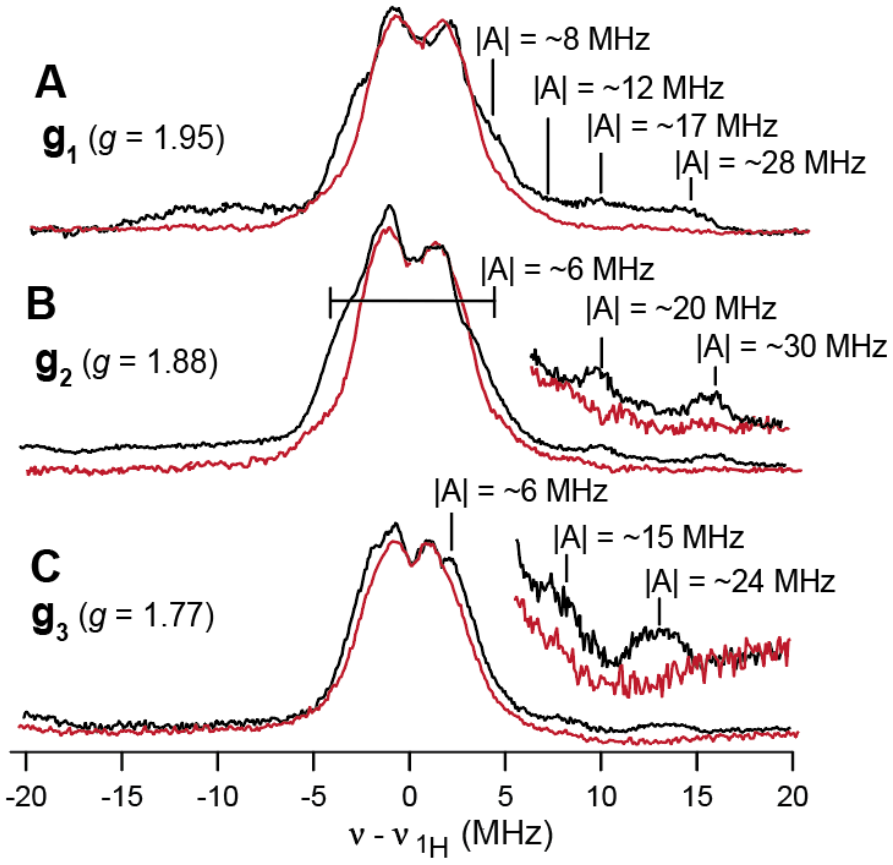

Figure 5.3. frequency-swept (high rf frequency to low) Q-band CW ENDOR spectra of mixed-valent MbnBC in H_2O buffer (black) and exchanged into buffer prepared D_2O (red). As is typical in swept ENDOR spectra of diiron systems,[145] the ν+ features are better-resolved than the ν- features. Some parts of the spectrum are magnified for better view. CW ENDOR conditions: 2 K, 34.88 GHz (H_2O) and 34.83 GHz (D_2O) MW Frequency, 4 G Modulation, 1.8 μW MW power, 0.5 MHz/s scan, 32 ms time constant, 200 KHz RF bandwidth, reverse sweeps to allow for resolution of ν+ signals, ~200 scans each.

^{1}H CW ENDOR spectra taken at the three canonical g-values for mixed-valent MbnBC prepared in H_2O (**Figure 5.3A-C, black**)and D_2O (**Figure 5.3A-C, red**) buffers show the presence of doublets from exchangeable protons with large hyperfine couplings, as seen previously for -OH_x ligands to such systems.

Starting with the spectrum at g_2, one observes large, exchangeable proton couplings of ~20 MHz and ~30 MHz,(**Figure 5.3**), which previous work identifies as a part of the signature of a bridging -μ-OH ligand (DeRose). The observation that a single proton from a bridged μ-OH exhibits multiple couplings at g_2 was explained previously in terms of rhombic hyperfine tensor, A = [-25, -5, +30] MHz.[122] Exchange-coupled diiron centers have been found in systems with both μ-oxo and μ-hydroxo bridges, and the

presence of the latter, not the former, is supported by the temperature dependence of the spin-lattice relaxation of the MbnBC mixed-valence site. The EPR signal of mixed-valence MbnBC is lost by ~40 K, the result of rapid spin-lattice relaxation. A μ-oxo bridge center supports a larger exchange-coupling than μ-hydroxo diiron centers, which allows the S = ½ EPR signal to be observed at higher temperatures (~ 77K).[146]

The spectra at both g_1 and g_3 also reveal exchangeable proton signals with a coupling approaching near 30 MHz, but these signals cannot be from the established μ-OH bridge, as the observation of such couplings observed at g_2 implies that the hydroxyl proton would exhibit couplings of A = ~15 MHz at these the extremal g-values (which are observed, see **Figure 5.3**). These signals must then be assigned to the maximum coupling to -OH_x protons terminally bound to Fe(III) water/hydroxo ligands, as shown previously for such ligands to spin coupled Fe(III) ions[139]. Such a large coupling to this type of ligand arises because the maximum coupling for an OH_x proton on a mononuclear ferric center ~8-12 MHz, is multiplied by the spin-coupling coefficient, 7/3 (**eq. 5.1**); the breadth of the signal precludes determination of whether x = 1 or 2 H-atoms on the coordinated oxygen.

However, the ^{1}H hyperfine tensor for protons on a terminal OH_x is roughly dipolar in character and so a single Fe(III)-aquo ligand cannot give rise to the large couplings seen at *both* g_1 *and* g_3. We thus assign these signals to two distinct OH_x ligands bound terminally to the Fe(III) ion. This assignment is consistent with the X-ray crystal structure of OB3b MbnBC which shows density modeled as two non-protein oxygen atoms coordinated to Fe_B (**Figure 5.1**), which was determined to be the Fe(III) site based on the above analysis of the ^{15}N ENDOR signals. Spectra taken under a variety of conditions, **Figure 5.3** and **Figure S5.3**, further show poorly resolved exchangeable features with A ~10-16 MHz. These are assignable to the smaller components of the dipolar tensors of the terminal Fe(III) OHx ligands, supporting their identification.

Finally, there are exchangeable features in the ^{1}H spectra with A ≤ ~8 MHz. The observation of an exchangeable doublet at g_1 with ~8 MHz coupling (**Figure 5.3A**), correlates with the ~6 MHz exchangeable doublets observed a g_2 (**Figure 5.3B**) and g_3 (**Figure 5.3C**). These again form a near-axial tensor expected for a terminal water or hydroxyl ligand on the Fe(II) site: A_{1H} = [-8+6, +6] MHz, where the signs are not measured, but assumed from **eq. 5.1**. [122, 144] Crystal structures reported for OB3b MbnBC exhibit density modeled as an oxygen atom to the Fe_A site,[134] which was determined to be the Fe(II) site in the ^{15}N

experiments. We conclude that the MbnBC diiron center contains such a water ligand in both diferric and mixed-valent states, and suggest this Fe(II) ligand could be displaced upon O_2 binding to the MV state, as observed in previous mixed-valent dioxygenase enzymes[137, 147]

We lastly note that at all three g-values one observes nonexchangeable proton signals wotj small couplings, < 5 MHz (**Figure 5.3A-C, red**). We assign these as multiple, overlapping doublets deriving from couplings of e-H and d-H within the rings of the histidine ligands, as well as deriving from b-carbon protons on the other chelating carboxyl residues to both sites, all as seen in the crystal structures (**Figure 5.1**). In summary, the ^{15}N ENDOR an ^{1}H ENDOR measurements complete a picture of the active site of mixed-valence MbnBC, as depicted in **Figure 5.4**.

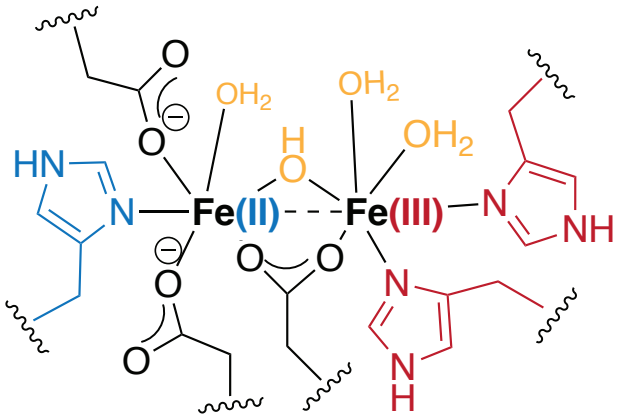

Figure 5.4. The mixed-valent MbnBC active site chemical architecture determined through a combination of X-ray crystallography (black)[134], ^{15}N Davies ENDOR (blue and red), and ^{1}H CW ENDOR (gold)

ENDOR studies of the MbnABC complex

The EPR signal from the mixed-valence state of the MbnBC diiron center is perturbed upon anaerobic addition of the substrate peptide MbnA, with a collapsed set of g-values compared to the center without substrate [134] To gauge whether this perturbation was indeed due to MbnA binding to the diiron center, and if so to understand how it binds to the diiron cofactor, we performed ^{2}H ENDOR of MbnA where the 'leader-end' cysteine β-protons are deuterated, denoted DMbnA. We hypothesized that this cysteine residue binds initially during catalysis to the iron center because previous biochemical studies showing sole modification of MbnA at that cysteine position and not the second modifiable residue, as well as the

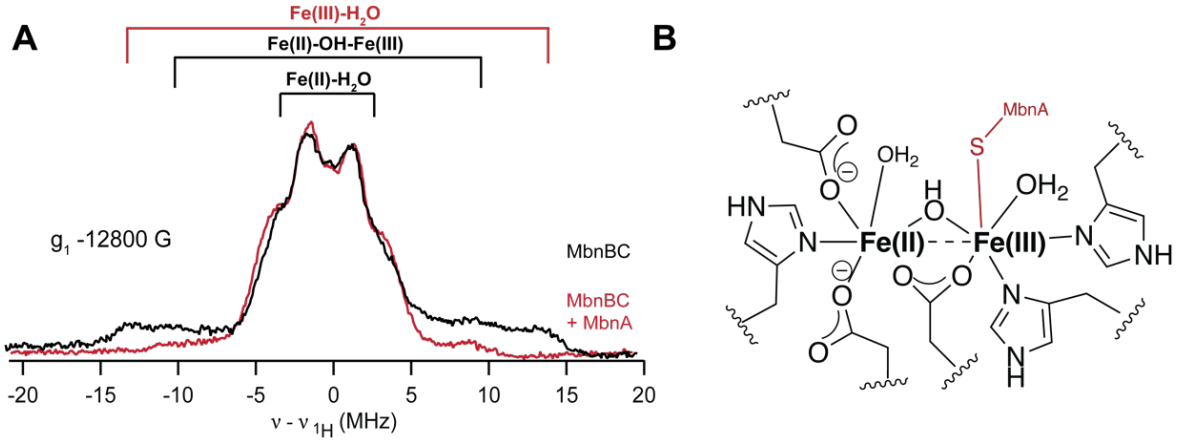

Figure 5.5 1H CW ENDOR of MbnA binding to MbnBC mixed-valent diiron center. A. 1H Q-band CW ENDOR of mixed-valent MbnBC (black) and mixed-valent MbnABC complex (red) at g1. The brackets represent ^{1}H |A| and are centered at the ^{1}H Larmor frequency. The loss of the 24 MHz coupling when substrate is added is associated with MbnA displacing a terminal H_xO to coordinate the Fe(III) center. CW ENDOR conditions: 2 K, 34.81 GHz, 4 G Modulation, 1.8 μW MW power, 0.5 MHz/s scan, 32 ms time constant, reverse sweep, ~200 scans each. **B**. Model depiction of the substrate bound active site of MbnBC as determined by the previous experiments and the ^{1}H CW ENDOR.

appearance of a 650 nm feature observed upon substrate addition to the inactive Fe(III)-Fe(III) state that was assigned as Fe(III) -> S charge transfer band.[148] The Cys-β-protons are not exchangeable, and therefore ^{2}H ENDOR enables detection of an MbnA interacting with the diiron center of MbnBC. This approach had been used previously for a mixed-valent diiron enzyme.[140]

The ^{2}H Mims ENDOR of the MbnBC-DMbnA complex reveals significant ^{2}H signals at several field positions examined (**Figure S5.4**), indicating indeed the leader-end sulfur is binding to the Fe(II)Fe(III) center, and that this sulfur coordination is indeed causes the perturbation of its EPR spectrum. This establishes a key mechanism step that we expand upon below. However, further analysis of the ENDOR is ongoing is required to fully understand the couplings to the diiron core and the further understanding of the electronic structure of the substrate to the center.

Due to MbnA being a large substrate peptide, it conjures the possibility of multiple points of chelation to diiron center, especially as the mixed-valent state was established above by ^{1}H ENDOR to contain several ligands to both the Fe(II) and Fe(III) sites. To address this, ^{1}H CW ENDOR was again performed as before to deduce whether any above identified H_xO ligands were displaced during MbnBC-MbnA binding. ^{1}H CW ENDOR taken at the 3 principal g-values showed near identical features to the

spectra without MbnA added. Of note, the presence of the large couplings at g_2 are present, albeit sharper in the spectrum with substrate added (**Figure S5.5**). These large signals (~ 20, ~ 30 MHz) at g_2, signifies the couplings to the μ-OH-bridge were unchanged upon addition of MbnA. Also, the presence of an ~8 MHz coupling at g_1 (**Figure 5.5**) and ~6 MHz coupling at g_2 and g_3 (**Figure S5.5)** teaches that the Fe(II)-OHx ligand was not displaced with the binding of MbnA.

The striking difference between the ^{1}H ENDOR of samples with and without MbnA is the absence of the ~28 MHz coupling at g_1 for the MbnABC complex (**Figure 5.5A, red**) that was present in the MbnBC ^{1}H ENDOR spectrum (**Figure 5.5A, black**). Above (**Figure 5.3A**), this doublet was assigned as proton couplings from an Fe(III)-OH_x ligand. The lack of these couplings now suggests it was displaced upon MbnA binding. The second Fe(III)-OH_x ligand, which maximizes it coupling at g_3 is still present, as the doublet is observed again in the MbnABC ^{1}H ENDOR spectrum (**Figure S5.5**). Interestingly, when the ^{1}H ENDOR of the MbnBC and MbnABC is scaled so the near Larmor couplings are the same intensity (**Figure 5.5A**), one can see they do not scale perfectly at ν = ~ ±10 MHz. From the results of the D-MbnA ENDOR experiments (**Figure S5.4),** we rationalize this difference due to the now presence of the β-protons of the bound cysteine.

Interestingly, the crystal structures of MbnABC (PDB 7FC0 and 7DZ9) show the first modifiable Cys of MbnA bound to the Fe_B (**Figure 5.1**) established as the Fe(III) by ^{15}N ENDOR, in a position where structures of MbnBC had modeled water molecule (PDB 7TCX). The available structure of the Type V MbnABC complex exhibits no modeled coordinated exogenous oxygen ligand on the Fe(III). It is possible the Type V systems do not need this addition water, as they only have one cysteine residue in their MbnA to catalyze.[25, 27] But, the CW ^{1}H ENDOR at g_3 for the Type I MbnABC studied here exhibits a doublet of about ~ 26 MHz, or a Fe(III)-OHx ligand couplings (**Figure S5.5**).

With the ^{2}H ENDOR and ^{1}H ENDOR on the MbnABC complex, as well as the previous ^{15}N and ^{1}H ENDOR on the MbnBC complex, we can combine these findings and create an accurate depiction of the active site with MbnA bound (**Figure 5.5B**).

CONCLUSIONS

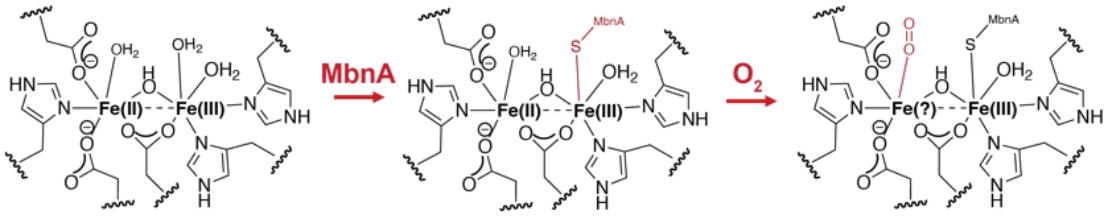

Figure 5.6 Schematic of the MbnBC mechanism of MbnA and O_2 binding. This scheme is devised from crystal structures and the ENDOR experiments and analysis presented in this work. The final step of the O_2 binding is assumed from other MVDOs.

From these studies, we establish the basic steps in the MbnBC mechanism of catslysis of its substrate, MbnA. The ^{15}N and ^{1}H ENDOR of MbnBC allows for structural assignment, as well as the individual valance state of each of the sites observed in the crystal structure (**Figure 5.1 and Figure 5.6, right**). The MbnABC complex studied again with $^{1,2}H$ ENDOR and allows for the determination of how MbnA binds to the diiron center (Figure 5.6, middle). This binding mechanism validates previous proposals of the MbnBC mechanism. Interestingly, X-band EPR studies of NO addition to the MbnABC complex abolishes the S = ½ signal (**Figure S5.6**). Due to this loss of signal, we propose that the NO molecule, which serves as an O2 analogue, binds to the Fe(II) center and the spin-coupled center is no longer non-integer spin (**Figure 5.6, right**). The Fe(II) center is suggested as O_2 binding center from other studies of MVDOs as well as MbnBC mechanism proposals by others. After this binding the mechanism likely continues, and further validation of those steps will likely require rapid freeze quenched samples in combination with Mossbauer, EPR, and ENDOR to fully elucidate.

Besides understanding the mechanism of a universal step in Mbn biosyntheiss, this work highlights the ability of ENDOR to determine key molecular and electronic structure details of a MVDO enzyme active site, We propose that as natural product biosynthetic enzymes are continued to be studied, the use of ENDOR can further structural and mechanistic understanding, as well as provides key information for the creation of abundant earth metal synthetic mimics.

METHODS

Protein expression and purification

The constructs used, heterologous expression protocol, and the purification of natural abundance *Ms. trichosporium* OB3b MbnBC were described previously.[27, 134] The preparation of the mixed valent by anaerobic addition of ascorbate, loaded into a custom made quartz Q-band tubes, and froze in liquid N_2 was performed as reported previously.[134] For preparation of ^{15}N MbnBC, MbnBC was expressed in M9 minimal media with 99% ^{15}N enriched NH_4Cl (Cambridge Isotope Laboratories) and then purified in the same methods as natural abundance MbnBC. Both the MbnA and DMbnA (see text) were synthesized by Bio-Synthesis Inc., Lewisville, TX and 2 molar equivalents were added to samples of ascorbate reduced MbnBC anaerobically and left to incubate for ~ 40 minutes at 4ºC, similar to previous preparations of MbnA bound MbnBC.[134] For D_2O exchanged samples, purified MbnBC was exchanged in D_2O prepared MOPS (99.5% D_2O from Sigma Aldrich) buffer and was left to allow for proton exchange for 24 hours. The ascorbate solution added to achieve the mixed valent was also prepared in D_2O MOPS buffer anaerobically. All samples were examined by X-band EPR at 10 K, under conditions reported previously, to assess the success of the sample preparation for subsequent ENDOR experiments.[134]

ENDOR and EPR Spectroscopy

All continuous wave (CW) Q-band EPR and ENDOR was performed on a Varian E-110 spectrometer equipped with a helium immersion dewar, described previously.[72] Pulsed Q-band ENDOR was collected on custom built spectrometer described previously.[70, 74] The instrument is equipped with SpinCore PulseBlaster ESR_PRO 400 MHz digital word generator and Agilent Technologies Acquiris DP235 500 MS/s digitizer using SpecMan4EPR software.[71] X-band EPR was carried out on a in house modified Bruker ESP-300 spectrometer with a variable-temperature liquid helium flow Oxford Instruments ESR-900 cryostat.

Fe(II)Fe(III) hyperfine coupling analysis

As established previously, A nucleus, a, that has hyperfine couplings to the individual iron ions of $a^i(a)$ has a hyperfine coupling of A(a) to the cluster spin

$$A(\alpha) = \frac{7}{3}a^j(\alpha) - \frac{4}{3}a^i(\alpha) \qquad \textbf{(5.1)}$$

Where a^j is interactions with the Fe(III) and a^i is interactions with the Fe(II). The 7/3 and -4/3 factors are simply spin-projection coefficients for the ferric and ferrous sites, respectively. From this equation, if the nucleus only interacts with one of the irons, it only has the component of that iron. For example, the hyperfine coupling of a nuclei only coupled to the Fe(II) would result in just $\mathrm{A}(\alpha) = -\frac{4}{3}\mathrm{a}^{\mathrm{i}}(\alpha)$. A proton that interacts with both iron sites, such as a bridging ligand, has both non-zero a^j and a^i components.

CHAPTER 6: Computational chemistry applied to radical SAM enzyme intermediates

Results from this chapter have been published previously in the following articles:

H. Yang, E. C McDaniel, S. Impano, A. S. Byer, R. J. Jodts, K. Yokoyama, W. E. Broderick, J. B. Broderick, B. M. Hoffman, J. Am. Chem. Soc., **2019**, 141 (30), 12139-12146

A. Pagnier, H. Yang, R. J. Jodts, C. D. James, E. M. Shepard, S. Impano, W. E. Broderick, B. M. Hoffman, and J. B. Broderick, J. Am. Chem. Soc., **2020**, *142* (43), 18652-18660

S. Impano*, H. Yang*, R. J. Jodts*, A. Pagnier, R. Swimley, E. C. McDaniel, E. M. Shepard, W. E. Broderick, J. B. Broderick, B. M. Hoffman, J. Am. Chem. Soc., **2021**, 143 (1), 335-348

INTRODUCTION

Radical S-adenosyl-L-methionine (SAM) enzymes (RS enzymes) are ubiquitous, performing essential roles in many biological processes. The diverse radical *S*-adenosyl-l-methionine (radical SAM, RS) enzyme superfamily contains hundreds of thousands of distinct sequences found throughout all kingdoms of life.[149-151] More than 80 distinct radical SAM reactions have been identified, catalyzing key steps in critical processes including DNA repair, protein and tRNA modification, and the synthesis of vitamins, antibiotics, protein cofactors, and complex metal clusters. These RS enzymes all contain a site-differentiated [4Fe-4S] cluster that binds SAM through a distinctive methionyl amino/carboxylate chelation of the unique iron of the [4Fe-4S] cluster.[152-154]

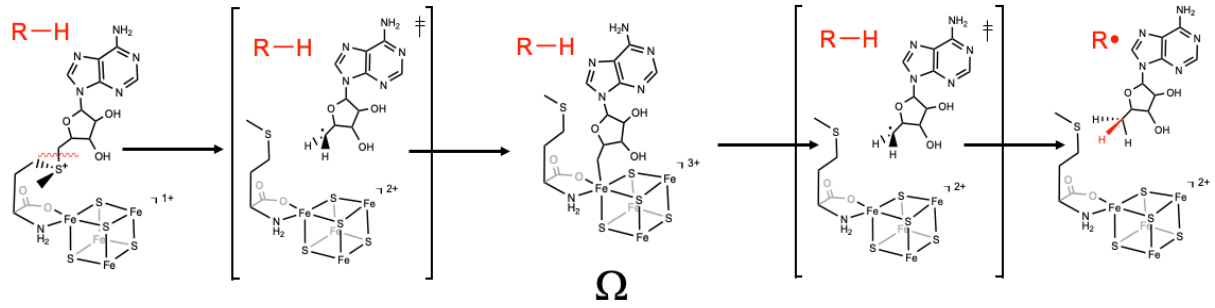

Figure 6.1 Radical SAM mechanism schematic. Pathway for liberating 5′-dAdo· for H atom abstraction through formation of catalytically competent Ω upon SAM cleavage. The 5′-dAdo· is then again liberated by an unknown mechanism to eventually abstract the proton from substrate.

The reduced $[4Fe\text{-}4S]^{+}$ cluster of RS enzymes reductively cleaves the S-C5' bond of the bound SAM to generate a 5'-deoxyadenosyl radical (5'-dAdo•), the species that initiates catalysis by abstracting a specific hydrogen atom from substrate.[155] However, we showed that the reductive cleavage of SAM during enzymatic catalysis does not simply liberate 5'-dAdo•.[32] Rather, rapid freeze-quench spectroscopic studies of a collection of RS enzymes that span the range of reaction types catalyzed by the superfamily have shown that in all cases, SAM cleavage generates a paramagnetic organometallic intermediate denoted Ω in which the unique Fe atom of the [4Fe-4S] cluster forms a bond with C5' of 5'-dAdo•.[32, 33] This has been proposed to again liberate the 5'-dAdo• and begin the substrate catalysis. A summary of the mechanism scheme of these enzymes is depicted in **Figure 6.1**.

This 5'-dAdo radical species, and other radical intermediates, as well as the intermediate state of the reductive cleavage are all discussed here. Computational chemistry methods have been applied to these intermediate states to enhance our analysis and understanding of the intermediates. This thesis chapter illustrates the work done in recent years to apply computational chemistry to spectroscopic studies in the Hoffman lab.

RESULTS

Analysis and DFT modeling of the 5'-dAdo radical

We begin with an analysis of the 5'-dAdo radical that was captured from studies of pyruvate formate-lyase (PFL) activating enzyme (PFL-AE). SAM and PFL-AE/$[4Fe{-}4S]^{1+}$ were combined and photolyzed in the absence of substrate PFL, circumstances in which SAM is not enzymatically cleaved and Ω does not form. Surprisingly, irradiation of such samples in the EPR cavity at 450 nm and 12 K results in rapid conversion of the SAM-bound $[4Fe{-}4S]^{+}$ state of PFL-AE. This radical was investigated with both X-band and Q-band EPR under non-saturating conditions in order to resolve spectra to simulate all the ^{1}H hyperfine splittings observed (**Table 6.1**). The identification of the radical as the 5'-dAdo as well as to individually assign simulated hyperfine to specific protons were confirmed through isotopically labeling the SAM cofactor.

5′-dAdo•	A_1	A_2	A_3
5′-C-$^{1}H\alpha_a$	-15(-28)	-105(-104)	-60(-63)
5′-C-$^{1}H\alpha_b$	-20(-25)	-95(-101)	-60(-61)
4′-C-$^{1}H\beta$	+80(+90)	+80(+90)	+110(+105)
5′-$^{13}C\alpha$	+10(+2)	+10(+3)	+230(+240)
4′-^{13}C	60(+69)	80(+86)	60(+68)
3′-^{13}C	40(-36)	40(-33)	50(-37)
1′-or 2′-^{13}C	0.8	0.8	3

Table 6.1. Hyperfine tensors (MHz) of 5′-dAdo• from experiment[a] plus DFT-computed values in parenthesis[b]

Beyond the experimental observations of 5′-dAdo•, the observed hyperfine interactions teach us about its electronic and geometric structure. The two $^{1}H\alpha$ and the 5′-$^{13}C\alpha$ coupling tensors are in good agreement with those for the odd electron in the $2p\pi$ orbital of the planar (sp^2) carbon-centered radical of x-irradiated malonic acid (**Table 6.1**). The match, notably in the isotropic couplings, indicates that the spin

density in the 2pπ orbital on C5′of 5′-dAdo• ($\rho\pi$) is comparable to that in malonic acid, $\rho\pi \sim 0.7$. Of particular note, the spin-polarization-induced isotropic coupling of the 2pπ spin of planar ^{13}C5′ would have been sharply increased by a pseudo-tetrahedral 'doming' distortion at C5′, which would introduce 2s character, with its large isotropic coupling,[156] into the odd-electron orbital. Thus, we infer that the H_2-C5′-C4′ fragment is essentially planar. The isotropic coupling of a proton β to a carbon 2pπ electron spin, such as ^{1}H-C4′, is known to obey the relationship, $a_{iso} \approx \rho_\pi \beta \cos^2\varphi$ MHz, where B reflects the transmission of spin to ^{1}H through hyperconjugation, $\rho_\pi\beta \approx 140$ MHz, and φ is the dihedral angle between the $2\pi\pi$ orbital and the Cβ-H bond,[156] corresponding to the angle between the [4′CH-4′C-5′C] plane and of the 2pπ orbital (normal to the plane formed by C5′ and its two H-atoms). Applying this relationship to the measured ^{1}H-C4′ isotropic coupling (**Table 6.1**) indicates $\varphi \approx 37^o$.

These conclusions from the experimental finding are confirmed and extended by DFT computations[157] for 5′-dAdo. Firstly, the computations yield an energy-minimized structure that reproduces the observed hyperfine couplings extremely well, **Table 6.1**, with a value for the spin density in the C5′ 2pπ orbital of $\rho_\pi = 0.7$, in agreement with the experimental 'traditional' analysis. The computations further generate the radical's structure (**Fig. 6.2, top**), which exhibits both a rigorously planar

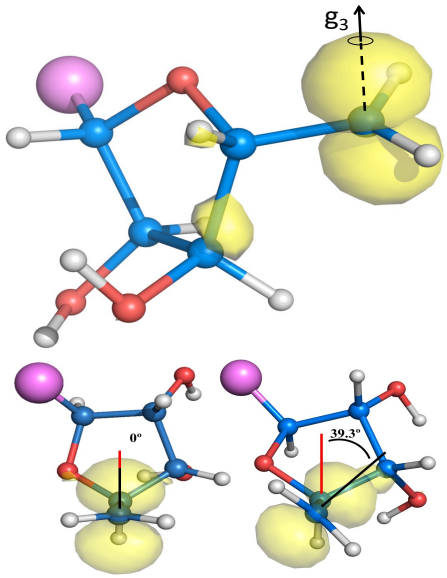

Figure 6.2. DFT model of 5'dAdo Top: Perspective view of the optimized structure. Adenosine is represented by a violet sphere; the isosurface plot of the calculated HOMO (yellow) uses an isodensity of 0.08 au and shows the direction of g3 normal to the C5′H2 plane. Bottom: left, conformer with a dihedral "twist" at the C5′–C4′ bond, φ = 0; right, optimized structure geometry φ = 39.3

geometry at C5′ and a dihedral ‘twist’ at the C5′-C4′ bond, as inferred above. The dihedral (twist) angle in the energy-minimized geometry φ ≈ 39° (**Figure 6.2, bottom**) is quite close to that indicated by the experimental estimation of the angle, analysis above, and creates a structure with a C5′-H antiperiplanar to the oxygen of the ribose ring, which helps stabilize the radical against elimination of 4′-H, as suggested long ago.

Computational modeling and EPR analysis of SPL stable protein radicals

Spore photoproduct lyase is a radical SAM enzyme with the unusual property that addition of SAM to the [4Fe-4S]1+ enzyme absent substrate results in rapid electron transfer to SAM with accompanying homolytic S-C5’ bond cleavage. It was observed reaction forms the organometallic intermediate, Ω. This was further investaged to show using hand-quenching at times up to 10 min, and thus with multiple SAM turnovers, the fate of the 5’-dAdo• radical liberated by Ω. It was then observed in the absence of substrate, Ω undergoes low-probability conversion to a stable protein radical.

The assignment of the protein radical accumulated in WT *Gt*SPL was established to be valine at position 172, as a valine side chain radical is confirmed and its structure is established by the simulation of its spectrum, **Figure 6.3**. The Cγ of Val172 sits closest to the C5’ of SAM, but the tertiary Cβ of the valine sidechain is the most susceptible to H-atom abstraction due to its weaker C-H bond, and due to the fact that it would give rise to a more stable tertiary radical. We therefore initially evaluated the more stable Cβ radical as the first candidate for the origin of the observed signals a planar 2pπ radical on the sp^2-hybridized tertiary carbon of Cβ. Such a radical would exhibit proton hyperfine couplings to the six H-atoms of the two side-chain methyls, $C_{\gamma 1}$-H_3 and $C_{\gamma 2}$-H_3, and the Cα-H proton, all of which are ‘β’ to the half-occupied 2pπ orbital on Cβ. β-proton hyperfine couplings are essentially isotropic, with a dependence on the spin density in the carbon radical 2pπ orbital, denoted, ρ_π, that obeys the semi-empirical relationship, $a_{iso} \approx \rho_\pi B\cos^2\varphi$ MHz where φ is the dihedral angle between the 2pπ orbital and the C-H bond of the β-proton, while the constant, B represents the transmission of spin to the β-^{1}H through hyperconjugation; canonical values are, $\rho_\pi \approx 0.7$, $\rho_\pi B \approx 140$ MHz.[156]

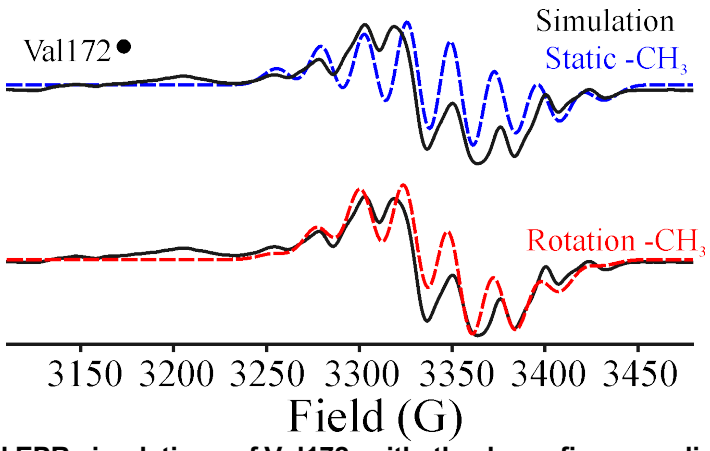

Figure 6.3. The X-band EPR simulations of Val172• with the hyperfine coupling parameters from DFT. The computation data was simulated assuming the static methyl and for rotational methyl, with results best matching the rotational methyl groups.

To analyze the observed radical spectra, we turned to DFT to generate an energy minimized conformation and estimate for the hyperfine couplings. As a first approximation, we examined the neutral Cβ 2pπ radical *in vacuo*, namely uninfluenced by interactions with the surrounding active-site protein scaffold. Starting with the conformation of the crystal structure (PDB 4FHD) and abstracting an H-atom from C_β, the computations yielded a 2pπ radical on C_β and planar propyl group, with a dihedral angle between the 2pπ orbital and the C_α-H bond, of φ = 62°. For the C_α-H coupling the calculation gave a_{iso}(H) = 48 MHz and a 2pπ spin density of $\rho_\pi \approx 0.7$, thus validating the conventional approach**.** However, simulations using this C_α-H coupling showed a minor discrepancy with experiment that was simply eliminated by slightly reducing the dihedral angle from φ = 62° to φ = 55° and repeating the (**Figure 6.3**). According to the treatment described above, this increases the C_α-H coupling to $a_{iso}(C_\alpha\text{-H})$ = 69 MHz. The protons on both Cγ had the same orientation relative to the 2pπ radical orbital and the calculation (B3LYP) gave the same three distinct ^{1}H hyperfine couplings for the two methyl group protons: $a_{iso}(H_a,H_b,H_c)$ = 127 MHz, 65 MHz, 14 MHz. Simulations of the EPR spectrum assuming rotating Cγs methyls and thus equivalent methyl-^{1}H with $a_{iso} \approx \rho_\pi\beta\langle\cos^2\varphi\rangle$ MHz = $\rho_\pi/2$ MHz were slightly better than those assuming the γ-methyls were static, with inequivalent ^{1}H couplings. The resulting simulations using the dihedral angle, φ = 55° and corresponding C_α-H coupling match the experimental spectrum within error, **Figure 6.3.**

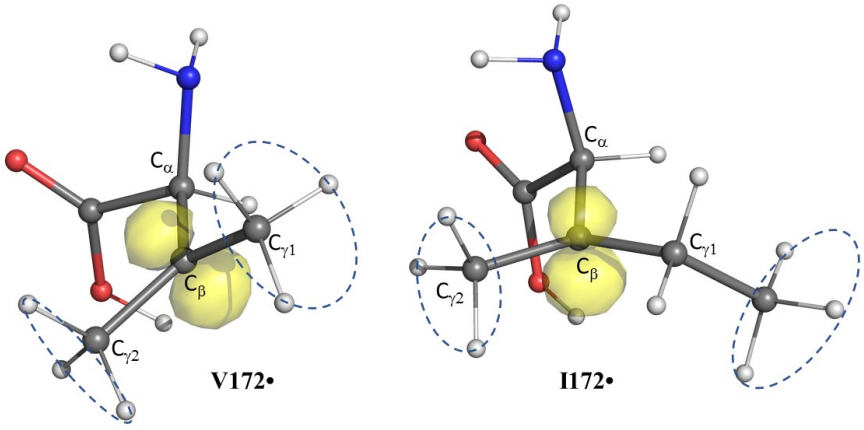

Figure 6.4. Computational Models of V172 and I172 radicals. The models pictured here have the Cβ–Cα torsion angles manually adjusted to agree with the experimental results (Val172•, φ ≈ 55°; Ile172•, φ ≈ 90°) as described in the text. Dashed circle denotes the rotation of the methyl group of V172• and I172•. 2pπ radical orbitals are visualized in Pymol with an isodensity of 0.08 au

We also used DFT to compute β-proton hyperfine coupling of the radical located on C_β of Ile172• (**Table S6.1**). This EPR spectrum is well-simulated assuming $C_{\gamma 2}H_3$ is rotating, giving isotropic couplings from three equivalent ^1H, but with inequivalent couplings from the locked $C_{\gamma 1}$ (H_a,H_b). The *in vacuo* DFT gives a C_β-C_α torsion angle for the Ile172• radical that is the same as that for the starting point of V172•, but simulations of the Ile172• radical spectrum require that the C_α-H coupling is near-zero, which implies a dihedral angle between the 2pπ radical orbital and the C_α-H bond of φ ~ 90º, **Figure 6.4, Figure 6.5.**We postulate that the altered conformation with φ ~90º for the isoleucine variant versus φ ~ 55^0 determined here for the radical on the native valine residue occurs because steric clashes between the 'elongated' Ile residue and other residues within the protein scaffold, causes a twist around the C_α-C_β bond; this analysis is confirmed by modeling both radicals in the GtSPL active site. **Figure 6.4** visualizes

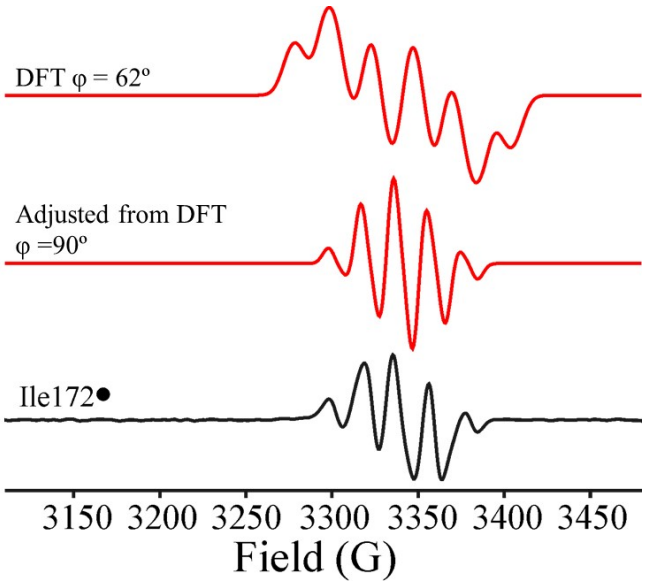

Figure 6.5. X-band EPR simulation of Ile172•. Simulation performed with DFT computed 1H hyperfine coupling parameters corresponding to φ= 62° and the simulation with DFT computed 1H hyperfine coupling parameters by adjusting φ= 90°. After the adjustment, the simulation matches best to the experimental spectrum.

the DFT models of these two radical-residues with φ for Ile172• as manually adjusted to match experiment, and also displays the C_β 2pπ SOMO.

Computational modeling to understand the Jahn-Teller effect in SAM Enzymes

Similar to the studies of photolysis that showed the 5'dAdo radical was release, other enzymes revealed that under photolysis conditions instead of cleaving the S-5'C bond, instead a methyl radical was formed.[158] The striking bifurcation in regioselectivity for cryogenic photoinduced reductive SAM cleavage, where some RS enzymes cleave S-C5' while others cleave S-CH_3, is surprising given that all these RS enzymes cleave the S-C5' bond during enzyme catalysis.[149, 150] What is the origin of the two classes of regioselectivity? The most obvious possible source for the regioselectivity of photoinduced homolytic SAM S-C bond cleavage would be differences in distance(s)/angles that define the geometric relationship between the unique cluster Fe and the sulfonium of SAM. However, there is no such correlation. Indeed, when one compares the SAM-bound structures of SPL,[159] a photochemical 5'-dAdo•-former, and HydE,[160] a •CH_3-former, we see there is little alteration in the positioning and orientation of the sulfonium centers of SAM relative to the unique Fe of the [4Fe-4S] cluster. This positioning is anchored by the methionyl amino-

acid chelation of the unique cluster Fe on one end of SAM and by non-bonding interactions of the adenine with neighboring residues on the other end of SAM, as previously recognized and detailed by Vey and Drennan.[161]

In contrast, as also noted by Vey and Drennan, the SAM ribose conformation does vary among RS enzymes, and as seen in **Figure 6.6** there are clear differences in the ribose conformations in the SPL and HydE SAM-bound structures.[159, 160] To explore whether such structural details of the enzyme-bound SAM correlate to photolytic regioselectivity, we began by comparing the SAM structure in PFL-AE,[162] a 5'-dAdo•-forming host, and HydG,[163] a •CH_3-former. The ribose ring of SAM in PFL-AE has the 2'-endo conformation with an axial C4'-C5' bond, and with an OH-C3'-C4'-C5' dihedral angle ~140°. In contrast, the •CH_3 forming host HydG has the ribose ring in a 3'-endo conformation with an equatorial C4'-C5' bond, and correspondingly, with a sharply smaller OH-C3'-C4'-C5' dihedral angle of ~ 80°**.** This latter HydG ribose conformation is the most common in RS enzymes examined by Vey and Drennan,[161] and is that of the classical B-DNA conformation; the former PFL-AE ribose conformation is that in A-DNA.[164]

To determine whether such a difference in SAM ribose configuration is found for other members of the two classes of RS enzymes that differ in regioselective photoinduced S-C bond cleavage, we examined all five known SAM-bound structures of the enzymes studied here. In **Figure 6.6** we orient all structures so that the ribose C2', C1' and ring O atoms overlay. On the left, the figure shows that when SAM of PFL-AE[162] (5'-dAdo•-forming) and HydG[163] (•CH_3-forming) are so oriented and overlain they exhibit a dramatic axial *vs* equatorial orientation of C5'. The right side of the figure likewise aligns and overlays the five published SAM-bound structures of the enzymes studied here (PFL-AE (3cb8.pdb),[162] HydG (4wcx.pdb),[163] SPL (4fhf.pdb),[159] HydE (3iiz.pdb),[160] and LAM (2a5h.pdb)[165]), revealing that the two regioselectivity classes exhibit the same sharp axial/equatorial differences seen for PFL-AE and HydG. Moreover, members of each class exhibit the same SAM structure with minimal deviations: 5'-dAdo• -forming hosts have the 2'-endo ribose-ring conformation with an axial C4'-C5' bond; •CH_3-forming hosts have a 3'-endo ribose ring with equatorial C4'-C5' bond.

To gain insight into the active-site influences that produce the SAM conformational differences exhibited by the members of the two classes of RS enzymes, we took the PDB coordinates of a SAM structure from each class (SPL[159] from 5'-dAdo•-forming and HydE[160] from •CH_3-forming) and carried out a DFT energy minimization to obtain the favored geometry *in vacuo*, namely without environmental influences. The SAM structure from HydE optimized with small changes in geometry, but that from SPL underwent an 2'- endo → 3'-endo flip of the ribose ring with concomitant axial → equatorial shift of the

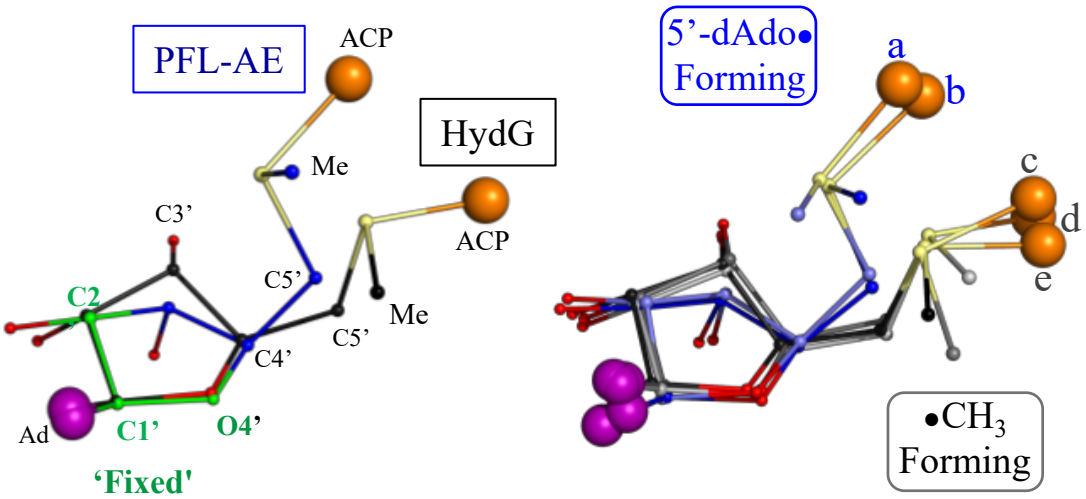

Figure 6.6. Comparisons of SAM configurations that yield photo- induced cleavage to form 5′-dAdo· or ·CH3, with orientation adjusted so that in all cases the ribose C2′, C1′, and ring O atoms overlay. (Left) Overlay of PFL-AE (3cb8.pdb) and HydG (4wcx.pdb). (Right) Overlay of (a) SPL (4fhf.pdb), (b) PFL-AE, (c) HydE (3iiz.pdb), (d) LAM (2a5h.pdb), (e) HydG, demonstrating the axial orientation of the C4′–C5′ bond in 5′-dAdo· formers and the equatorial orientation in ·CH3 formers.

C4'-C5' bond, and it converged to the same structure observed for SAM bound to HydE (**Fig S6.1**) and in most canonical RS enzymes considered by Vey and Drennan.[161] In short, in HydE and the other two RS enzymes that form •CH_3 photochemically, SAM binds with little distortion from its intrinsically most stable conformation, whereas in PFL-AE and SPL, which photochemically form 5'-dAdo•, active-site interactions force SAM to undergo a major change in ribose conformation upon binding.

The electronic structure of this sulfur center provides the foundation for an understanding of regioselective C-S bond cleavage. To begin, we note that the basic idea of independent SAM S-C bonds, with the S-C5' antibonding orbital simply acting as the electron-acceptor orbital on SAM is incorrect: a hypothesis of ET into an *individual* S-C anti-bond, either catalytically or via direct ET as occurs in these studies, oversimplifies the process and precludes our understanding of the S-C bond-cleavage step. It is not in general appropriate to consider the LUMOs of an R_3S^+ center as comprising three independent S-C anti-bonds, each potentially functioning as an independent electron-acceptor orbital, just as it is correspondingly inappropriate to consider the R_3S^+ center as comprising three independent S-C bonds (**Figure 6.7**).

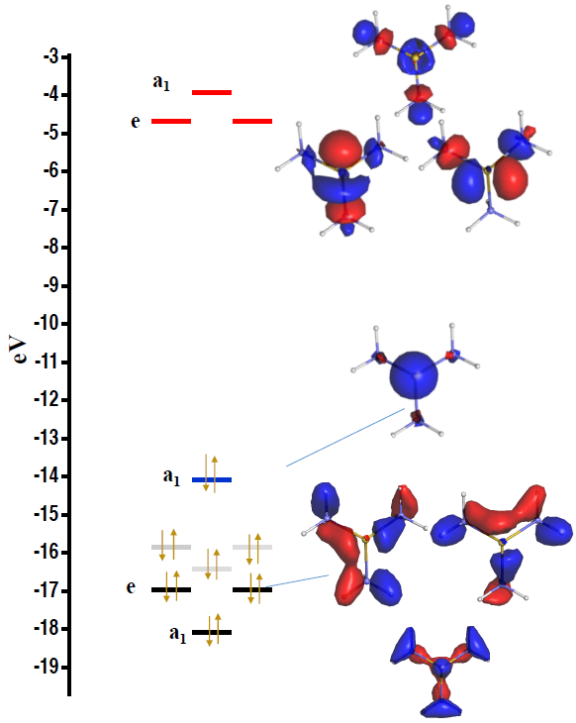

Figure 6.7: DFT computed energy levels and MO diagrams for $S(CH_3)_3^+$: (left) Black, carbon-sulfur based orbitals; gray, the highest-lying C-H based bonding orbitals; blue, sulfur lone pair HOMO; red, C-S based antibonding orbitals. (right) blue, positive orbital coefficients; red negative. The orbitals are visualized with an isodensity of 0.08 au in PyMol. For completeness we note that the components of a degenerate (*e*) level are not uniquely defined.

To illustrate this remark, we begin by again considering the electronic structure of the $(CH_3)_3S^+$ cation (**Figure 6.7, Figure S6.2**). Firstly, as can be seen, S-C bonding is delocalized. There is a low-lying, doubly-occupied, a_1 S-C orbital uniformly delocalized among the three S-C 'bonds'. Above this is a filled, doubly-degenerate S-C *e* level whose non-uniquely defined components involve pairs of bonds, and whose

total density again is uniformly delocalized. The LUMO of this trigonally-symmetric ion, which would accept the electron during reduction, is an orbitally-degenerate doublet (*e*) whose overall density again is uniform, **Figure 6.7**. Correspondingly, one-electron reduction of an R_3S^+ with this idealized trigonal geometry at S would create an R_3S^0 radical whose unpaired electron occupies a doubly-degenerate *e* level delocalized over the three S-C anti-bonds. To achieve regioselective bond cleavage this added electron must somehow become localized in the priority S-C anti-bond.

Turning to regioselectivity in SAM reductive cleavage, neither the bonding to the sulfur nor its environment is symmetric. Thus, the question, which of these effects, or what combination of them, controls regioselective cleavage?

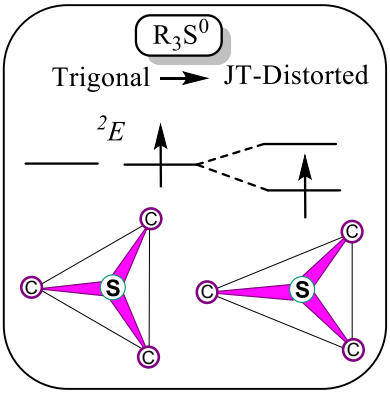

Figure 6.8: Splitting of 2E orbital degeneracy with JT distortion

One-electron reduction of the R_3S^+ sulfonium cation adds an electron to its doubly-degenerate S-C anti-bonding LUMO to give the R_3S^0 radical in a ^2E state (**Figure 6.7**), which is subject to JT distortion through vibronic coupling to (*e*) vibrations.[166, 167] In this vibronic distortion the R_3S^0 triangle of carbons undergoes an equilateral → acute-isosceles transformation through changes in S-C bond lengths, in particular elongation of the apex bond, along with changes in C-S-C angles, as visualized in the cartoon of **Figure 6.8** (obtuse triangles also are possible).[167] This splits the ^2E orbital doublet, and the resultant lower-energy component of the doublet is the actual R_3S^0 HOMO, as also shown in **Figure 6.8**. However, as we next explain, the JT-distorted state *by itself* could not exhibit regioselective homolysis. Regioselectivity is *only* introduced when 'environmental' influences acting on R_3S^0 *through* the JT effect create and stabilize a component of the ^2E doublet with a distortion that localizes the R_3S^0 antibonding electron in one particular SAM S-C 'priority' bond, which proceeds to undergo homolysis. The difference in photoinduced

regioselectivity in the two enzyme classes must then arise because a difference in forces operative at the sulfur within the two different SAM structures of **Figure 6.6**, as controlled by active-site interactions, leads to selection of different bonds for cleavage.

Further aspects and analysis of the mechanism of JT effect influenced regioselectivity is discussed in lengths in the published paper.[168] More so, to further understand the JT effect a study with computations that utilize the multiconfiguration complete active space self-consistent field (CASSCF) methods is currently underway. These high-level computations accurately describe the intermediate states and the electronic structure associated with it in the regioselectivity problem.

CONCLUSIONS

Electron paramagnetic spectroscopies and biochemical tools have allowed great progress in the study of radical SAM enzymes, but the data can only be modeled or analyzed to a natural extent. As exhibited here, DFT methods can support the analysis of the spectroscopic data, allow for further analysis of molecular and electronic structure, and can even expand on the results to elements of radical SAM intermediates that are not observable by experiment due to the time scale or ground state.

METHODS

Computational Aspects

All calculations were performed using the ORCA program developed by Neese. Throughout these projects several different versions of ORCA were used (3.8.1, 4.0.1, 4.2.1), but the functionality is essentially the same throughout the various studies.

DFT of the 5'dAdo radical

Initial coordinates for the 5′-dAdo fragment were taken from PFL-AE (2.77 Å resolution) with SAM bound to the [4Fe−4S] cluster (PDB 3CB8).[162] All protein residues, water, and other molecules were removed, and the adenine was replaced with a methyl group. Hydrogens were added appropriately to the structure with the unbiased starting geometry of the 5′-CH2 hydrogens being in a pseudo-tetrahedral conformation. Both geometry optimizations and single-point calculations used the spin unrestricted B3LYP[169-172] hybrid functional and the Ahlrichs' valence triple-ξ with a polarization function basis set.[173] Hyperfine and **g** tensors were calculated by the coupled−perturbed self-consistent field (SCF) approach as

implemented in ORCA 4.0 using the B3LYP hybrid functional and EPR-III basis[174] in combination with the accurate spin−orbit coupling operator RI-SOMF(1X)[175]. Calculations using the BP86 functional were carried out in parallel.

DFT of the SPL residue radicals

The initial geometry for the valyl radical was generated by extracting valine 172 coordinates from the crystal structure of SPL (PDB 4FHD, 2.0 Å resolution).[159] Hydrogens were added to make the molecule a neutral valine with the hydrogen from the beta carbon absent in order to generate the radical. The isoleucyl radical was created using the above-described valine and adding an additional methyl group to the gamma carbon of the V172 residue coordinates. For the two radicals, geometry and single point calculations utilized the spin-unrestricted B3LYP/G Hybrid functional.[169-172] Hyperfine and **g** tensors were calculated by the coupled−perturbed self-consistent field (SCF) approach as implemented in ORCA 4.0 using the B3LYP hybrid functional and EPR-III basis[174] in combination with the accurate spin−orbit coupling operator RI-SOMF(1X)[175]. Calculations using the BP86 functional were carried out in parallel.

Jahn-teller computations

For the small sulfur-centered molecule models, the starting geometry was created in Avogadro completely in silico. The basis and functional were applied as was done as described ab SPL residue radicals and the 5'-dAdo radical. For calculations of the SAM molecule, the crystal structure of the cofactor served as the starting geometry and hydrogens were added, assuming neutral pH for simplicity.

CHAPTER 7: Computational description of alkylated multi-iron clusters

Results from this chapter are part of a submitted publication:
R. J. Jodts, M Wittkop, M. B. Ho, W. E. Broderick, J. B. Broderick, B. M. Hoffman, M. A. Mosquera, **2023**

INTRODUCTION

Radical *S*-adenosyl-L-methionine (SAM) enzymes are ubiquitous amongst life, comprising one of the largest enzyme superfamilies.[149 28 176] These enzymes catalyze the reductive cleavage of SAM by electron transfer from a [4Fe-4S]$^{1+}$ cluster to the sulfonium group of the coordinated SAM to form the highly reactive 5´-deoxyadenosyl radical (5´-dAdo•), which then ultimately abstracts a hydrogen atom from substrates.[177 178 179] However, rapid freeze-quench electron paramagnetic (EPR) and electron nuclear double resonance (ENDOR) spectroscopies have shown that prior to H-abstraction from substrate, 5´-dAdo• forms an organometallic intermediate, denoted Ω, that is characterized by a direct bond between the [4Fe-4S]$^{3+}$ cluster and the 5´C of 5´-dAdo (**Figure 7.1, left**).[32, 33] Later, it was shown that photo-reductive cleavage of SAM in a broad subset of RS enzymes releases either 5´-dAdo• or a methyl radical (CH_3•);[158, 168, 177] upon annealing, the latter forms an alternative organometallic species, denoted Ω_M, which was shown by ENDOR to have a [4Fe-4S]$^{3+}$ cluster with an Fe-CH_3 bond (**Figure 7.1, middle**).[158,168, 180] Inspired by these discoveries, the M-CH_3 analogue of Ω_M (**Figure 7.1**, **right**) was synthesized and extensively characterized by crystallography as well as with Mossbauer and ENDOR spectroscopic methods,[135, 181] with additional alkylated iron-sulfur clusters being synthesized and characterized.[182 183]

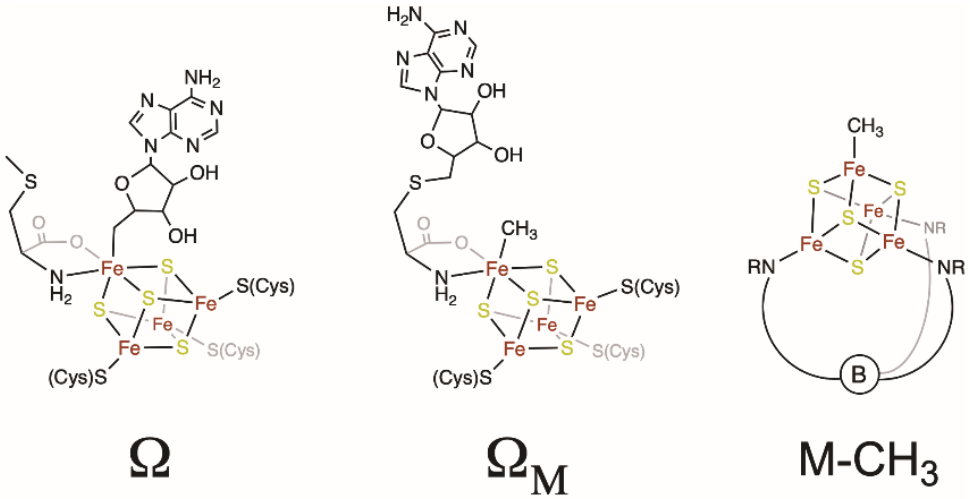

Figure 7.1. Representative structures of three [4Fe-4S] clusters with an alkylated unique iron. Here shown, from left to right, are the proposed structure of the SAM intermediate Ω, the proposed methyl bound analogue Ω_M, and the crystallographically determined synthetic M-CH_3.

The discovery of these multi-metallic iron-sulfur organometallic complexes creates the necessity for accurate computation of their properties. The goal in this work is to devise a method to reliably describe a complex with an alkyl bound to a multi-metallic iron-sulfur cluster, to use this as a means of describing the properties of the crystallographically characterized M-CH_3, and ultimately to probe the structures of the enzymatic intermediates Ω and Ω_M.

Multireference methods have become the cornerstone for capturing molecular properties, especially the complete active space self-consistent field (CASSCF) computational method, which has been shown to accurately replicate electronic structure and magnetic parameters derived from experiments. Multireference methods, unlike standard DFT, do not have issues with localization of metal electrons and incorporate electron-spin as a good quantum number, and thus are able to accurately replicate properties observed in experiment on metal complexes. However, currently it is impracticable to apply this approach to the [4Fe-4S] clusters, as their large number of localized electrons render them too computationally expensive.

The alternative approach, simple density functional theory (DFT) methods, is inadequate for the systems of interest, **Figure 7.1**, but the use of broken symmetry density functional theory (BS-DFT) has been shown to accurately capture the properties of [4Fe-4S] clusters as well as other iron-sulfur based clusters.[184] [185] [186] [187] [188] However, although 'simple' BS-DFT takes advantage of the ability of unrestricted standard DFT to render localized orbitals at each of the metal sites, it does not give wavefunctions of well-defined total spin, which is important in calculating the signature HFCC to nuclei of ligands bound to a multi-metallic iron-sulfur cluster

Presented here is a readily applied, 2-configuration version of BS-DFT, denoted 2C-DFT, designed to allow the accurate description of an alkyl group bound to a multi-metallic iron-sulfur cluster, with a *focus* on computing the hyperfine coupling constants (HFCCs) for nuclei of the complex, which are commonly used in defining the molecular and electronic structure of an unknown system. This approach has been validated by the agreement of its results with those of high-level CASSCF computations for a series of model complexes, **Figure 7.2**, and with the spectroscopic results for the crystallographically-characterized complex, M-CH_3 (**Figures 7.1, 7.2**). 2C-DFT computations for Ω are in excellent agreement with the

spectroscopic properties of this intermediate, confirming its identity as an organometallic complex with a bond between an Fe of its [4Fe-4S] cluster and C5´ of the deoxyadenosyl moiety, as first proposed.[32]

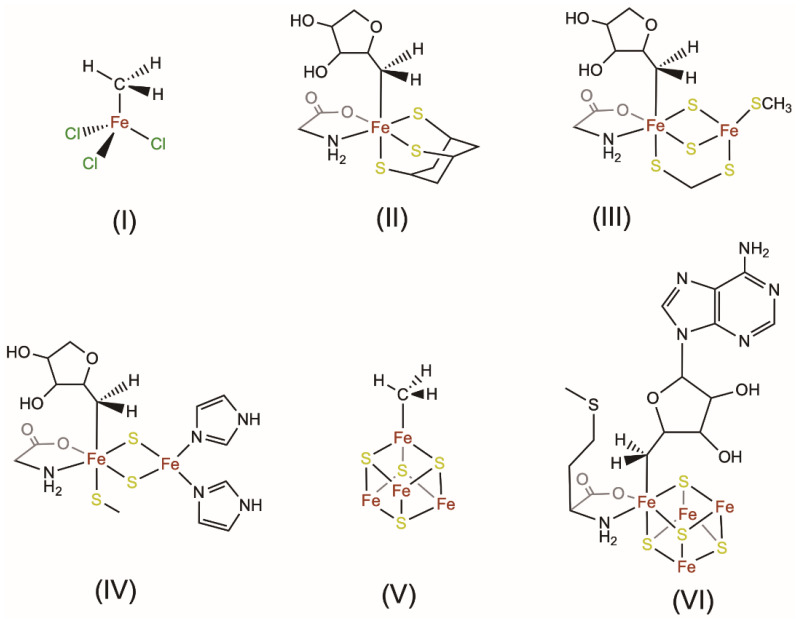

Figure 7.2. Structures of computational models examined in this chapter. I was a previously studied model. **II, III**, and **IV** are systems that mimic the coordination of the unique iron, yet are not too complex for advanced methods. Structure **V** is simplified illustration of the four-coordinate iron-methyl model synthesized and spectroscopically characterized previously, and **VI** is the ENDOR derived/proposed Ω species structure, with cysteinyl ligands to the three cluster Fe truncated as CH_3S^-.

THEORY

In [4Fe-4S] clusters the spins localized on the metal ions are strongly coupled and a successful approach in describing this phenomenon is the Heisenberg-van Vleck-Dirac model (HVVD). In the HVVD approach, a cluster is treated as a set of metallic spins with exchange couplings (and if necessary, double-exchange, and biquadratic couplings). As an example, the Spin-Hamiltonian for a set of spins with J-coupling can be taken as:

$$\boldsymbol{H} = \sum_{i>j} J_{ij} \boldsymbol{S}_i \boldsymbol{S}_j + \sum_i \mu_B \boldsymbol{B}^T \boldsymbol{g}_i \boldsymbol{S}_i + \sum_{k,i} \boldsymbol{I}_k^T \boldsymbol{A}_{k,i} \boldsymbol{S}_i, \qquad \textbf{(7.1)}$$

where k and i label the spin sites within the molecule. The g-tensor of site i is given by the symbol $\boldsymbol{g}_i$, whereas the hyperfine coupling tensor of electronic spin i to nucleus k is denoted as $\boldsymbol{A}_{k,i}$. The hyperfine ($k = i$) tensor has isotropic and anisotropic components. The isotropic part is given by the well-known Fermi

contact term. With careful coupling constant selection, this is a model that describes, in many cases very accurately, experimentally observable quantities associated with the cluster spin.

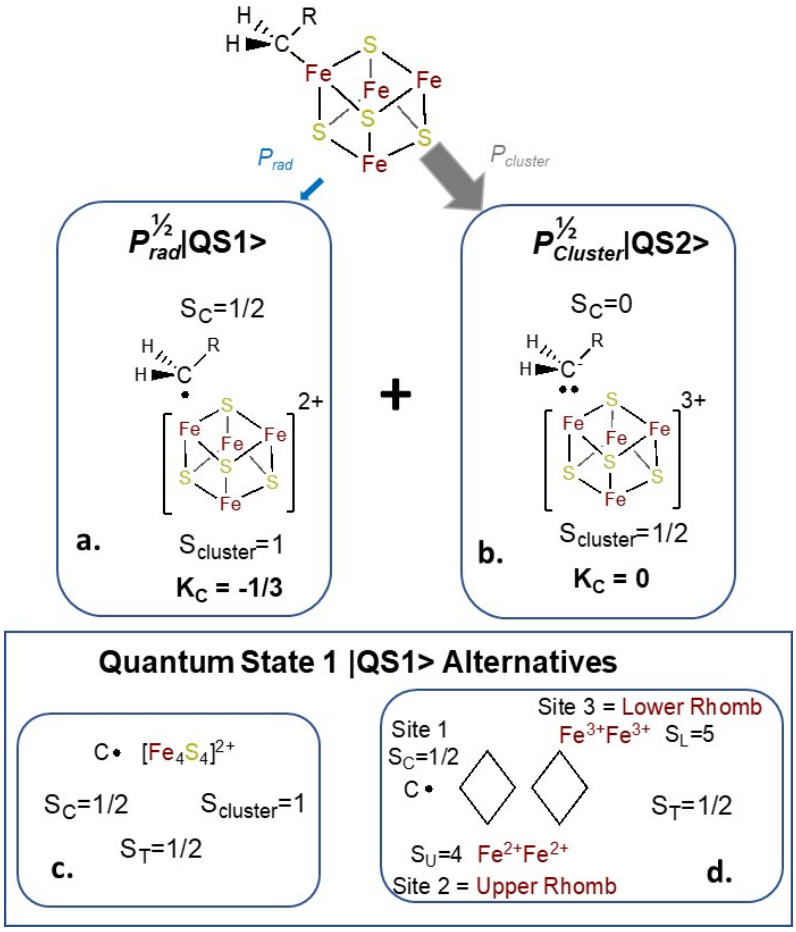

Figure 7.3. 2C-DFTmodel for the analysis of the HFCC of an alkyl bound to a [4Fe-4S] cluster. The wavefunction for the system is taken as a superposition of two states: **a)**, quantum state 1, or QS1, with spin on the alkyl S_C = ½ and HFCC to the ligand nuclei, that is spin-coupled to a cluster with spin $S_{cluster}$ = *1*, and **b)**, quantum state 2, or QS2, where the alkyl group has S_C = 0, and does not exhibit ligand HFCC. **c)** shows a simple coupling scheme between alkyl with S_C = ½ and 'monolithic' cluster with $S_{cluster}$ = *1.* **d)** defines a three-site model where the radical is coupled to a cluster comprised of two rhombs with total spins of, 4 and 5, respectively, spin-couple to give $S_{cluster}$ = *1*.

The BS-DFT wavefunction is a single multi-electron determinant that is not an eigenfunction of the total spin, and hence is not applicable for use in computing HFCCs. There are multiple ways to generate the eigenfunction of total spin from a BS-DFT wavefunction, which is required to achieve accurate HFCCs. An earlier approach for ligand site HFCCs, proposed by Noodleman et al.,[189 190] averages the product of the spin-coupling factors of the metallic sites, and uses the result to obtain HFCC to the ligand nuclei

(absolute values). An alternative method suggested by Rapatskyi et al.[191] corresponds to simply summing over all products of spin-coupling factors (absolute value) to obtain the ligand HFCC. We propose an alternative theoretical approach in this work that leads to a simple, general prescription for treating the BS-DFT calculated hyperfine couplings of alkylated FeS clusters and show that it yields accurate ligand site hyperfine couplings by comparison to CASSCF computations on a suite of model complexes.

We define a 2-configuration DFT approach (2C-DFT) to achieving a wavefunction with total spin S_T = ½ as described visually in **Figure 7.3** and given by **eq 7.2,**

$$|\Psi\rangle = P_{\mathrm{rad}}^{1/2}|\mathrm{QS1}\rangle + P_{\mathrm{cluster}}^{1/2}|\mathrm{QS2}\rangle. \qquad P_{\mathrm{rad}} + P_{\mathrm{cluster}} = 1; \quad P_{\mathrm{rad}} << P_{\mathrm{cluster}} \tag{7.2}$$

where P_{rad} and $P_{cluster}$ are the probabilities of the QS1 and QS2 configurations, respectively. In the dominant configuration, |QS2⟩, the cluster can be viewed as a $[4Fe\text{-}4S]^{3+}$ cluster with $S_{cluster}$ = ½, while the C1 carbon of the organic moiety is anionic, closed-shell, and without spin. As a result, this configuration makes no contribution to the HF couplings to the alkyl spins.

Hyperfine couplings to the alkyl are introduced by the minority configuration, |QS1⟩, which contains a $[4Fe\text{-}4S]^{2+}$ cluster with $S_{cluster}$ = 1, antiferromagnetically spin-coupled to the S_C = ½ neutral alkyl free-radical spin, which has hyperfine couplings to the alkyl nuclear spins. In the simplest approach, it is straightforward to generate |QS1⟩ as an eigenfunction of total spin of the complex, S_T = ½ (wavefunctions, |QS1, S_T = ½, m_T⟩; m_T denoting the secondary spin quantum-number) through treatment of the complex as a two-spin entity, **Figure 7.3c**: a cluster with spin $S_{cluster}$ = 1 (wavefunctions $|1,m_{cl}\rangle_{cluster}$, m_{cl} denoting the secondary spin quantum-number of the cluster) antiferromagnetically spin-coupled to the S_C = ½ radical (wavefunctions $|½, m_C\rangle_{alkyl}$, m_C denoting the secondary spin quantum-number of the radical). In this case the spin-coupled QS1 component of the 2C-DFT wavefunction is given by,

$$|\mathrm{QS1}, ½, +½\rangle = \sqrt{2/3}\ |1,1\rangle_{\mathrm{cluster}}|½, -½\rangle_{\mathrm{alkyl}} \ - \sqrt{1/3}|1,0\rangle_{\mathrm{cluster}}|½, +½\rangle_{\mathrm{alkyl}} \tag{7.3}$$

with this component weighted in the 2C-DFT wavefunction (**eq 7.2**) by $P_{\mathrm{rad}}^{1/2}$.

The observed isotropic HFCC to nucleus *I* (a_i^{obs}) of a complex with an alkyl moiety bonded to an Fe of a multi-metallic iron-sulfur cluster, total complex spin S_T, is incorporated in the hyperfine contribution to the complex's spin-Hamiltonian through a term involving the operators for the total complex spin ($\boldsymbol{S}_T$) and nuclear spin ($\boldsymbol{I}_i$),

$$\boldsymbol{H_i} = a_i^{\mathrm{obs}}\, \boldsymbol{S}_T \bullet \boldsymbol{I}_i \qquad \textbf{(7.4a)}$$

whereas the intrinsic hyperfine coupling of the isolated (non-interacting) radical spin with the nucleus (a_i^{alk}) is defined in terms of the operator for the local alkyl electron-spin ($\boldsymbol{S}^{\mathrm{alk}}$)

$$\boldsymbol{H_i^{alk}} = a_i^{\mathrm{alk}}\, \boldsymbol{S}^{\mathrm{alk}} \bullet \boldsymbol{I}_i \qquad \textbf{(7.4b)}$$

The observed HF coupling parameter, a_i^{obs}, is determined in terms of the parameter for the isolated radical, a_i^{alk}, by the matrix element of the local alkyl electron-spin (S_z^{alk}) with the spin-coupled QS1 wavefunction component (**eq 3**) as follows:

$$\begin{aligned} a_i^{\mathrm{obs}} &= P_{\mathrm{rad}} \langle \mathrm{QS1},\ ½,\ +½ |\ 2a_i^{\mathrm{alk}}\, S_z^{\mathrm{alk}} | \mathrm{QS1},\ ½,\ +½ \rangle \\ &= (-1/3)\, P_{\mathrm{rad}}\, a_i^{\mathrm{alk}} \\ &\equiv K_C\, P_{\mathrm{rad}}\, a_i^{\mathrm{alk}} \end{aligned} \qquad \textbf{(7.5)}$$

Thus, use of the 2C-DFT wavefunction, **eqs 7.2, 7.3**, to compute a_i^{obs} gives a simple result, the product of three factors: K_C = -1/3, the coefficient that results from spin coupling within the exchange-coupled, QS1 configuration, and which weights the radical contribution to the total spin S_T = ½; P_{rad}, the contribution of the QS1 configuration to the total wavefunction; and a_i^{alk}, the hyperfine coupling to the nucleus of the isolated alkyl radical. However, the product of the latter two factors is accurately given by the straightforwardly computed BS-DFT coupling constant, a_i^{BS}, leading to the final result for use in comparing the 2C-DFT results for the alkyl-bound cluster to those from CASSCF and from experiment,

$$\begin{aligned} a_i^{\mathrm{obs}} &= K_{\mathrm{C}} P_{\mathrm{rad}} a_i^{\mathrm{alk}} \\ &\approx K_{\mathrm{C}} a_i^{\mathrm{BS}} \end{aligned} \qquad \textbf{(7.6)}$$

Alternatively, we may follow Noodleman and Case[187] in treating the $[4Fe\text{-}4S]^{2+}$ cluster as two spin-coupled rhombs containing two Fe each, denoted upper (with the Fe-C bond) and lower, **Figure 7.3d**, where the rhombs are of intermediate spins, 4 and 5, and spin-coupled to give an overall cluster spin, S_{cluster} = *1*; this cluster spin is then coupled with S_C = ½ to achieve the total system spin of S_T = ½, as in the simpler

approach of **Figure 7.3c**. Using the 2-rhomb approach, if we define the configurational quantum states as $|S_{\mathrm{C}}, S_{\mathrm{U}}, S_{\mathrm{cluster}};\ S_{\mathrm{T}}\rangle$, then the two-configuration 2C-DFT wavefunction for the organometallic cluster becomes the eigenfunction of total spin S_{T} = ½, ***eq 7.3***

$$\left|\Psi, \frac{1}{2}\right\rangle = P_{\mathrm{rad}}^{\frac{1}{2}} \left|\frac{1}{2}, 4, 1; \frac{1}{2}\right\rangle + P_{\mathrm{cluster}}^{\frac{1}{2}} \left|0, \frac{9}{2}, \frac{1}{2};\ \frac{1}{2}\right\rangle \qquad \textbf{(7.7)}$$

more complex than the 2-spin case detailed above, as the spin-coupling between the cluster and radical is nonetheless the same, the resulting hyperfine coupling calculated for an alkyl nucleus is identical to that given by **eq 7.6**.

Of key importance, for multi-Fe systems the spin-coupling factor in **eqs 7.5** and **7.6** for the hyperfine coupling to an alkyl-spin is K_{C}= -1/3, *and* for the systems with a [4Fe-4S] cluster this is true *regardless* of whether the complex is taken as the two-spin system of **Figure 7.3c** or the three-spin system of **Figure 7.3d**. In short, the final 2C-DFT formula for the ligand site bound to a multi-Fe cluster, **eq 7.6**, is merely the product of the BS-DFT computed HFCC of the alkyl site (a_i^{BS}), and the factor K_{C} = -1/3, regardless of the description of the S_{cluster} = 1 cluster. Thus, the 2C-DFT approach straightforwardly and universally introduces two extraordinarily significant corrections to the 'raw', single-determinantal, BS-DFT value for a ligand HFCC, $\mathrm{a_i^{BS}}$: (i) the magnitude of the 2C-DFT HFCC is 1/3 that computed by BS-DFT; (ii) the sign of the HFCC in 2C-DFT is inverted from that given by BS-DFT. We validate the 2C-DFT approach through extensive comparisons to the results of high-level, multiconfigurational CASSCF computations on the model complexes of **Figure 7.2**, and then apply the method to the experimentally characterized complexes

For completeness, it is important to further recognize that one can simply obtain the ^{57}Fe HFCC for the multi-iron systems (**Figure 7.2**) through the approach outlined for [4Fe-4S]$^{3+}$ clusters by Noodleman, which involves multiplication of the BS-DFT-computed a_{Fe}^{BS} by the vector-coupling coefficient, *K*, for Fe site *i* within the S_C = ½ total-spin cluster state, and the ratio, $\mathrm{Ms_{total}/Ms_{site}}$, **eq 7.7**. For the diiron complexes in this study, K = +$^{7}/_{3}$ for the ^{57}Fe(III) center. For the 4-iron systems we used *K* = +$^{55}/_{27}$, as derived by Noodleman,[192]

$$a_{\mathrm{Fe}}^{\mathrm{obs}} = K \frac{Ms_{\mathrm{total}}}{Ms_{\mathrm{site}}} a_{\mathrm{Fe}}^{\mathrm{BS}} \qquad \textbf{(7.8)}$$

Parenthetically, the result for the alkyl ligand to a monoiron complex is even simpler than **eq 7.6** For the $S_{\mathrm{T}} = 5/2$ monoiron models, the 2C-DFT approach for the observed HFCC of the alkyl site simply 'collapses' to the raw DFT value ($a_i^{\mathrm{obs}} = a_i^{\mathrm{DFT}}$). This is explained as follows: In the QS1 of the single iron systems $S_{\mathrm{C}} = 1/2$ and $S_{\mathrm{Fe}} = 2$, then $K_{\mathrm{C}} = 1/5$, but this factor is cancelled by the ratio of the total spin and alkyl site spin ($Ms_{\mathrm{total}}/Ms_{\mathrm{site}} = 5$), so the raw BS-DFT HFCC of the alkyl site does not require a correction in these cases.

As a last remark about the 2C-DFT method, in principle, an S = 1/2 alkylated cluster smoothly 'dissociates' the 'free' S = 1/2 radical as the Fe-C distance is increased. In such dissociation, the "quantum state 1" picture becomes increasingly more dominant, and ultimately QS2 can be neglected. As required, the coupling of the radical to the cluster becomes weak at relatively long distances, and the contribution of the $S_{\mathrm{cluster}} = 1$ configuration, which would yield measurable ^{57}Fe HFCC, can be taken into account straightforwardly through quantum perturbation theory and 2C-DFT (with proper exchange-correlation functional selection), and the same for the HFCC couplings of the alkyl. At quite long distances, the radical and the cluster eventually decouple and the configuration with $S_{\mathrm{cluster}} = 0$ cluster and $S = 1/2$ radical would completely describe the entire system.

RESULTS

Validation of 2C-DFT through comparison to CASSCF computations on the models and to experiment

Both CASSCF and 2C-DFT computations for the model species **I – IV** depicted in **Figure 7.1** were performed. The HFCCs computed by these two methods, and further compare them to those from raw BS-DFT and to the observed experimental HFFCs reported for Ω, M-CH_3, and Ω_M (**Table 7.1;** See SI for model coordinates).

Table 7.1: Isotropic HFCC for Observed Complexes (MHz)

Molecule/site	$^{13}C_1$	^{57}Fe	^{1}H
Ω	9	-34	8
M-CH_3	+5.5	--	-8.5
Ω_M	+18	--	--

Model I: To begin this computational study, we first examined an inorganic mono-iron model with a methyl group bound to an Fe(III), $FeCl_3CH_3$ (**I**) **(Figure 7.2)**, the simplest model for the Fe-CH_3 bond of Ω_M and M-CH_3. As mentioned above, the electronic structure of **I** was previously examined;[181] here we extend the analysis methodologically to compute magnetic properties. For all the nuclei the differences between CASSCF and DFT couplings, which latter are merely equal to the raw DFT values as discussed after **eq 7.8,** are within the expected variation between methods, and are most likely due the inherent uncertainties of the common density functional approximations for metal systems. Using CASSCF (7,6) with the above described basis and functional, the calculated magnitudes of ^{13}C HFCC for the $^{13}C_1$, as well as the C_1-^1H proton hyperfine coupling values in **I,** are in agreement with the ^{13}C HFCC for W_M and the more extensive ENDOR data for the biomimetic organometallic complex M-CH_3 **(Table 7.1**); for **I**, a($^{13}C_1$) ~17 MHz, a(^1H) = 11 MHz, and a(^{57}Fe) = 4.7 MHz is of expected magnitude (**See Table 7.2**). Use of either BP86 or TPSSh in calculating the BS-DFT coupling a_i^{BS}, yields a_i^{obs} for $^{13}C_1$ and ^{57}Fe of **I** of comparable, if slightly higher, values than those given by the CASSCF method, and slightly lower values for the methyl proton HFCCs (**Table 7.2**). This agreement in the HFCCs for **I** calculated by both the CASSCF and BS-DFT methods validates the ability of DFT to describe the Fe-alkyl bond, a foundational requirement for the 2C-DFT approach to alkyl complexes of multi-metallic iron-sulfur clusters, **eq 7.6** and **7.8.**

	CASSCF				2C-DFT (BP86)			
Molecule/site	$^{13}C_1$	$^{13}C_2$	^{57}Fe	$^1H_{avg}$	$^{13}C_1$	$^{13}C_2$	^{57}Fe	$^1H_{avg}$
I	17.0	--	4.7	11.0	14.4	--	8.1	4.3
II	10.3	1.4	18.4	12.5	15.7	2.5	10.5	0.6
III	2.9	1.0	20.5	5.1	10.9	0.2	19.2	2.7
IV	6.8	1.3	11.3	6.2	20.9	0.7	16.6	2.1
V	Not currently applicable				+9.3	--	-10.1	-11.5
VI					+10.5	+0.1	-15.6	-1.3

Table 7.2. Computed HFCCs of the models described in Figure 1. CASSCF calculations with the active space (7,6) were carried out for I and II, whereas the active space (13,11) was used for III and IV, which involve two iron sites. The CASSCF calculations are run on the BP86-optimized molecular geometries. CASSCF is currently not applicable for V and VI. For all the models we report results from the BP86 DFT functional. Results from the TPSSh functional are shown in the SI. For easy interpretation we average the HFCCs of hydrogen sites. ^{57}Fe HFC listed in models III-VI refer to the alkyl-bound iron.

Model II: Increasing the complexity of an monoiron-alkyl system, we examined a monoiron center **II** whose Fe exhibits the same direct coordination sphere as the alkylated Fe of Ω and Ω_M, particularly the direct C5´-Fe bond of W. Again, CASSCF (7,6) computations (**Table 7.2**) for **II** yield both a ^{13}C HFCC for the Fe-bound carbon and ^{1}H HFCC for the C5´-^{1}H protons, that are close to the experimental values found for the Ω enzyme intermediates, and even roughly comparable to that measured for the structurally characterized M-CH_3 (**Table 7.1**). The BS-DFT calculations with the BP86 (**Table 7.2**) and TPSSh (**Table S7.1**) functionals give comparable values for $^{13}C_1$, regarding both CASSCF and experimental measurements on Ω, and M-CH_3, again validating the ability of BS-DFT to describe the Fe-alkyl bond.

The BS-DFT computed C5´-^{1}H proton HFCC is slightly underestimated compared to the nonetheless small values observed for M-CH_3 and Ω (a_{iso} = ~1 MHz vs ~8 MHz).[135] We attribute this discrepancy in **II**, which **I** did not have, to an effect of the higher coordination[193] of the unique iron of **II** reducing the delocalization of spin amongst the coordinated ligands, and thus decreasing the $a_{i,site}$ factor of **eq 7.8**.

Model III: This is a Rieske-*inspired* diiron cluster model whose dominant configuration |QS2> features an Ω-like-coordinated Fe(III) antiferromagnetically coupled with a Fe(IV) partner site, a non-physical oxidation state that is adopted so that 5´-C is bonded to Fe(III); if the III/II valence is adopted, then the 5´-C becomes bonded to the Fe(II). Nonetheless, for this model both CASSCF and the 2C-DFT computation according to **eq 7.6** yield identical ^{57}Fe HFCCs for the alkyl-coordinated Fe. Overall, the 5´^{13}C and 5´C-^{1}H HFCCs computed by the two methods essentially reproduce those observed experimentally in the structurally determined M-CH_3 complex (**IV)**, and the 2C-DFT $^{13}C_1$ HFCC exactly matches that of Ω. In this case the ^{1}H couplings are equivalent for the two methods, while the ^{13}C couplings diverge somewhat (Table 2). Note, that if one simply applied the standard BS-DFT protocol for the HF coupling without incorporation of the factor, K_C = -1/3 (**eq 7.6**), the resultant coupling (a_{C1}^{BS} = 33 MHz) is far greater (4-fold!) than the value seen for omega.

Model IV: This is an Ω-*based* Rieske system in which the dominant |QS2> configuration of the diiron center is the classical Fe(II)-Fe(III) spin-coupled pair, as is the case in biological diiron centers. This configuration

is a simplified version of the [4Fe-4S] |QS2> spin-coupling configuration described in **Figure 7.3d** – with the upper rhomb represented by the spin-coupled Fe(II)/Fe(III) diiron pair and no lower rhomb. Both CASSCF and 2C-DFT computations resulted in a C_1-Fe(III) bond as in the three experimentally studied organometallic complexes (**Figure 7.1)**, and the magnitudes of all nuclear hyperfine couplings again are comparable for the two methods (**Table 7.2**). As with **III**, the CASSCF and 2C-DFT ^{57}Fe and ^{1}H HFCCs are in excellent agreement with the three experimentally explored [4Fe-4S] systems (**Figure 7.1, Table 7.1 and 7.2**), and likewise the 4´-^{13}C ($^{13}C_2$) and beta-^{1}H proton couplings, but with slight differences in $^{13}C_1$ HFCCs. To perhaps belabor the point, once again the 'raw' BS-DFT produces value by itself too large for such a system: one cannot accurately capture the nature of a multi-iron system without treatment of the factor, K_C (**eq 7.6**). We conclude that the essential equivalence of the results of CASSCF and 2C-DFT computations indeed validates the new, and readily implemented method for alkyl-bound multi-iron systems such as those of the biological intermediates.

The correspondence between the results of CASSCF and 2C-DFT computation for Fe-bound alkyl groups and the agreement with available experimental data from such systems, in contrast to the failure of simple, uncorrected BS-DFT computations, whose magnitudes would be three-fold greater because of the absence of the factor, K_C (**eq 7.6**) validates the use of 2C-DFT in calculating HFCC for the experimentally studied, alkylated 4Fe clusters of interest here, which are beyond the current reach of CASSCF methods.

2C-DFT of experimentally observed alkylated-4Fe4S clusters.

We here apply the 2C-DFT method to the crystallographically characterized synthetic complex (M-CH_3, **V**) and the key catalytic intermediate (Ω, **VI**), systems that are too complex for current application of the CASSCF multi-configuration calculations.

Complex V: Model **V (Figure 7.2)** is a model for the Ω_M enzymatic intermediate and a faithful representation of the synthetic, structurally characterized M-CH_3, which furthermore has the most completely determined hyperfine couplings among the three current experimental systems (**Figure 7.1**).[135] To carry out two-rhomb computations for |QS1> (**Figure 7.3C)** one must first choose one of the other three Fe to partner with Fe1 as the upper rhomb when carrying out the 2C-DFT computation of **V**, which is equivalent to choosing which

Fe spins are 'flipped' in constructing the BS-DFT wavefunction. However, it should not matter which of the other three is chosen because the three-fold symmetry around the four-coordinate unique Fe makes all three possible rhomb configurations essentially equivalent, and indeed, the three possible rhomb configurations do indeed produce essentially equivalent HFCC (**Table S7.2**).

As a foundational result, the 2C-DFT calculations of **V**, the [4Fe-4S]-CH_3 representation of M-CH_3 (**Figure 7.1**) gives $g_{iso} > 2$ in agreement with experiment, an initial confirmation that this computational method accurately represents the observed electronic structure of M-CH_3. The magnitudes of the experimentally observed $^{13}C_1$ and C_1-^1H hyperfine coupling constants of M-CH_3 (**Table 7.1**) are well-reproduced by the calculated values (**Table 7.2**), even considering the slight overestimate of the $^{13}C_1$ value. If one were instead to consider only a "pure" BS-DFT $^{13}C_1$ HFCC results, omitting the required factor, K_C (**eq 7.6**), use of the optimal BP86 functional gives a coupling that is three-fold too large, and the discrepancy becomes even larger (five-fold) if one uses the sub-optimal TPSSh functional (**SI Table S7.3**).

Of signal importance, the 2C-DFT $^{13}C_1$ HFCC has a positive sign, as experimentally determined for M-CH_3, whereas pure BS-DFT HFCC yields a negative coupling, and as such qualitatively fails to reproduce experiment. ^{57}Fe ENDOR was not collected on M-CH_3, but the computed ^{57}Fe HFCC for **V** are quite similar in magnitude to what was observed in the analogous Ω experiments. These results demonstrate the ability of 2C-DFT to accurately describe the HFCC to the nuclei of an alkyl group bound to a crystallographically characterized [4Fe-4S] cluster, and the failure of simple BS-DFT to do so.

Complex VI: With a foundation of the computational validation of 2C-DFT and its success in describing the structurally characterized M-CH_3, we now consider the representation of the catalytically central Ω (**VI**) intermediate, with its six-coordinate, alkylated-iron site revealed through considerations of ENDOR-derived HFCCs.[32] Unlike **V**, with three-fold symmetry at the Fe-CH_3, for the six-coordinate unique iron of **VI** the three choices for upper rhomb within the cluster are no longer equivalent because the 3-fold symmetry has been lost. The best results (**Table 7.1**) are attained when treating the iron denoted as Fe2 as forming the upper rhomb (S= 4) with Fe1 (see **Figure S7.1** for iron labeling scheme and **Table S7.2** for results of other

rhomb configurations). Using this configuration of the [4Fe-4S] cluster and the BP86 functional, the resulting 2C-DFT calculation accurately reproduces the experimental g-tensor, with $g_{iso} > 2$, and $g_{||} > g_{\perp}$, and reproduces with great accuracy the magnitude of the experimental $^{13}C_1$ HFCC. Moreover, this methodology yields a positive $^{13}C_1$ HFCC, which could not be measured but can be assumed based on the sign for the methyl-carbon coupling of M-CH_3, as well as the sign obtained in Ω_M. It does equally well in reproducing the magnitude of the ^{57}Fe HFCC of the unique iron (again, the sign of the coupling presumed to be negative from W_M and M-CH_3) (**Table 7.2**). Use of the TPPSh function not only yields magnitudes for the couplings that are somewhat too large for the $^{13}C_1$, *but* also gives the opposite sign compared to the BP86 (**Table S7.3**). Moreover, we note that the calculated C_1-proton ^{1}H HFCC are themselves reasonably close to experiment in magnitude, although somewhat underestimated (~2 vs ~8 MHz, **Table 7.1 and 7.2**). The other possible rhomb configurations overestimate the magnitude of the $^{13}C_1$ coupling, and therefore are eliminated as models to represent the actual Fe configurations of Ω (**Table S7.2**).

CONCLUSIONS

The readily-applied 2C-DFT approach enables an accurate description of alkyl-bound multi-metallic iron-sulfur clusters, as validated by the excellent agreement of its results with those of the multi-reference CASSCF computations for the mono- and diiron models of **Figure 7.2**, and in particular by its strong agreement with the spectroscopic results for the crystallographically-characterized M-CH_3, whose structure and Fe-CH_3 bond are well-modeled by **V**, as well as its agreement with the results for Ω itself. The success of the 2C-DFT approach reveals that the incorporation of a second determinantal configuration of the BS-DFT wavefunction (**eq 7.2**) provides a simple and accurate way to explicitly account for spin on the alkyl group, and thereby to attain accurate molecular properties, most notably the HFCCs (**eqs 7.6, 7.8**).

Finally, having achieved the ability to reliably compute the hyperfine coupling constants for nuclei of an alkyl bound to a multi-metallic iron-sulfur cluster, we conclude that the excellent agreement between spectroscopic results and 2C-DFT computations for the Ω model, **VI**, confirm that Ω is indeed the organometallic complex visualized by **VI** and in **Figure 7.1**, with an Fe-C5'dAdo bond, as initially proposed[32] and as is increasingly accepted.[194]

METHODS

All computations were carried out in vacuo with the ORCA 4.2 program.[157] Geometry optimizations for all models described in **Figure 7.1** were performed using the BP86 exchange correlation functional and the relativistic zeroth order regular approximation (ZORA), where the atoms where assigned the ZORA-def2-TZVP basis set.[195] We also employ the D3 van der Waals correction, and the density fitting functionality SARC/J; samples of our input files can be found in the supporting information section. Employed also was the self-consistent field threshold "TightSCF" and optimization threshold "TightOpt". The regular convention of optimizing the molecular geometry with the iron clusters set in the high spin configurations was used. With the optimized geometries obtained, we ran CASSCF and DFT calculations where the carbon ligated to the iron atom (denoted C_1 in the text and tables) and its ^{1}H atoms of interest are assigned the EPR-III basis set, otherwise other C and H atoms (including the following carbon bound to the C_1 carbon, denoted C_2) are described with the EPR-II.[174] All Fe atoms are treated with the CP(PPP) set, and the S atoms have def2-TZVP applied to them.[196] The multireference CASSCF calculations were performed using a (7,6) active space [wherein for (n,m), n is the number of electrons and m the number of orbitals] for the monoiron models, and an active space of (13,11) for diiron systems. The DFT calculations performed for magnetic properties used the same basis set selection, in conjunction with the exchange coupling functionals BP86, or TPSSh.[169 170 197 198] These two functionals are commonly employed for magnetic-property calculations.[199] Details of the standard treatments of the projection factors and isotropic hyperfine couplings are detailed in the text.

CHAPTER 8: Conclusions and Outlook

PROSPECTUS

Advances in understanding particulate methane monooxygenase

Studying particulate methane monooxygenase (pMMO) is driven by the goal of elucidateinghow the selective oxidation of methane to methanol occurs under ambient conditions. It has been said that pMMO is one of the remaining major unsolved problems in bioinorganic chemistry. This is largely due to the fact pMMO, as a very large membrane-bound enzyme, presents challenges for study. However, recent studies[14-16] and the work presented in this thesis have made significant advances in understanding the atomic factors involved in biological methane oxidation by characterizing the copper center. These developments in the characterization of the copper centers of pMMO will aid future biochemical, theoretical, and synthetic biomimetics to eventually take inspiration from Nature's methane oxidation method and apply them within an impactful setting.

Chapter 2 presents a way to directly probe the second Cu(II) species (Cu_C or Cu_D site) observed in pMMO, which allowed for the first detailed advanced characterizations of this site with spectroscopic methods. This method will continue to be useful in the studies of pMMO, as the Cu_D site is consistently implicated in methane oxidation activity and currently is the only means to directly probe the Cu_D site without interference from Cu_B signals. This ENDOR approach was already utilized in the study of pMMO with product analogs as shown in **Chapter 3**, and will be important in future work, as explained in detail below.

Chapter 3 presents a milestone for the field of methanotrophy and pMMO: the first evidence of a copper center interacting with an inhibitor/product analog, and moreover the first interaction of any pMMO copper center with a hydrocarbon-like molecule. This allows for more informed, new mechanistic proposals and computational modeling, as the study suggests the Cu_D is the site of methane and oxygen activation. It also encourages synthetic mimics of this Cu_D site, both in single molecule catalysts as well as monocopper binding sites in zeolites or perovskites. Currently no mimics for the site exist.

Of note, the work in **Chapter 3** also highlights the use of advanced paramagnetic spectroscopies in combination with cryoEM. The combination of these techniques allows for a more complete picture of metal active sites, and the methods and results could be applied to more than just pMMO.

Lastly, both pMMO chapters have results supporting current proposals that the Cu_B is not directly involved in the oxidation of methane.[14, 16, 84] While **Chapter 2** continues the work of using ENDOR to

characterize the Cu_B site's electronic structure, as well as establishes the conservation of its properties amongst pMMOs from type I and type II methanotrophs, it offers no direct insight into the role it may perform in pMMO catalysis or downstream metabolism. This site may be involved in electron transfer or may be solely structural, but further study is required to determine its function.

Implications from determining the mechanism of MbnBC

Methanobactin (Mbn) biosynthesis is a complex process that enables bacteria to efficiently scavenge copper from their environment and maintain copper homeostasis. As recent work established the enzyme complex MbnBC as performing the universal step on the Mbn precursor peptide, the understanding of this enzyme's mechanism is therefore the key to understanding Mbn biosynthesis. **Chapter 4** establishes the basis of the Mbn synthesis mechanism by identifying the active form of the MbnBC cofactor as a mixed-valent diiron center through a parallel biochemical and spectroscopic study. After this, ENDOR studies in **Chapter 5** led to the determination of the coordination environments and valency of the individual sites in the active mixed-valent diiron state, as well as establishing the details of MbnA binding. These findings not only advance the knowledge of the chemistry of Mbn biosynthesis, but also advance the community's knowledge of an emerging, but lesser studied, family of diiron enzymes, the mixed-valent diiron oxygenase and oxidase (MVDO) family. These chapters also outline a path to determine the mechanisms of other DUF692 enzymes and homologs. These enzymes are important to study as they teach us more about other steps in methanobactin biosynthesis[26], the biosynthesis of other interesting natural products, [200] and play roles that can impact global health, such as virulence factors.[201]

Oxazolone groups are important in drugs, with their presence shown to have biological activity such as anti-viral,[202] antimicrobial,[203] and anti-inflammatory.[204] Mbn itself has generated interest as a promising therapy for Wilson's disease.[205] It has also been proposed as a method of wastewater remediation, using its properties to remove toxic metals.[206] However, the currently utilized synthetic methods for oxazolone groups involve rare earth metal catalysts, such as samarium and ruthenium,[207] or are performed in halogenated solvents and under conditions of high temperatures,[208] aspects that conjure environmental, energy, and cost concerns. The only present means of obtaining modified Mbns is by purifying the spent media of copper "starved" methanotroph cultures, which comes with its own challenges. The use of MbnBC

as an biocatalyst, which could be bioengineered or implemented in a large-scale fermentation method, or the biomimetic creation of an iron catalyst could allow for better production of molecules with oxazolones, including different Mbns. The identification of the mixed-valent active form and the further elucidation of the molecular and electronic structure of this iron center in solution will provide useful information for future MbnBC-inspired chemical or biological technologies.

Establishing computational modeling of radical SAM enzyme intermediates

There are over 330,000 members of the radical *S*-adenosyl-L-methionine (SAM) super family,[209] all of which implement the same initial mechanism in generating the 5'-dAdo· radical. **Chapter 6** characterizes this important intermediate with density functional theory (DFT) methods, allowing for accurate molecular and electronic structural modeling by benchmarking the calculation against experimental hyperfine values and calculated ones to validate accuracy. The capturing and characterization, both spectroscopically and computationally, of the 5'-dAdo· intermediate was important progress in the field of radical SAM enzymes. Later in **Chapter 6**, the mechanism of how the specific 5'-C bond is cleaved is explored through the aid of DFT. By computing the electronics of the SAM sulfonium, we were able to support proposals that pseudo Jahn-Teller effects play an essential role in the regioselectivity of S-C bond cleavage, again understanding an essential intermediate state of radical SAM enzyme catalysis.[168]..As radical SAM enzymes abstract a hydrogen atom from a substrate as part of the catalysis, the generation of new radical species intermediate will occur. This again will lend itself to study through methods of EPR and ENDOR, as shown in **Chapter 6** with the study of SPL, where protein residue radicals are able to be identified. More so, DFT again lends itself to this study, by modeling and computing the hyperfine couplings of the radicals and allowing the geometry to be determined and the EPR to be well simulated. This will continue to be useful methodology for product radicals and has already been applied to a recent study.[178]

The other established step in the pathway of radical SAM enzyme reactions is the organometallic intermediate, Ω.[32, 33] **Chapter 7** establishes theory and computational methods for the accurate modeling of this intermediate, comparing the results to the experimental hyperfine coupling constants. This is a step forward in the abilities to model Ω, and can be used to to validate furture BS-DFT computations attempting to model the mechanism of the subsequent 5'-dAdo· liberation from Ω **Chapter 7** establishes the ability to

accurately model the synthetic analogue of Ω, M-CH3.[181].Several additional synthetic [4Fe-4S] clusters have since been reported, and their properties, and ENDOR analysis, could be expanded by the outlined 2C-DFT, furthering the field's understanding of these interesting organometallic clusters.

FUTURE WORK

Determining metal loading in the PmoC subunit

As mentioned above, **Chapter 2** presents the first advanced spectroscopic characterization of the second EPR Cu(II) species observed in pMMO. At the time of that study, before cryoEM structures of pMMO revealed a new copper site, only the Cu_C was identified. It therefore was assigned as the center observed in detergent-solubilized pMMO from the EPR and ENDOR data, but this site, which has only been observed in some crystal structures, may not be present in DDM when in aqueous enviornments. It remains an open question of what copper site is occupied in detergent-solubilized pMMO and gives rise to the EPR signal observed for this sample.

Preliminary CryoEM structures of detergent-solubilized pMMO, prepared from the same sample investigated in **Chapter 2**, reveal structural disorder in the Cu_D site region and strong metal-like density within the Cu_C site. If structural evidence persists that a copper-loaded Cu_C is present in detergent solubilized pMMO, and as established in **Chapter 3,** the Cu_D is occupied when pMMO is reconstituted in nanodisc, then further work is required to characterize the Cu_D spectroscopically as was done for the Cu_C site.[84] More important, per the scope of this thesis, would be to obtain spectroscopic evidence of this conditional copper site dichotomy. Also, the ability to discern whether Cu_C or Cu_D is occupied without need of a full cryoEM experiment will aid future work in pMMO, such as testing other purification and reconstitution conditions, and drawing conclusions of metal loading based on activity.

As established by **Chapter 2** and **Chapter 3**, the EPR signals that arise from the Cu_C site and Cu_D site appear identical. This is expected as the direct coordination (2N1O) and relative geometries of the sites are the same. Preliminary ^{15}N Davies ENDOR experiments of nanodisc pMMO shows the directly coordination ^{15}N at the low field edge where the Cu_D/Cu_C signals persist (see **Chapter 2**) is near identical between DDM and NLND pMMO samples (**Figure 7.1**). It is noted that there are some differences in shape of the 15N couplings when comparing the two samples, but it is hard to determine whether it is discerning

between the two different copper sites with the same direct coordination but a slight difference in geometry, the environmental influences from two membrane mimetic conditions.

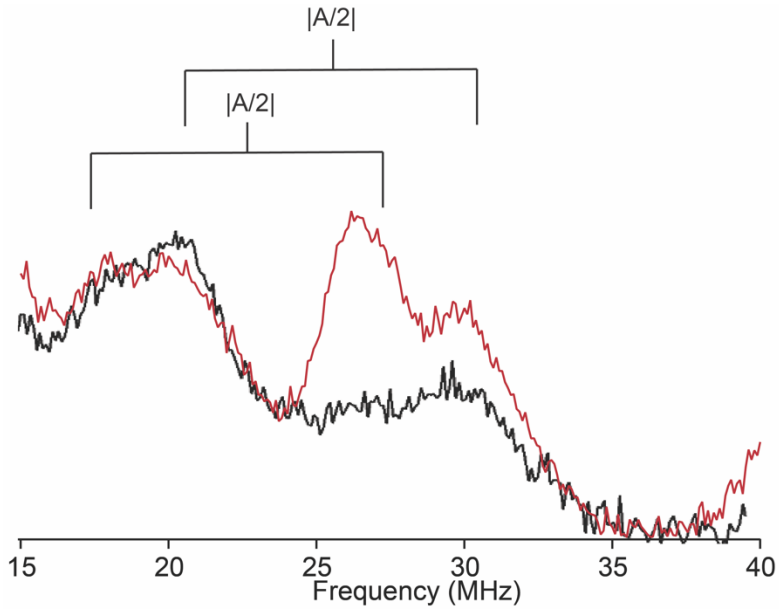

Figure 8.1 ^{15}N Davies ENDOR of Nanodisc pMMO and detergent pMMO. Both nanodisc pMMO (black) and detergent pMMO (red) have ^{15}N couplings of A = -45 and -50 MHz. The ENDOR was taken at g = 2.32 where only the CuD/CuC signals are present to avoid any ^{15}N couplings from Cu_B nitrogen. Conditions: 2K, ~34.6 GHz,100ms repetition time, π=80ns, τ=600ns, TRF=35μs, RF tail = 5 μs, ~100 scans.

It is moore promising to try and discern differences in weakly coupled ^{15}N ENDOR signals. The cryoEM structures of nanodisc pMMO reveal that the Cu_D site features copper that is coordinated by Asn227 through the oxygen atom, with the nitrogen of the asparagine residue is in a hydrogen bonding network. As the Cu_C contains Asp156, there is a difference in a distal nitrogen between the two species. Mims ^{15}N ENDOR, which can resolve weakly coupled ^{15}N, reveals a coupling of ~0.5 MHz at both $g_{||}$ and $g_{\perp}$ in prepared ^{15}N nanodisc pMMO samples. As shown previously,[14, 84] the “backside” nitrogen of the coordinated histidine residues couple copper at ~1-1.5 MHz, so this ~0.5 MHz coupling does not derive from those atoms.

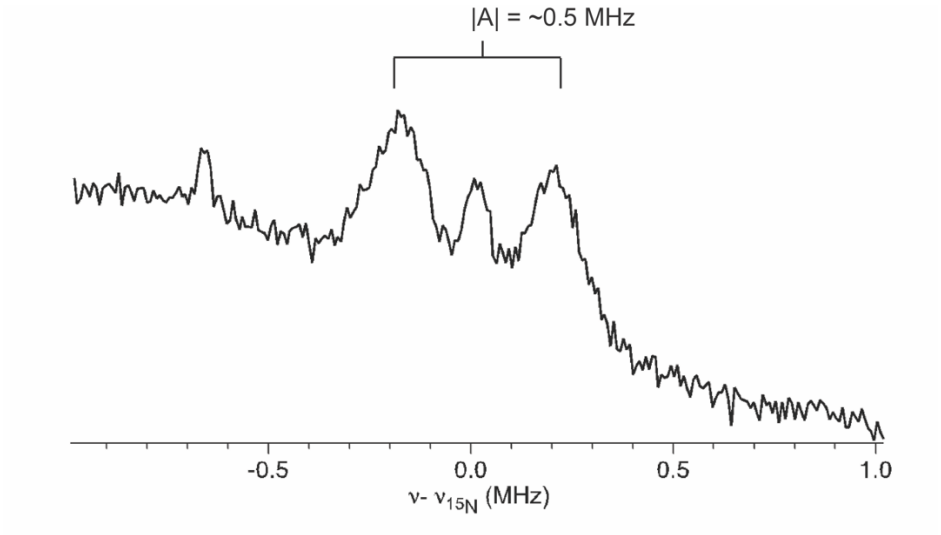

Figure 8.2 ^{15}N Mims ENDOR of Nanodisc pMMO. The ~0.5 MHz ^{15}N coupling is likely the uncoordinated nitrogen of the Cu_D asparagine residue. Conditions: 2 K, microwave frequency 34.7 GHz, π = 100 ns, τ = 750 ns, trf = 35 μs, rf tail = 5 μs, repetition time 100 ms

It is possible this coupling is indeed the uncoordinated nitrogen atom of Asn227 in the Cu_D site. Performing the same experiment in whole cell pMMO as well as DDM pMMO will be conclusive if these signals do not appear. Near the Larmor frequency, there are signals likely from the peptide backbone around the copper centers. It is also worth an examination of ^{1}H ENDOR across the EPR envelope with Cu_B subtraction, as another means of discerning the Cu_C or Cu_D site, as it would be a less expensive way than preparing ^{15}N enriched samples.

Another possible approach to resolving spectroscopically Cu_D and Cu_C is studying pMMO isolated from type III methanotrophic Verrucomicrobia.[49] These pMMOs are desirable for EPR and ENDOR experiments as they do not have the residues in the PmoB subunit to coordinate a Cu_B site, and therefore their EPR spectra should not have interference from Cu_B signals as in the type I and II pMMOs.[85] If conditions could be found where the Cu_D is occupied and observed by cryoEM, and others where the Cu_C is, performing parallel EPR would allow for isolated spectra of each of these metal sites, which may have discernable differences that are currently unobserved due to the overlapping Cu_B signals in the studied pMMOs. However, obtaining pure and concentrated samples for EPR and ENDOR studies has been difficult.

Lastly, double electron-electron resonance (DEER) spectroscopy may be able to discern if Cu_C is present in detergent and Cu_D in nanodiscs. Previous studies utilized Cu(II)-Cu(II) DEER in detergent-

solublilized pMMO, resolving a Cu_C-Cu_C distance of ~4.5 Å that arises due to the protomer arrangement in the trimer complex.[14] Examination of the cryoEM structures of NLND pMMO reveals a Cu_D - Cu_D distance of ~3.5 Å.[16] DEER therefore could support the observed sample copper loading dichotomy hypothesis, and is a method that does not require isotopic enrichment in order to determine which copper is present.

The fact there are two metal sites adjacent to each other is strange, and possibly occupancy of both sites may be required for activity. EPR spectroscopy may again be useful here, as one could observe and resolve low levels of a coupled dicopper site or two adjacent Cu(II) centers. Again, for examining a dicopper or dual loaded PmoC subunit, the type III pMMO as well as DEER have the advantages discussed above. Interestingly, as shown in **Chapter 3**'s study with TFE, if detergent-solubilized pMMO indeed houses a Cu_C site, it likely cannot interact with hydrocarbons, and like the Cu_B site, its role in methane oxidation and methanotrophy remains unknown.

EPR and ENDOR of Ammonia monooxygenase

Ammonia monooxygenase (AMO) is a homolog of pMMO found and expressed in ammonia oxidizing bacteria (AOB).[210] Just like pMMO, AMO has three subunits (AmoA, AmoB, AmoC) with metal binding residues in the AmoB and AmoC subunits, and has been found to be a copper-dependent, membrane-bound enzyme.[211, 212] As with pMMO, EPR and ENDOR spectroscopy could help elucidate enzyme's copper sites structure, which is not only of interest due to AMOs impact on the nitrogen cycle, but also because it enriches understanding of pMMO in parallel. However, AMO has remained largely unstudied due to the difficulty in growing the AOB and obtaining pure and active samples in vitro for characterization.

Recent efforts in the Rosenzweig lab have produced solubilized and nanodisc-reconstituted AMO samples for further study, utilizing methods described previously[16] and in **Chapter 3**. To begin, X-band EPR spectra of AMO in nanodisc exhibit signals attributable to two type 2 Cu(II) centers, with g-values and ^{63}Cu $A_{||}$ splittings for both sites that in exact agreement with pMMO Cu_B and $Cu_C/_D$ site (**Figure 8.2**) parameters.[84] The nanodisc reconstituted AMO exhibits less of the secondary (Cu_C/Cu_D) EPR signal, however.

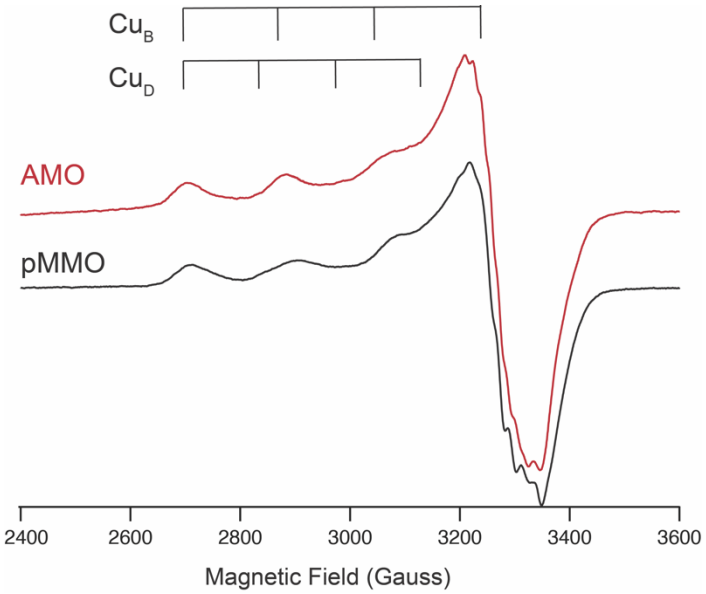

Figure 8.3 X-band EPR of nanodisc AMO. The EPR spectrum of nanodisc AMO is compared to one of nanodisc pMMO, with the assignment of the two Cu(II) species based on pMMO. The AMO spectrum exhibits much lower intensity in the Cu_D signals compared to pMMO. Conditons: 9.37 GHz, 30 K, 160μW MW power, 12.5 G Modulation, 320 ms time constant, 10G/s scan, 10 scans averaged.

signals compared to nanodisc pMMO, as evident by the $A_{||}$ hyperfine intensity (**Figure 8.2**). This lack of signal could either be lack of metal loading or oxidation of the site, and without spin quantification, it is unknown. From this initial result, we can assume that there are copper centers in the AmoB and AmoC subunits, like pMMO, and likely an occupied Cu_B and Cu_D site. The preliminary Davies ^{14}N and ^{1}H ENDOR support this, with maybe slight differences in Cu_B ^{1}H couplings (**Figure 8.3**). This difference in the ^{1}H ENDOR suggest a difference in solvation of the Cu_B site (lack of a ~10 MHz coupling at $g_{||}$), and not in amino acid coordination. The identical ^{14}N couplings are a promising sign that the sites in the two enzymes are identical. However, further study and more resolved spectra are required for more conclusive results. The ability to compare EPR and ENDOR data to cryoEM structures will also be beneficial to understanding AMO and will advances the copper monooxygenase field.

AMO could also be used validate and expand the results of **Chapter 3**, using another enzyme to probe substrate binding at a copper site. Addition of ^{15}N NH_3 to AMO would allow for direct detection by ENDOR if the substrate interacts with the observed Cu(II) centers (**Figure 8.2**). ^{15}N is an easily detected nucleus by ENDOR methods, and this experiment would allow detection of the true substrate, advancing the work that was done with pMMO in **Chapter 3**.

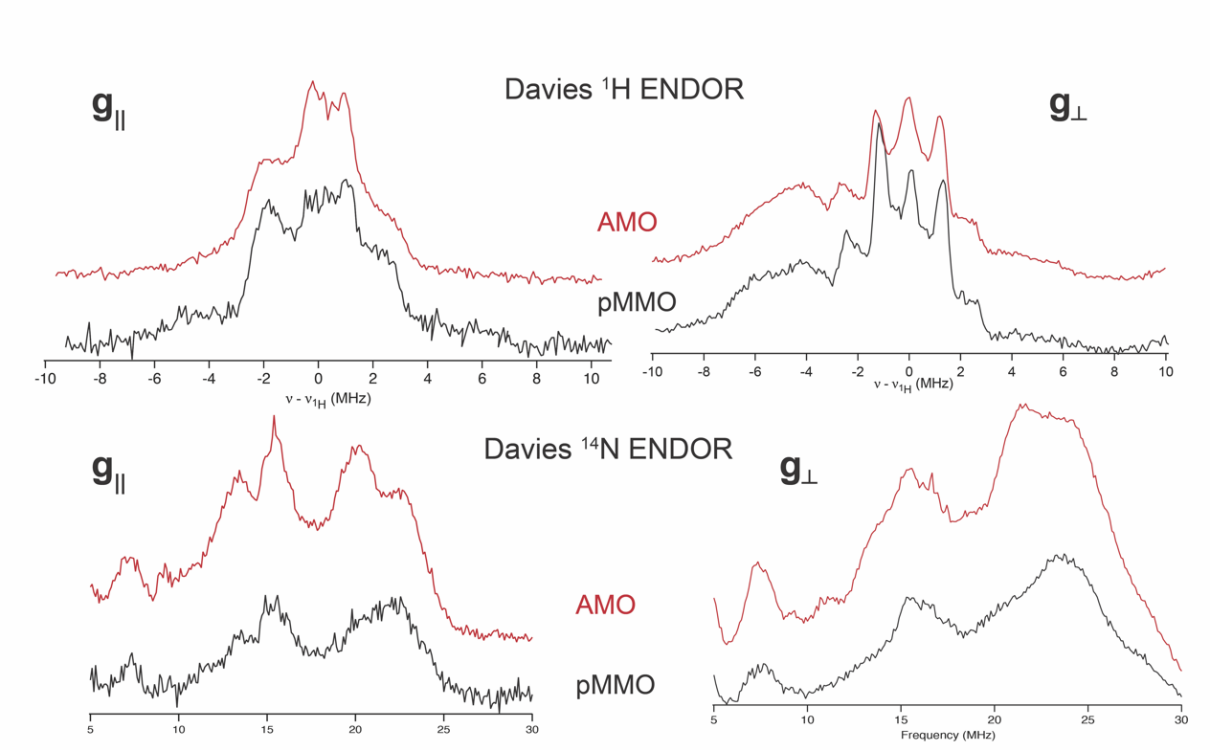

Figure 8.4 Q-band Davies ^{1}H and ^{14}N ENDOR of Nanodisc AMO. The ^{1}H ENDOR at both $g_{||}$ and $g_{\perp}$ appears near identical to the ENDOR for ^{14}N nanodisc pMMO samples. The main difference appears to be a lack of the ~10 MHz ^{1}H coupling at $g_{||}$ in AMO samples. The ^{14}N ENDOR appears identical between the samples at both field positions.

REFERENCES

(1) Bertini, I.; Gray, H. B.; Lippard, S. J.; Valentine, J. S. *Bioinorganic chemistry*; University science books, 1994.
(2) Lippard, S. J.; Berg, J. M. *Principles of Bioinorganic Chemistry*; University Science Books, 1994.
(3) Groves, J. T. High-valent iron in chemical and biological oxidations. *Journal of inorganic biochemistry* **2006**, *100* (4), 434-447.
(4) Valdez, C. E.; Smith, Q. A.; Nechay, M. R.; Alexandrova, A. N. Mysteries of Metals in Metalloenzymes. *Accounts of Chemical Research* **2014**, *47* (10), 3110-3117.
(5) Solomon, E. I.; Brunold, T. C.; Davis, M. I.; Kemsley, J. N.; Lee, S.-K.; Lehnert, N.; Neese, F.; Skulan, A. J.; Yang, Y.-S.; Zhou, J. Geometric and Electronic Structure/Function Correlations in Non-Heme Iron Enzymes. *Chemical Reviews* **2000**, *100* (1), 235-349.
(6) Hoffman, B. M. ENDOR of Metalloenzymes. *Accounts of Chemical Research* **2003**, *36* (7), 522-529.
(7) Abragam, A.; Bleaney, B. *Electron Paramagnetic Resonance of Transition Ions*; Dover Publications, Inc., 1986.
(8) Schweiger, A. Electron Nuclear Double Resonance of Transition Metal Complexes with Organic Ligands. In *Structure and Bonding*, Clarke, M. J., Goodenough, J. B., Hemmerich, P., Ibers, J. A., Jorgenson, C. K., Neilands, J. B., Reinen, D., Weiss, R., Williams, R. J. P. Eds.; Transition Metal Complexes, Vol. 51; Springer-Verlag, 1982; pp 1-121.
(9) Hoffman, B. M. Electron nuclear double resonance (ENDOR) of metalloenzymes. *Accounts of Chemical Research* **1991**, *24*, 164-170.
(10) Telser, J.; Ross, M. O.; Doan, P. E.; Cutsail III, G. E.; Lees, N. S.; Hoffman, B. M. Advanced Paramagnetic Resonance of Iron-Sulfur Proteins and Enzymes. In 18th International Conference on Biological Inorganic Chemistry (ICBIC-18), Florianopolis, SC, Brazil 2017.
(11) Schweiger, A.; Jeschke, G. *Principles of Pulse Electron Paramagnetic Resonance*; Oxford University Press, 2001.
(12) Ross, M. O.; Rosenzweig, A. C. A tale of two methane monooxygenases. *J. Biol. Inorg. Chem.* **2017**, *22* (2-3), 307-319.
(13) Lieberman, R. L.; Rosenzweig, A. C. Crystal structure of a membrane-bound metalloenzyme that catalyses the biological oxidation of methane. *Nature* **2005**, *434*, 177-182.
(14) Ross, M. O.; MacMillan, F.; Wang, J.; Nisthal, A.; Lawton, T. J.; Olafson, B. D.; Mayo, S. L.; Rosenzweig, A. C.; Hoffman, B. M. Particulate methane monooxygenase contains only mononuclear copper centers. *Science* **2019**, *364* (6440), 566-570.
(15) Ro, S. Y.; Schachner, L. F.; Koo, C. W.; Purohit, R.; Remis, J. P.; Kenney, G. E.; Liauw, B. W.; Thomas, P. M.; Patrie, S. M.; Kelleher, N. L.; Rosenzweig, A. C. Native top-down mass spectrometry provides insights into the copper centers of membrane-bound methane monooxygenase. *Nature Communications* **2019**, *10* (1), 2675.
(16) Koo, C. W.; Tucci, F. J.; He, Y.; Rosenzweig, A. C. Recovery of particulate methane monooxygenase activity in a lipid bilayer. *Science* **2022**, *375*, 1287-1291.
(17) Walsh, C. T.; Tang, Y. *Natural product biosynthesis*; Royal Society of Chemistry, 2017.
(18) Li, C.; Zhang, R.; Wang, J.; Wilson, L. M.; Yan, Y. Protein Engineering for Improving and Diversifying Natural Product Biosynthesis. *Trends in Biotechnology* **2020**, *38* (7), 729-744.
(19) Kao, W.-C.; Chen, Y.-R.; Eugene, C. Y.; Lee, H.; Tian, Q.; Wu, K.-M.; Tsai, S.-F.; Yu, S. S.-F.; Chen, Y.-J.; Aebersold, R. Quantitative Proteomic Analysis of Metabolic Regulation by Copper Ions in Methylococcus capsulatus (Bath). *Journal of biological chemistry* **2004**, *279* (49), 51554-51560.
(20) Kim, H. J.; Graham, D. W.; DiSpirito, A. A.; Alterman, M. A.; Galeva, N.; Larive, C. K.; Asunskis, D.; Sherwood, P. M. A. Methanobactin, a copper-acquisition compound from methane oxidizing bacteria. *Science* **2004**, *305*, 1612-1615.
(21) DiSpirito, A. A.; Zahn, J. A.; Graham, D. W.; Kim, H. J.; Larive, C. K.; Derrick, T. S.; Cox, C. D.; Taylor, A. Copper-binding compounds from Methylosinus trichosporium OB3b. *Journal of bacteriology* **1998**, *180* (14), 3606-3613.

(22) Behling, L. A.; Hartsel, S. C.; Lewis, D. E.; Dispirito, A. A.; Choi, D. W.; Masterson, L. R.; Veglia, G.; Gallagher, W. H. NMR, mass spectrometry and chemical evidence reveal a different chemical structure for methanobactin that contains oxazolone rings. *J. Am. Chem. Soc.* **2008**, *130*, 12604-12605.
(23) Hakemian, A. S.; Tinberg, C. E.; Kondapalli, K. C.; Telser, J.; Hoffman, B. M.; Stemmler, T. L.; Rosenzweig, A. C. The Copper Chelator Methanobactin from Methylosinus trichosporium OB3b Binds Copper(I). *Journal of the American Chemical Society* **2005**, *127* (49), 17142-17143.
(24) Kenney, G. E.; Goering, A. W.; Ross, M. O.; DeHart, C. J.; Thomas, P. M.; Hoffman, B. M.; Kelleher, N. L.; Rosenzweig, A. C. Characterization of Methanobactin from Methylosinus sp. LW4. *J Am Chem Soc* **2016**, *138* (35), 11124-11127.
(25) Kenney, G. E.; Rosenzweig, A. C. Genome mining for methanobactins. *BMC Biology* **2013**, *11* (1), 17.
(26) Dassama, L. M.; Kenney, G. E.; Rosenzweig, A. C. Methanobactins: from genome to function. *Metallomics* **2017**, *9* (1), 7-20.
(27) Kenney, G. E.; Dassama, L. M. K.; Pandelia, M.-E.; Gizzi, A. S.; Martinie, R. J.; Gao, P.; DeHart, C. J.; Schachner, L. F.; Skinner, O. S.; Ro, S. Y.; Zhu, X.; Sadek, M.; Thomas, P. M.; Almo, S. C.; Bollinger, J. M.; Krebs, C.; Kelleher, N. L.; Rosenzweig, A. C. The biosynthesis of methanobactin. *Science* **2018**, *359* (6382), 1411-1416.
(28) Broderick, J. B.; Broderick, W. E.; Hoffman, B. M. Radical SAM enzymes: Nature's choice for radical reactions. *FEBS Letters* **2023**, *597* (1), 92-101.
(29) Booker, S. J. Radical SAM enzymes and radical enzymology. *Biochim. Biophys. Acta, Proteins Proteomics* **2012**, *1824* (Copyright (C) 2012 American Chemical Society (ACS). All Rights Reserved.), 1151-1153, 10.1016/j.bbapap.2012.07.006.
(30) Ghosh, S.; Marsh, E. N. G. Viperin: An ancient radical SAM enzyme finds its place in modern cellular metabolism and innate immunity. *Journal of Biological Chemistry* **2020**, *295* (33), 11513-11528.
(31) Benjdia, A.; Balty, C.; Berteau, O. Radical SAM enzymes in the biosynthesis of ribosomally synthesized and post-translationally modified peptides (RiPPs). *Frontiers in Chemistry* **2017**, *5*, 87.
(32) Horitani, M.; Shisler, K.; Broderick, W. E.; Hutcheson, R. U.; Duschene, K. S.; Marts, A. R.; Hoffman, B. M.; Broderick, J. B. Radical SAM catalysis via an organometallic intermediate with an Fe-[5'-C]-deoxyadenosyl bond. *Science* **2016**, *352* (6287), 822-825.
(33) Byer, A. S.; Yang, H.; McDaniel, E. C.; Kathiresan, V.; Impano, S.; Pagnier, A.; Watts, H.; Denler, C.; Vagstad, A. L.; Piel, J.; Duschene, K. S.; Shepard, E. M.; Shields, T. P.; Scott, L. G.; Lilla, E. A.; Yokoyama, K.; Broderick, W. E.; Hoffman, B. M.; Broderick, J. B. Paradigm Shift for Radical S-Adenosyl-l-methionine Reactions: The Organometallic Intermediate Omega Is Central to Catalysis. *J Am Chem Soc* **2018**, *140* (28), 8634-8638.
(34) Orio, M.; Pantazis, D. A.; Neese, F. Density functional theory. *Photosynthesis Research* **2009**, *102* (2), 443-453.
(35) Hioe, J.; Mosch, M.; Smith, D. M.; Zipse, H. Dissociation energies of Cα-H bonds in amino acids - a re-examination. *RSC Adv.* **2013**, *3* (30), 12403-12408.
(36) Ipsen, J. Ø.; Hallas-Møller, M.; Brander, S.; Lo Leggio, L.; Johansen, K. S. Lytic polysaccharide monooxygenases and other histidine-brace copper proteins: structure, oxygen activation and biotechnological applications. *Biochemical Society Transactions* **2021**, *49* (1), 531-540.
(37) Koo, C. W.; Rosenzweig, A. C. Biochemistry of aerobic biological methane oxidation. *Chemical Society reviews* **2021**, *50* (5), 3424-3436.
(38) Klinman, J. P. The copper-enzyme family of dopamine beta-monooxygenase and peptidylglycine alpha-hydroxylating monooxygenase: resolving the chemical pathway for substrate hydroxylation. *J Biol Chem* **2006**, *281* (6), 3013-3016.
(39) Eipper, B. A.; Quon, A. S.; Mains, R. E.; Boswell, J. S.; Blackburn, N. J. The catalytic core of peptidylglycine alpha-hydroxylating monooxygenase: investigation by site-directed mutagenesis, Cu X-ray absorption spectroscopy, and electron paramagnetic resonance. *Biochemistry* **1995**, *34* (9), 2857-2865.
(40) Quist, D. A.; Diaz, D. E.; Liu, J. J.; Karlin, K. D. Activation of dioxygen by copper metalloproteins and insights from model complexes. *J Biol Inorg Chem* **2017**, *22* (2-3), 253-288.
(41) Que, E. L.; Duncan, F. E.; Lee, H. C.; Hornick, J. E.; Vogt, S.; Fissore, R. A.; O'Halloran, T. V.; Woodruff, T. K. Bovine eggs release zinc in response to parthenogenetic and sperm-induced egg activation. *Theriogenology* **2019**, *127*, 41-48, 10.1016/j.theriogenology.2018.12.031.
(42) Buckel, W.; Thauer, R. K. Flavin-Based Electron Bifurcation, Ferredoxin, Flavodoxin, and Anaerobic Respiration With Protons (Ech) or NAD+ (Rnf) as Electron Acceptors: A Historical Review. *Frontiers in Microbiology* **2018**, *9* (401), Review.

(43) Lawton, T. J.; Rosenzweig, A. C. Methane-Oxidizing Enzymes: An Upstream Problem in Biological Gas-to-Liquids Conversion. *J. Am. Chem. Soc.* **2016**, *138* (30), 9327-9340.
(44) Smith, S. M.; Balasubramanian, R.; Rosenzweig, A. C. Metal reconstitution of particulate methane monooxygenase and heterologous expression of the pmoB subunit. *Methods Enzymol.* **2011**, *495*, 195-210.
(45) Sirajuddin, S.; Barupala, D.; Helling, S.; Marcus, K.; Stemmler, T. L.; Rosenzweig, A. C. Effects of zinc on particulate methane monooxygenase activity and structure. *J. Biol. Chem.* **2014**, *289* (31), 21782-21794.
(46) Ro, S. Y.; Ross, M. O.; Deng, Y. W.; Batelu, S.; Lawton, T. J.; Hurley, J. D.; Stemmler, T. L.; Hoffman, B. M.; Rosenzweig, A. C. From micelles to bicelles: Effect of the membrane on particulate methane monooxygenase activity. *J Biol Chem* **2018**, *293* (27), 10457-10465.
(47) Cao, L.; Caldararu, O.; Rosenzweig, A. C.; Ryde, U. Quantum refinement does not support dinuclear copper sites in crystal structures of particulate methane monooxygenase. *Angewandte Chemie (International ed. in English)* **2018**, *130* (1), 168-172.
(48) Cutsail, G. E., 3rd; Ross, M. O.; Rosenzweig, A. C.; DeBeer, S. Towards a unified understanding of the copper sites in particulate methane monooxygenase: an X-ray absorption spectroscopic investigation. *Chem Sci* **2021**, *12* (17), 6194-6209
(49) Koo, C. W.; Rosenzweig, A. C. Particulate methane monooxygenase and the PmoD protein. In *Encylopedia of Inorganic and Bioinorganic Chemistry*, Vol. DOI: 10.1002/9781119951438.eibc2740; John Wiley & Sons, Ltd., **2020**.
(50) Culpepper, M. A.; Cutsail, G. E., 3rd; Gunderson, W. A.; Hoffman, B. M.; Rosenzweig, A. C. Identification of the valence and coordination environment of the particulate methane monooxygenase copper centers by advanced EPR characterization. *J. Am. Chem. Soc.* **2014**, *136* (33), 11767-11775.
(51) Semrau, J. D.; DiSpirito, A. A.; Yoon, S. Methanotrophs and copper. *FEMS Microbiology Reviews* **2010**, *34* (4), 496-531.
(52) Hakemian, A.; Kondapalli, K.; Telser, J.; Hoffman, B.; Stemmler, T.; Rosenzweig, A. The Metal Centers of Particulate Methane Monooxygenase from *Methylosinus trichosporium* OB3b. *Biochemistry* **2008**, *47* (26), 6793-6801.
(53) Smith, S. M.; Rawat, S.; Telser, J.; Hoffman, B. M.; Stemmler, T. L.; Rosenzweig, A. C. Crystal structure and characterization of particulate methane monooxygenase from *Methylocystis* species strain M. *Biochemistry* **2011**, *50* (47), 10231-10240.
(54) Yuan, H.; Collins, M. L. P.; Antholine, W. E. Low-frequency EPR of the copper in particulate methane monooxygenase from Methylomicrobium albus BG8. *Journal of the American Chemical Society* **1997**, *119* (21), 5073-5074.
(55) Lemos, S. S.; Collins, M. L. P.; Eaton, S. S.; Eaton, G. R.; Antholine, W. E. Comparison of EPR-visible Cu^{2+} sites in pMMO from *Methylococcus capsulatus* (Bath) and *Methlyomicrobium album* BG8. *Biophys. J.* **2000**, *79*, 1085-1094.
(56) Peng, W.; Qu, X.; Shaik, S.; Wang, B. Deciphering the oxygen activation mechanism at the CuC site of particulate methane monooxygenase. *Nature Catalysis* **2021**, *4* (4), 266-273.
(57) Peisach, J.; Blumberg, W. E. Structural implications derived from the analysis of electron paramagnetic resonance spectra of natural and artificial copper proteins. *Arch. Biochem. Biophys.* **1974**, *165*, 691-708.
(58) Pogni, R.; Baratto, M. C.; Diaz, A.; Basosi, R. EPR characterization of mono(thiosemicarbazones) copper(II) complexes. Note II. *J. Inorg. Biochem.* **2000**, *79* (1-4), 333-337.
(59) Doan, P. E.; Hoffman, B. M. Making hyperfine selection in Mims ENDOR independent of deadtime. *Chemical Physics Letters* **1997**, *269* (3-4), 208-214.
(60) Chang, W.-H.; Lin, H.-H.; Tsai, I.-K.; Huang, S.-H.; Chung, S.-C.; Tu, I.-P.; Yu, S. S.-F.; Chan, S. I. Copper centers in the cryo-EM Structure of particulate methane monooxygenase reveal the catalytic machinery of methane oxidation. *J. Am. Chem. Soc.* **2021**,
(61) Atherton, N. M.; Horsewill, A. J. Proton ENDOR of $Cu(H2O)_6^{2+}$ in $Mg(NH_4)_2(SO_2)$ *Mol. Phys.* **1979**, *37* (5), 1349-1361,
(62) Burns, C. S.; Aronoff-Spencer, E.; Dunham, C. M.; Lario, P.; Avdievich, N. I.; Antholine, W. E.; Olmstead, M. M.; Vrielink, A.; Gerfen, G. J.; Peisach, J.; Scott, W. G.; Millhauser, G. L. Molecular features of the copper binding sites in the octarepeat domain of the prion protein. *Biochemistry* **2002**, *41* (Copyright (C) 2013 American Chemical Society (ACS). All Rights Reserved.), 3991-4001, 1
(63) Kim, D.; Kim, N. H.; Kim, S. H. 34 GHz pulsed ENDOR characterization of the copper coordination of an amyloid β peptide relevant to Alzheimer's disease. *Angewandte Chemie (International ed. in English)* **2013**, *52* (4), 1139-1142.

(64) Fujimoto, M.; McDowell, C. A.; Takui, T. Ligand ENDOR spectra of Cu(II) impurity complexes in α-glycine crystals. *J. Chem. Phys.* **1979**, *70*, 3694-3701.
(65) Rist, G. H.; Hyde, J. S. Ligand ENDOR of Metal Complexes in Powders. *Journal of Chemical Physics* **1970**, *52* (9), 4633-4643.
(66) Manikandan, P.; Epel, B.; Goldfarb, D. Structure of copper(II)-histidine based complexes in frozen aqueous solutions as determined from high-field pulsed electron nuclear double resonance. *Inorg. Chem.* **2001**, *40* (4), 781-787.
(67) VanCamp, H. L.; Sands, R. H.; Fee, J. A. Electron-nuclear double resonance on copper (II) tetraimidazole. *Journal of Chemical Physics* **1981**, *75* (5), 2098-2107.
(68) Denisov, I. G.; Grinkova, Y. V.; Lazarides, A. A.; Sligar, S. G. Directed self-assembly of monodisperse phospholipid bilayer nanodiscs with controlled size. *J. Am. Chem. Soc.* **2004**, *126* (11), 3477-3487.
(69) Stoll, S.; Schweiger, A. EasySpin, a comprehensive software package for spectral simulation and analysis in EPR. *J Magn Reson* **2006**, *178* (1), 42-55.
(70) Davoust, C. E.; Doan, P. E.; Hoffman, B. M. Q-band pulsed electron spin-echo spectrometer and its application to ENDOR and ESEEM. *Journal of Magnetic Resonance Series A* **1996**, *119* (1), 38-44.
(71) Epel, B.; Gromov, I.; Stoll, S.; Schweiger, A.; Goldfarb, D. Spectrometer manager: A versatile control software for pulse EPR spectrometers. *Concepts in Magnetic Resonance Part B-Magnetic Resonance Engineering* **2005**, *26b* (1), 36-45.
(72) Werst, M. M.; Davoust, C. E.; Hoffman, B. M. Ligand spin densities in blue copper proteins by Q-band ^{1}H and ^{14}N ENDOR spectroscopy. *Journal of the American Chemical Society* **1991**, *113* (5), 1533-1538.
(73) Bruggemann, W.; Niklas, J. R. Stochastic Endor. *J. Magn. Reson., Ser. A* **1994**, *108* (1), 25-29.
(74) Doan, P. E. Combining steady-state and dynamic methods for determining absolute signs of hyperfine interactions: Pulsed ENDOR Saturation and Recovery (PESTRE). *Journal of Magnetic Resonance* **2011**, *208* (1), 76-86, doi: DOI: 10.1016/j.jmr.2010.10.008.
(75) Arndtsen, B. A.; Bergman, R. G.; Mobley, T. A.; Peterson, T. H. Selective intermolecular carbon-hydrogen bond activation by synthetic metal complexes in homogeneous solution. *Acc. Chem. Res.* **1995**, *28* (3), 154-162.
(76) Blanksby, S. J.; Ellison, G. B. Bond dissociation energies of organic molecules. *Acc. Chem. Res.* **2003**, *36* (4), 255-263.
(77) Tang, P.; Zhu, Q. J.; Wu, Z. X.; Ma, D. Methane activation: the past and future. *Energy Environ. Sci.* **2014**, *7* (8), 2580-2591.
(78) Haynes, C. A.; Gonzalez, R. Rethinking biological activation of methane and conversion to liquid fuels. *Nature chemical biology* **2014**, *10* (5), 331-339, Article.
(79) Ravi, M.; Ranocchiari, M.; van Bokhoven, J. A. The direct catalytic oxidation of methane to methanol-a critical assessment. *Angewandte Chemie (International ed. in English)* **2017**, *56* (52), 16464-16483.
(80) Dummer, N. F.; Willock, D. J.; He, Q.; Howard, M. J.; Lewis, R. J.; Qi, G. D.; Taylor, S. H.; Xu, J.; Bethell, D.; Kiely, C. J.; Hutchings, G. J. Methane oxidation to methanol. *Chem. Rev.*
(81) Hanson, R. S.; Hanson, T. E. Methanotrophic bacteria. *Microbiol Rev* **1996**, *60* (Copyright (C) 2012 U.S. National Library of Medicine.), 439-471.
(82) Banerjee, R.; Jones, J. C.; Lipscomb, J. D. Soluble methane monooxygenase. *Annual review of biochemistry* **2019**, *88*, 409-431.
(83) Prior, S. D.; Dalton, H. The effect of copper ions on membrane content and methane monooxygenase activity in methanol-grown cells of *Methylococcus capsulatus* (Bath). *J. Gen. Microbiol.* **1985**, *131*, 155-163.
(84) Jodts, R. J.; Ross, M. O.; Koo, C. W.; Doan, P. E.; Rosenzweig, A. C.; Hoffman, B. M. Coordination of the Copper Centers in Particulate Methane Monooxygenase: Comparison between Methanotrophs and Characterization of the CuC Site by EPR and ENDOR Spectroscopies. *J Am Chem Soc* **2021**, *143* (37), 15358-15368.
(85) Op den Camp, H. J.; Islam, T.; Stott, M. B.; Harhangi, H. R.; Hynes, A.; Schouten, S.; Jetten, M. S. M.; Birkeland, N.-K.; Pol, A.; Dunfield, P. F. Environmental, genomic and taxonomic perspectives on methanotrophic Verrucomicrobia. *Environ. Microbiol. Rep.* **2009**, *1*, 293-306.
(86) Kruse, T.; Ratnadevi, C. M.; Erikstad, H. A.; Birkeland, N. K. Complete genome sequence analysis of the thermoacidophilic verrucomicrobial methanotroph "*Candidatus* Methylacidiphilum kamchatkense" strain Kam1 and comparison with its closest relatives. *BMC genomics* **2019**, *20* (1), 642.

(87) Hakemian, A. S.; Kondapalli, K. C.; Telser, J.; Hoffman, B. M.; Stemmler, T. L.; Rosenzweig, A. C. The metal centers of particulate methane monooxygenase from *Methylosinus trichosporium* OB3b. *Biochemistry* **2008**, *47*, 6793-6801.
(88) Sirajuddin, S.; Barupala, D.; Helling, S.; Marcus, K.; Stemmler, T. L.; Rosenzweig, A. C. Effects of Zinc on Particulate Methane Monooxygenase Activity and Structure*. *Journal of Biological Chemistry* **2014**, *289* (31), 21782-21794.
(89) Griese, J. J.; Högbom, M. Location-specific quantification of protein-bound metal ions by X-ray anomalous dispersion: Q-XAD. *Acta crystallographica. Section D, Structural biology* **2019**, *75* (Pt 8), 764-771.
(90) Yu, S. S.-F.; Chen, K. H.-C.; Tseng, M. Y.-H.; Wang, Y.-S.; Tseng, C.-F.; Chen, Y.-J.; Huang, D. S.; Chan, S. I. Production of high-quality particulate methane monooxygenase in high yields from *Methylococcus capsulatus* (Bath) with a hollow-fiber membrane bioreactor. *J. Bacteriol.* **2003**, *185* (20), 5915-5924.
(91) Davydov, R.; Valentine, A. M.; Komar-Panicucci, S.; Hoffman, B. M.; Lippard, S. J. An EPR Study of the Dinuclear Iron Site in the Soluble Methane Monooxygenase from *Methylococcus capsulatus* (Bath) Reduced by One Electron at 77K: The Effects of Component Interactions and the Binding of Small Molecules to the Diiron(III) Center. *Biochemistry* **1999**, *38*, 4188-4197.
(92) Smoukov, S. K.; Kopp, D. A.; Valentine, A. M.; Davydov, R.; Lippard, S. J.; Hoffman, B. M. Product Binding to the Diiron(III) and Mixed-Valence Diiron Centers of Methane Monooxygenase Hydroxylase Studied by ^{1,2}H and ^{19}F ENDOR Spectroscopy. *J. Am. Chem. Soc.* **2002**, *124* (11), 2657-2663.
(93) Smith, D. D. S.; Dalton, H. Solubilisation of methane monooxygenase from *Methylococcus capsulatus* (Bath). *Eur. J. Biochem.* **1989**, *182*, 667-671.
(94) Furuto, T.; Takeguchi, M.; Okura, I. Semicontinuous methanol biosynthesis by Methylosinus trichosporium OB3b. *Journal of Molecular Catalysis a-Chemical* **1999**, *144* (2), 257-261.
(95) Wieczorek, A. S.; Drake, H. L.; Kolb, S. Organic acids and ethanol inhibit the oxidation of methane by mire methanotrophs. *FEMS Microbiol. Ecol.* **2011**, *77* (1), 28-39.
(96) Mims, W. B. Pulsed endor experiments. *Proceedings of the Royal Society of London* **1965**, *283*, 452-457.
(97) Grupp, A.; Mehring, M. Pulsed ENDOR Spectroscopy in Solids. In *Modern Pulsed and Continuous-Wave Electron Spin Resonance*, Kevan, L., Bowman, M. K. Eds.; John Wiley & Sons, 1990; pp 195-229.
(98) Doan, P. E.; Lees, N. S.; Shanmugam, M.; Hoffman, B. M. Simulating Suppression Effects in Pulsed ENDOR, and the 'Hole in the Middle' of Mims and Davies ENDOR Spectra. *Applied Magnetic Resonance* **2010**, *37* (1-4), 763-779.
(99) Erlandsen, H.; Flatmark, T.; Stevens, R. C.; Hough, E. Crystallographic analysis of the human phenylalanine hydroxylase catalytic domain with bound catechol inhibitors at 2.0 A resolution. *Biochemistry* **1998**, *37* (45), 15638-15646.
(100) Goldfeder, M.; Kanteev, M.; Isaschar-Ovdat, S.; Adir, N.; Fishman, A. Determination of tyrosinase substrate-binding modes reveals mechanistic differences between type-3 copper proteins. *Nat. Commun.* **2014**, *5*, 4505.
(101) Houseman, A. L.; Oh, B. H.; Kennedy, M. C.; Fan, C.; Werst, M. M.; Beinert, H.; Markley, J. L.; Hoffman, B. M. ^{14,15}N, ^{13}C, ^{57}Fe, and ^{1,2}H Q-band ENDOR study of Fe-S proteins with clusters that have endogenous sulfur ligands. *Biochemistry* **1992**, *31* (7), 2073-2080.
(102) Burrows, K. J.; Cornish, A.; Scott, D.; Higgins, I. J. Substrate specificities of the soluble and particulate methane monooxygenases of *Methylosinus trichosporium* OB3b. *J. Gen. Microbiol.* **1984**, *130*, 327-3333.
(103) Bligh, E. G.; Dyer, W. J. A rapid method of total lipid extraction and purification. *Can. J. Biochem. Physiol.* **1959**, *37* (8), 911-917.
(104) Fang, J. S.; Findlay, R. H. The use of a classic lipid extraction method for simultaneous recovery of organic pollutants and microbial lipids from sediments. *Journal of Microbiological Methods* **1996**, *27* (1), 63-71.
(105) Bayburt, T. H.; Sligar, S. G. Membrane protein assembly into nanodiscs. *FEBS Lett.* **2010**, *584* (9), 1721-1727, Review.
(106) Doan, P. E.; Telser, J.; Barney, B. M.; Igarashi, R. Y.; Dean, D. R.; Seefeldt, L. C.; Hoffman, B. M. ^{57}Fe ENDOR Spectroscopy and 'Electron Inventory' Analysis of the Nitrogenase E4 Intermediate Suggest the Metal-Ion Core of FeMo-cofactor Cycles Through Only One Redox Couple. *Journal of the American Chemical Society* **2011**, *133* (43), 17329–17340.

(107) Hoffman, B. M.; Martinsen, J.; Venters, R. A. General-Theory of Polycrystalline Endor Patterns - g and Hyperfine Tensors of Arbitrary Symmetry and Relative Orientation. *Journal of Magnetic Resonance* **1984**, *59* (1), 110-123.
(108) Punjani, A.; Rubinstein, J. L.; Fleet, D. J.; Brubaker, M. A. cryoSPARC: algorithms for rapid unsupervised cryo-EM structure determination. *Nature methods* **2017**, *14* (3), 290-296.
(109) Zheng, S. Q.; Palovcak, E.; Armache, J. P.; Verba, K. A.; Cheng, Y.; Agard, D. A. MotionCor2: anisotropic correction of beam-induced motion for improved cryo-electron microscopy. *Nature methods* **2017**, *14* (4), 331-332.
(110) Rohou, A.; Grigorieff, N. CTFFIND4: Fast and accurate defocus estimation from electron micrographs. *Journal of structural biology* **2015**, *192* (2), 216-221.
(111) Zhang, K. Gctf: Real-time CTF determination and correction. *Journal of structural biology* **2016**, *193* (1), 1-12.
(112) Punjani, A.; Zhang, H.; Fleet, D. J. Non-uniform refinement: adaptive regularization improves single-particle cryo-EM reconstruction. *Nature methods* **2020**, *17* (12), 1214-1221.
(113) Rubinstein, J. L.; Brubaker, M. A. Alignment of cryo-EM movies of individual particles by optimization of image translations. *Journal of structural biology* **2015**, *192* (2), 188-195.
(114) Sanchez-Garcia, R.; Gomez-Blanco, J.; Cuervo, A.; Carazo, J. M.; Sorzano, C. O. S.; Vargas, J. DeepEMhancer: a deep learning solution for cryo-EM volume post-processing. *Communications biology* **2021**, *4* (1), 874.
(115) Scheres, S. H.; Chen, S. Prevention of overfitting in cryo-EM structure determination. *Nature methods* **2012**, *9* (9), 853-854.
(116) Müller, J. C.; Lichtmannegger, J.; Zischka, H.; Sperling, M.; Karst, U. High spatial resolution LA-ICP-MS demonstrates massive liver copper depletion in Wilson disease rats upon Methanobactin treatment. *Journal of trace elements in medicine and biology : organ of the Society for Minerals and Trace Elements (GMS)* **2018**, *49*, 119-127.
(117) Kenney, G. E.; Rosenzweig, A. C. Chalkophores. *Annual review of biochemistry* **2018**, *87*, 645-676.
(118) Krentz, B. D.; Mulheron, H. J.; Semrau, J. D.; DiSpirito, A. A.; Bandow, N. L.; Haft, D. H.; Vuilleumier, S.; Murrell, J. C.; McEllistrem, M. T.; Hartsel, S. C.; Gallagher, W. H. A comparison of methanobactins from *Methylosinus trichosporium* OB3b and *Methylocystis* strain SB2 predicts methanobactins are synthesized from diverse peptide precursors modified to create a common core for binding and reducing copper ions. *Biochemistry* **2010**, *49* (47), 10117-10130, Article.
(119) El Ghazouani, A.; Basle, A.; Gray, J.; Graham, D. W.; Firbank, S. J.; Dennison, C. Variations in methanobactin structure influences copper utilization by methane-oxidizing bacteria. *Proc. Natl. Acad. Sci. USA* **2012**, *109* (22), 8400-8404.
(120) Baslé, A.; El Ghazouani, A.; Lee, J.; Dennison, C. Insight into metal removal from peptides that sequester copper for methane oxidation. *Chemistry (Weinheim an der Bergstrasse, Germany)* **2018**, *24* (18), 4515-4518.
(121) Park, Y. J.; Roberts, G. M.; Montaser, R.; Kenney, G. E.; Thomas, P. M.; Kelleher, N. L.; Rosenzweig, A. C. Characterization of a copper-chelating natural product from the methanotroph *Methylosinus* sp. LW3. *Biochemistry* **2021**, *60* (38), 2845-2850.
(122) DeRose, V. J.; Liu, K. E.; Lippard, S. J.; Hoffman, B. M. Investigation of the Dinuclear Fe Center of Methane Monooxygenase by Advanced Paramagnetic Resonance Techniques: On the Geometry of the DMSO Binding. *Journal of the American Chemical Society* **1996**, *118* (1), 121-134.
(123) Davydov, R. M.; Smieja, J.; Dikanov, S. A.; Zang, Y.; Que, L., Jr.; Bowman, M. K. EPR properties of mixed-valent μ-oxo and μ-hydroxo dinuclear iron complexes produced by radiolytic reduction at 77 K. *J. Biol. Inorg. Chem.* **1999**, *4* (3), 292-301.
(124) Makris, T. M.; Chakrabarti, M.; Münck, E.; Lipscomb, J. D. A family of diiron monooxygenases catalyzing amino acid beta-hydroxylation in antibiotic biosynthesis. *Proc. Natl. Acad. Sci. USA* **2010**, *107* (35), 15391-15396.
(125) Xing, G.; Hoffart, L. M.; Diao, Y.; Prabhu, K. S.; Arner, R. J.; Reddy, C. C.; Krebs, C.; Bollinger, J. M., Jr. A coupled dinuclear iron cluster that is perturbed by substrate binding in myo-inositol oxygenase. *Biochemistry* **2006**, *45*, 5393-5401.
(126) Wörsdorfer, B.; Lingaraju, M.; Yennawar, N. H.; Boal, A. K.; Krebs, C.; Bollinger, J. M., Jr.; Pandelia, M. E. Organophosphonate-degrading PhnZ reveals an emerging family of HD domain mixed-valent diiron oxygenases. *Proc. Natl. Acad. Sci. USA* **2013**, *110* (47), 18874-18879, Article.

(127) Rajkovich, L. J.; Pandelia, M. E.; Mitchell, A. J.; Chang, W. C.; Zhang, B.; Boal, A. K.; Krebs, C.; Bollinger, J. M., Jr. A new microbial pathway for organophosphonate degradation catalyzed by two previously misannotated non-heme-iron oxygenases. *Biochemistry* **2019**, *58* (12), 1627-1647.
(128) Jasniewski, A. J.; Que, L. Dioxygen activation by nonheme diiron enzymes: diverse dioxygen adducts, high-valent intermediates, and related model complexes. *Chem. Rev.* **2018**, *118* (5), 2554-2592.
(129) Rajakovich, L. J.; Zhang, B.; McBride, M. J.; Boal, A. K.; Krebs, C.; Bollinger, J. M., Jr. 5.10 - Emerging structural and functional diversity in proteins with dioxygen-reactive dinuclear transition metal cofactors. In *Comprehensive Natural Products III*, Liu, H.-W., Begley, T. P. Eds.; Elsevier, 2020; pp 215-250.
(130) Stubbe, J.; Nocera, D. G.; Yee, C. S.; Chang, M. C. Radical initiation in the class I ribonucleotide reductase: long-range proton-coupled electron transfer? *Chem. Rev.* **2003**, *103* (6), 2167-2201.
(131) Krebs, C.; Bollinger, J. M., Jr.; Booker, S. J. Cyanobacterial alkane biosynthesis further expands the catalytic repertoire of the ferritin-like 'di-iron-carboxylate' proteins. *Curr. Opin. Chem. Biol.* **2011**, *15* (2), 291-303.
(132) Fox, B. G.; Lyle, K. S.; Rogge, C. E. Reactions of the diiron enzyme stearoyl-acyl carrier protein desaturase. *Acc. Chem. Res.* **2004**, *37*, 421-429.
(133) Roach, P. L.; Clifton, I. J.; Hensgens, C. M. H.; Shibata, N.; Schofield, C. J.; Hajdu, J.; Baldwin, J. E. Structure of isopenicillin *N* synthase complexed with substrate and the mechanism of penicillin formation. *Nature* **1997**, *387* (6635), 827-830.
(134) Park, Y. J.; Jodts, R. J.; Slater, J. W.; Reyes, R. M.; Winton, V. J.; Montaser, R. A.; Thomas, P. M.; Dowdle, W. B.; Ruiz, A.; Kelleher, N. L.; Bollinger, J. M.; Krebs, C.; Hoffman, B. M.; Rosenzweig, A. C. A mixed-valent Fe(II)Fe(III) species converts cysteine to an oxazolone/thioamide pair in methanobactin biosynthesis. *Proceedings of the National Academy of Sciences* **2022**, *119* (13), e2123566119.
(135) Dou, C.; Long, Z.; Li, S.; Zhou, D.; Jin, Y.; Zhang, L.; Zhang, X.; Zheng, Y.; Li, L.; Zhu, X.; Liu, Z.; He, S.; Yan, W.; Yang, L.; Xiong, J.; Fu, X.; Qi, S.; Ren, H.; Chen, S.; Dai, L.; Wang, B.; Cheng, W. Crystal structure and catalytic mechanism of the MbnBC holoenzyme required for methanobactin biosynthesis. *Cell Research* **2022**, *32* (3), 302-314.
(136) Xing, G.; Barr, E. W.; Diao, Y.; Hoffart, L. M.; Prabhu, K. S.; Arner, R. J.; Reddy, C. C.; Krebs, C.; Bollinger, J. M., Jr. Oxygen activation by a mixed-valent, diiron(II/III) cluster in the glycol cleavage reaction catalyzed by myo-inositol oxygenase. *Biochemistry* **2006**, *45*, 5402-5412.
(137) Rajakovich, L. J.; Pandelia, M.-E.; Mitchell, A. J.; Chang, W.-c.; Zhang, B.; Boal, A. K.; Krebs, C.; Bollinger, J. M., Jr. A New Microbial Pathway for Organophosphonate Degradation Catalyzed by Two Previously Misannotated Non-Heme-Iron Oxygenases. *Biochemistry* **2019**, *58* (12), 1627-1647.
(138) Bollinger, J. M.; Krebs, C. Stalking intermediates in oxygen activation by iron enzymes: Motivation and method. *Journal of Inorganic Biochemistry* **2006**, *100* (4), 586-605.
(139) Shanmugam, M.; Doan, P. E.; Lees, N. S.; Stubbe, J.; Hoffman, B. M. Identification of the Protonated Oxygenic Ligands of Ribonucleotide Reductase Intermediate X. *Journal of the American Chemical Society* **2009**, *131* (9), 3370–3376.
(140) Kim, S. H.; Xing, G.; Bollinger, J. M., Jr.; Krebs, C.; Hoffman, B. M. Demonstration by ^{2}H ENDOR Spectroscopy that myo-Inositol Binds via an Alkoxide Bridge to the Mixed-Valent Diiron Center of myo-Inositol Oxygenase. *Journal of the American Chemical Society* **2006**, *128* (32), 10374-10375.
(141) Bertrand, P.; Guigliarelli, B.; More, C. The Mixed-Valence [Fe(III), Fe(II)] Binuclear Centers of Biological Molecules Viewed through EPR Spectroscopy. *New Journal of Chemistry* **1991**, *15* (6), 445-454.
(142) Doan, P. E.; Shanmugam, M.; Stubbe, J.; Hoffman, B. M. Composition and Structure of the Inorganic Core of Relaxed Intermediate X(Y122F) of Escherichia coli Ribonucleotide Reductase. *J Am Chem Soc* **2015**, *137* (49), 15558-15566.
(143) Willems, J.-P.; Lee, H.-I.; Burdi, D.; Doan, P. E.; Stubbe, J.; Hoffman, B. M. Identification of the Protonated Oxygenic Ligands of Ribonucleotide Reductase Intermediate X by Q-band ^{1,2}H CW and Pulsed ENDOR. *Journal of the American Chemical Society* **1997**, *119* (41), 9816-9824.
(144) DeRose, V. J.; Liu, K. E.; Kurtz, D. M., Jr.; Hoffman, B. M.; Lippard, S. J. Proton ENDOR Identification of Bridging Hydroxide Ligands in Mixed-Valent Diiron Centers of Proteins: Methane Monooxygenase and Semimet Azidohemerythrin. *Journal of the American Chemical Society* **1993**, *115*, 6440-6441.
(146) Davydov, R. M.; Menage, S.; Fontecave, M.; Graslund, A.; Ehrenberg, A. Mixed-valent μ-oxo-bridged diiron complexes produced by radiolytic reduction at 77 K studied by EPR. *J. Biol. Inorg. Chem.* **1997**, *2* (2), 242-255.

(147) Xing, G.; Barr, E. W.; Diao, Y. H.; Hoffart, L. M.; Prabhu, K. S.; Arner, R. J.; Reddy, C. C.; Krebs, C.; Bollinger, J. M., Jr. Oxygen activation by a mixed-valent, diiron(II/III) cluster in the glycol cleavage reaction catalyzed by *myo*-inositol oxygenase. *Biochemistry* **2006**, *45* (17), 5402-5412, Article.
(148) Gardner, J. D.; Yi, L.; Ragsdale, S. W.; Brunold, T. C. Spectroscopic insights into axial ligation and active-site H-bonding in substrate-bound human heme oxygenase-2. *J Biol Inorg Chem* **2010**, *15* (7), 1117-1127, Research Support, N.I.H., Extramural.
(149) Broderick, J. B.; Duffus, B. R.; Duschene, K. S.; Shepard, E. M. Radical S-adenosylmethionine enzymes. *Chem Rev* **2014**, *114* (8), 4229-4317.
(150) Frey, P. A.; Hegeman, A. D.; Ruzicka, F. J. The Radical SAM Superfamily. *Crit Rev Biochem Mol Biol* **2008**, *43* (1), 63-88.
(151) Holliday, G. L.; Akiva, E.; Meng, E. C.; Brown, S. D.; Calhoun, S.; Pieper, U.; Sali, A.; Booker, S. J.; Babbitt, P. C. Chapter One - Atlas of the Radical SAM Superfamily: Divergent Evolution of Function Using a “Plug and Play” Domain. In *Methods in Enzymology*, Bandarian, V. Ed.; Vol. 606; Academic Press, 2018; pp 1-71.
(152) Walsby, C. J.; Ortillo, D.; Broderick, W. E.; Broderick, J. B.; Hoffman, B. M. An Anchoring Role for FeS Clusters: Chelation of the Amino Acid Moiety of *S*-Adenosylmethionine to the Unique Iron Site of the [4Fe-4S] Cluster of Pyruvate Formate-Lyase Activating Enzyme. *Journal of the American Chemical Society* **2002**, *124* (38), 11270-11271.
(153) Walsby, C. J.; Hong, W.; Broderick, W. E.; Cheek, J.; Ortillo, D.; Broderick, J. B.; Hoffman, B. M. Electron-Nuclear Double Resonance Spectroscopic Evidence That S-Adenosylmethionine Binds in Contact with the Catalytically Active [4Fe−4S]$^{+}$ Cluster of Pyruvate Formate-Lyase Activating Enzyme. *Journal of the American Chemical Society* **2002**, *124* (12), 3143-3151.
(154) Krebs, C.; Broderick, W. E.; Henshaw, T. F.; Broderick, J. B.; Huynh, B. H. Coordination of Adenosylmethionine to a Unique Iron Site of the [4Fe-4S] of Pyruvate Formate-Lyase Activating Enzyme: A Moessbauer Spectroscopic Study. *Journal of the American Chemical Society* **2002**, *124* (6), 912-913.
(155) Henshaw, T. F.; Cheek, J.; Broderick, J. B. The [4Fe-4S]$^{1+}$ Cluster of Pyruvate Formate-Lyase Activating Enzyme Generates the Glycyl Radical on Pyruvate Formate-Lyase: EPR-Detected Single Turnover. *Journal of the American Chemical Society* **2000**, *122* (34), 8331-8332.
(156) Atherton, N. M. *Principles of Electron Spin Resonance*; Ellis Horwood, 1993.
(157) Neese, F. The ORCA program system. *Wiley Interdisciplinary Reviews-Computational Molecular Science* **2012**, *2* (1), 73-78.
(158) Yang, H.; Impano, S.; Shepard, E. M.; James, C. D.; Broderick, W. E.; Broderick, J. B.; Hoffman, B. M. Photoinduced Electron Transfer in a Radical SAM Enzyme Generates an *S*-Adenosylmethionine Derived Methyl Radical. *J Am Chem Soc* **2019**, *141* (40), 16117-16124.
(159) Benjdia, A.; Heil, K.; Barends, T. R. M.; Carell, T.; Schlichting, I. Structural insights into recognition and repair of UV-DNA damage by Spore Photoproduct Lyase, a radical SAM enzyme. *Nucleic Acids Research* **2012**, *40* (18), 9308-9318.
(160) Nicolet, Y.; Amara, P.; Mouesca, J. M.; Fontecilla-Camps, J. C. Unexpected electron transfer mechanism upon AdoMet cleavage in radical SAM proteins. *Proc Natl Acad Sci U S A* **2009**, *106* (35), 14867-14871.
(161) Vey, J. L.; Drennan, C. L. Structural Insights into Radical Generation by the Radical SAM Superfamily. *Chemical Reviews* **2011**, *111* (4), 2487-2506.
(162) Vey, J. L.; Yang, J.; Li, M.; Broderick, W. E.; Broderick, J. B.; Drennan, C. L. Structural basis for glycyl radical formation by pyruvate formate-lyase activating enzyme. *Proc Natl Acad Sci U S A* **2008**, *105* (42), 16137-16141.
(163) Dinis, P.; Suess, D. L. M.; Fox, S. J.; Harmer, J. E.; Driesener, R. C.; De La Paz, L.; Swartz, J. R.; Essex, J. W.; Britt, R. D.; Roach, P. L. X-ray crystallographic and EPR spectroscopic analysis of HydG, a maturase in [FeFe]-hydrogenase H-cluster assembly. *Proceedings of the National Academy of Sciences* **2015**, *112* (5), 1362.
(164) Broyde, S. B.; Stellman, S. D.; Wartell, R. M. The A and B conformations of DNA and RNA subunits. Potential energy calculations for dGpdC. *Biopolymers* **1975**, *14* (12), 2625-2637.
(165) Lepore, B. W.; Ruzicka, F. J.; Frey, P. A.; Ringe, D. The X-ray crystal structure of lysine-2,3-aminomutase from Clostridium subterminale. *Proceedings of the National Academy of Sciences of the United States of America* **2005**, *102* (39), 13819-13824.
(166) Bersuker, I. B.; Polinger, V. Z. *Springer Series in Chemical Physics, Vol. 49: Vibronic Interactions in Molecules and Crystals*; 1989.

(167) Bersuker, I. B. *The Jahn-Teller Effect*; Cambridge University Press, 2006.
(168) Impano, S.; Yang, H.; Jodts, R. J.; Pagnier, A.; Swimley, R.; McDaniel, E. C.; Shepard, E. M.; Broderick, W. E.; Broderick, J. B.; Hoffman, B. M. Active-Site Controlled, Jahn-Teller Enabled Regioselectivity in Reductive S-C Bond Cleavage of S-Adenosylmethionine in Radical SAM Enzymes. *J Am Chem Soc* **2021**, *143* (1), 335-348.
(169) Becke, A. D. Density-functional exchange-energy approximation with correct asymptotic behavior. *Physical Review A: Atomic, Molecular, and Optical Physics* **1988**, *38* (6), 3098-3100.
(170) Perdew, J. P. Density-functional approximation for the correlation energy of the inhomogeneous electron gas. *Physical Review B* **1986**, *33* (12), 8822-8824.
(171) Perdew, J. P. Erratum: Density-functional approximation for the correlation energy of the inhomogeneous electron gas. *Physical Review B* **1986**, *34* (10), 7406
(172) Lee, C.; Yang, W.; Parr, R. G. Development of the Colle-Salvetti correlation-energy formula into a functional of the electron density. *Physical Review B: Condensed Matter and Materials Physics* **1988**, *37* (2), 785-789.
(173) Schäfer, A.; Horn, H.; Ahlrichs, R. Fully optimized contracted Gaussian basis sets for atoms Li to Kr. *The Journal of Chemical Physics* **1992**, *97* (4), 2571-2577.
(174) Barone, V.; Bencini, A.; Ciofini, I.; Daul, C. A.; Totti, F. Density Functional Modeling of Couble Exchange Interactions in Transition Metal Complexes. Calculation of the Ground and Excited State Properties of $[Fe_2(OH)_3(tmtacn)_2]^{2+}$. *Journal of the American Chemical Society* **1998**, *120*, 8357-8365.
(175) Neese, F. Efficient and accurate approximations to the molecular spin-orbit coupling operator and their use in molecular g-tensor calculations. *Journal of Chemical Physics* **2005**, *122* (3), 034107.
(176) Oberg, N.; Precord, T. W.; Mitchell, D. A.; Gerlt, J. A. RadicalSAM.org: A Resource to Interpret Sequence-Function Space and Discover New Radical SAM Enzyme Chemistry. *ACS Bio & Med Chem Au* **2022**, *2* (1), 22-35.
(177) Yang, H.; McDaniel, E. C.; Impano, S.; Byer, A. S.; Jodts, R. J.; Yokoyama, K.; Broderick, W. E.; Broderick, J. B.; Hoffman, B. M. The Elusive 5'-Deoxyadenosyl Radical: Captured and Characterized by Electron Paramagnetic Resonance and Electron Nuclear Double Resonance Spectroscopies. *J Am Chem Soc* **2019**, *141* (30), 12139-12146.
(178) Lundahl, M. N.; Sarksian, R.; Yang, H.; Jodts, R. J.; Pagnier, A.; Smith, D. F.; Mosquera, M. A.; van der Donk, W. A.; Hoffman, B. M.; Broderick, W. E.; Broderick, J. B. Mechanism of Radical S-Adenosyl-l-methionine Adenosylation: Radical Intermediates and the Catalytic Competence of the 5'-Deoxyadenosyl Radical. *J Am Chem Soc* **2022**, *144* (11), 5087-5098.
(179) Sayler, R. I.; Stich, T. A.; Joshi, S.; Cooper, N.; Shaw, J. T.; Begley, T. P.; Tantillo, D. J.; Britt, R. D. Trapping and Electron Paramagnetic Resonance Characterization of the 5'dAdo(•) Radical in a Radical S-Adenosyl Methionine Enzyme Reaction with a Non-Native Substrate. *ACS Cent Sci* **2019**, *5* (11), 1777-1785.
(180) Impano, S.; Yang, H.; Shepard, E. M.; Swimley, R.; Pagnier, A.; Broderick, W. E.; Hoffman, B. M.; Broderick, J. B. S-Adenosyl-l-ethionine is a Catalytically Competent Analog of S-Adenosyl-l-methione (SAM) in the Radical SAM Enzyme HydG. *Angew Chem Int Ed Engl* **2021**, *60* (9), 4666-4672.
(181) McSkimming, A.; Sridharan, A.; Thompson, N. B.; Müller, P.; Suess, D. L. M. An [Fe4S4]3+–Alkyl Cluster Stabilized by an Expanded Scorpionate Ligand. *Journal of the American Chemical Society* **2020**, *142* (33), 14314-14323.
(182) Ye, M.; Brown, A. C.; Suess, D. L. M. Reversible Alkyl-Group Migration between Iron and Sulfur in [Fe4S4] Clusters. *Journal of the American Chemical Society* **2022**, *144* (29), 13184-13195.
(183) Brown, A. C.; Suess, D. L. M. Valence Localization in Alkyne and Alkene Adducts of Synthetic $[Fe_4S_4]^+$ Clusters. *Inorganic Chemistry* **2022**.
(184) Raugei, S.; Seefeldt, L. C.; Hoffman, B. M. Critical computational analysis illuminates the reductive-elimination mechanism that activates nitrogenase for N_2 reduction. *Proceedings of the National Academy of Sciences* **2018**, *115* (45), E10521, 10.1073/pnas.1810211115.
(185) Lovell, T.; Li, J.; Liu, T.; Case, D. A.; Noodleman, L. FeMo Cofactor of Nitrogenase: A Density Functional Study of States M^N, M^{OX}, M^R, and M^I. *Journal of the American Chemical Society* **2001**, *123* (49), 12392-12410.
(186) Mouesca, J. M.; Noodleman, L.; Case, D. A.; Lamotte, B. Spin-Densities and Spin Coupling in Iron-Sulfur Clusters - a New Analysis of Hyperfine Coupling-Constants. *Inorganic Chemistry* **1995**, *34* (17), 4347-4359.

(187) Noodleman, L.; Case, D. A. Local Density Functional Approaches to Spin Coupling in Transition Metal Clusters. In *Theory and Applications of Density Functional Approaches to Chemistry*, Labanowski, J. K., Andzelm, J. W. Eds.; Springer Verlag, 1991.
(188) Benediktsson, B.; Bjornsson, R. Quantum Mechanics/Molecular Mechanics Study of Resting-State Vanadium Nitrogenase: Molecular and Electronic Structure of the Iron–Vanadium Cofactor. *Inorganic Chemistry* **2020**, *59* (16), 11514-11527.
(189) Han, W.-G.; Liu, T.; Lovell, T.; Noodleman, L. Active Site Structure of Class I Ribonucleotide Reductase Intermediate X: A Density Functional Theory Analysis of Structure, Energetics, and Spectroscopy. *Journal of the American Chemical Society* **2005**, *127* (45), 15778-15790.
(190) Han, W.-G.; Noodleman, L. DFT calculations of comparative energetics and ENDOR/Mössbauer properties for two protonation states of the iron dimer cluster of ribonucleotide reductase intermediate X. *Dalton Transactions* **2009**, (30), 6045-6057, 10.1039/B903847G.
(191) Rapatskiy, L.; Ames, W. M.; Pérez-Navarro, M.; Savitsky, A.; Griese, J. J.; Weyhermüller, T.; Shafaat, H. S.; Högbom, M.; Neese, F.; Pantazis, D. A.; Cox, N. Characterization of Oxygen Bridged Manganese Model Complexes Using Multifrequency 17O-Hyperfine EPR Spectroscopies and Density Functional Theory. *The Journal of Physical Chemistry B* **2015**, *119* (43), 13904-13921.
(192) Moulis, J.-M.; Lutz, M.; Gaillard, J.; Noodleman, L. Characterization of $[4Fe\text{-}4S]^{+2+/3+}$High-Potential Iron-Sulfur Protein from *Chromatium vinosum*. *Biochemistry* **1988**, *27* (24), 8712-8719.
(193) Johnson, E. R.; Otero-de-la-Roza, A.; Dale, S. G. Extreme density-driven delocalization error for a model solvated-electron system. *The Journal of Chemical Physics* **2013**, *139* (18), 184116.
(194) Balo, A. R.; Caruso, A.; Tao, L.; Tantillo, D. J.; Seyedsayamdost, M. R.; Britt, R. D. Trapping a cross-linked lysine-tryptophan radical in the catalytic cycle of the radical SAM enzyme SuiB. *Proceedings of the National Academy of Sciences* **2021**, *118* (21), e2101571118.
(195) van Lenthe, E.; Baerends, E. J.; Snijders, J. G. Relativistic total energy using regular approximations. *The Journal of Chemical Physics* **1994**, *101* (11), 9783-9792.
(196) Schafer, A.; Horn, H.; Ahlrichs, R. Fully Optimized Contracted Gaussian-Basis Sets for Atoms Li to Kr. *Journal of Chemical Physics* **1992**, *97* (4), 2571-2577.
(197) Tao, J.; Perdew, J. P.; Staroverov, V. N.; Scuseria, G. E. Climbing the Density Functional Ladder: Nonempirical Meta--Generalized Gradient Approximation Designed for Molecules and Solids. *Physical Review Letters* **2003**, *91* (14), 146401.
(198) Neese, F. Prediction and interpretation of the 57Fe isomer shift in Mössbauer spectra by density functional theory. *Inorganica Chimica Acta* **2002**, *337*, 181-192.
(199) Hedegård, E. D.; Kongsted, J.; Sauer, S. P. Improving the calculation of Electron Paramagnetic Resonance hyperfine coupling tensors for d-block metals. *Phys Chem Chem Phys* **2012**, *14* (30), 10669-10676.
(200) Ayikpoe, R. S.; Zhu, L.; Chen, J. Y.; Ting, C. P.; van der Donk, W. A. Macrocyclization and Backbone Rearrangement During RiPP Biosynthesis by a SAM-Dependent Domain-of-Unknown-Function 692. *ACS Central Science* **2023**.
(201) Ahearn, C. P.; Kirkham, C.; Chaves, L. D.; Kong, Y.; Pettigrew, M. M.; Murphy, T. F. Discovery and Contribution of Nontypeable Haemophilus influenzae NTHI1441 to Human Respiratory Epithelial Cell Invasion. *Infection and Immunity* **2019**, *87* (11), e00462-00419.
(202) Pinto, I. L.; West, A.; Debouck, C. M.; DiLella, A. G.; Gorniak, J. G.; O'Donnell, K. C.; O'Shannessy, D. J.; Patel, A.; Jarvest, R. L. Novel, selective mechanism-based inhibitors of the herpes proteases. *Bioorganic & Medicinal Chemistry Letters* **1996**, *6* (20), 2467-2472.
(203) Pasha, M.; Jayashankara, V.; Venugopala, K.; Rao, G. K. Zinc oxide (ZnO): an efficient catalyst for the synthesis of 4- arylmethylidene- 2- phenyl 5 (4H)- oxazolones having antimicrobial activity. *Journal of pharmacology and toxicology* **2007**, *2* (3), 264-270.
(204) Yogita, D.; Ravikant, R.; Versha, P.; Rahul, S.; Richa, C. Design, synthesis and evaluation of phenyl oxazolone derivatives as cardioprotective drugs. *World Journal of Pharmaceutical Sciences* **2014**, *2* (12), 1712-1722.
(205) Summer, K. H.; Lichtmannegger, J.; Bandow, N.; Choi, D. W.; DiSpirito, A. A.; Michalke, B. The biogenic methanobactin is an effective chelator for copper in a rat model for Wilson disease. *Journal of Trace Elements in Medicine and Biology* **2011**, *25* (1), 36-41.
(206) Salem, R.; ElDyasti, A.; Audette, G. F. Biomedical Applications of Biomolecules Isolated from Methanotrophic Bacteria in Wastewater Treatment Systems. *Biomolecules* **2021**, *11* (8), 1217.

(207) Tikdari, A. M.; Fozooni, S.; Hamidian, H. Dodecatungstophosphoric Acid (H3PW12O40), Samarium and Ruthenium (III) Chloride Catalyzed Synthesis of Unsaturated 2-Phenyl-5(4H)-oxazolone Derivatives under Solvent-free Conditions. *Molecules* **2008**, *13* (12), 3246-3252.
(208) Mesaik, M. A.; Rahat, S.; Khan, K. M.; Zia, U.; Choudhary, M. I.; Murad, S.; Ismail, Z.; Atta ur, R.; Ahmad, A. Synthesis and immunomodulatory properties of selected oxazolone derivatives. *Bioorganic & Medicinal Chemistry* **2004**, *12* (9), 2049-2057.
(209) Akiva, E.; Brown, S.; Almonacid, D. E.; Barber, A. E., 2nd; Custer, A. F.; Hicks, M. A.; Huang, C. C.; Lauck, F.; Mashiyama, S. T.; Meng, E. C.; Mischel, D.; Morris, J. H.; Ojha, S.; Schnoes, A. M.; Stryke, D.; Yunes, J. M.; Ferrin, T. E.; Holliday, G. L.; Babbitt, P. C. The Structure–Function Linkage Database. *Nucleic Acids Research* **2013**, *42* (D1), D521-D530.
(210) Kowalchuk, G. A.; Stephen, J. R. Ammonia-Oxidizing Bacteria: A model for Molecular Microbial Ecology. *Annual Review of Microbiology* **2001**, *55* (1), 485-529.
(211) Norton, J. M.; Alzerreca, J. J.; Suwa, Y.; Klotz, M. G. Diversity of ammonia monooxygenase operon in autotrophic ammonia-oxidizing bacteria. *Archives of Microbiology* **2002**, *177* (2), 139-149.
(212) Beeckman, F.; Motte, H.; Beeckman, T. Nitrification in agricultural soils: impact, actors and mitigation. *Curr Opin Biotechnol* **2018**, *50*, 166-173.

APPENDIX 1: Supplemental Figures

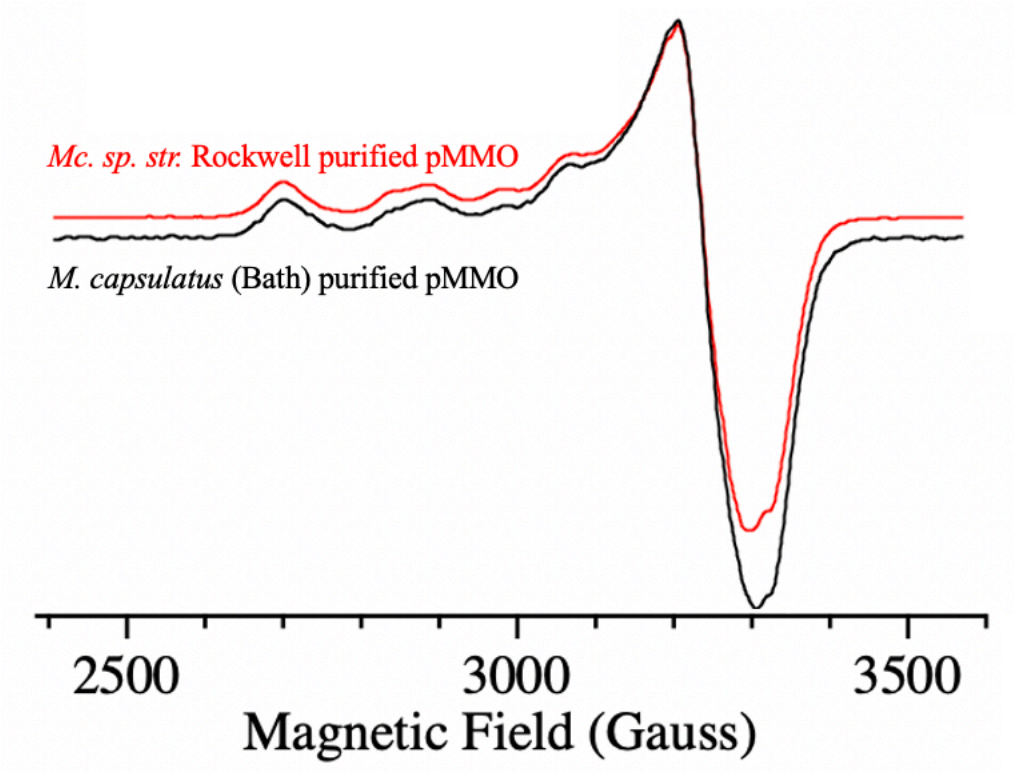

Figure S2.1. Overlay of X-band EPR spectra of purified *Mc.* sp. str. Rockwell (red) and *M. capsulatus* (Bath) pMMOs. The spectra are identical in terms of g and ^{63}Cu $A_{||}$ values, the most definitive features for Cu(II) EPR. *Conditions:* 9.37 GHz, 20 K, 12.5 G modulation, 320 ms time constant, 200 μW MW power. The spectra were collected on the same day for accurate comparison.

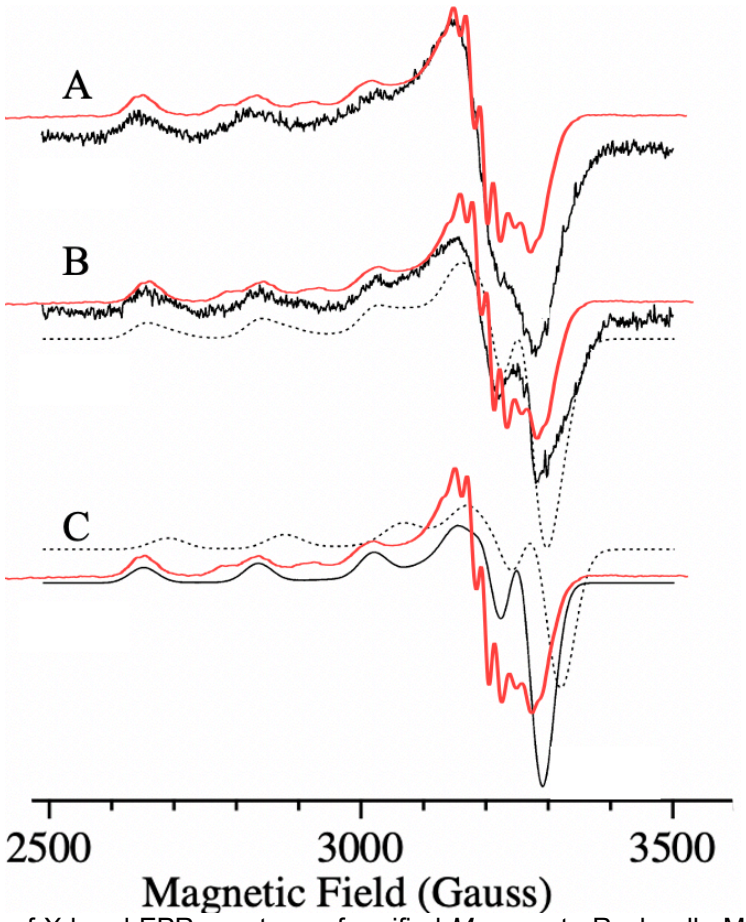

Figure S2.2. Overlay of X-band EPR spectrum of purified *Mc.* sp. str. Rockwell pMMO presented in this paper (red, from **Figure 2C** main text) with the three previously reported EPR spectra of type II *Mc.* sp. str. M pMMO[53] (black), including (A) membrane-bound pMMO (B) solubilized pMMO, and (C) simulations of the two Cu(II) signals observed in (C) from ref. 10. The overlay of the *Mc.* sp. str. Rockwell spectrum (red) shows that the Cu_C site was not observed in the type II pMMOs in previous samples. Its absence may be due to not adding copper to the lysis buffer. As shown in Figure S4, this leads to only Cu_B being observed by EPR for *Mc.* sp. str. Rockwell pMMO. It is possible that there is some underlying Cu_C signal in (B), as evident by $\mathbf{g}_\perp$, but due to the resolution, it is not obvious. *Conditions* are reported in ref. 10, with those for the red trace in **Figure 2.2**

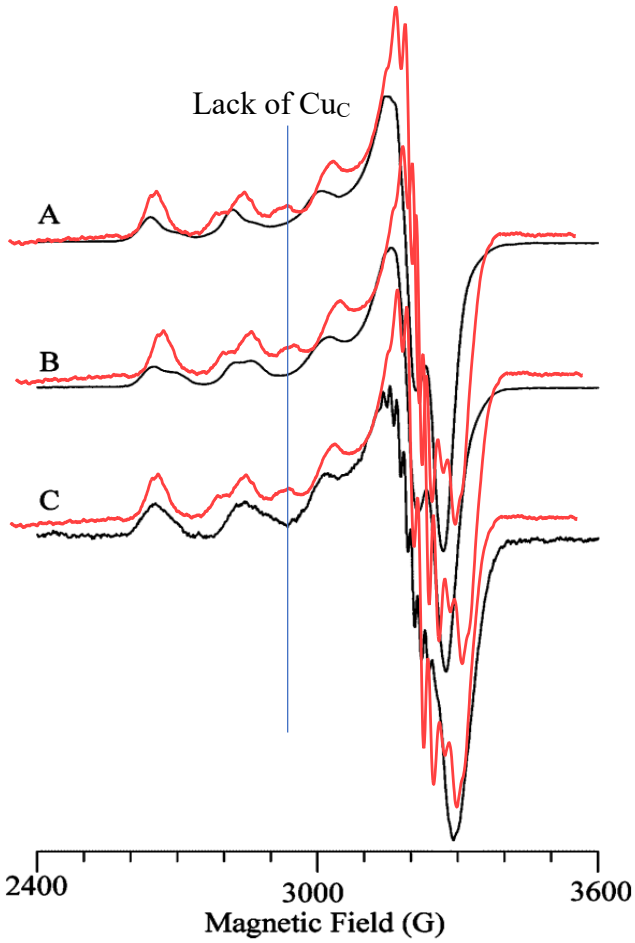

Figure S2.3. Overlay of purified *Mc.* sp. str. Rockwell pMMO X-band EPR spectrum presented in this paper (red, **Figure 2.2C**) with the three previously reported EPR spectra of type II *Methylosinus trichosporium* OB3b pMMO[87] (black), including (A) membrane-bound pMMO, (B) solubilized pMMO, and (C) purified pMMO The Cu(II) spectra in (A) and (B) are not related to pMMO since the g|| and the $^{63/65}$Cu A|| do not match those of the Cu$_B$ or Cu$_C$ site. The purified pMMO spectrum appears to only have the Cu$_B$ site. The lack of the Cu$_C$ site in the purified pMMO spectrum is evident by the lack of the +1/2 hyperfine line, as shown with the blue vertical line. *Conditions* of black are described in the referece, red is described in text.

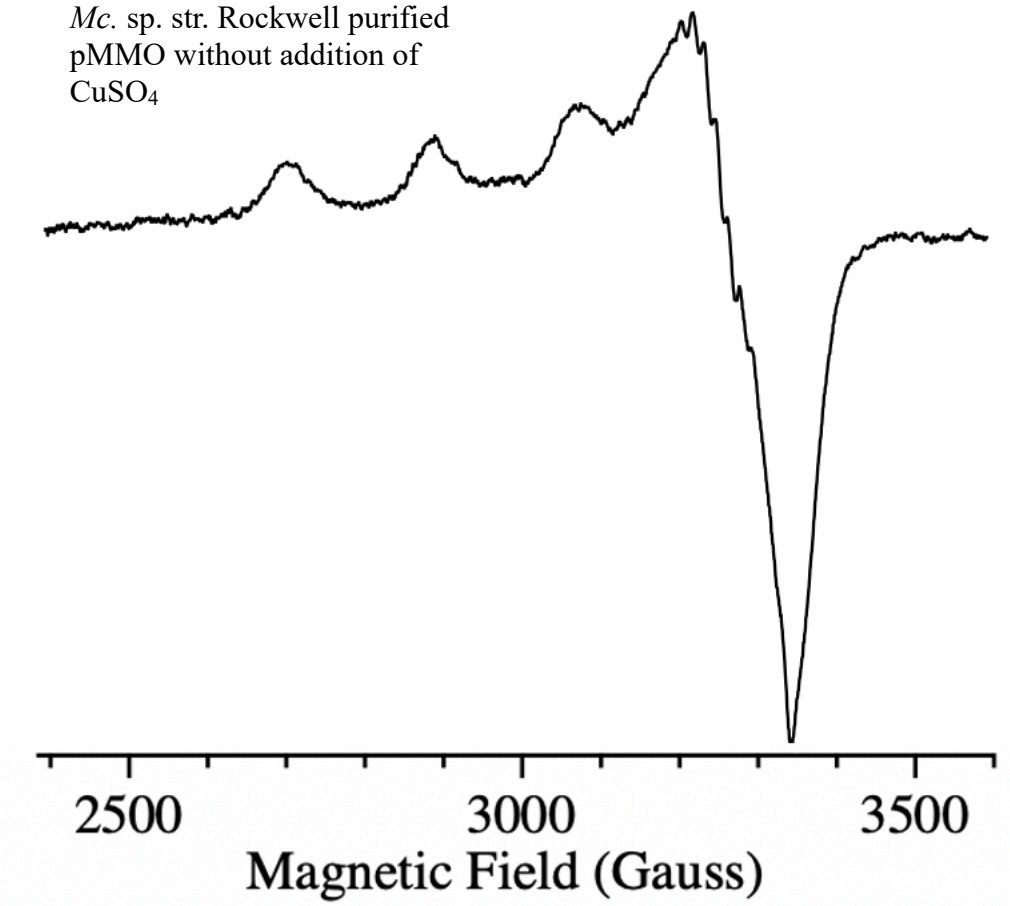

Figure S2.4. X -Band EPR spectrum of *Mc.* sp. str. Rockwell purified pMMO without the addition of $CuSO_4$ at lysis. The spectrum exhibits only the Cu_B signal, and is identical to that of *Mc.* sp. str. Rockwell whole cells (**Figure 2.2A**) and purified/reduced *Mc.* sp. str. Rockwell pMMO (**Figure 2.2D**), with no Cu_C signal. These samples do not have methane oxidation activity. *Conditions:* 77K, 12.5 G modulation, 10G/s sweep rate, 320 ms time constant, 200μW MW power, 9.34 GHz MW frequency.

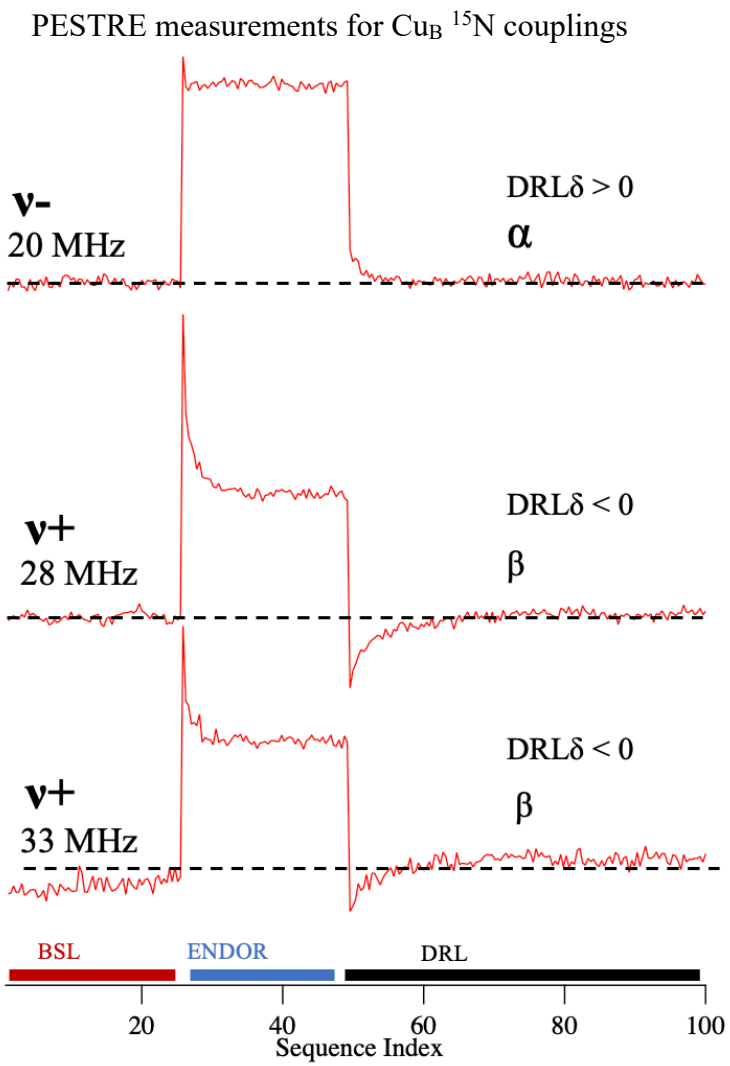

Figure S2.5. PESTRE measurements for sign determination of the strongly coupled Cu_B ^{15}N in *Mc.* sp. str. Rockwell in vivo pMMO. The couplings were found to be negative in sign for both peaks shown in **Figure 3**. *Conditions:* 34.77 GHz, 100 ms repetition time, π = 120 ns, τ = 600 ns, TRF = 15 μs, RF tail = 5 μs, 25 shots, 24 off.

PESTRE measurements for Cu_B ^1H couplings

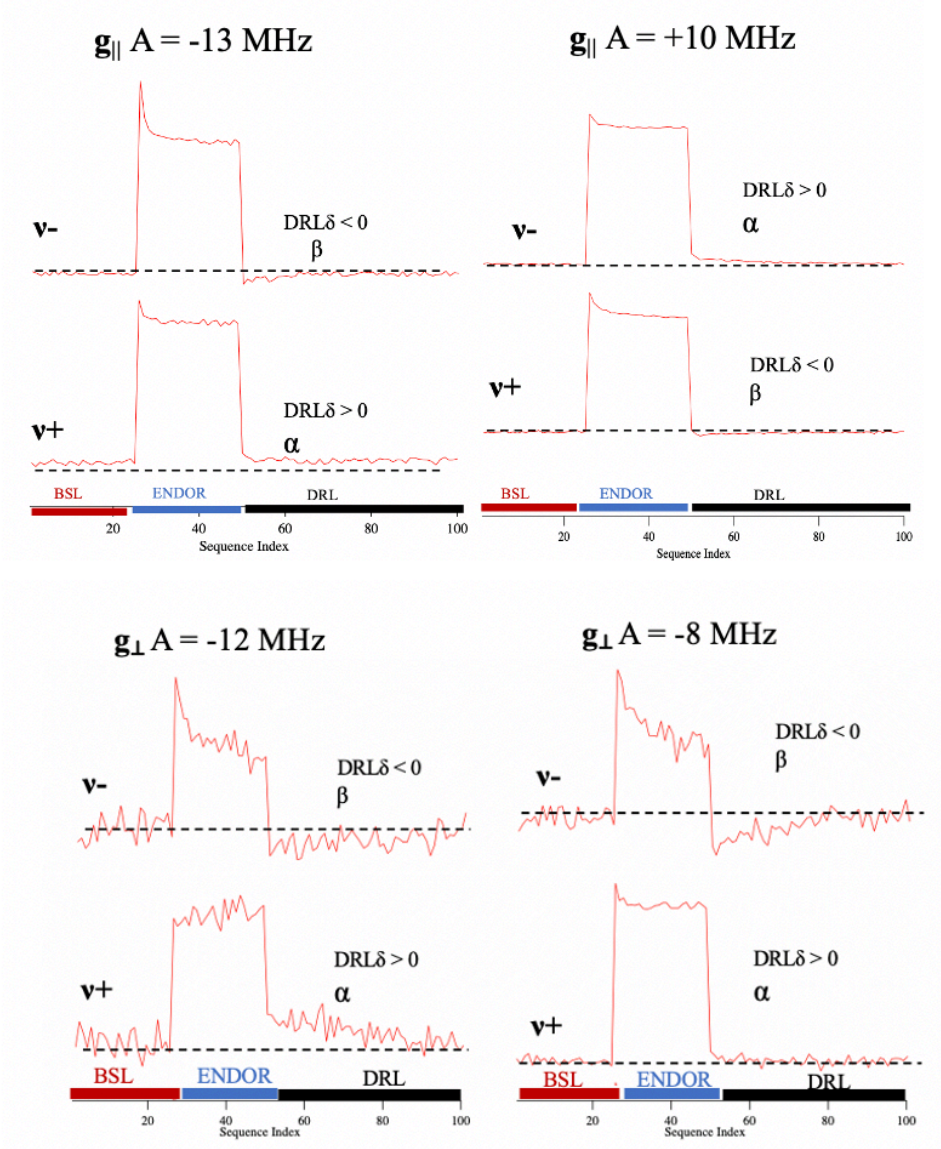

Figure S2.6. PESTRE measurements on the large couplings of in vivo *Mc.* sp. str. Rockwell pMMO (Cu_B site) as resolved from the stochastic ^1H ENDOR experiment at both $\mathbf{g}_\perp$ and $\mathbf{g}_\parallel$ (**Figure 4**). The measurement resulted in A = -13 and +10 at $\mathbf{g}_\parallel$ and A = -12 and -8 at $\mathbf{g}_\perp$. *Conditions:* 34.72 GHz, 100 ms repetition time, π = 120 ns, τ = 600 ns, TRF = 15 µs, RF tail = 5 µs, 25 shots, 24 off.

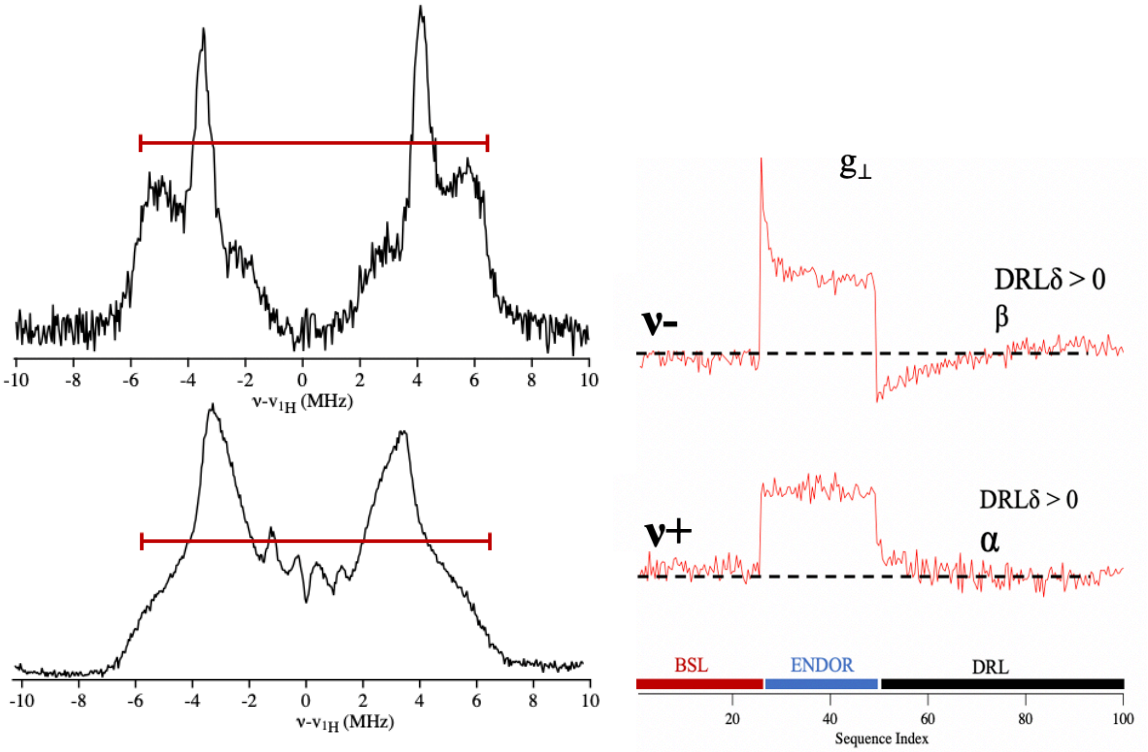

Figure S2.7. Q-band stochastic ^{1}H ENDOR and PESTRE measurements of Cu(II)$(NH_3)_4$ in H_2O buffer with ~20% ethylene glycol at $g_{||}$ (10800G) (top) and $g_{\perp}$ (12020 G). Red brackets represent |A| for the largest ^{1}H couplings, A ~ 12 MHz. Since $[Cu(II)(NH_3)_4]^{2+}$ does not contain axial ligands, the ~12 MHz ^{1}H couplings at both $g_{||}$ and $g_{\perp}$must come from the in-plane amine ligands. PESTRE measurements revealed the couplings at both g-values to be negative in sign. DFT model of $[Cu(II)(NH_3)_4]^{2+}$yields a hyperfine tensor, **A** = [-15, 1.5, -16] for an in-plane amine proton. This highly rhombic tensor is achieved due to large spin delocalization from the copper to the protons of the amine when they are oriented within the x^2-y^2 orbital of the unpaired electron. The tensor matches the signs and the identical relative magnitudes of those seen for the for the copper complex as well as for Cu_B.

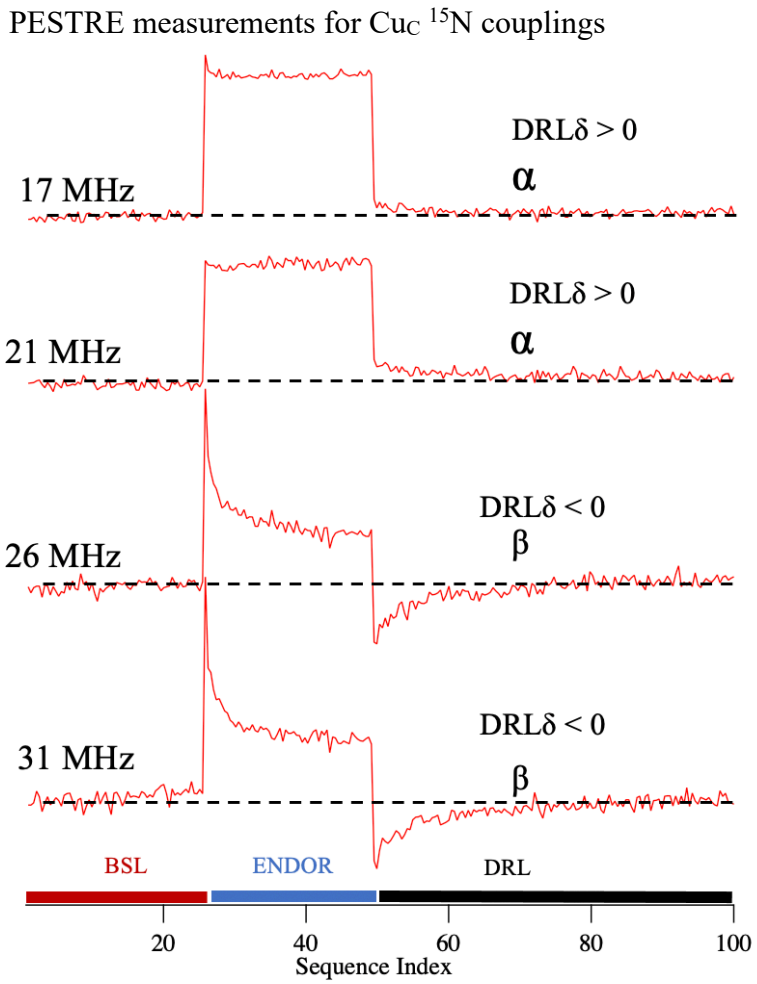

Figure S2.8. PESTRE measurements on Cu$_C$ ^{15}N couplings at **g** = 2.33. The peaks examined at the frequency defined above are shown in **Figure 6**. The results of the PESTRE measurements reveal both strongly coupled ^{15}N to the Cu$_C$ to be negative in sign. *Conditions:* 34.71 GHz, 100 ms repetition time, π = 120 ns, τ = 600 ns, TRF = 15 μs, and RF tail = 5 μs. 25 shots, 24 off.

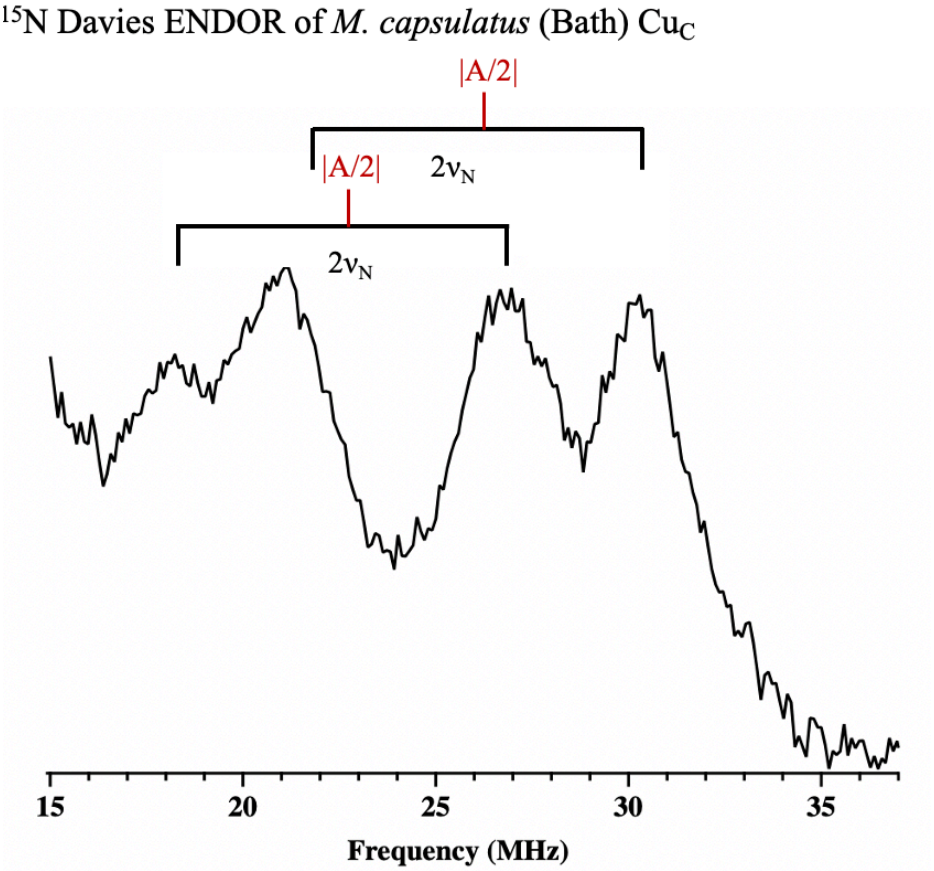

Figure S2.9. Medium Davies ^{15}N ENDOR at a field of a corresponding g-value of g = 2.32 for ^{15}N ^{63}Cu *M. capsulatus* (Bath) pMMO. The ^{5}N couplings observed here are exclusive to the Cu_C site at this magnetic field and are identical in |A| to the type II *Mc.* sp. str. Rockwell pMMO, as shown in **Figure 6**, |A| ~ 50 MHz and |A| ~ 46 MHz. Brackets indicate twice the ^{15}N Larmor frequency, and the center of the bracket (red) indicates |A/2|. *Conditions* are identical to **Figure 6** in the main text.

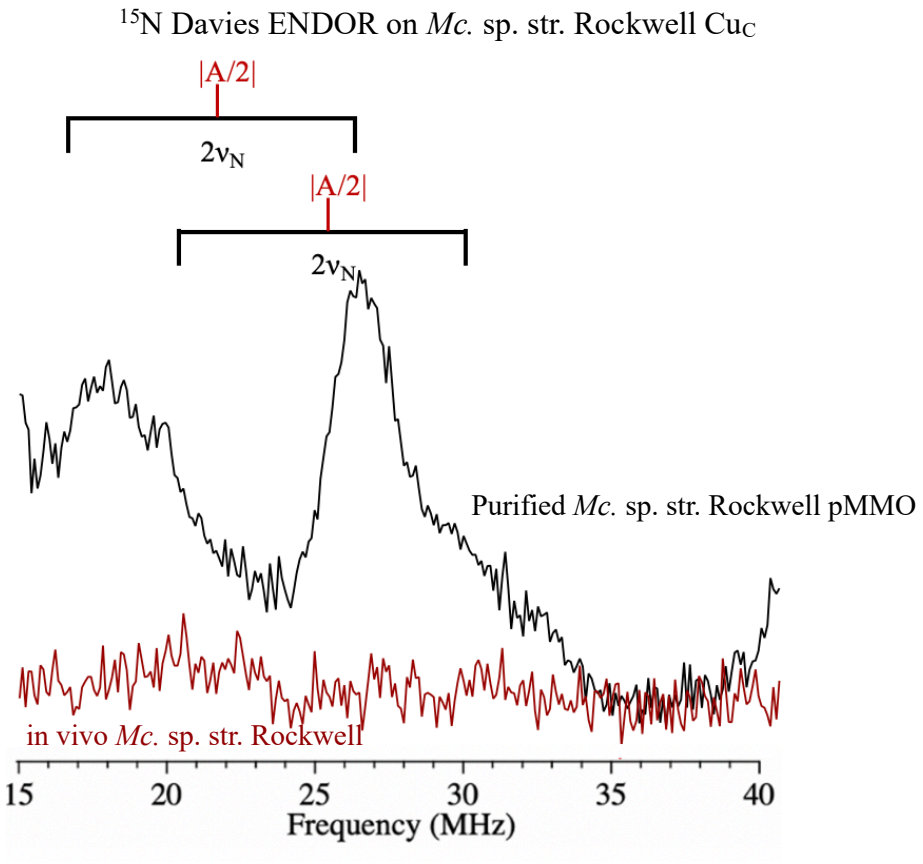

Figure S2.10. ^{15}N Davies pulsed ENDOR of *Mc.* sp. str. Rockwell pMMO Cu$_C$ (black trace) site at the low-field end of the EPR signal, at a field with a corresponding g-value of g = 2.34, (~10600 G). The red trace is in vivo *Mc.* sp. str. Rockwell pMMO, which exhibits an EPR signal from Cu$_B$ only, at the same field position. The two spectra were echo-normalized. Brackets indicate twice the ^{15}N Larmor frequency and the center of the bracket (red) indicates |A/2|. The larger coupling is not well resolved at this field. *Conditions* are identical to **Figure 2.6.**

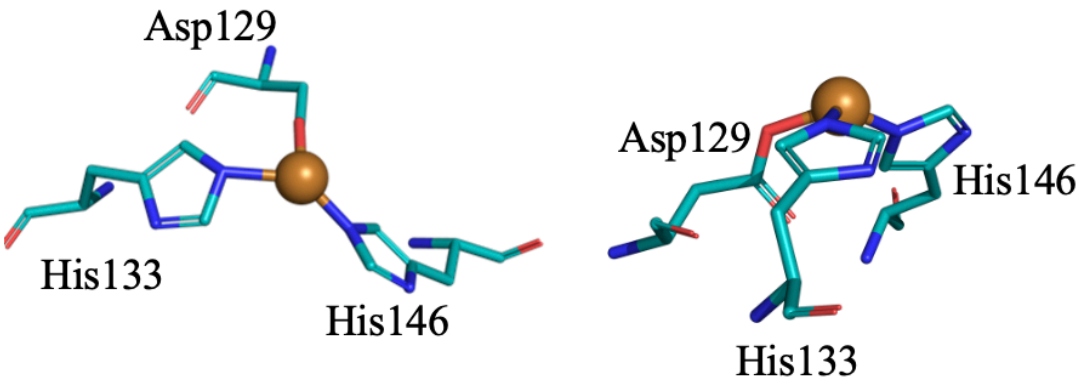

Figure S2.11. Alternative view of PmoC copper site from the crystal structure of *Mc.* sp. str. Rockwell (PDB accession code 4PHZ). The view shows the distortion (lack of symmetry) of the two His coordinating ligands to the copper center.

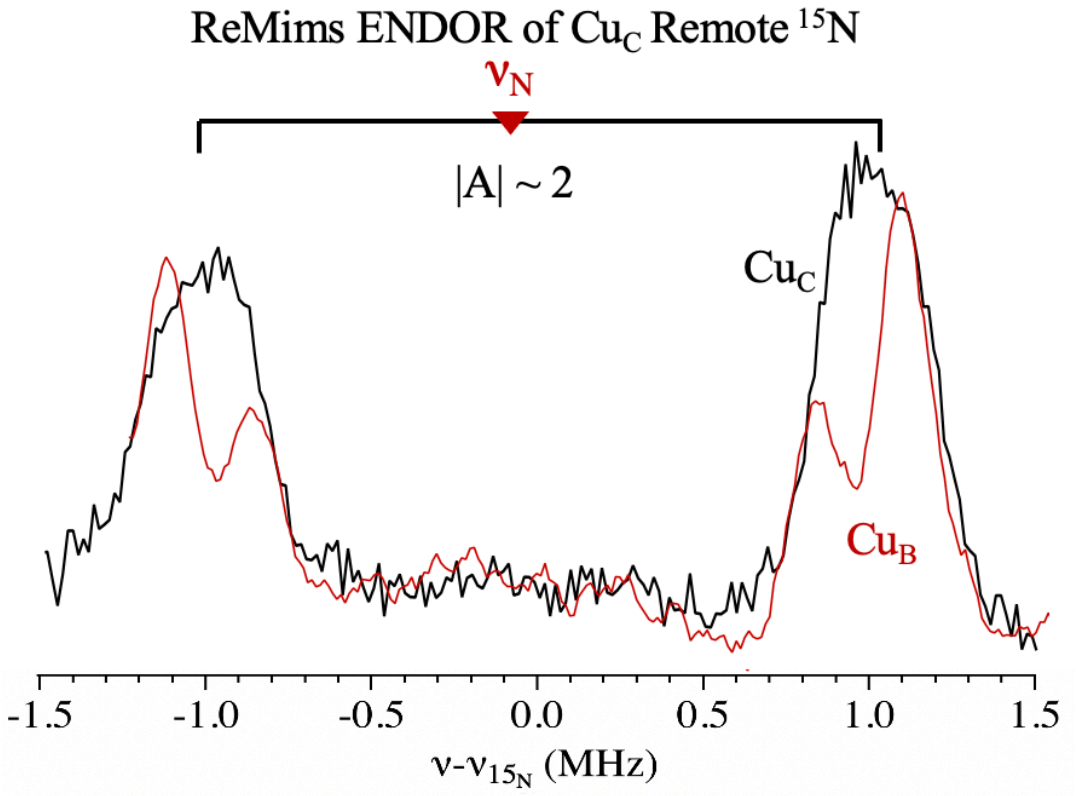

Figure S2.12. Overlay of ReMims ENDOR remote ^{15}N couplings from the Cu_B (red, from **Figure 2**) and Cu_C (black, from **Figure 7**). Comparing the breadth of the unresolved doublet to the doublets in the Cu_B spectrum reveal that the couplings in the Cu_C spectrum likely arise from more than one remote ^{15}N coupling as discussed in the text.

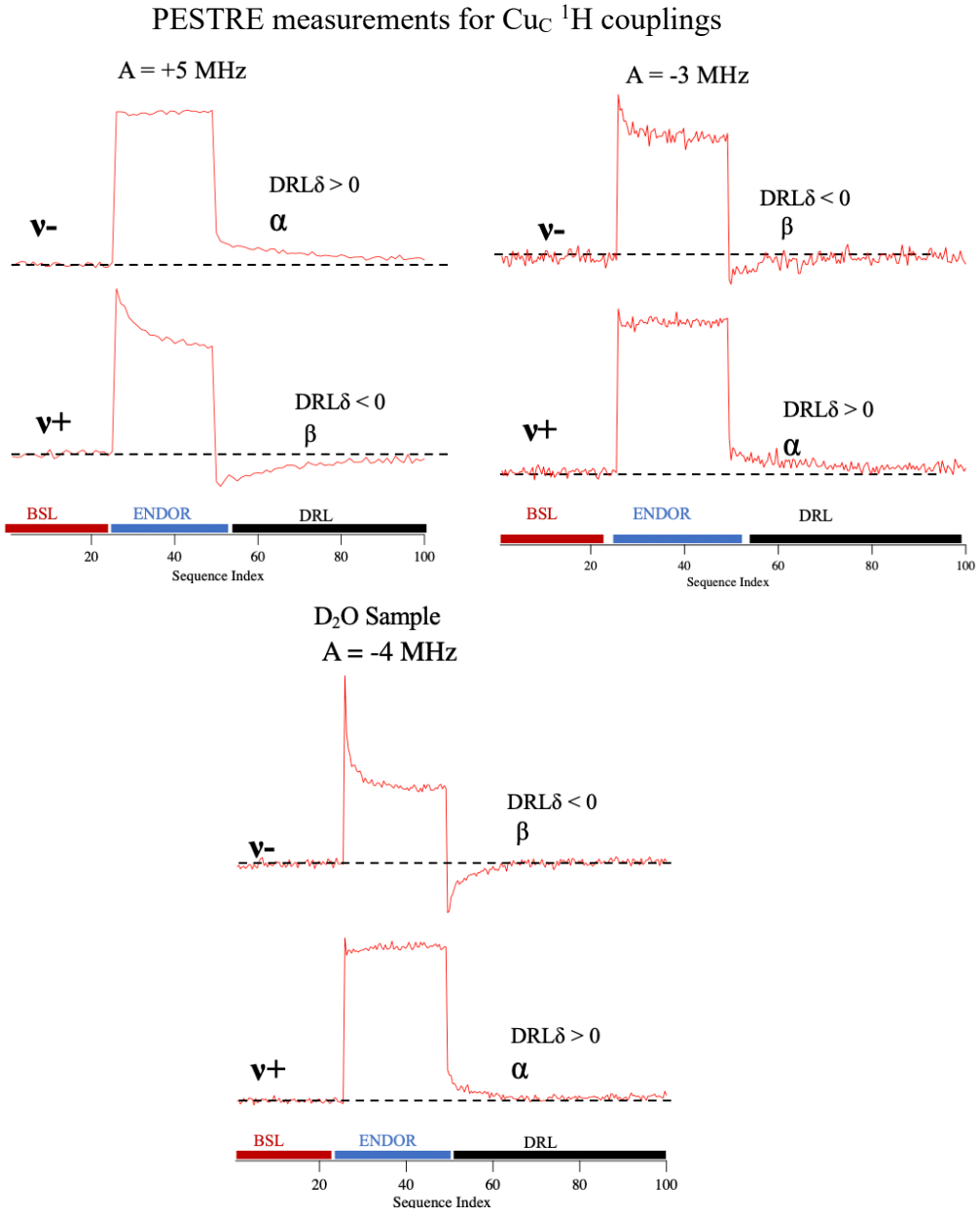

Figure S2.13. 35 GHz PESTRE performed on the Cu$_C$ ^{1}H couplings at g = 2.34 (10700G). The +5 MHz and -2.5 MHz couplings were determined using a purified sample in H_2O, while the -4 MHz coupling was determined using a purified *Mc.* sp. str. Rockwell pMMO sample exchanged into D_2O. *Conditions:* 34.67 – 34.69 GHz, 100 ms repetition time, π = 120 ns, τ = 600 ns, TRF = 15 μs, and RF tail = 5 μs. 25 shots, 24 off.

^{17}O Mims ENDOR on *M. capsulatus* (Bath) Cu_C

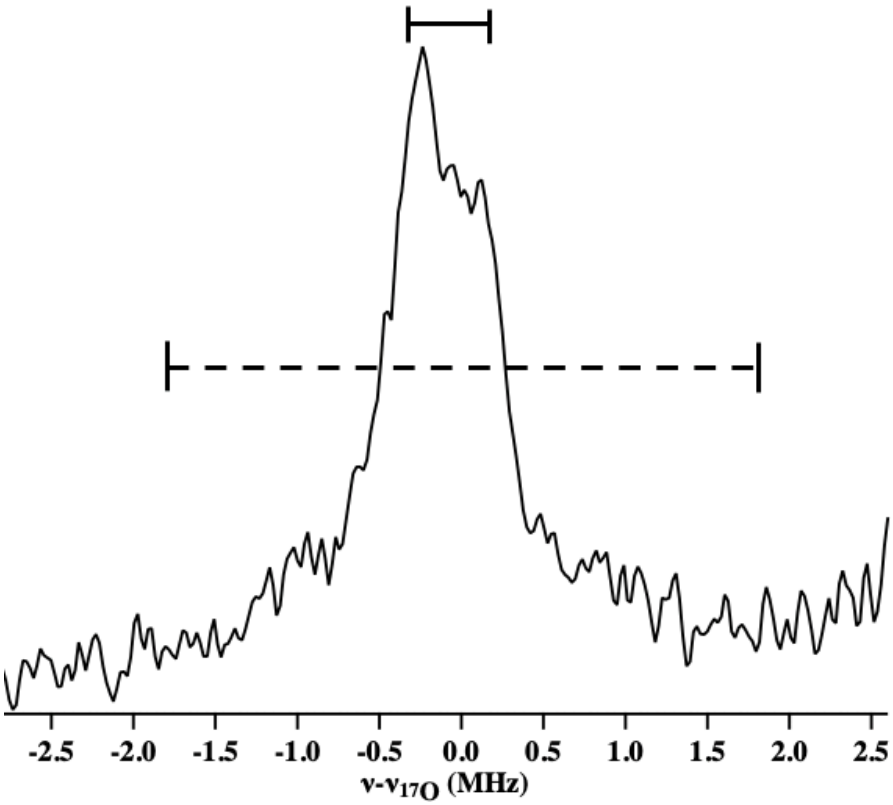

Figure S2.14. ^{17}O ENDOR at g = 2.33 (Cu_C site). The spectrum specifically lacks the ~3.6 MHz doublet (indicated by the dashed 'goalposts') previously reported observing at g = 2.01 for Cu_C. The spectrum instead exhibits a response centered at the Larmor frequency, which is expected for remote $H_2{}^{17}O$ solvent in the sample, and may exhibit unresolved intensity, breadth ~ 2 MHz, from a secondary coordination sphere water, whose ^{1}H ENDOR response is discussed in Figure 8.

^{17}O Mims ENDOR on purified *M. capsulatus* (Bath) pMMO

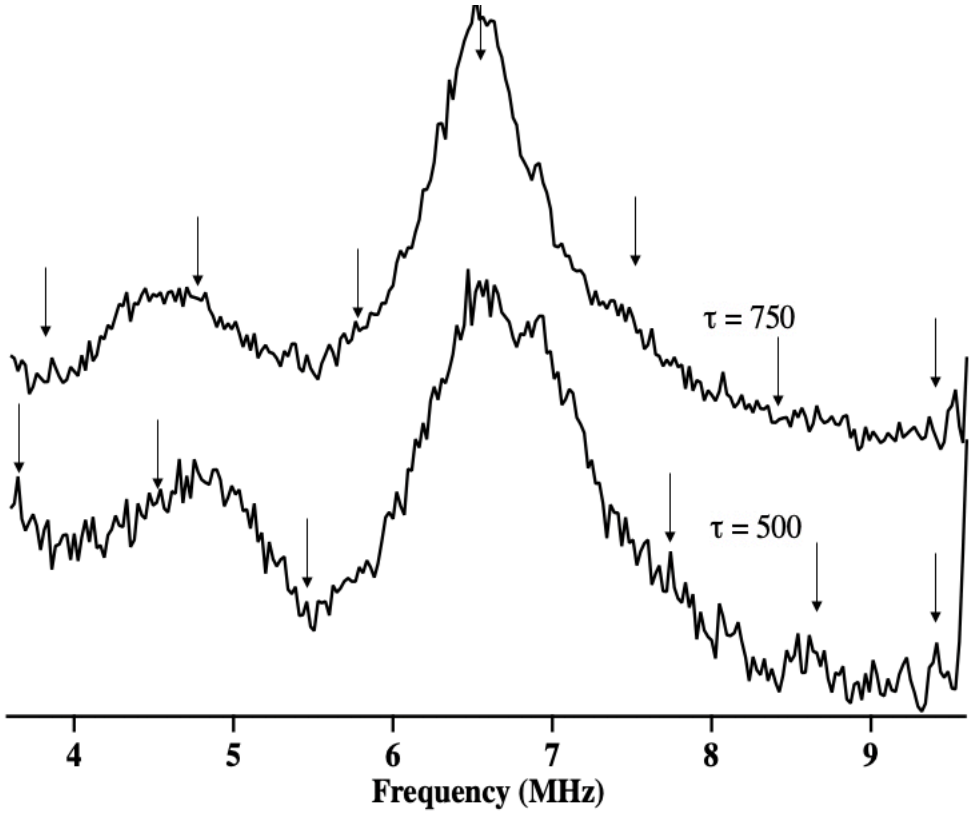

Figure S2.15. ^{17}O Mims Pulsed ENDOR of purified *M.* capsulatus (Bath) pMMO in 45% enriched $H_2{}^{17}O$ buffer at g = 2.02 (~12050 G). This experiment was conducted at different τ values to observe whether there is suppression of the large coupling (3.5 MHz). The τ = 750 experiment should suppress the coupling, but it looks quite resolved here. The coupling is now believed to derive from either a weakly coupled ^{14}N or 5/2 quadrupole of the Cu_B axial H_2O ligand.

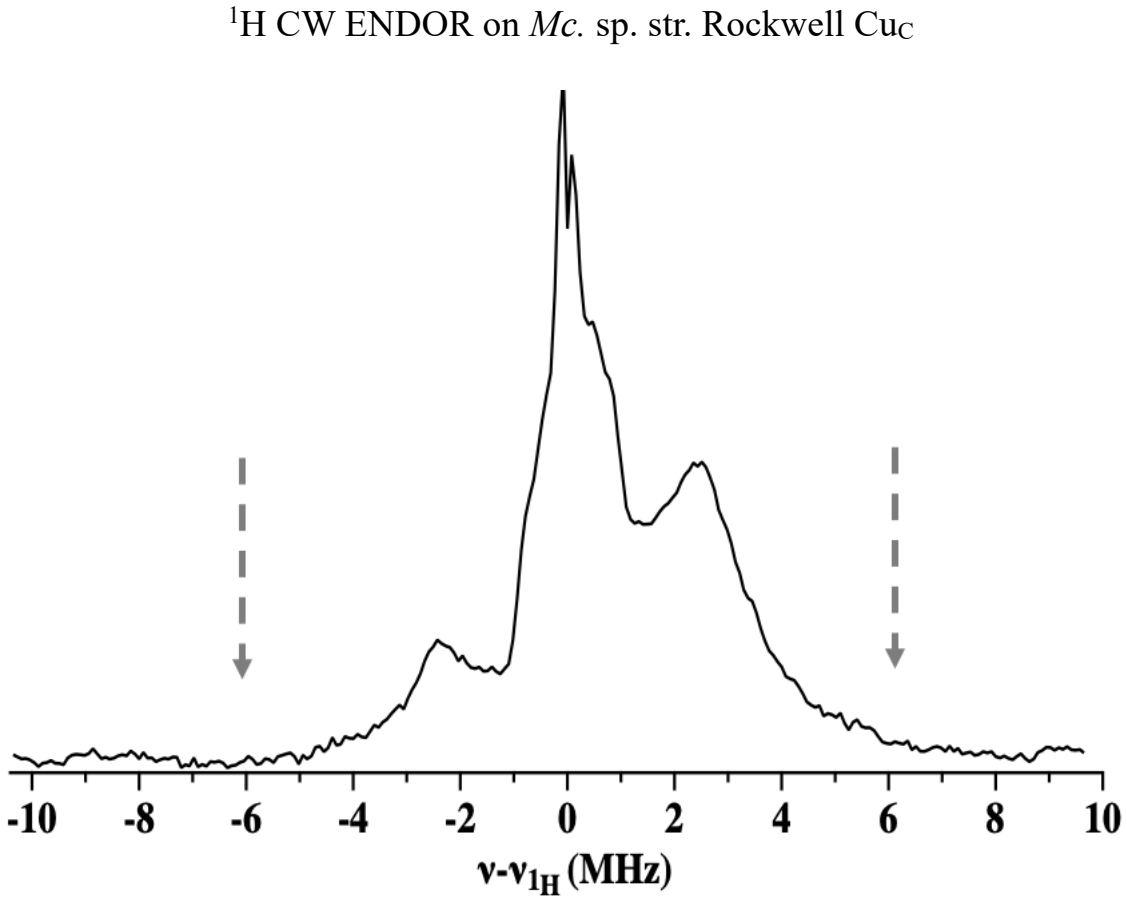

Figure S2.16. ^{1}H CW ENDOR spectrum at g = 2.35 of *Mc.* sp. str. Rockwell purified pMMO Cu$_C$ site. The gray dashed arrows highlight the absence of any couplings with A >8 MHz, which signifies the absence of a bound axial solvent molecule. This also serves as an additional control that only the Cu$_C$ site is observed at this field position since the Cu$_B$ site exhibits couplings of ~12 MHz at $g_{||}$.

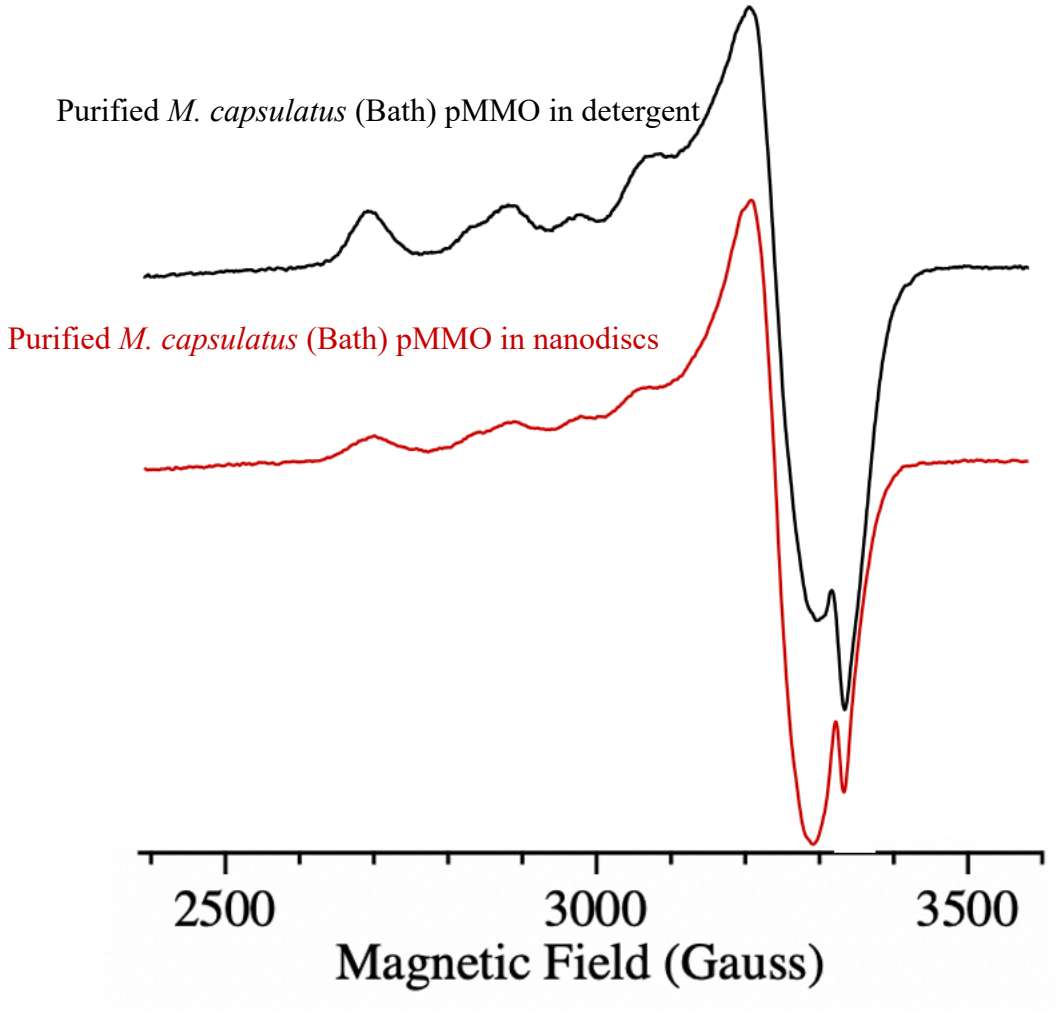

Figure S2.17. X-band EPR spectra of detergent-purified natural abundance *M.* capsulatus (Bath) pMMO (black) and purified *M.* capsulatus (Bath) pMMO in nanodiscs (red). The spectra are scaled by EPR intensity to facilitate comparison. The two sites exhibit identical g values and ^{63}Cu A values. *Conditions:* 9.37 GHz MW Frequency, 30 K, 12.5 G modulation, 10 G/s sweep rate, 320 ms time constant, 200μW power.

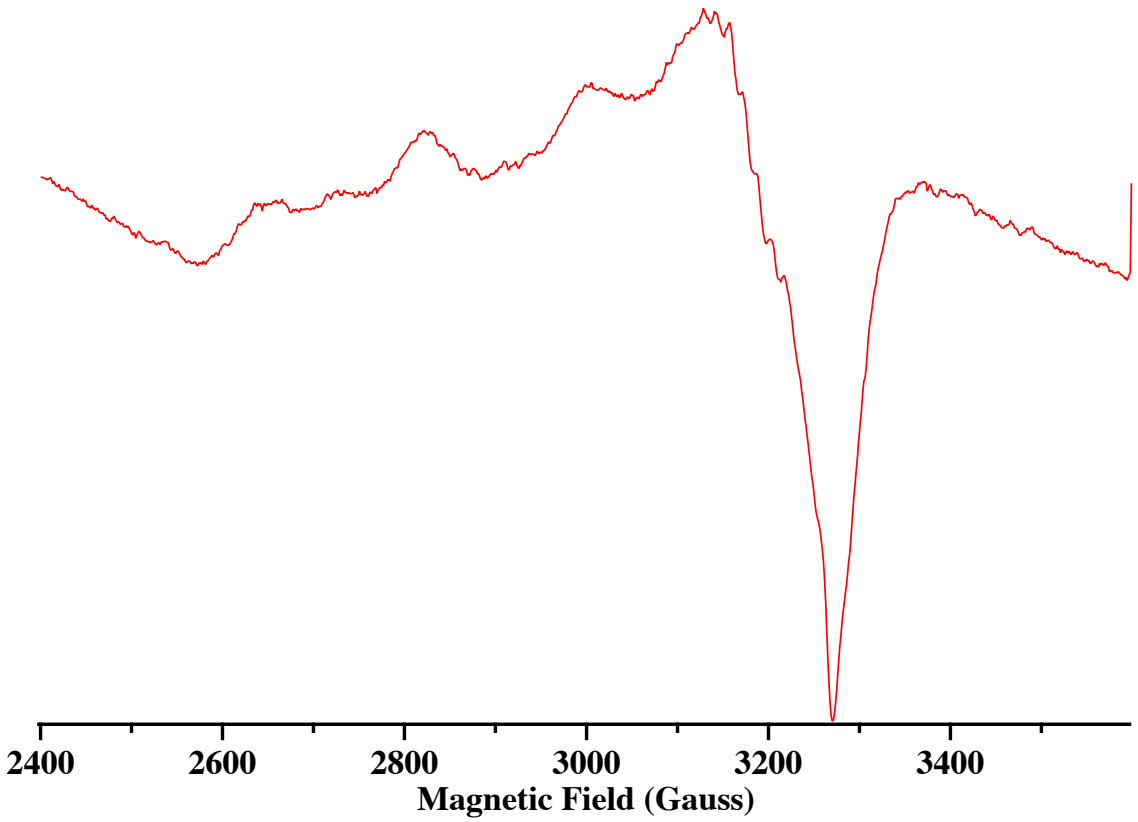

Figure S2.18. X-band EPR spectrum of reduced *M. capsulatus* (Bath) pMMO in nanodiscs. 12:1 ascorbic acid per 100 kDa protomer of pMMO was added to reduce the Cu_C site and obtain a pure Cu_B site to investigate with ENDOR. *Conditions:* 77K, 12.5 G modulation, 200μW MW power, 320 ms time constant, 9.37 GHz frequency. .

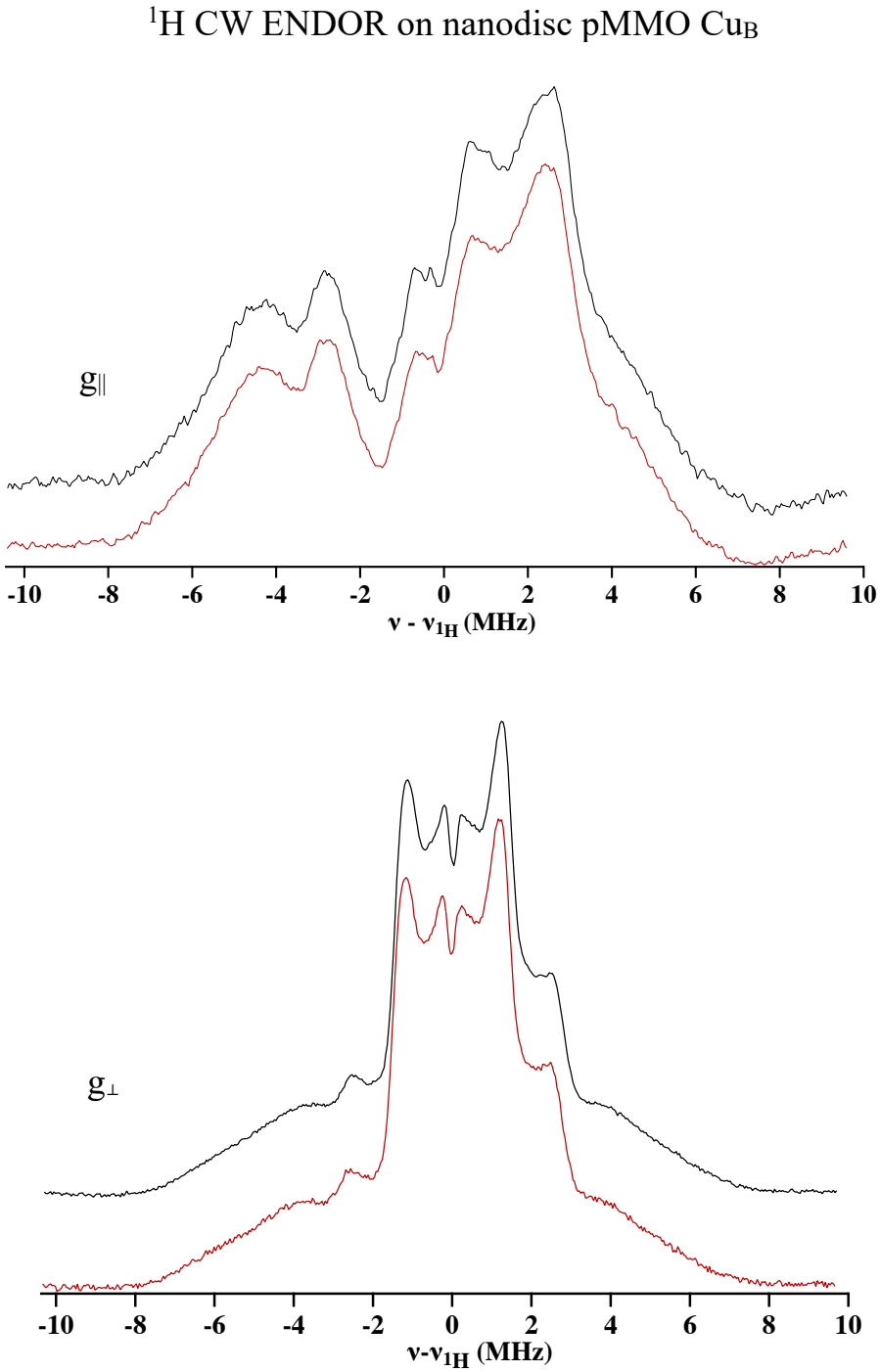

Figure S2.19. ^{1}H CW ENDOR of Cu_B in reduced purified *M. capsulatus* (Bath) pMMO in detergent (black trace) and in nanodiscs (red trace) at g|| (top) and $g_{\perp}$ (bottom). The ENDOR spectra show no differences, indicating that Cu_B is identical within the two different environments, unlike Cu_C in which the secondary coordination sphere loses a solvent molecule (**Figure 9**). *Conditions:* 2K, 34.89 GHz MW frequency, 3.2 G modulation, 0.5 MHz/s scan rate, 30dB MW power, 13dB RF power, 32 ms time constant. Spectra were collected with RF swept low to high frequency.

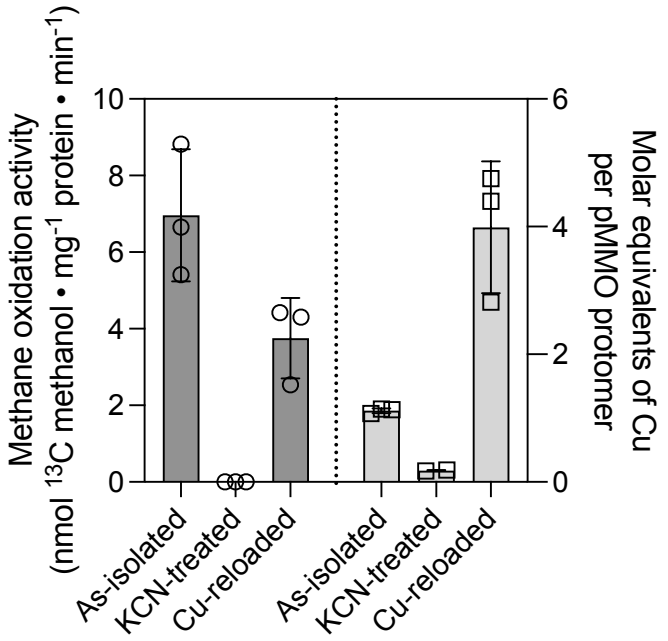

Figure S3.1. Copper-dependent pMMO activity in native lipid nanodiscs. The methane oxidation activities of as-isolated, KCN-treated, and copper-reloaded pMMO in native lipid nanodiscs are shown. ICP-MS was used to measure the molar equivalents of copper per pMMO protomer. KCN treatment depletes copper and abolishes methane oxidation activity, but copper reloading partially recovers activity. Error bars represent the standard error from the mean with n=3 independent replicates.

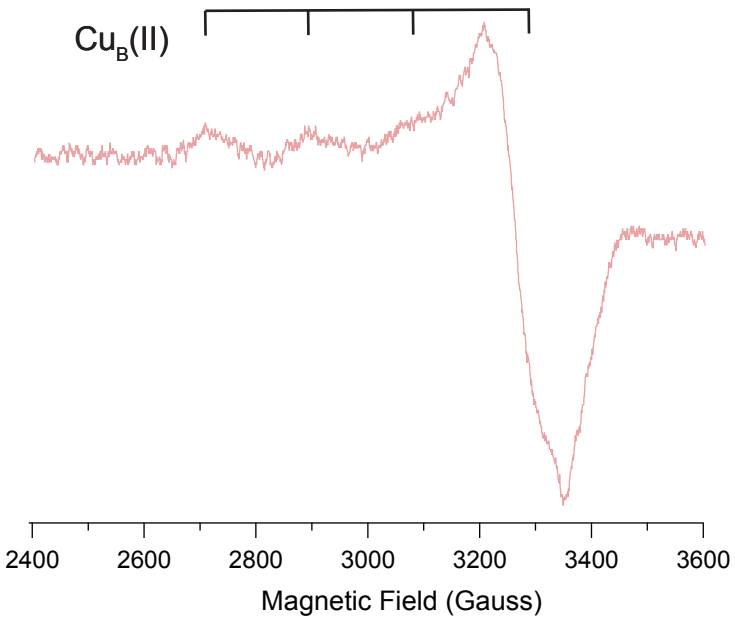

Figure S3.2. Magnified X-band EPR spectrum of metal-depleted pMMO. The signal is multiplied 10x compared to Fig. 2a in the main text, with all the samples first run at the same signal gain. The spectrum shows the presence of the Cu_B site, as well as the presence of other unresolvable type 2 Cu(II) features. Conditions: 9.37 GHz MW frequency, 30 K, 12.5 G modulation, 250 μW microwave power, 320 ms time constant, 10G/s scan rate.

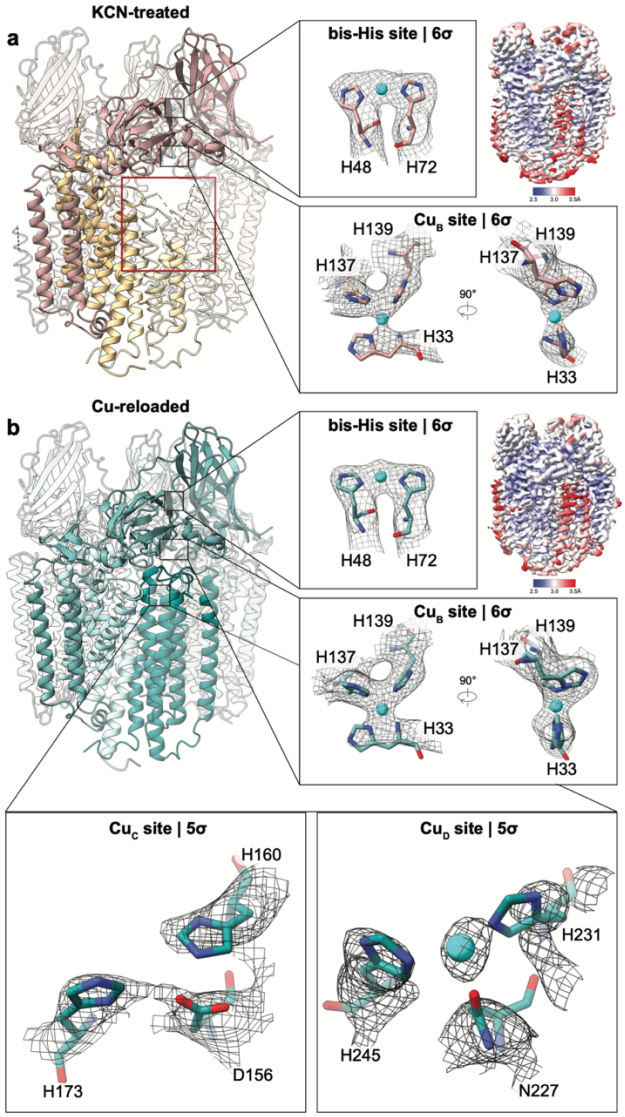

Figure S3.3. CryoEM structures of KCN-treated and copper-reloaded pMMO in native lipid nanodiscs. a, Structure of KCN-treated pMMO solved to 3.22 Å resolution. A red box is shown around the region of PmoC that is disrupted by KCN treatment. The bis-His site, Cu(I), does not appear to be affected by KCN treatment. The map colored by local resolution (blue 2.5 Å, white 3.0 Å, red 3.5 Å) shows relatively low local resolution in the PmoC subunit, with missing density for much of PmoC, particularly the region that would house the Cu_C or Cu_D sites. While the ligands for the Cu_B site remain intact, the density for the copper ion is attenuated. **b,** Overall structure of KCN-treated, then Cu-reloaded pMMO. The structure of PmoC is recovered, allowing for tracing of the protein backbone and fitting of side chains. The bis-His site appears unchanged by KCN treatment and copper reloading. The map colored by local resolution (blue 2.5 Å, white 3.0 Å, red 3.5 Å) shows lower local resolution in the PmoC subunit, but density for this region is recovered upon copper reloading. Density for the Cu_B site is regenerated upon copper reloading. CryoEM densities for the ligands for the Cu_C site are recovered upon copper reloading, but no density corresponding to a metal ion is apparent in this site. CryoEM densities for the ligands for the Cu_D site are recovered upon copper reloading, along with a spherical density modeled as a copper ion on the basis of the recovered EPR signal and methane oxidation activity.

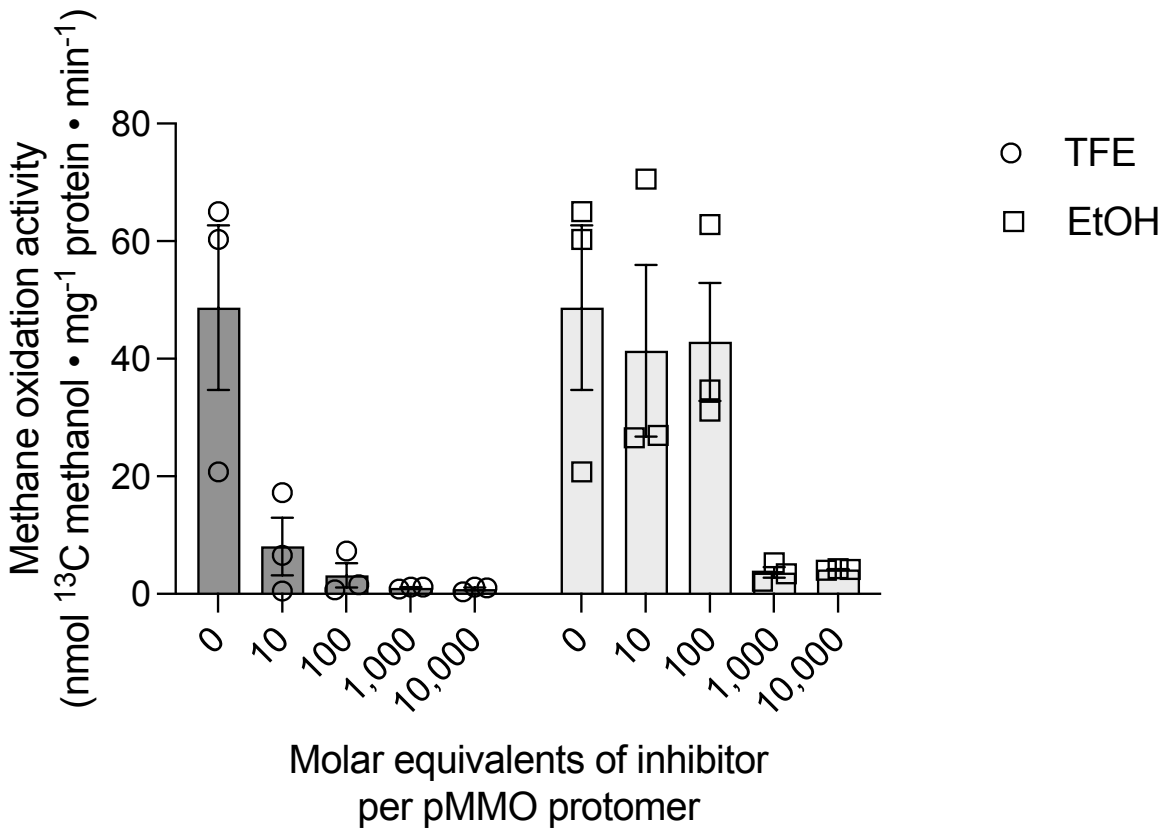

Figure S3.4. Inhibition of pMMO in isolated membranes by 2,2,2-trifluoroethanol (TFE) and ethanol. TFE and ethanol were added in 10, 100, 1,000, and 10,000 molar equivalents per protomer of pMMO. TFE inhibits pMMO activity in membranes with as little as 10 molar equivalents, while ethanol requires as much as 1000 molar equivalents to achieve a significant reduction in methane oxidation activity. NADH was used as the source of reducing equivalents for these reactions. Error bars represent standard error from the mean with n=3 replicates.

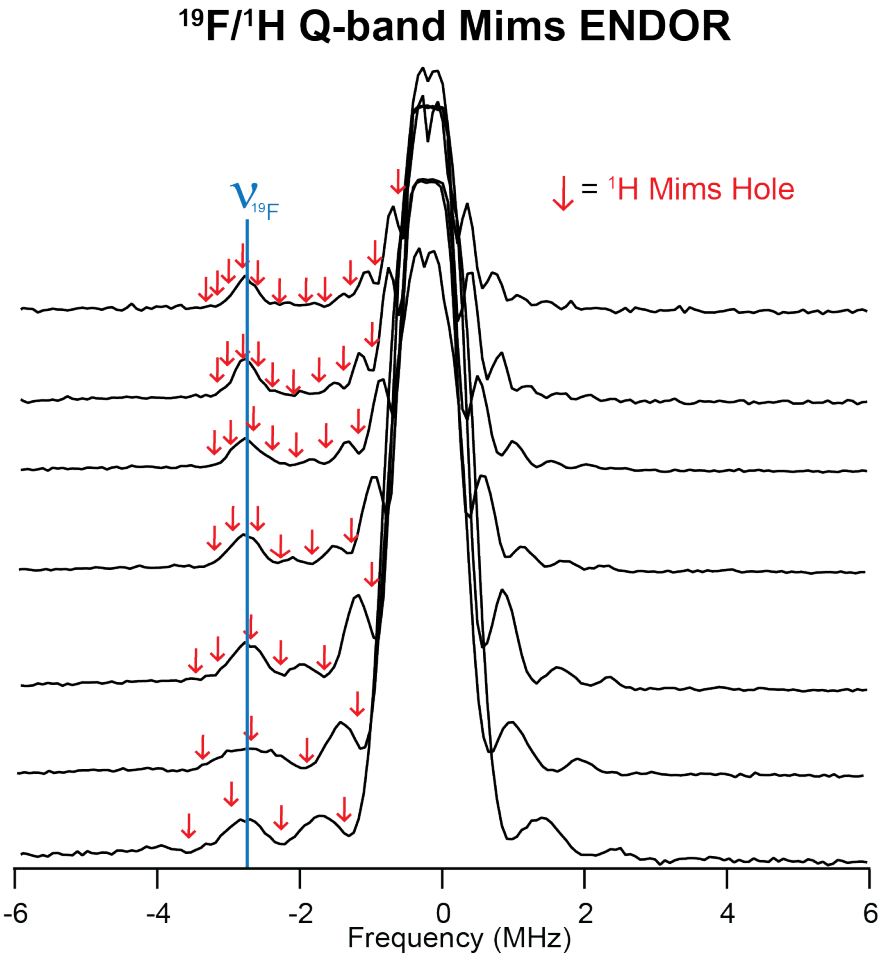

Figure S3.5. $^{19}F/^{1}H$ Q-band Mims ENDOR of pMMO with 20x TFE while varying τ values. The presence of ENDOR signal at the ^{19}F Larmor frequency, ~3 MHz blow the ^{1}H Larmor frequency at multiple τ values that put ^{1}H Mims suppression "holes" on the signal establishes that the response is from ^{19}F present near the copper centers and not the ^{1}H response associated with couplings of ~6 MHz. Mims conditions: 34.72 GHz MW frequency, magnetic field set to *g* = 2.10, 2 K, T_{RF} = 35 μs, RF tail = 15 μs, repetition time of 100 ms, ~20 scans each.

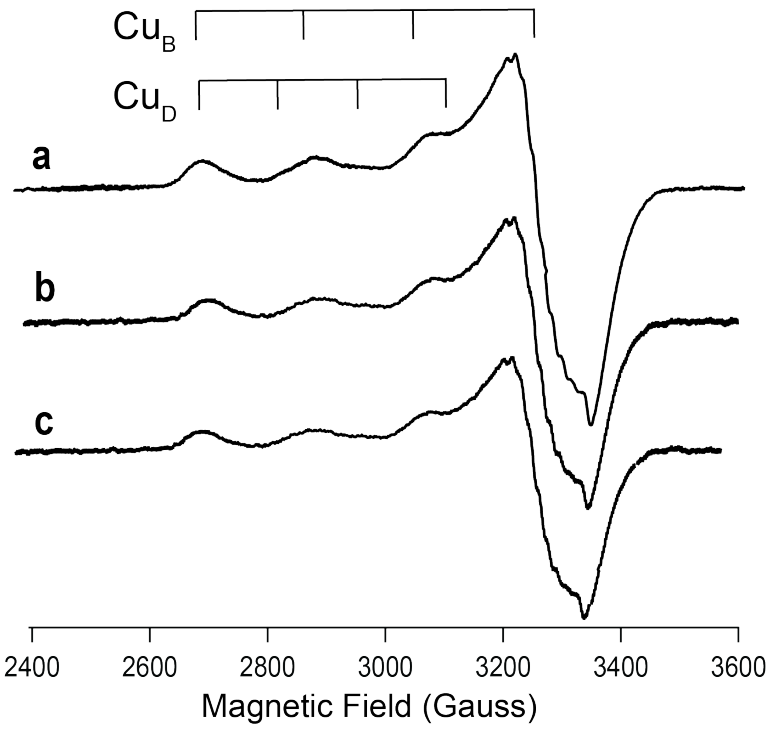

Figure S3.6 CW X-band EPR of pMMO with the addition of fluorinated molecules. a, pMMO plus 20x TFE **b,** crosslinked pMMO plus 20x TFE. **c,** pMMO plus 20x 4-fluorophenol. All three spectra exhibit the $^{63/65}$Cu $A_{\|}$ splitting associated with the Cu_B and Cu_D sites. Conditions: 9.37 GHz MW frequency, 30 K, 12.5 G modulation, 250 μW microwave power, 320 ms time constant, 10G/s scan rate, 10 scans each, intensity normalized.

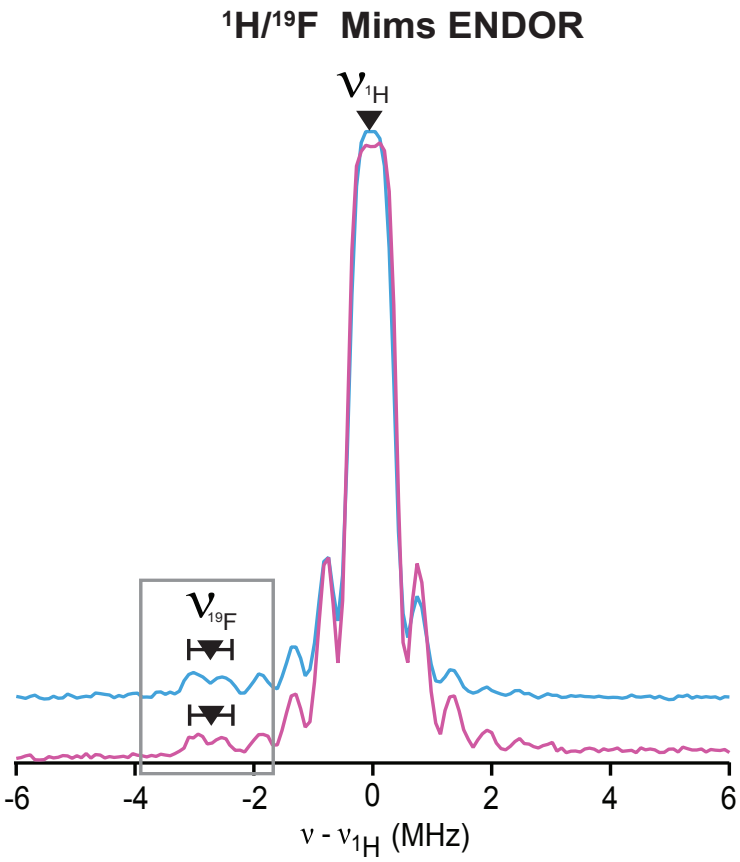

Figure S3.7 ^{19}F/^{1}H Q-band Mims ENDOR of pMMO plus 20 equivalents TFE without (blue) and with (pink) the prior addition of a 0.05% glutaraldehyde crosslinker, spectra taken at $g_{||}$. Both spectra reveal TFE ^{19}F doublets with identical couplings, showing that the TFE interaction is the same between the samples. Mims conditions: 2 K, π/2 = 50 ns, τ = 900 ns, T_{RF} = 60 μs, RF tail = 5 μs, repetition time of 100 ms, ~40 scans each.

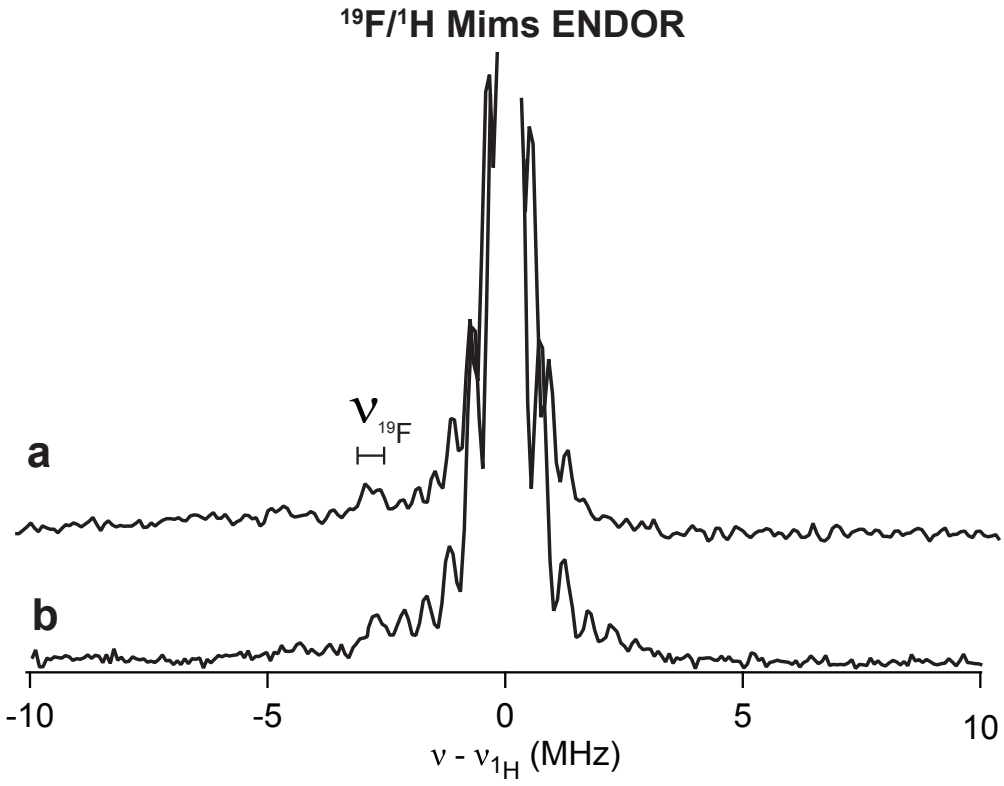

Figure S3.8. 19F/1H Mims ENDOR of pMMO with the addition of 20x TFB. a, crosslinked pMMO with 20x TFB; **b,** non-crosslinked pMMO with 20x TFB. The crosslinked pMMO with TFB reveals a ^{19}F doublet with splitting of ~0.4 MHz at $g_{\perp}$, which is consistent with fluorine ~ 7 Å away from Cu(II), in plane with the coordinating residues. Signal is largely absent in **b**, indicating that at a minimum, the TFB is not ordered. Mims conditions: MW frequency 34.69 GHz (**a**) and 34.71 GHz (**b**), 2 K, π/2 = 50 ns, τ = 1250 ns, T_{RF} = 60 μs, RF tail = 5 μs, repetition time of 100 ms, ~100 scans each.

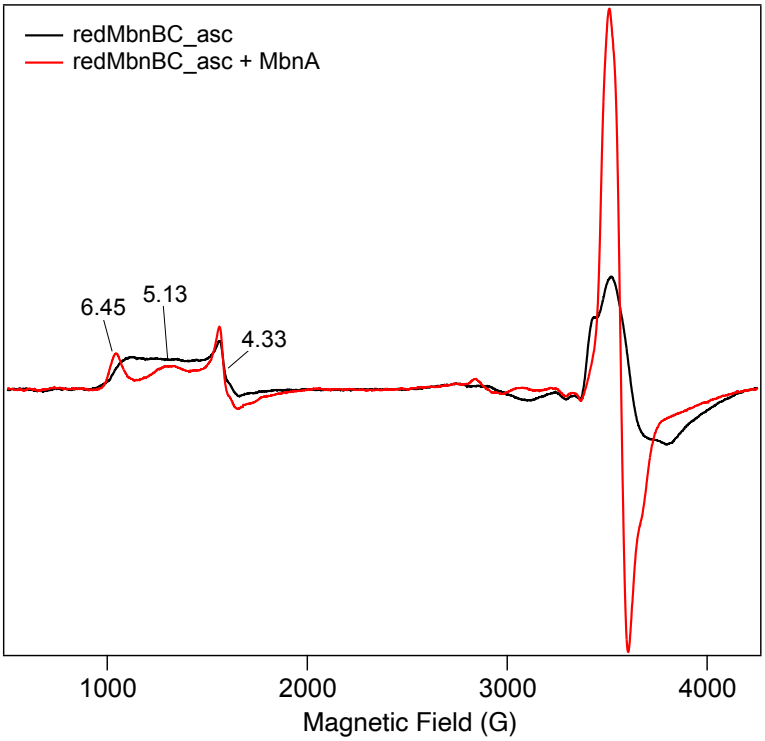

Figure S4.1 Full EPR spectra of redMbnBC_asc and redMbnBC_asc with MbnA showing potential perturbations of features in the low field region upon an addition of MbnA.

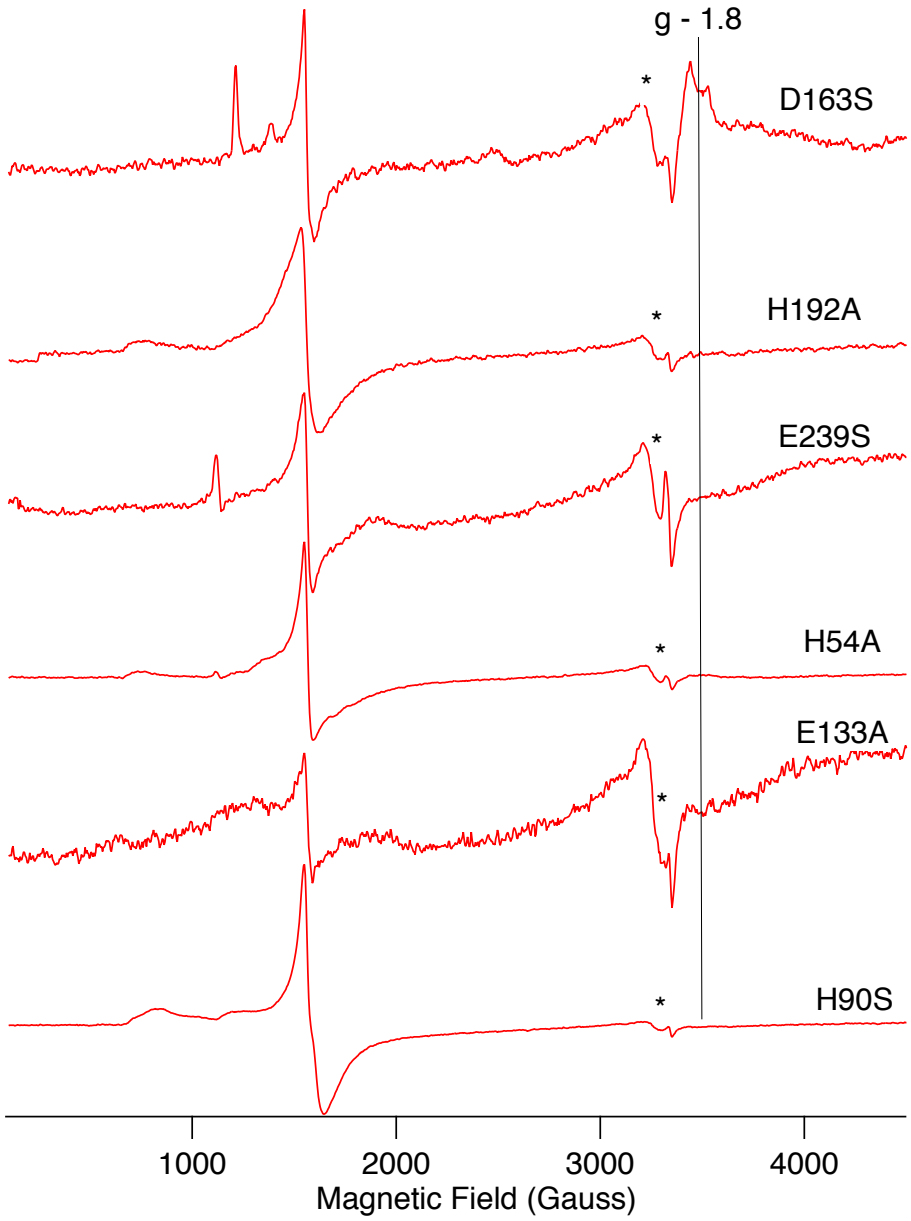

Figure S4.2. EPR spectra of MbnBC variants. Only D163S has the mixed valent g = 1.8 feature while the others exhibit only S = 5/2 high spin monoiron features. Each spectrum also contains a small Cu(II) contaminant marked with the asterisks.

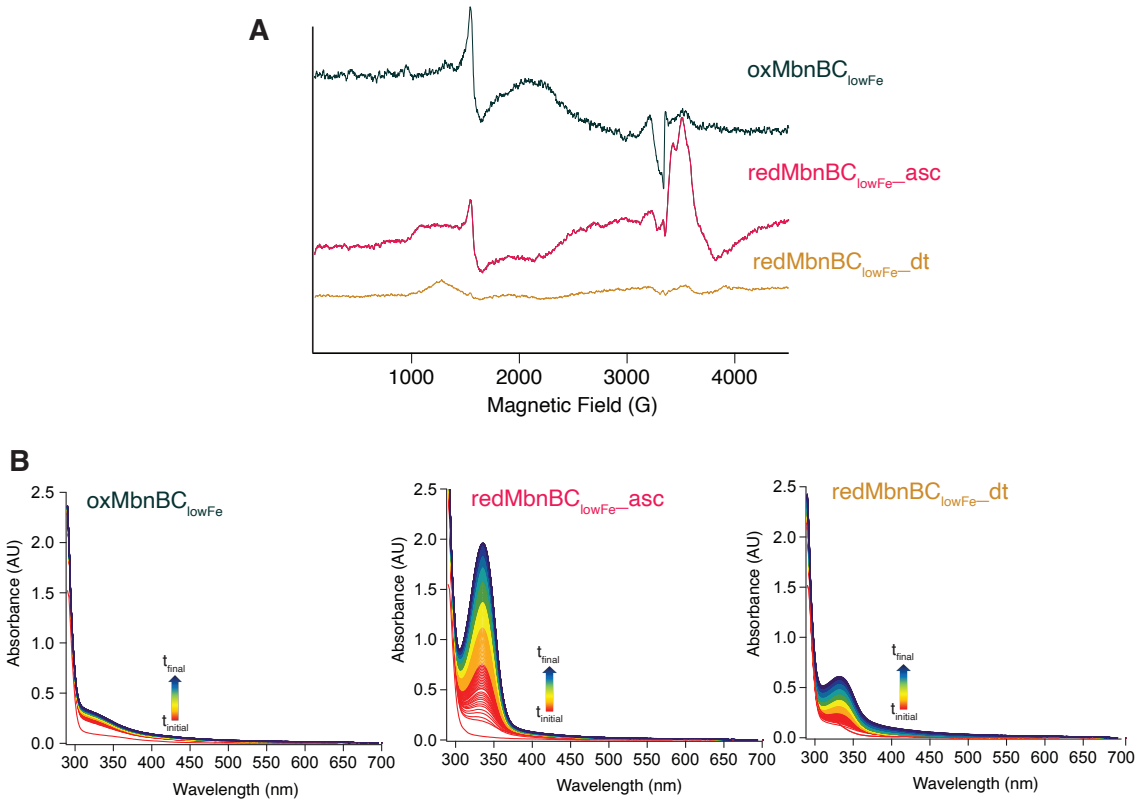

Figure S4.3 EPR spectra and activity analysis of MbnBC$_{lowFe}$. (*A*) EPR spectra of MbnBC$_{lowFe}$ treated with ascorbate (asc) and dithionite (DT). A small amount of a Cu(II) contaminant (~3200 G) associated with the buffer is also present. (*B*) Reactions of 40 μM of MbnBC with 200 μM of MbnA under aerobic conditions were monitored for 1 h and the spectra were collected with an interval of 15 s. Arrows indicate the increase at 335 nm as a function of time with the starting spectrum colored red and the ending spectrum colored purple.

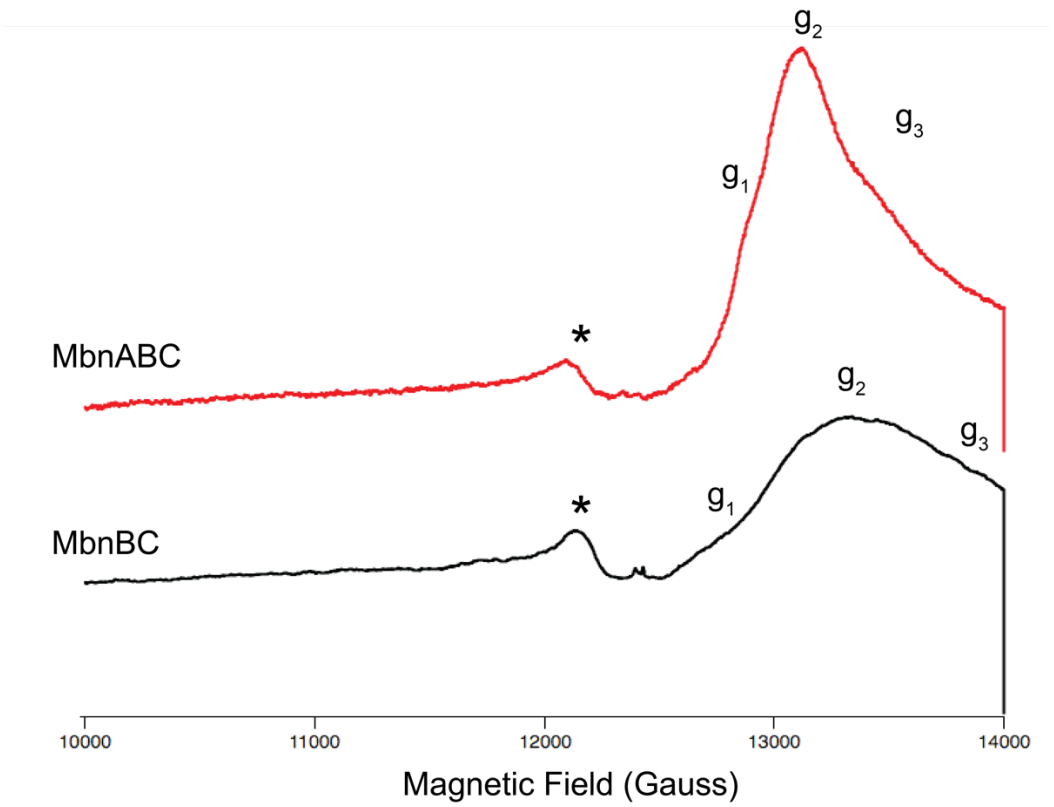

Figure S5.1 Q-band CW EPR of MbnBC and MbnABC. Ascorbate reduced MbnBC with 2 equivalents of MbnA added anaerobically is in red, and without in black. The EPR is in absorption mode to allow for easy view of the principal g-values and the differences between the two species. The asterisks mark small amounts of Cu(II) signal present in the samples.

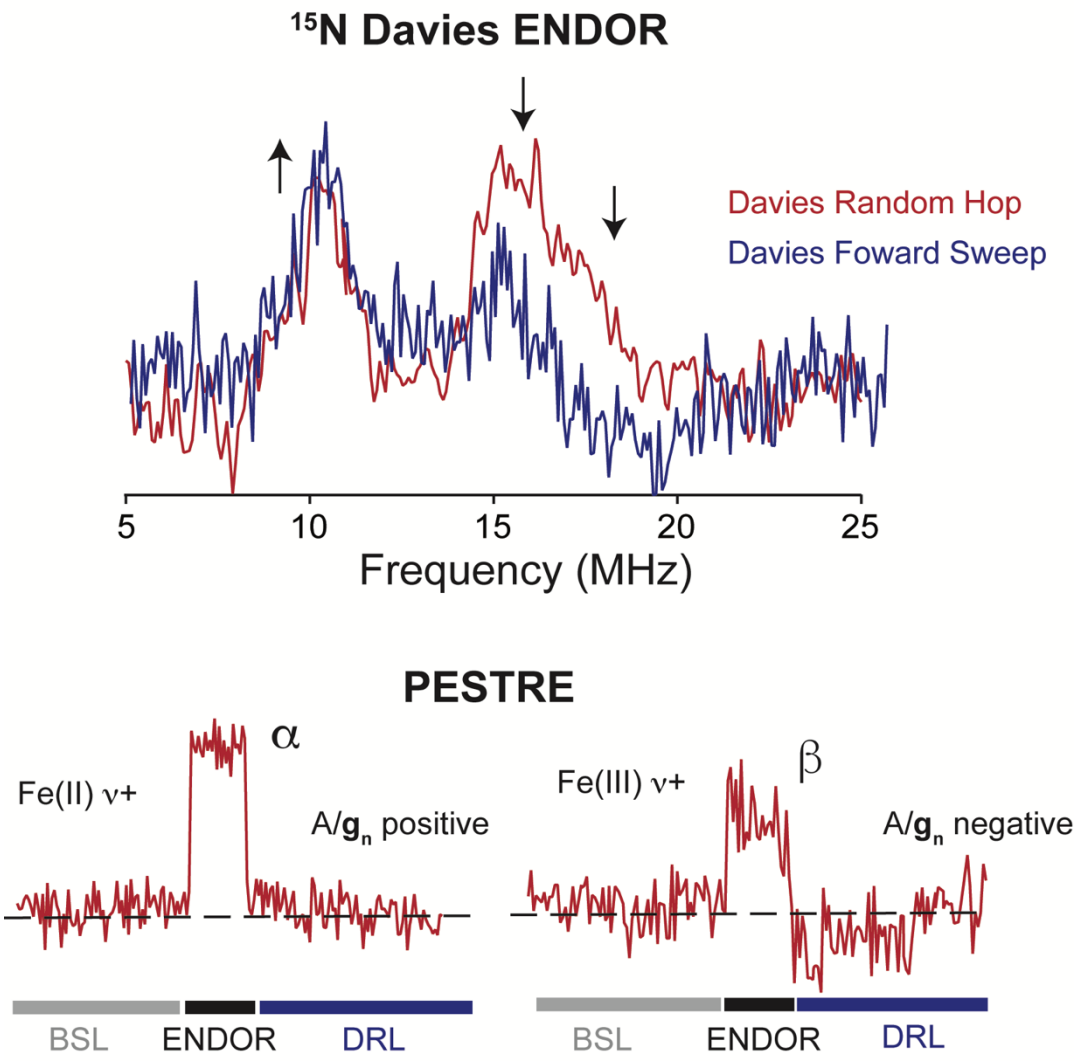

Figure S5.2. Sign determination of the 15N couplings. **Top.** A comparison of random hop 15N Hard Davies ENDOR at g = and swept 15N Hard Davies ENDOR. The change in intensity, more for the lower frequency Fe(II) peak, less for the Fe(III) ^{15}N signals, is another way to visualize the DRL response and achieve hyperfine sign determination. Bottom PESTRE: Left, the PESTRE experiment performed at 10 MHz, right the PESTRE performed at 17 MHz.

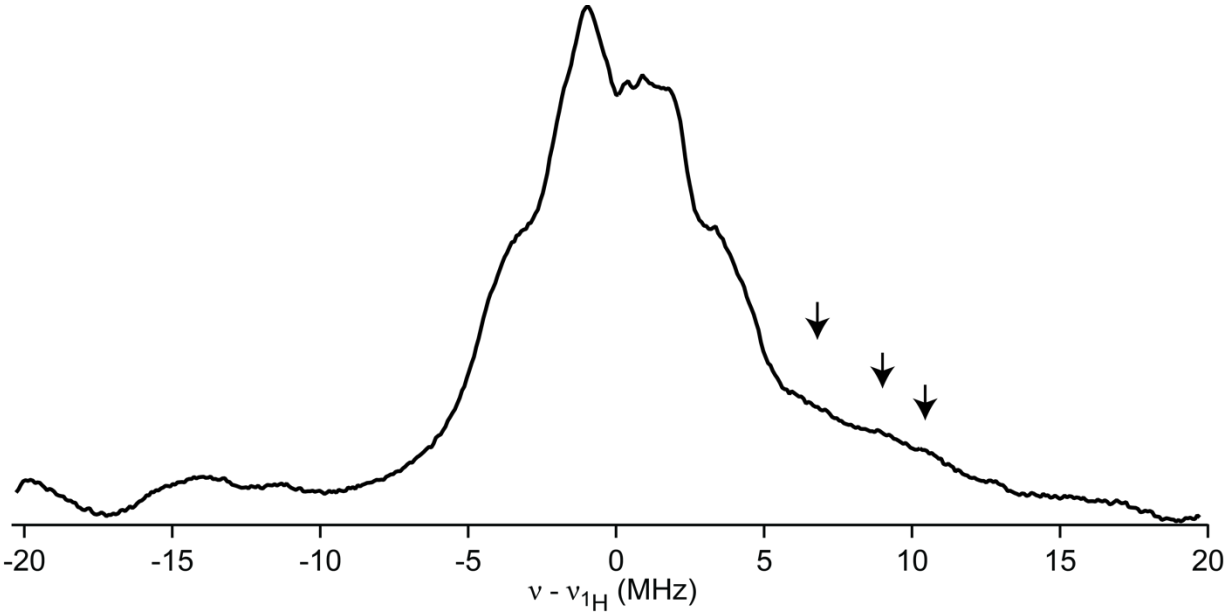

Figure S5.4. CW ^{1}H ENDOR of MbnBC under high modulation conditions. 1H ENDOR is performed under conditions here which resolve couplings from the two different Fe(III)-OHx ligand protons but lose resolution of the μ-OH couplings. This spectrum was taken at g2 at the same field and conditions as **Figure 5.3,** except Modulation is 6.3 G**.**

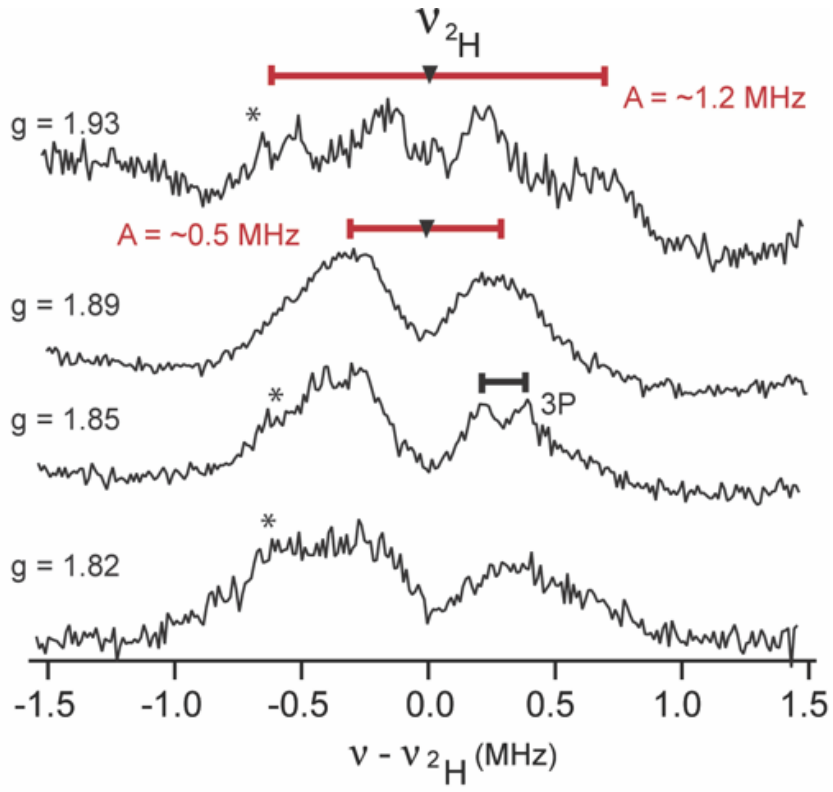

Figure S5.5. Q-band Pulsed Mims ^{2}H ENDOR of MbnBC with D-MbnA added. The Mims ENDOR reveals substantial ^{2}H couplings from the specifically labeled substrate peptide. As this deuterated label is unexchangeable, the couplings can only stem from interaction of the iron center with the peptide. The magnitude of the couplings suggest it is bound the Fe(III) site, but more analysis is required. The * signifies signals from the ^{1}H harmonic, and not ^{2}H ENDOR responses. The bracket represents |A| and the ▼ represents the ^{2}H Larmor frequency. *Mims ENDOR conditions*: 2 K, 34.70 GHz, 100 ms repetition time, π/2 = 50 ns, τ = 500 ns, T_{RF} = 35 μs, RF tail = 5 μs.

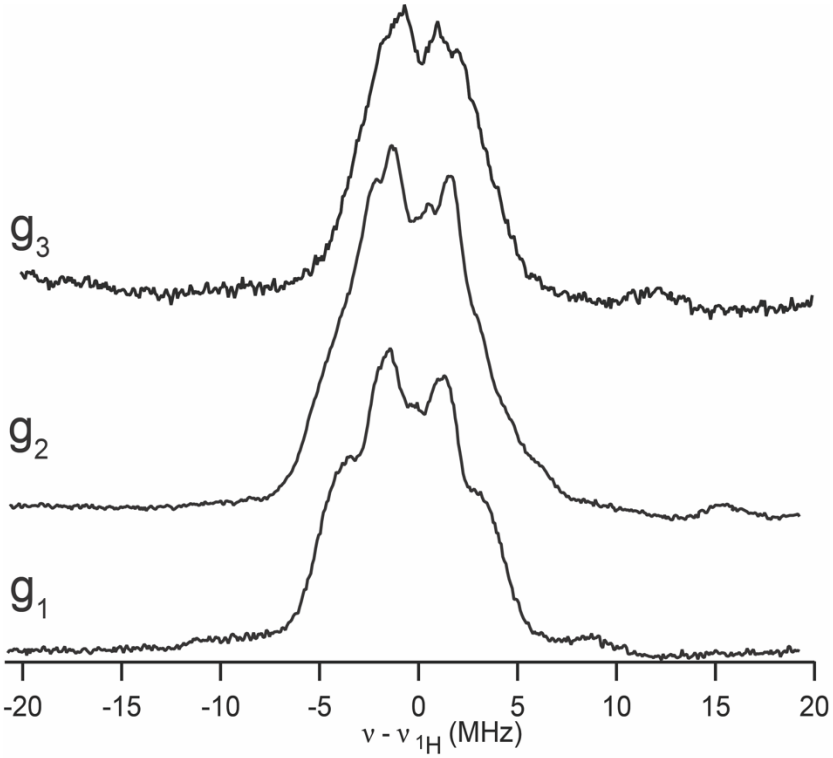

Figure S5.6 Q-band CW ^{1}H ENDOR of MbnABC. The results of this experiment are discussed in the text of **Chapter 5,** comparing these results of the CW ^{1}H ENDOR collected for MbnBC . The conditions are the same as what is reported in **Figure 5.3**.

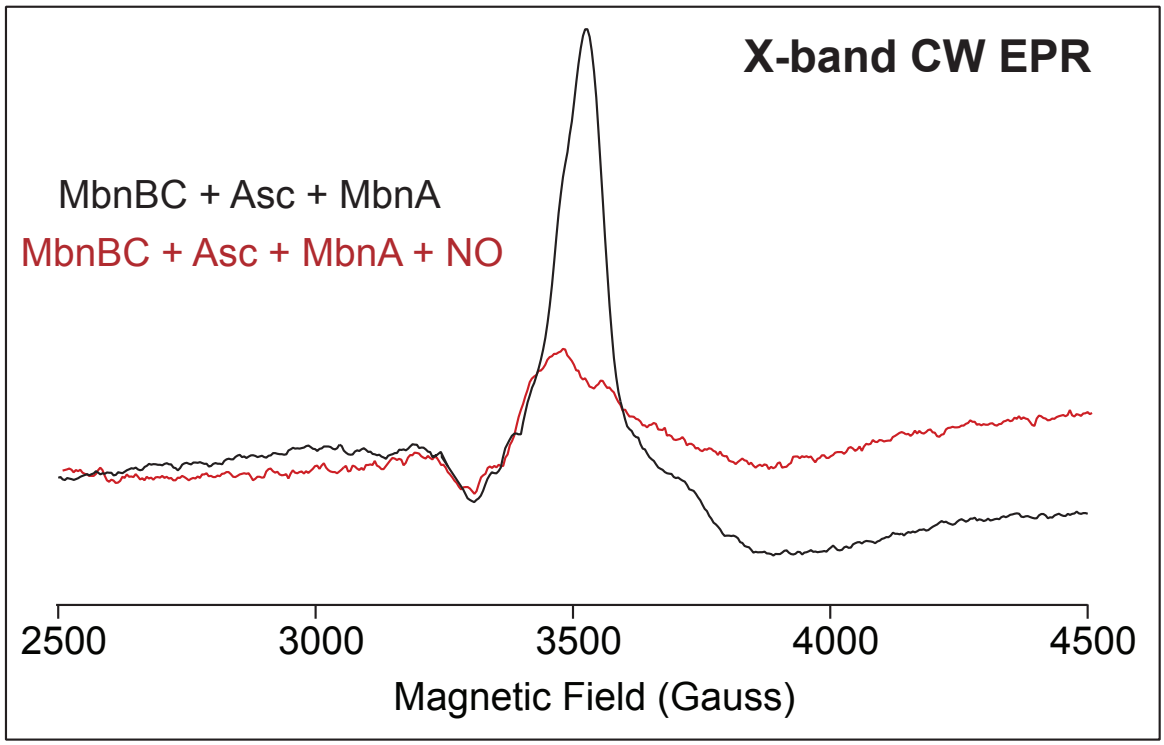

Figure S5.6 X-band EPR of MbnABC and MbnABC + NO. The MbnABC samples was subjected to 5 equivalents of NONOate (prepared in MOPS buffer) anaerobically. The signals from MbnABC are no longer observed after NO addition, but signals of MbnBC seem to remaining, suggesting samples without MbnA bound cannot react with NO. Conditions: 8 K, 9.37 GHz, 10 G modulation, 10 G/s, 320 ms time constant.

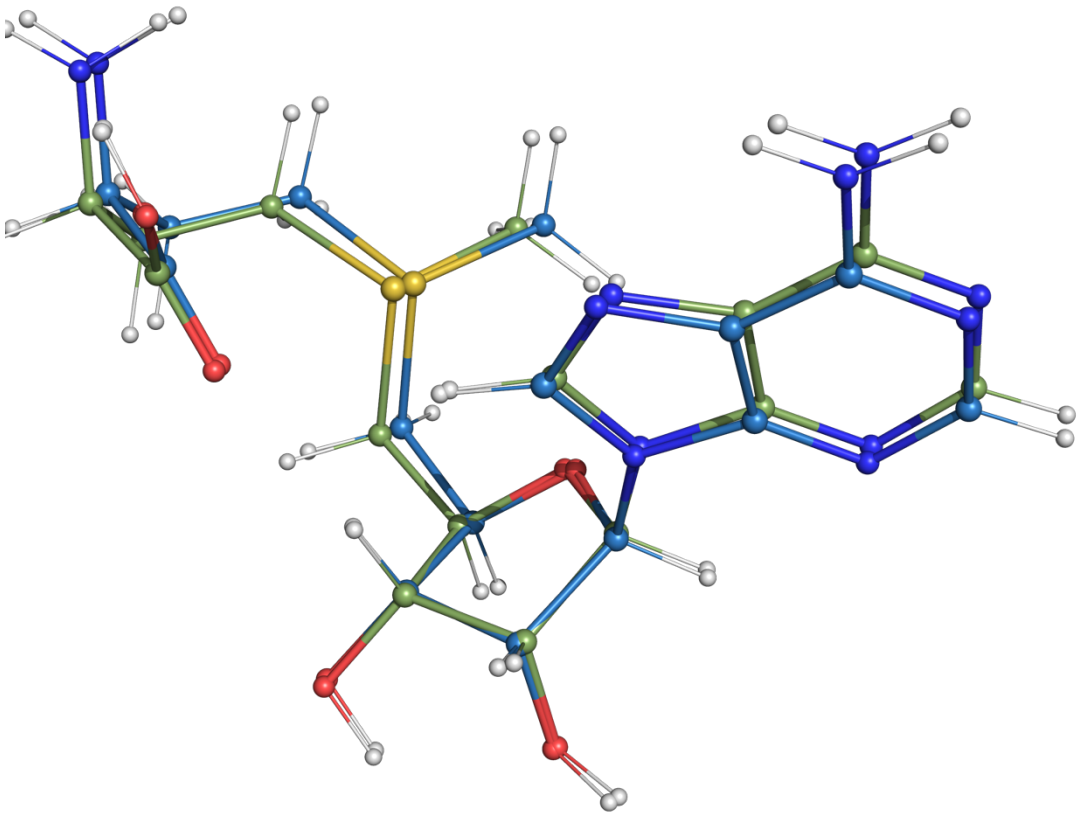

Figure S6.1 “Relaxed” DFT Computed SAM Cofactors – DFT geometry optimized structures (B3LYP/G with TVZP basis) of the SAM Cofactor of both 5’-dAdo• former (SPL - PDB: 4fhd 2.0Å) and a •CH_3 former (HydE – PDB: 3CIW 1.35Å), with protonated carboxylic acid and unprotonated amine. The crystal structure of each was used as the starting coordinates with hydrogens added. As shown they both relaxed to a near identical geometry – with the PFL-AE SAM making the drastic switch from 2’-endo/axial C4’-C5’ bond to a 3’-endo structure with an equatorial C4’-C5’ bond, while the HydE SAM undergoes almost no change in conformation.

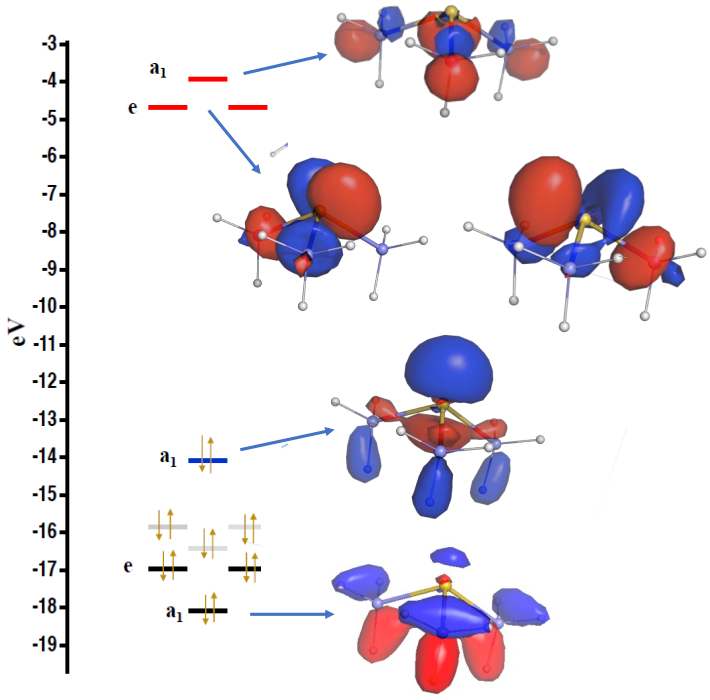

Figure S6.2: Perspective views of selected orbitals seen ‘top-down’ in **Figure 6.7**

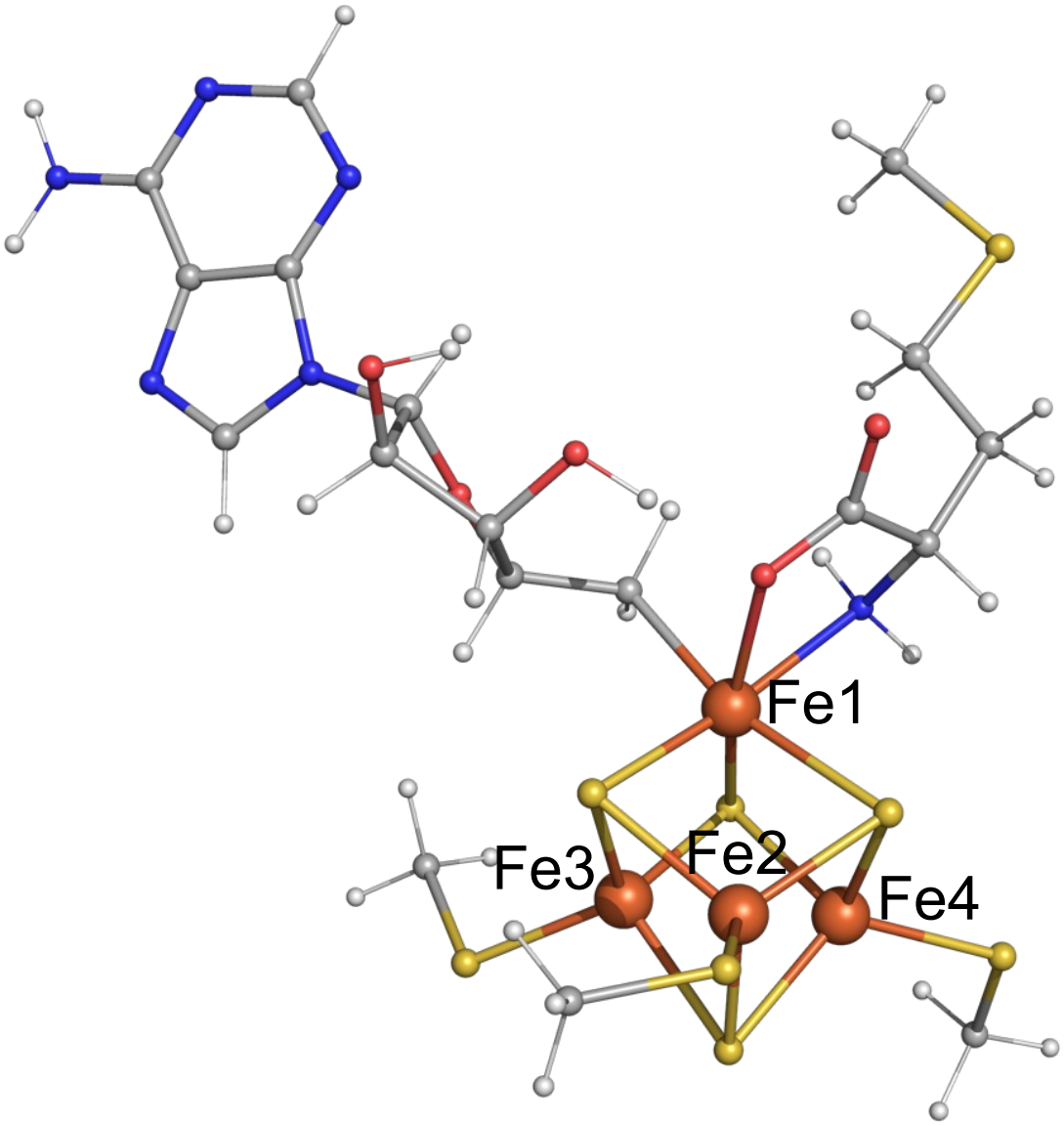

Figure S7.1. Model VI iron labeling scheme. The broken-symmetry spin flips listed in the following tables follow this iron site naming convention. For example, abab corresponds to a spin on Fe1 and Fe3, where as Fe2 and Fe4 would have b spin.

APPENDIX 2: Supplemental Tables

	2C-DFT (TPSSh)			
Molecule	$^{13}C_1$	$^{13}C_2$	^{57}Fe	^{1}H
I	18.3	--	-10.2	3.81
II	18.4	2.0	-13.0	0.39
III	16.7	1.0	19.0	1.8
IV	0.0	0.0	0.0	0.0

Table S7.1: Computed HFCCs using 2C-DFT TPSSh functional for Models **I-IV**

2C-DFT computed values (BP86) Absolute values	$^{13}C_1$	$^{13}C_2$	^{57}Fe	$^{1}H_{avg}$	g_{iso}
	M-CH_3 **(V)**				
αββα	9.3	--	10.1	11.5	2.019
αβαβ	10.9	--	11.1	11.7	2.020
ααββ	8.9	--	9.6	11.2	2.018
	Ω **(VI)**				
αββα	10.5	0.0	15.6	1.3	2.024
αβαβ	21.0	0.5	17.1	3.3	2.015
ααββ	17.8	0.5	14.4	3.2	2.014

Table S7.2: All spin configuration HFCCs results for **V** and **VI,** using the BP86 functional.

2C-DFT computed values (TPSSh) Absolute values	$^{13}C_1$	$^{13}C_2$	^{57}Fe	$^{1}H_{avg}$	g_{iso}
	M-CH_3 **(V)**				
αββα	10.2	--	7.3	11.1	2.019
αβαβ	10.7	--	6.3	11.0	2.020
ααββ	11.5	--	7.3	11.1	2.019
	Ω **(VI)**				
αββα	30.5	1.3	21.9	1.3	2.024
αβαβ	29.7	0.3	19.9	3.3	2.015
ααββ	43.1	2.7	24.0	3.2	2.014

Table S7.3: All spin configuration results for models **V** and **VI,** using the TPSSh functional.